LEABHARLANN CHOLÁISTE NA TRÍONÓIDE, BAILE ÁTHA CLIATH | TRINITY COLLEGE LIBRARY DUBLIN
Ollscoil Átha Cliath | The University of Dublin

Terms and Conditions of Use of Digitised Theses from Trinity College Library Dublin

Copyright statement

All material supplied by Trinity College Library is protected by copyright (under the Copyright and Related Rights Act, 2000 as amended) and other relevant Intellectual Property Rights. By accessing and using a Digitised Thesis from Trinity College Library you acknowledge that all Intellectual Property Rights in any Works supplied are the sole and exclusive property of the copyright and/or other IPR holder. Specific copyright holders may not be explicitly identified. Use of materials from other sources within a thesis should not be construed as a claim over them.

A non-exclusive, non-transferable licence is hereby granted to those using or reproducing, in whole or in part, the material for valid purposes, providing the copyright owners are acknowledged using the normal conventions. Where specific permission to use material is required, this is identified and such permission must be sought from the copyright holder or agency cited.

Liability statement

By using a Digitised Thesis, I accept that Trinity College Dublin bears no legal responsibility for the accuracy, legality or comprehensiveness of materials contained within the thesis, and that Trinity College Dublin accepts no liability for indirect, consequential, or incidental, damages or losses arising from use of the thesis for whatever reason. Information located in a thesis may be subject to specific use constraints, details of which may not be explicitly described. It is the responsibility of potential and actual users to be aware of such constraints and to abide by them. By making use of material from a digitised thesis, you accept these copyright and disclaimer provisions. Where it is brought to the attention of Trinity College Library that there may be a breach of copyright or other restraint, it is the policy to withdraw or take down access to a thesis while the issue is being resolved.

Access Agreement

By using a Digitised Thesis from Trinity College Library you are bound by the following Terms & Conditions. Please read them carefully.

I have read and I understand the following statement: All material supplied via a Digitised Thesis from Trinity College Library is protected by copyright and other intellectual property rights, and duplication or sale of all or part of any of a thesis is not permitted, except that material may be duplicated by you for your research use or for educational purposes in electronic or print form providing the copyright owners are acknowledged using the normal conventions. You must obtain permission for any other use. Electronic or print copies may not be offered, whether for sale or otherwise to anyone. This copy has been supplied on the understanding that it is copyright material and that no quotation from the thesis may be published without proper acknowledgement.

Electron and Spin Injection in Short-Channel Organic Semiconducting Devices

Simone Alborghetti

School of Physics, Department of Science

Trinity College Dublin

A thesis submitted to the University of Dublin in partial fulfillment of the requirements for the degree of

Doctor of Philosophy

October 2011

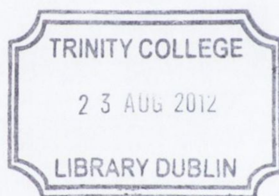
TRINITY COLLEGE
2 3 AUG 2012
LIBRARY DUBLIN

Thesis 9500

Declaration

I declare that this thesis has not been submitted as an exercise for a degree at this or any other university and it is entirely my own work.

I agree to deposit this thesis in the University's open access institutional repository or allow the library to do so on my behalf, subject to Irish Copyright Legislation and Trinity College Library conditions of use and acknowledgement.

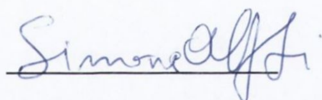

Simone Alborghetti

I would like to dedicate this thesis to my wonderful great-grandmother...

Acknowledgements

First and foremost I would like to express my greatest thanks to my advisor, Prof. J.M.D. Coey. His curiosity about nature in all its aspects is exemplary and I like considering it the most significant teaching in my many years of study. His support, encouragement and patient guidance made this thesis possible. No words could express my appreciation.

Following, my gratitude goes to Dr. P. Stamenov; for discussing and solving together most of the aspects of this work. His ability in problem solving is second to none.

Many thanks to Dr. M. Venkatesan, for interesting discussion in the lab, and to Zhu, for the training on many of the equipment I have used in these last few years, and for the great time we spent together. Ciaran, Damaris, Darragh, Fiona, Hongjun, Huseyin, Lorena, Peter (in alphabetical order) made the time in the lab always enjoyable, and we often labored together over equipment, samples and any sort of problem.

A large number of people have spent time in the group D labs during my stay, I would like to acknowledge them for the many aspects of life in a lab we shared, again in alphabetical order: Adriele, Cathy, Franklyn, Gen, Huseyin, Kaan, Karl, Karsten, Jia Feng, Jonathan, Lorenzo, Marita, Nigel and Robbie. I am probably skipping someone.

People from other groups, departments and universities with whom I have worked at some stages of this thesis are Edmund, Giovanni, Greg, Niall, Ruggero and Tarek. I would like to thank them for their friendliness and professionalism, and for sharing good ideas.

Last but not least, thanks to my entire family and to my friends.

Summary

The realization of an active device that combines electric control of the source-drain current, as in transistors, with the memory effect of spin valves, has long been sought for the next generation spin electronics. The development of the field depends upon the existence of materials and structures that may be used as effective spin-polarized current injectors, transmitters, manipulators and detectors. Spin injection into semiconductors at a contact with a ferromagnetic metal is one of the possibilities that are currently being explored.

The experiments described in this thesis are devised to explore the problem of spin injection into organic semiconductor at the metal /organic interface.

In the first chapter, the theory of Schottky junctions and tunneling contact is presented; experimental results on various approaches towards the detection of spin-polarization using Schottky barriers are then presented, followed by the illustration of the models to describe charge transport mechanisms in organic mediums.

In the second chapter, the experimental aspects of preparing hybrid organic /metal /insulator devices are illustrated. During this work, we optimized the preparation of small-molecule thin films of Alq_3, oligoacene single crystals of pentacene, and conductive-polymer thin films of P3HT, which have been included, as active channels, in field effect transistors made with ferromagnetic source and drain contacts. The lithographic methods adopted for patterning high-resolution features, with source-drain gap as low as 7 nm, are reviewed.

In the third chapter, we study the temperature dependence of the electrical characteristics of devices based on pentacene single crystals; we observed that current injection at the contact area occurs via the two parallel mechanisms of tunneling and thermoionic emission, and that the response to a local electric field exhibits the general behavior of a hole transporting system. No sign of spin accumulation was detected, suggesting that there may exist an intrinsic mechanism that depolarizes the spin current during hole-transport.

The magneto-transport properties of thin films of Alq_3 were also investigated, revealing the dominant role played by the charges temporarily trapped in localized states, naturally existing in the amorphous organic medium.

In the fourth chapter the electrical characteristics of transistors using polythiophene as active material are considered. An energy barrier is shown to build up when a polymer and a metal are brought together. The height of the barrier appears independent of the work function of the metals used; this is understood in terms of the large density of surface states due to defects in the polymer morphology at the contact area. The presence of a barrier is a fundamental impediment to injection of spin, and no spin valve effect was detected. A spin depolarizing mechanism due to the formation of bipolarons is suggested, which occurs when the conductivity of the organic media is enhanced by increasing the carrier density.

In chapter 5, we give a short summary of the work in this thesis.

Contents

Acknowledgements i

Summary ii

CONTENTS V

List of figures viii

List of tables xix

Nomenclature xx

CHAPTER 1 1

INTRODUCTION 1

Overview 1

Spin electronics 2

Giant magneto-resistance 4

Tunneling magneto-resistance 7

Triode devices 9

Metal-semiconductor contacts: Schottky junctions 11

Tunneling contacts 16

Organic electronics 21

Organic based FET and LED 22

Organic spin electronics 24

Materials for organic electronics 29

Transport mechanisms **32**
Amorphous films 33
Partially ordered thin films 42
Single crystals 48
Contacts 52

This Work **60**

Bibliography **63**

CHAPTER 2 .... **74**

EXPERIMENTAL METHODS **74**

Overview **74**

Nanofabrication **74**
Lithography: elementary concepts 74
UV exposure 76
Electron beam lithography 76
Electron sensitive resists 79
Proximity effect corrections 84
Metal and oxide deposition 85

Fabrication and initial characterization of single crystal organic FETs **88**
Vapor processing technique 88
Nano-manipulation: dual beam system 90
High impedance testing station 92

Preparation of organic thin film transistors **93**
Thin films of Alq_3 93
Thin films of poly(3-hexylthiophene) 95

High impedance transport measurements **98**

Bibliography **99**

CHAPTER 3 ..... **100**

CHARACTERIZATION OF CRYSTALLINE PENTACENE **100**

Introduction **100**

Fabrication of the crystals **101**

Pentacene crystal structure **102**

Transport mechanisms in organic crystals **105**

Fabrication of short-channel devices **108**

High-impedance electrical characterization **112**

Conclusions **120**

Appendix A: Amorphous thin films of Alq_3 ..... **122**

Appendix B: Fabrication of C_{60} single crystal-lateral devices **126**

Bibliography **129**

CHAPTER 4 ..... **132**

SHORT-CHANNEL FIELD-EFFECT TRANSISTORS BASED ON POLYTIOPHENE WITH FERROMAGNETIC ELECTRODES **132**

Introduction **132**

Conjugated polythiophene derivatives **134**

Transport mechanisms in conjugated polymers **137**

Organic FETs operation **145**

Design of the experiment **148**

High impedance electrical characterization **150**

Parasitic effects 150

CoFe electrodes 155
NiFe electrodes 165
Insertion of a tunnel barrier 166
Gold electrodes 171

Conclusions 174

Bibliography 177

CHAPTER 5 181

CONCLUSIONS 181

Bibliography 186

List of figures

Figure 1.1 *Magneto-resistance traces of three Fe/Cr multilayers, at 4.2K. The current and the applied field are in the plane of the layers, from* (Baibich, 1988) **4**

Figure 1.2 *Representation of a GMR device consisting of two ferromagnets (FM) and a non-magnetic spacer (NM) in the parallel (top-left) and anti-parallel (top-right) configuration. The magnetization is indicated by the white arrows. The trajectory of electrons with opposite spin direction is represented with black solid and dotted lines. A corresponding resistor model is given (bottom) for the two configurations. The size of the resistors indicates how large the electrical resistance is for the corresponding spin species. As in* (Naber W. , 2007). **5**

Figure 1.3 *Schematics of a current-perpendicular to plane GMR device. The dotted arrows represent the spin current. The resistor model is shown at the bottom. Bigger resistors represent a larger resistance for the indicated spin state.* **6**

Figure 1.4 *Illustration of electron tunneling in MTJ, in the parallel (left) and antiparallel (right) configuration; and corresponding spin density of d-states in ferromagnetic metals (unequal due to exchange spin splitting). The magnetization direction (white arrow) in the ferromagnetic regions is determined by the majority spin sub-band. Dashed lines depict the spin conserved tunneling.* **8**

Figure 1.5 *Resistance of a CoFe/Al_2O_3/Co junction as a function of H in the film plane, at 295 K. The arrows indicate the direction of M in the two films. It is also shown the variation in resistance of the CoFe and Co films, from* (Moodera, 1995). **9**

Figure 1.6 *Scheme of a Datta-Das spin-FET. Source and drain are ferromagnetic metals, with parallel magnetic moment. The role of the gate is to generate an effective magnetic field which causes the electron spin to precess. The current flowing is largeif*

the precession period is larger than the time of flight, and small if the spin direction is reversed. 9

Figure 1.7 *Energy diagram for two portions of metal (M) and semiconductor (S) separated by vacuum (V).* 11

Figure 1.8 *Energy diagram for a Schottky junction, with no applied external bias. Symbols have their usual meaning;* x_d *refers to the width of the depletion region.* 12

Figure 1.9 *Current contributions in a Schottky barrier, a: thermoionic emission over the top of the barrier and b: tunneling through the barrier.* $\Delta\Phi_0$ *is the barrier reduction coming from the image forces.* 13

Figure 1.10 *Qualitative illustration of the I:V characteristics of an ohmic contact and a Schottky barrier.* 14

Figure 1.11 *Simplified energy diagram of two similar metals separated by vacuum and by insulator.* 17

Figure 1.12 *Energy diagrams of two dissimilar metals before (left) and after (right) they have been bought in contact with an insulating layer.* 17

Figure 1.13 *Energy diagram of a rectangular barrier with image force included for the case of zero (left) and a small voltage* V_a *(right) applied across the junction; from (Simmons, 1963).* 18

Figure 1.14 *Schematic diagram of the wave function in the three regions, having matching k vectors.* 19

Figure 1.15 *Diagram of two constant energy surfaces of* $E=E_F$ *and their projections on the plane of the tunnel interface. From* (Stamenov, 2007). 20

Figure 1.16 *Representation of the two channel model. The differential conductance of the up and down spin channels is related to the transverse Fermi surface cross sections for spin-up and spin-down electrons. When the magnetization of the two electrodes is parallel, the total conductance is equal to the sum of the conductances of the individual channels. For the anti-parallel case, the conductance is smaller, as it is*

proportional to the sum of the smaller of the two cross sections. From (Stamenov, 2007). 21

Figure 1.17 *Chemical structures of some of the most studied organic small molecule and oligomers semiconductors.* 30

Figure 1.18 *Structure of some polymer semiconductors used in electronics, for LED and FET applications (see text for details).* 31

Figure 1.19 *Energy levels in a doped and compensated semiconductor. E_d is the ionization energy of a donor, W_d the spread of energy levels. From* (Mott, 1968). 34

Figure 1.20 *Polarization well for two donor states in a glass, an electron is in the left hand well. a) Unexcited, b) excited, c) fully excited in a way that the electron can hop from one to the other. From* (Mott, 1968). 35

Figure 1.21 *Left: representation of a Gaussian DOS with a charge hopping upwards in an empty state. Right: simplified constant DOS used for the analysis of Mott's variable range hopping.* 36

Figure 1.22 *Temperature dependence of the electron drift mobility in amorphous silicon, the inset shows the change in gradient near the temperature T_c, which reflects a change in the transport mechanism. Note the log-linear scale. Taken, as an illustrative example, from* (Le Comber, 1970). 42

Figure 1.23 *Sketch of density of states of valence and conduction bands, showing the region (shaded) in which the states are localized and the regions in which the carriers move with a short mean free path. From* (Davis, 1970) 43

Figure 1.24 *The horizontal lines show the traps in the semiconductor; if the density of trap is high, the bottom of the conduction band is replaced by the mobility edge. Below the mobility edge the electrons move by thermal activated hopping (shown by the arrow) whereas the dotted line show the motion by trap and release, and sequent trapping. From* (Mott, 1973) 44

Figure 1.25 *Molecular structure of regio-regular PQT and three dimensional packing of the molecules. Note the symmetric side chain $C_{12}H_{25}$. From* (Zhao, 2004). 46

Figure 1.26 *Illustration of the electric field lowering of a Coulomb barrier* E_0 *by the Pool-Frenkel* (ΔE_{pf}) *mechanism. From* (Davis, 1970). **47**

Figure 1.27 *Electron and hole mobilities as a function of temperature for anthracene. From* (Karl, 1991). **48**

Figure 1.28 *Mobility of naphthalene measured by transient photoconductivity from 54 to 324 K. From* (Schein, 1978). **49**

Figure 1.29 *Equivalent circuit of an FET including nonlinear source and drain contact resistances. From* (Necliudov, 2000). **53**

Figure 1.30 *Circuit model from* (Necliudov, 2003). R_L *are resistors responsible for gate leakage currents.* **53**

Figure 1.31 *Output characteristics of P3HT thin film transistor with Au electrodes at 7 K. The non-linear increase at low biases is highlighted by an arrow.* **55**

Figure 1.32 *Profiles of the electrostatic potential across the channel of operating transistors with Schottky barrier height* > 0.3 *eV, from* (Burgi, 2003) **56**

Figure 1.33 *Profiles of the electrostatic potential across the channel of operating transistors with Schottky barrier height* < 0.3 *eV, from* (Burgi, 2003) **56**

Figure 1.34 *Diagram of the energy levels illustrating the effect of* V_G *on the hole injecting Au/6T contact. As* V_G *becomes more negative, the depletion width decreases, due to a higher concentration of induced carriers. From* (Chwang, 2000). **57**

Figure 1.35 *AFM images showing the different nano-morphology of P3HT at the contact edges of a) normal and b) planar FET. The contact edges introduce a visible distortion compared to the continuous semi-crystalline fibrils of the planar FET. From* (Singh, 2010). **58**

Figure 1.36 *Equivalent circuits of FETs. The top circuit includes a tunnel diode in series with the left and right contact resistances and the channel. To explicitly account for the temperature dependence a diode in parallel with the tunneling contact is added in the bottom circuit.* **61**

Figure 2.1 *Schematic of the sequential steps included in a typical lithography process. From* (Ramos, 2009). 75

Figure 2.2 *Left: SEM column structure from* pemtron.com. *Right: representation of the various elements in a column of a Zeiss Supra 40; electrons are field-emitted and consequently collimated through electromagnetic lenses, from* Zeiss.com. 77

Figure 2.3 *Scattering of electrons in a resist/ siliconn substarte obtained by Monte CArlo SImulatioN of electrOn trajectory in solid (CASINO), at accelaration voltages of 5 KV and 15 KV.* 78

Figure 2.4 *Illustration of the deposition occurring at the edges between the resist and the substrate in the case of directional (right) and non-directional /sputtering deposition (left). This effect becomes more visible when dealing with nanoscale patterns, in which the gap is comparable or smaller than the resist thickness.* 86

Figure 2.5 *SEM pictures of pair of electrodes resulting by lift-off of structure deposited by sputtering (left) and e-beam evaporation (right). The appearance of "rabbit ears" at the edges of the electrodes is clearly shown.* 87

Figure 2.6 *Schematic of a single crystal organic field effect transistor with spin polarized electrodes. The SiO_2 surface is chemically modified with self-assembled monolayer (SAM).* 88

Figure 2.7 *Physical vapor transport method: purified source material is placed in a quartz tube, heated by a resistive heating element to its sublimation temperature, and carried down a temperature gradient by a stream of inert carrier gas. The material resublimes in the coldest zone of the furnace to form crystals.* 90

Figure 2.8 *Picture of the internal of the chamber, showing the electron column and the manipulator. The stage is tilted to allow simultaneous exposure to electrons and ions from the SEM and FIB columns.* 91

Figure 2.9 *Schematics of fabrication of pentacene single crystal pentacene FET. A crystal is placed on the patterned substrate by mean of a piezo-manipulator mounted inside the FIB vacuum chamber and remotely controlled; in situ chemical vapor deposition (CVD) of SiO_2 allowed securing the micron object.* 92

Figure 2.10 *Picture of the first version of the organic vacuum chamber: (1) evaporation sources, (2) main chamber, (3) load lock, (4) turbo molecular pump, (5) gate valve, (6) vacuum gauge.* **95**

Figure 3.1 *Schematic of a single crystal organic field effect transistor with spin polarized electrodes. The SiO_2 surface is chemically modified with self-assembled monolayer (SAM).* **101**

Figure 3.2 *Crystal structure of pentacene. Left: stacked layers of molecules, along the c axis. The unit cell has been simplified by using a simple orthorhombic cell, ignoring α, β and γ to facilitate the view. The side view of the unit cell is also indicated. Right: molecular packing in the a-b layer, it is evident the herringbone arrangement. Developed using Mercury 2.4.5 (developed at Cambridge for crystal structure visualization, free download at www.ccdc.cam.ac.uk).* **103**

Figure 3.3 *View of independent pentacene crystals on a metallized SiO_2 substrate (SEM). The tungsten tip of a piezo manipulator mounted inside the vacuum chamber is also shown; it allowed precise manipulation of the micron sized objects on the sample substrate while imaging via the SEM.* **103**

Figure 3.4 *AFM image of the top surface of a pentacene crystal. It is highlighted the amplitude (A), contrast (B), and profile (C) information (C is obtained along line 1) on a 500 x 500 nm scan, molecular steps are separated about 100 nm.* **104**

Figure 3.5 *Left: Scanning electron micrograph of a partially broken hexagonal pentacene crystal; the b axis of the unit cell is traced, lying parallel to the top surface. The nano-manipulator tip, used to precisely orientate the crystal during the device preparation, is seen on left side of the SEM image. Right: schematic of a hexagonal crystal and of the three unit cell axes.* **104**

Figure 3.6 *EDX elemental analysis of a pentacene crystal. The structure, very rich in carbon, does not contain any heavy impurity, the Si and Au peaks come from the metallized SiO_2 substrate, as shown in the inset.* **105**

Figure 3.7 *Band structure of pentacene along the stacking directions $a^* + b^*$ and $a^* - b^*$(from Γ to K and from Γ to K'). In these directions the bandwidths exceed the polaron binding energy and band transport is possible. And along a^*, b^* and c^* (from*

Γ to X, from Γ to Y and from Γ to Z), here the conduction band shows hardly any dispersion, while a small bandwidth is found for the valence band. From (Endres, 2004). **107**

Figure 3.8 *Distribution of localized states centered at the bottom and top of, respectively, the conduction and valence band.* **107**

Figure 3.9 *SEM micrographs of a set of interdigitated electrodes. Each pair of electrodes consists of two contacts of different width, as highlighted on the right side of the figure, of 200 and 400 nm, separated by a gap of 90 nm. Each electrode is 60 μm long.* **109**

Figure 3.10 *Point electrodes of CoFe separated by about 7.3 nm, prepared by e-beam lithography and lift-off.* **110**

Figure 3.11 T*he schematics of the fabrication of single crystal pentacene FET are shown. A crystal is placed on the patterned substrate by mean of a piezo-manipulator mounted inside the FIB vacuum chamber and remotely controlled; in situ chemical vapor deposition (CVD) allowed securing the micron objects.* **111**

Figure 3.12 *Scanning electron micrographs of organic single crystal FET.* **112**

Figure 3.13 *I:V characteristic of the device at room temperature; on the right hand side is shown the zoom view around the origin, to reveal the potential activation barrier.* **112**

Figure 3.14 *Equivalent circuit of an FET including nonlinear source and drain contact resistances.* **113**

Figure 3.15 *Left: FET characteristics at different gate voltages at 300 K. Right: output characteristic at constant source-drain voltage of V_{SD}= 15 V.* **115**

Figure 3.16 *Plot of the channel resistance vs. the applied gate voltage; the values of the resistance are extrapolated from the I:V characteristics recorded at 300 K.* **116**

Figure 3.17 *Left: FET characteristics at different gate voltages at 10 K. Right: FET characteristics at constant source-drain voltages, V_{SD}= 21 V.* **117**

Figure 3.18 *I:V curves at different temperature, from 10 K to 300K, at -50V applied gate. Resistance is plotted as a function of temperature, for different source-drain bias.* **.118**

Figure 3.19 *Equivalent circuit consisting of a tunneling contact in parallel to a Schottky diode, at each terminal access of the FET.* **118**

Figure 3.20 *Plot of current vs. magnetic field at temperatures 10-300 K.* **120**

Figure 3.21 *I:V characteristic measured at 300 K, under no gate bias applied.* **123**

Figure 3.22 *Left: Transfer Characteristic at constant V_{SD}= -5 V, at 300 K; right: leakage current going to gate during the same scan.* **123**

Figure 3.23 *V:I curve at 300 K fitted to two tunneling contacts.* **124**

Figure 3.24 *Scanning electron micrograph of sub-micron C_{60} rods.* **127**

Figure 3.25 *Set of SEM images showing the fabrication steps to place and secure a C_{60} rod on top of pair of electrodes. From the left: the rod is individuated and approached with the tungsten tip of the piezo-manipulator, in situ CVD of a stripe of SiO_2 allows to move the crystallite onto the desired set of electrodes, SiO_2 wires are deposited to hold the rod in position on the substrate, before the tip is FIB cut or, simply, pulled away breaking the tip of the crystallite.* **127**

Figure 3.26 *I:V curve of a C_{60} rod between Co/Al_2O_3 electrodes, at room temperature, in air.* **128**

Figure 4.1 *Schematics of a polymer based FET, with NiFe electrodes and a self-assembled monolayer (SAM) between the dielectric and the organic semiconductor.* **133**

Figure 4.2 *A: Chemical structure of polythiophene; B: Representation of poly-alkythiophene with the solubilizing alkyl side chains; C: Possible regio-chemical couplings of the alkyl-thiophene molecules, the orientation refers to the relative position of the side groups, head to head (H-H) and head to tail (H-T); D: twisted molecule of regio-random polymer; E: Side view of two chains self-assembled in an ordered structure, as confirmed by X-ray studies.* **135**

Figure 4.3 *Left: Illustration of the structure of a lamella of regio-regular poly-(3-hexylthiophene). For simplicity it is shown the ordering of only two adjacent chains; it is evident that the thiophene rings face each other, within a single sheet of molecules. Right: Two independent lamellas having interdigitation of the side groups. The delocalization of the carriers occurs within a single lamella, giving a two dimensional character to the transport.* **136**

Figure 4.4 *Left: Schematic view of polymer chain segments broken by defects, kinks and twists between which the charge carriers hop. Right: Representation of the energy distribution of the localized states approximated by a Gaussian distribution for the LUMO and HOMO levels.* **138**

Figure 4.5 *Radical cation (polaron) formed by the removing of 1 electron (a hole is marked with +) on the 4th thiophene ring of a polythiophene chain; the re-arrangement of the bond alternation is shown.* **138**

Figure 4.6 *Schematic illustration of how the valence bands of ordered lamellas and disordered grain boundaries line up to give a barrier to holes transfer between lamellas. As in* (Street, 2005). **142**

Figure 4.7 *Illustration of possible grain boundary structures for small-angle (left) and large-angle (right) orientations. The large-angle boundary has more disorder. Each line here represents a polymer chain, aligned to the neighboring chain within a lamella, indicated by a square.* **143**

Figure 4.8 *It is shown a transport path along a preferential direction with low-angle grain boundaries, which form a high-mobility percolation path. As in* (Street, 2005). **143**

Figure 4.9 *Left: I:V curve with no gate voltage applied, at 300 K. Right: transfer characteristic at 2 V drain-source bias, at 300 K.* **151**

Figure 4.10 *Left: family of I:V curves at different gate voltage, at 300 K. Right: gate scan at drain-source bias of 2 V.* **151**

Figure 4.11 *Left: room temperature gate-leakage current with no gate bias applied or at -50 V. Right: gate current at 150K at zero and -50 applied volts on the gate. The*

leakage at 0 V on gate is largely reduced on lowering the temperature but it persisted for high applied gate. **152**

Figure 4.12 *(1) Schematics of a dislocation extending across the whole oxide thickness, which bring the polymer in direct contact with the conductive substrate; (2) a fracture which lengthens deeply within the dielectric, through which charges can tunnel; (3) superficial defect-fracture and (4) deep dislocation underneath an electrode.* **153**

Figure 4.13 *I:V curves at -70 V on the gate at different temperatures from 300 K to 10 K. There is a pronounced non-linearity appearing on the lowering of the temperature. On the right side the log-linear plot of a curve at 100 K is shown.* **155**

Figure 4.14 *I:V characteristics measured at constant gate bias of – 25 V, at decreasing temperature from 300 to 7 K.* **156**

Figure 4.15 *Results of gate scans at different temperatures. The source drain bias was constant at 5 V at high temperatures (left), and 7 V for lower temperatures (right).* **157**

Figure 4.16 *Equivalent circuit consisting of a tunneling contact in parallel to a Schottky diode, at each terminal access of the FET* **158**

Figure 4.17 *Gate leakage current at 100 and 50 K, with -25 V applied on the gate.* **159**

Figure 4.18 *I:V curves clearly showing voltage asymmetry of the drain current, taken at -25 V applied on the gate.* **160**

Figure 4.19 *Plot of the V:I characteristic fitted by our circuit model. The fitting parameters are shown in the inset.* **161**

Figure 4.20 *I:V curves at 7 K as a function of the applied gate voltage.* **162**

Figure 4.21 *Plot of the organic channel resistance as a function of the applied gate voltage, at 7 K.* **163**

Figure 4.22 *Plot of drain current as a function of applied magnetic field, at 7 K.* **164**

Figure 4.23 *Output characteristics measured before and after exposing the device for 14 days at atmosphere. Constant source-drain bias of 5 V was applied during both scans, at a temperature of 300 K.* **164**

Figure 4.24 *Left: transfer characteristic of the FET at 7 K and -50 V, -47 V applied on the gate. Right: output characteristic recorded at 6 V between source and drain.* **165**

Figure 4.25 *Plot of the drain current vs. the applied magnetic field, at 7 K.* **166**

Figure 4.26 *Output characteristics of the Co /Al_2O_3 /P3HT device at decreasing temperature, with -50 V applied on the gate.* **167**

Figure 4.27 *Temperature dependence of the organic channel resistance when -50 V are applied on the gate.* **168**

Figure 4.28 *Set of I:V curves at 7 K at different gate voltage.* **169**

Figure 4.29 *Plot of the drain current vs. the applied magnetic field.* **169**

Figure 4.30 *Left: I:V curve at 7 K of CoFe /Al_2O_3 /P3HT; right: magnetic field scan and recorded drain current.* **170**

Figure 4.31 *Left: I:V curve at 7 K of CoFe /Al /Al_2O_3 /P3HT; right: magnetic field scan and recorded drain current.* **171**

Figure 4.32 *I:V curves of an Au /P3HT device at 7 K at different gate voltages.* **172**

Figure 4.33 *Plot of the extrapolated organic channel resistance as a function of the applied gate bias, at 7 K.* **174**

List of tables

Table 2.1 *Exposure parameters for PMMA 950 A3, optimized for high resolution lithography of dense structures.* **80**

Table 2.2 *Exposure parameters for TOK 2.5 cP, optimized for high resolution lithography of dense structures.* **81**

Table 2.3 D*oses to be assigned to the GDSII elements to achieve the feature sizes reported in the third column.* **82**

Table 2.4 *Exposure parameters for TOK 2.5 cP, optimized for fast exposure of large area patterns.* **83**

Table 4.1 *Resistance of the organic channel extrapolated from the I:Vs at different temperatures.* **160**

Table 4.2 *Values of the extrapolated organic channel resistance at 7 K for different gate voltages.* **168**

Table 4.3 *It listed the value of the drain current at -7 V applied between source and drain, at 7 K and -50 V on the gate. The extracted value of the barrier activation voltage (~barrier height) for the source and drain electrodes is also given, for the set of contact material studied in this work.* **172**

Table 4.4 *Values of the work function of the elemental metal employed in this work. Note that the ionization potential of P3HT is 4.7 eV.* **173**

Nomenclature

B	magnetic field
C_j	junction capacitance
D	density of states
e	≈ 2.718…
E	energy general
E_F	Fermi energy
E_g	main gap energy
f	probability
h	Planck's constant
I_s	saturation current
J	current density
k	wave vector
k_B	Boltzmann's constant
k_F	Fermi wave vector
$k_{\parallel}$	component of the momentum parallel to the interface
L	channel length
m^*	effective mass

N available density of states

n electron carrier concentration

T absolute temperature

Ʈ matrix element of a transition

v_F Fermi velocity

V general voltage

W channel width

x_a accumulation layer width

x_d depletion layer width

x_i insulator thickness

Greek symbols

α conduction electron spin polarization

χ electron affinity

δ Dirac's delta function

ε electrical permittivity

ε_0 permittivity of vacuum

F electric field

Φ work function (measured in J)

Φ electrical potential

Φ_0 energy barrier as seen from the metal (measure in J)

Φ_b barrier height as seen from the semiconductor (measured in V)

λ spin-flip length

μ carrier mobility

ψ electron wave function

τ spin-flip time

Subscripts

$\uparrow$ denotes spin up

$\downarrow$ denotes spin down

c denotes conduction band

e denotes electrons

g denotes gap state

h denotes holes

i denotes intrinsic

m denotes metal

n denotes electrons

p denotes holes

s denotes semiconductor

v denotes valence band

Chapter 1

Introduction

Overview

The motivation behind this thesis is the investigation of materials and devices that may be suitable for the emerging field of spin electronics.

Spin electronics is a multidisciplinary subject which combines the methods, materials and devices between the fields of magnetism and electronics. Its main goal is to understand the interaction between the particle spin and its solid state environment and to make useful devices using the acquired knowledge. The field began to flourish after the discovery of giant magneto-resistance (GMR) in multilayers in the late 1980s. GMR consists of an enhancement of the magneto-resistance due to spin scattering between ferromagnetic electrodes separated by a non-magnetic metal. The GMR stack is a two terminal device, having high or low resistance state depending on the relative magnetization of the ferromagnetic layers. Its successor, the tunnel magneto-resistance (TMR) stack, is a tunneling resistor with improved-performance and similar qualitative resistance states. Though they have largely proven to be commercially viable devices, through application in hard drive read heads, they are passive elements from the electronic standpoint.

The construction of spin transistors would provide the key toward digital spin circuitry, which has long been envisaged for the next generation spin electronics. Triode devices are the building blocks for the physical realization of all logic elements.

In order to realize three terminal devices utilizing spin-polarized electronic currents, materials and structures have first to be found to act as effective spin injectors, transmitters and manipulators. Potential injection structures include Schottky and tunnel barriers employing ferromagnetic metals or magnetic semiconductor. Injection of spin-polarized currents into semiconductors directly from a ferromagnetic metal is problematic because of the conductivity mismatch and the vastly different Fermi surfaces. The above problem is

slightly alleviated by the use of tunnel junctions which, however, are more difficult to control and permit a small current density to flow safely. On the other hand, junctions between a ferromagnetic semiconductor and a non-magnetic one present the difficulty of finding suitable candidates for the magnetic material, exhibiting Curie point above room temperature.

The remaining steps, the transmission and manipulation of spins, pose further requirements on the materials. An efficient medium must have a large spin diffusion length (a light material in terms of atomic number), small effective masses, high mobility and small carrier concentration in order to make electrostatic control possible (say via gating the device). For device applications electrostatic manipulation of the spin is also desirable (FET with spin orbit coupling). Potential candidates that are currently explored include classical IV, III-V, II-VI semiconductors, semimetals such as graphite and bismuth, and, only recently, the class of the organic based semiconductors. The latter is attracting rising interest following a number of reports of large spin valve effects observed in hybrid organic devices.

The main theme of this work is the study of the possibility of injecting spin-polarized electronic currents into organic media from ferromagnetic metals and metal-tunnel barrier junctions. What follows is a description of our experimental and analytical efforts, on developing devices and understanding the transfer mechanism within the organic media and at the contact with a metal. Some basic concepts for designing and understanding the experiments on organic spin electronics are first presented.

Spin electronics

If a material or device changes its electrical resistance under the influence of an external magnetic field, this property is generally referred to as magneto-resistance (MR). The first known phenomenon where the electrical resistance is altered by the direction of a magnetic moment is called anisotropic magneto-resistance (AMR) (Thomson, 1856), its physical origin lies in the spin-orbit coupling: as the magnetization rotates, the electron cloud about each nucleus deforms slightly, and this deformation changes the amount of scattering undergone by the conduction electrons in their passage through the lattice. The electrical resistance depends on the angle between the electrical current and the magnetic moment

and is maximum for current and field parallel. AMR in iron is about 0.4% and up to 5% in NiCo alloys (McGuire, 1975). When the conduction electrons are displaced from their trajectories by the Lorentz force a small change in the resistivity of less than 1% occurs, referred to as ordinary-MR; this effect can be a large in bismuth and silicon in some circumstances (Yang F. Y., 1999) (Delmo, 2009).

In 1936 a basis for understanding spin-polarized transport in ferromagnetic metals was provided which can explain various magneto-resistive phenomena, known as the two current model (Mott, 1936). It was realized that electrons of majority and minority spin, with magnetic moment parallel and antiparallel to the magnetization of a ferromagnet, respectively, do not mix in the scattering processes. This is equivalent to dividing the current into two independent parts with opposite spin. The probability of scattering of a current flowing through the material is proportional to the density of states (DOS) and, because in a ferromagnet the DOS is not the same for different spin states due to exchange splitting of the band, the two spin species have different bulk conductivities. The current is mostly carried by the electrons with the highest conductivity, normally the majority electrons, and it is therefore spin-polarized. The actual current polarization α close to the Fermi level in a ferromagnet is given by:

$$\alpha = \frac{\langle n_\uparrow v_{F\uparrow}^{\gamma} \rangle - \langle n_\downarrow v_{F\downarrow}^{\gamma} \rangle}{\langle n_\uparrow v_{F\uparrow}^{\gamma} \rangle + \langle n_\downarrow v_{F\downarrow}^{\gamma} \rangle} = \frac{J_\uparrow - J_\downarrow}{J_\uparrow + J_\downarrow}$$

where $n_\updownarrow$ are the concentrations of spin up/down electrons at the Fermi level, $v_{F\updownarrow}$ are the spin up/down Fermi velocities ($\gamma = 0$ for optical excitation, 1 for ballistic transport, and 2 for diffusive transport) and $J_\updownarrow$ are the corresponding current densities, valid when the spin up/down currents are taken to have the same relaxation time $\tau_\uparrow = \tau_\downarrow$.

When non-polarized current is passed across a magnetic material, the conductivity experienced by the spin species depends on the magnetization; carriers with spin antiparallel to the magnetic direction undergo more scattering events and the population of the parallel spin specie increases, because of larger number of available states near the Fermi level. Hence ferromagnetic conductors act as solid state spin filters as they can spin-polarize an electronic current (Esaki, 1967) (Moodera, 1988). In 1973 the spin polarization of the conduction band in a ferromagnetic material was determined experimentally, using a junction consisting of a ferromagnet, a tunnel barrier and a superconductor (Tedrow, 1973). It is noteworthy that this work showed that the tunneling current remains spin polarized even outside of the ferromagnetic region. Later, measuring the tunneling

conductance in ferromagnet/tunnel barrier/ferromagnet junctions, a change in the resistance state was observed between the parallel and antiparallel magnetization in the two magnetic regions (Jullière, 1975), which was related to asymmetry of the density of states of the spin sub-band on both side of the barrier. For the first time, the resistance of a device could be changed by manipulating the relative orientation of the magnetizations in the ferromagnetic contacts. Spin injection and transport in a nonmagnetic media was demonstrated with the discovery of the giant magneto-resistance effect.

Giant magneto-resistance

In 1988 it was found that the resistance in Fe/Cr/Fe multilayer depended strongly on the relative orientation of the magnetization within the ferromagnetic layers (Baibich, 1988) (Binash, 1989). The effect was named giant magneto-resistance (GMR), as it was found to be much larger than both ordinary and anisotropic MR.

The Cr spacer layer was about 1 nm thick, leading the Fe contacts to couple anti-ferromagnetically (with anti-parallel alignment of their magnetizations at zero fields). As the external magnetic field increased, the magnetization of the ferromagnetic layers progressively rotated towards the field, leading to observe a decrease in the resistance of the structure. At saturation, the magnetizations concluded being aligned parallel, showing the lowest resistance (Figure 1.1).

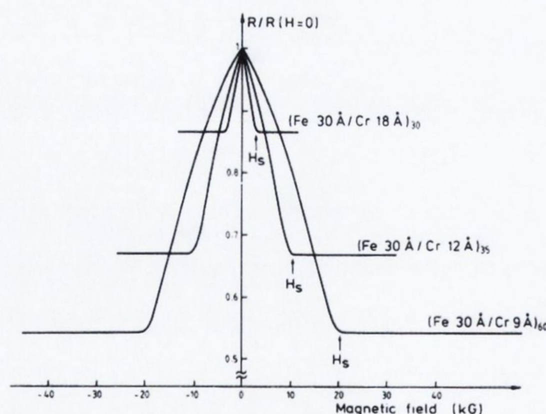

Figure 1.1 *Magneto-resistance traces of three Fe/Cr multilayers, at 4.2K. The current and the applied field are in the plane of the layers, from* (Baibich, 1988).

The underlying physical mechanism can be understood based on the above mentioned two current model, which describes the electrical conductivity in metals in terms of two independent conducting channels, for the spin-up and spin-down electrons, for which electrical conduction occurs in parallel (Mott, 1936). As anticipated, in a ferromagnet the density of states is not the same for different spin states at the Fermi level due to exchange split of the band; the scattering rate of a current flowing through the material is proportional to the density of states and, therefore, the scattering for the two spin states is different. As a consequence, the two spin species generally have different bulk conductivities, σ. The current in a ferromagnetic metal is mostly carried by the electrons with highest conductivity, normally the majority electrons, and is thus spin-polarized. The bulk current polarization α of a ferromagnetic metal can also be defined as $\alpha = \frac{\sigma_\uparrow - \sigma_\downarrow}{\sigma_\uparrow + \sigma_\downarrow}$. Scattering is weak for electrons with spin projection parallel to the magnetization of the layer in which scattering takes place, whereas it is strong for electrons with opposite spin. In parallel configuration, the resistivity of the majority spin channel is low (and viceversa high for the minority channel), resulting in an overall low resistance (Figure 1.2).

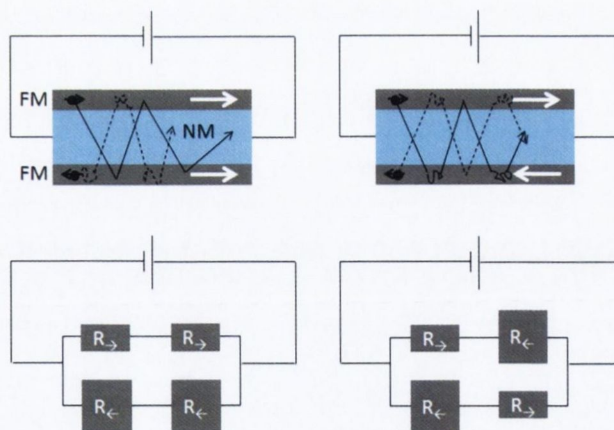

Figure 1.2 *Representation of a GMR device consisting of two ferromagnets (FM) and a non-magnetic spacer (NM) in the parallel (top-left) and anti-parallel (top-right) configuration. The magnetization is indicated by the white arrows. The trajectory of electrons with opposite spin direction is represented with black solid and dotted lines. A corresponding resistor model is given (bottom) for the two configurations. The size of the resistors indicates how large the electrical resistance is for the corresponding spin species. As in* (Naber W. , 2007).

In the case of antiparallel alignment, the carriers of both spin channels undergo considerable scattering, resulting in larger overall resistance.

GMR structures are often classified according to the fact that current can flow parallel (Figure 1.2) or perpendicular (Figure 1.3) to the interfaces between the different layers,

depending on the device geometry. The functioning can be described in both cases in terms of a parallel resistor model, even though the underlying mechanism is slightly different.

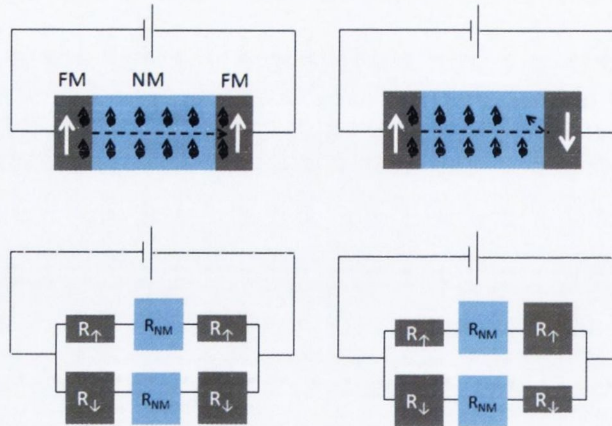

Figure 1.3 *Schematics of a current-perpendicular to plane GMR device. The dotted arrows represent the spin current. The resistor model is shown at the bottom. Bigger resistors represent a larger resistance for the indicated spin state.*

When a magnetic contact is connected to a non-magnetic material and a current is driven across the system, the current is different for the two spin state, due to the current polarization in the magnet. A magnetization builds up in the non-magnetic material, known as spin accumulation. The amount of the spin accumulation depends on the spin injection rate and on the spin relaxation time, and it typically decays exponentially away from the injecting contact, on a length scale referred as to spin diffusion length $\lambda_{sd} = \sqrt{\frac{\lambda v_F \tau_\updownarrow}{3}}$. The spin density resulting from the spin accumulation is much smaller than the charge density in the non-magnetic metal. However, it can be probed by the second magnetic contact which, whether it is separated from the injector by a distance smaller than the spin flip length, can act as a spin detector, showing either high or low resistance depending on the relative magnetization. This demonstrates the occurrence of spin transport through a non-magnetic metal. The resistance states are used to define the GMR ratio as:

$$GMR = \frac{R_{ap} - R_p}{R_p}$$

Notably, the critical length scale in a current perpendicular to plane GMR device is the spin relaxation length, while, in current in plane devices, it is the electron mean free path.

Multilayers of alternating magnetic and non-magnetic metals in which the resistance can be changed by manipulating the relative orientation of the magnetizations are typically referred to as spinvalves. Normally the magnetization of a bottom ferromagnetic layer is pinned by exchange coupling with a contiguous antiferromagnetic layer, while the magnetization of the next magnetic layer is free to rotate with the applied magnetic field. Independent switching can also be achieved by using materials having different coercive fields.

The realization of a large room-temperature GMR enabled a quick transition from fundamental physics studies to commercial applications in magnetic recording (Parkin, 1991) and triggered a tremendous amount of research on spin electronic devices.

While in GMR structures the orientation of the magnetization affects the current of spin-polarized carriers, in 1996 an interesting reverse effect was predicted. The flow of a spin-polarized current could transfer angular momentum from the carriers to the ferromagnet and affect the orientation of the corresponding magnetization (Slonczewski, 1996). This effect is known as spin-transfer torque, and current-induced magnetization reversal was successfully demonstrated (Katine, 2000).

Tunneling magneto-resistance

Tunneling measurements played a key role in early experimental work on spin-polarized transport (Tedrow, 1973). The change of conductance observed in ferromagnet /tunnel barrier /ferromagnet junctions (Jullière, 1975) for the parallel and antiparallel magnetization in the ferromagnetic regions, can be used to define the corresponding tunneling magneto-resistance ratio (TMR), as:

$$TMR = \frac{R_{ap} - R_p}{R_p} = \frac{G_p - G_{ap}}{G_{ap}}$$

Where R and G are the resistance and the conductance for the denoted configuration. TMR originates from the difference in the density of states at the Fermi level between spin up $n_{F\uparrow}$ and spin down $n_{F\downarrow}$ electrons. Assuming the conservation of spin orientation during tunneling, electrons can only tunnel from a given spin sub-band in the first ferromagnetic (FM) contact to the same spin sub-band in the second FM contact, as depicted in Figure 1.4. The tunnelling rate is proportional to the product of the corresponding spin sub-band

density of states (DOS) at the Fermi level and hence on the relative magnetization orientation of the contacts. In the antiparallel configuration spin conservation implies that electron tunnel from a majority to a minority band, equivalent to a high resistance state. *TMR* can then be also defined in terms of the polarization *P* of the two magnetic contacts:

$$TMR = \frac{2P_1P_2}{1 - P_1P_2}$$

Where $P_i = \frac{n_{F\uparrow} - n_{F\downarrow}}{n_{F\uparrow} + n_{F\downarrow}}$.

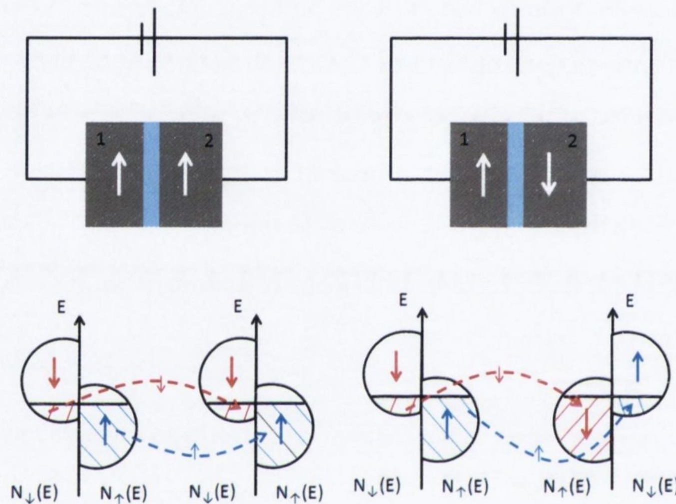

Figure 1.4 *Illustration of electron tunneling in MTJ, in the parallel (left) and antiparallel (right) configuration; and corresponding spin density of d-states in ferromagnetic metals (unequal due to exchange spin splitting). The magnetization direction (white arrow) in the ferromagnetic regions is determined by the majority spin sub-band. Dashed lines depict the spin conserved tunneling.*

The discovery of large room-temperature *TMR* renovated the interest in the study of magnetic tunnel junctions (MTJ) (Moodera, 1995). In their work, Moodera et al. prepared MTJs using Al_2O_3 tunnel barriers achieving *TMR* of 18% at room temperature (Figure 1.5) and 30% at 4 K.

MTJs are now the basis for magnetic read heads and several magnetic memory prototypes. It is noteworthy that TMR is a pure interface effect and does not require spin transport in the non-magnetic layer. The larger TMR effects are observed with MgO tunnel barriers and epitaxial Fe or CoFe electrodes.

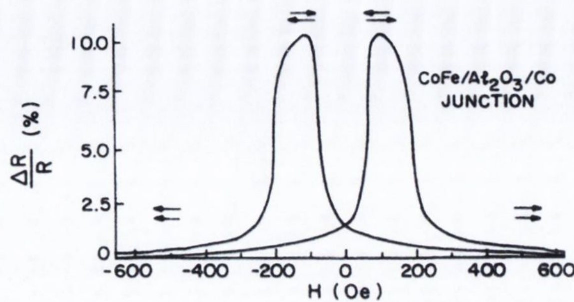

Figure 1.5 *Resistance of a CoFe/Al$_2$O$_3$/Co junction as a function of H in the film plane, at 295 K. The arrows indicate the direction of M in the two films. It is also shown the variation in resistance of the CoFe and Co films, from* (Moodera, 1995).

Triode devices

One of the main goals in spin electronics is the realization of an active device that combines electric control of the drain current, as in transistors, with the memory effect of spin valves. In a prototypical device, the spin field effect transistor (Datta, 1990), the current modulation between the ferromagnetic contacts arises from spin precession induced by gate controllable spin-orbit interaction (Figure 1.6).

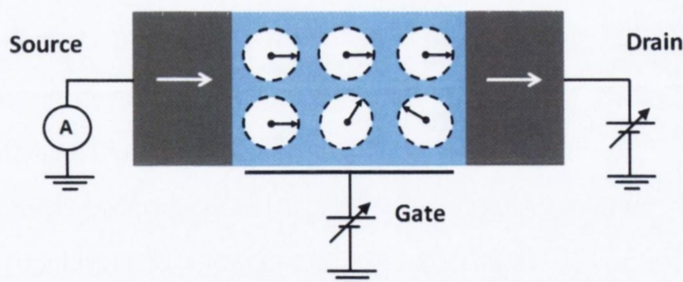

Figure 1.6 *Scheme of a Datta-Das spin-FET. Source and drain are ferromagnetic metals, with parallel magnetic moment. The role of the gate is to generate an effective magnetic field which causes the electron spin to precess. The current flowing is large if the precession period is larger than the time of flight, and small if the spin direction is reversed.*

For instance, the source injects electrons with spins parallel to the transport direction, electrons are transported ballistically through the channel and when they arrive at the drain, their spin is detected. An electron can enter the drain if its spin points in the same

direction as the magnetization of the drain (ON state). Otherwise it is scattered away (OFF state). The role of the gate is to generate an effective magnetic field, arising from the spin-orbit coupling, which is defined by the properties of the channel and the electrostatic potential of the gate. By modifying the gate voltage, one can cause the precession to lead to either parallel or antiparallel electron spin at the drain, effectively controlling the current. However, spin-ballistic transport is required, as well as large spin-orbit interaction in the channel, for gate voltage induced spin precession. Recently, the III-V semiconductor InAS was investigated by (Hyun Cheol Koo, 2009), demonstrating a very little modulation of the spin orbit interaction by applying a gate voltage.

Several other structures have been proposed for spin transistors that have at least one semiconductor region, aiming to integrate spin and charge transport within the scheme of the field effect transistors (Monsma, 1995) (Gregg, 1997) (Fabian, 2004).

The wish to combine semiconductors and spin electronics concepts stimulated efforts to inject spin into semiconductors. Intuitively, the injection and detection of a spin-polarized current in a semiconducting material could combine magnetic storage of information with electronic readout in a single semiconductor device, opening the possibility to further device designing and yielding many clear advantages (Hiro Akinaga, 2002).

Ferromagnetic metal /nonmagnetic semiconductor contacts may provide ways of efficient spin injection into semiconductors. However, the injection of spin polarized currents is problematic because of the conductivity mismatch and the vastly different Fermi surfaces (Schmidt, 2000) (Stamenov, 2007). Problems with injection from metallic contacts promoted the idea of using a diluted magnetic semiconductor as spin aligner (Oestreich, 1999), and consistent degree of spin polarization have been achieved in this way in gallium arsenide heterostructures from ZnMnSe (Fiederling, 1999) and GaMnAs (Ohno, 1999). Nevertheless, FM metals sources remain an indispensable tool for room temperature devices. Ways to avoid this problem are the injection of hot electrons through a tunnel barrier (Rashba, 2000) or Schottky barrier (Albrecht, 2003), at appropriate combination of the work function of the metal and the semiconductor or at high bias (Yu, 2002a) (Yu, 2002b). Limited success has been achieved and small resistance changes observed upon switching the magnetization direction of magnetic permalloy electrode in GaAs based Schottky junctions (Hammar, 1999). Room temperature spin injection from Fe into GaAs has also been detected optically (Hanbicki, 2003), here the performance was improved by the use of a thin, heavily doped surface region in GaAs, in a Fe /AlGaAs /GaAs heterostructure, which reduced the depletion width and the barrier height,

enhancing the probability for tunneling. More recently spin accumulation was demonstrated via the electrical Hanle effect at the Fe /n-type GaAs interface (Lou, 2007) and via spin-injection Hall effect[1] (Wunderlich, 2009). Following the progress realized in GaAs, injection of spin polarized hot electrons through a FM metal/ oxide tunnel barrier in moderately doped silicon has been detected optically (Jonker, 2007) and electrically in hot-electron spin-transistor device (Appelbaum, 2007), where spin transport across 10 μm was demonstrated. More recently, spin accumulation has been demonstrated by the Hanle effect at the Si interface with FM metal/ silicon dioxide contacts (Li C. H., 2011).

The attempts made with the class of the organic semiconductors are revised later in the chapter, at page 24.

Electronic spin transport in semimetals was also investigated and demonstrated via electrical Hanle effect in ferromagnetic metal /tunnel barrier /graphene and ferromagnetic metal/ bismuth devices in the non-local geometry (Tombros, 2007) (Wei, 2009) (Kyoung-Il Lee, 2009).

Metal-semiconductor contacts: Schottky junctions

An insight into the formation of the contact among a metal and a semiconductor, known as Schottky contact, can be obtained within the rigid band model. The contact builds up when bringing two semi-infinite portions of material together in vacuum, as in Figure 1.7.

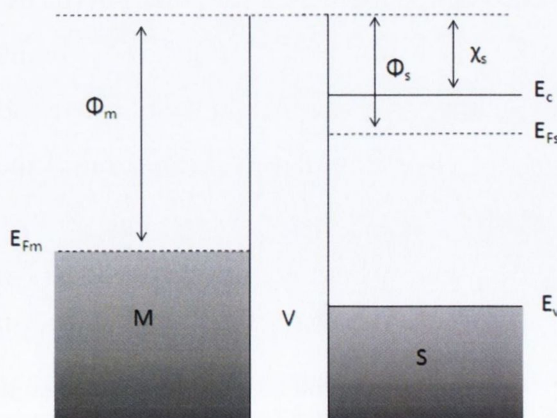

Figure 1.7 *Energy diagram for two portions of metal (M) and semiconductor (S) separated by vacuum (V).*

[1] Injecting a spin polarized electrical current into a non-magnetic semiconductor generates a Hall Effect which, if the spin remains coherent, yields transverse charge accumulation and is detectable electrically.

Where E_{Fm} and E_{Fs} are the Fermi level in the metal and semiconductor, Φ_m and Φ_s are the two work functions, χ_s is the electron affinity in the semiconductor, E_c and E_v the bottom and the top of the valence bands. Upon contact, the conduction and valence bands in the semiconductor will bend close to the interface to reach equilibrium of the Fermi level on both side of the junction $E_{Fm} = E_{Fs}$. A barrier builds up for electrons trying to cross the junction, when $\Phi_m > \Phi_s$ (as it is the case for common metals and, e.g., silicon). At the interface, thus, there is a built-in equilibrium potential (and a corresponding electric field) of amplitude $qV_b = \Phi_m - \Phi_s$; and the barrier Φ_0, as seen from the metal, will be $\Phi_0 = \Phi_m - \chi_s$ (Figure 1.8).

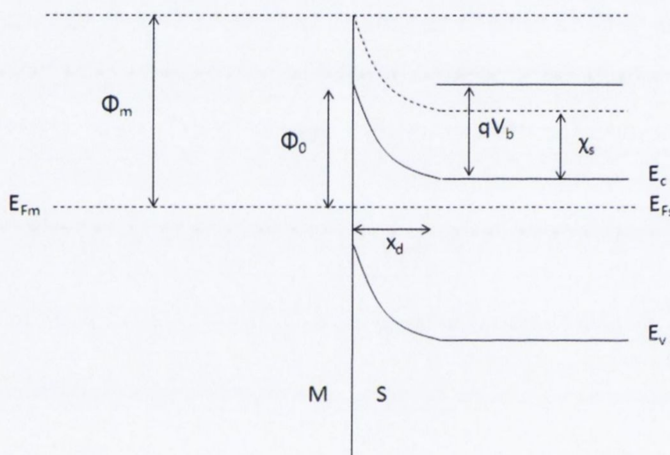

Figure 1.8 *Energy diagram for a Schottky junction, with no applied external bias. Symbols have their usual meaning; x_d refers to the width of the depletion region.*

This diagram is an approximation which is not often valid for polar interfaces, for example between metals and binary semiconductors, as there the Fermi level is pinned by a large density of surface states and the Schottky barrier height (the barrier at the metal-semiconductor interface) becomes independent from the work function of the metal used, hence simple modeling is not applicable.

In the opposite situation, when $\Phi_m < \Phi_s$, there would be very small or no barrier formed; however this situation is quite uncommon. To create contacts that can be highly ohmic another way is to create high surface doping, which leads to the formation of a very narrow depletion region that is tunneling-transparent for incident electrons.

The behavior of a Schottky junction under externally applied bias V_a can be qualitatively understood by considering that a positive shift of the chemical potential at the semiconductor side will lead to a Schottky barrier lowering, therefore increasing the

transmission probability and the current flow. Conversely, a negative shift leads to a barrier height increase and smaller current. Together with the change in barrier height there will be a small change in the width of the depletion zone x_d. The main transport mechanisms are illustrated in Figure 1.9, where the principal contributions are the thermionic emission of electrons from the semiconductor over the top of the barrier into the metal, and the quantum mechanical tunneling through the barrier. Minority mechanisms (non-illustrated) are the recombination in the space-charge zone and neutral region.

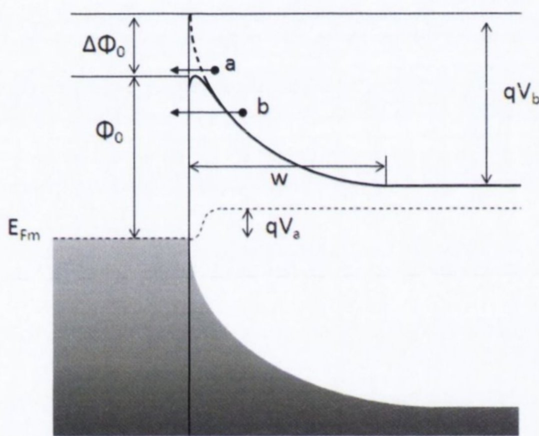

Figure 1.9 *Current contributions in a Schottky barrier, a: thermoionic emission over the top of the barrier and b: tunneling through the barrier. $\Delta\Phi_0$ is the barrier reduction coming from the image forces.*

Typically one finds that only one current mechanism dominates and the current can be expressed as due to the main contribution. Under the assumption that an electron from the metal can be injected once it has acquired a thermal energy sufficient to cross the potential maximum of the barrier (Richardson-Schottky model), the current can be written as follows:

$$J_n = qvN_c exp\left(-\frac{q\phi_b}{kT}\right)\left[exp\left(\frac{qV_a}{kT}\right) - 1\right]$$

This expression, valid for positive biases, reveals that J_n, the current density, is the product of the electronic charge q, a velocity v, and the density n of available carriers in the semiconductor located next to the interface $n = N_c\left[exp\left(\frac{qV_a}{kT}\right) - 1\right]$. The velocity equals the Richardson velocity, the velocity with which on average the carriers approach the

barrier $v_R = \sqrt{\frac{kT}{2\pi m_c^*}}$, where m_c^* is the effective mass. The minus one term ensure that the current is zero if no voltage is applied. In reversed bias V_r, the current expression is:

$$J_n \approx exp\left(-\frac{q\phi_b(V_r)}{kT}\right)\left[1 - exp\left(\frac{-qV_r}{kT}\right)\right]$$

In Figure 1.10 are illustrated the qualitative current characteristics of a thermo-emission limited Schottky barrier (at an arbitrary barrier height and temperature) and of an ohmic contact.

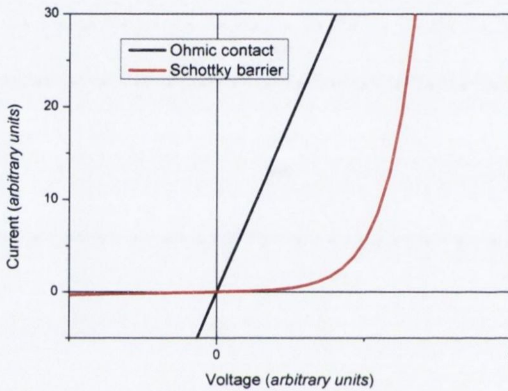

Figure 1.10 *Qualitative illustration of the I:V characteristics of an ohmic contact and a Schottky barrier.*

For thin enough barriers, at low temperature, the tunneling contribution may become important. Given the barrier shape the current is estimated by solving the Schrodinger equation; the tunneling current is obtained by the product of the carrier charge q, velocity v, density of carriers n and tunneling probability Θ; as $J_n = qnv_r\Theta$. The estimation of Θ, from $\Theta = \frac{\Psi(x_d)\Psi^*(x_d)}{\Psi(0)\Psi^*(0)}$, yields:

$$J_n = qv_RN_c exp\left(-\frac{4}{3}\frac{\sqrt{2m_c^*}}{\hbar}\sqrt{q\phi_b}x_d\right)\left[exp\left(\frac{qV_a}{kT}\right) - 1\right]$$

The tunneling current shows explicit temperature dependence only in the last term in the above equation, referred to the density of available states. This term shows thermal broadening proportional to the applied voltage, which, at small bias $V_a \to 0$, is vanishingly small and can be often neglected. The $\sqrt{T}$ term in the Richardson velocity is typically also ignored at low temperature. At high temperature, the smearing of the Fermi distribution of

states adds a linear temperature-dependent term; due to the increase in number of conductive states. The thermal voltage broadening is approximately $\Delta V \approx 3.84\frac{kT}{q}$, around 0.1 V at 300 K (Stamenov, 2007).

The weak temperature sensitivity of the tunneling current is in strong contrast with the exponential temperature dependence of the thermionic emission current over the barrier region, or even the normal metallic conduction through so-called pinholes, often present in low quality tunnel junctions, which exhibits almost linear temperature dependence in a broad region of temperatures. Hence, temperature-independent conduction is often considered a strong indication for a dominating tunnel current component in real junctions (Akerman, 2002) (Stamenov, 2007).

The potential of the junction to act as a spin-polarized current injector is limited by the vastly different Fermi surfaces of the semiconductor and the metal. The problem can be analyzed by considering a thin Schottky barrier (for example in the case of a δ-doped surface in the semiconductor), in which the tunneling current dominates the transport and the current density can be evaluated using the Fermi's golden rule (Bratkovsky, 2003) like:

$$J_{\updownarrow} = \frac{q}{h}\int dE[f(E - E_{Fm\updownarrow}) - f(E - E_F)]\int d^2k_{\parallel}\frac{T_{\updownarrow}(k)}{(2\pi)^2}$$

The current is thus proportional to the occupied density of states on the two sides, times a matrix element of the transmission T. Where $f(E)$ is the Fermi function, $f(E) = \frac{1}{e^{E-E_F+1}}$, and $T_{\updownarrow}(k)$ is the transmission probability for spin up and down electrons, assuming that the component of the momentum parallel to the interface $k_{\parallel}$ is conserved. The transmission probability for a triangular or rectangular barrier is:

$$T_{\updownarrow}(k) = 16a\frac{m^*_{m\updownarrow}m^*_s k_{\updownarrow x}k_x}{(m^*_s k_{\updownarrow x})^2 + \left(m^*_{m\updownarrow}k_s\right)^2}e^{-bk_s\delta}$$

Where $m^*_{m\updownarrow}$ is the spin dependent effective mass in the metal, m_s^* in the semiconductor, $k_{\updownarrow x}$ the x-component of the momentum in the metal, k_x the x-component in the semiconductor, k_s the average momentum in the semiconductor and a and b are dimensionless coefficients. See also (Shen, 2004) for a numerical approach to solve the problem.

Special attention must be paid to the pre-factor of the equation: it is because of the different effective masses and carrier momentum in metals and semiconductors that the

conductivity mismatch arises. It is this that actually limits the possibility for direct coherent transmission of spin-polarized electrons.

The conductivity mismatch between the semiconductor and the metal, assuming a diffusive regime, is shown in (Schmidt, 2000) to limit the spin injection. The spin injection coefficient (denoted with γ) is proportional to the ratio $\frac{\sigma_N}{\sigma_F}$, where σ_N and σ_F are the conductivities of the normal semiconductor and the ferromagnetic injector, and it is therefore $\gamma \propto \frac{\sigma_N}{\sigma_F} \ll 1$. This also explains the difference between injection from a ferromagnetic metal into a paramagnetic metal with $\frac{\sigma_N}{\sigma_F} \geq 1$ and a semiconductor with $\frac{\sigma_N}{\sigma_F} \ll 1$.

It has been theoretically (Rashba, 2000) and experimentally (Motsnyi, 2002) shown that the insertion of an artificial tunnel contact at the interface can alleviate this problem. This contact takes control over γ and eliminates the conductivity mismatch; the tunnel resistance for this purpose needs to be larger than the competing resistances making up the total contact resistance, in the ferromagnet and in the nonmagnetic conductor. The underlying mechanism is that the transmission coefficient for tunneling through an artificial barrier depends not only on the barrier energy profile, but also on the wave vector k of the tunneling particle in the contact regions. The barrier increases the probability of connecting states with matching k vectors on the two sides. The spin-polarized carriers exiting the tunnel barrier are not in equilibrium with the nonmagnetic conductor; therefore the effect of the barrier is to drive the semiconductor out of local equilibrium promoting spin accumulation. Hence the interfacial impediment to spin injection is removed.

A vast treatment of the nature and the transfer mechanisms of a Schottky junction can be found in (Stamenov, 2007).

Tunneling contacts

The tunneling current is not the dominant component in a Schottky junction (at least at high enough temperature and moderate forward bias) but it should be, ideally, the main contribution in purpose-built tunnel contacts which include a thin layer of insulating material between two conductors. Let's first analyze the case of two metal electrodes separated by vacuum and by an insulator (Figure 1.11).

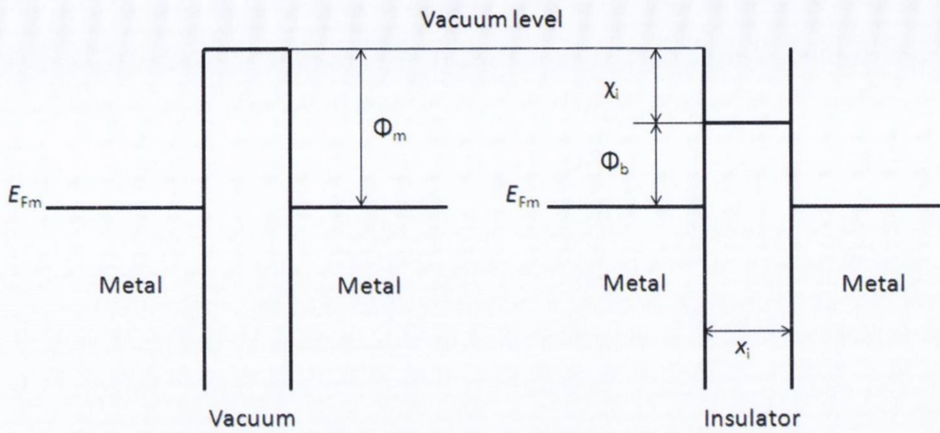

Figure 1.11 *Simplified energy diagram of two similar metals separated by vacuum and by insulator.*

In the idealized energy diagram χ_i is the electron affinity of the insulator and x_i its thickness. The influence of the insulator is to lower the barrier height Φ_b between the two metals by an amount χ_i.

For dissimilar metals with work functions Φ_m^L and Φ_m^R, respectively, and non-interacting surfaces (Figure 1.12), the potential profile can be evaluated as:

$$q\phi(x) = \Phi_m^L - \chi_i + (\Phi_m^R - \Phi_m^L)\frac{x}{x_i}$$

within the insulator thickness x_i.

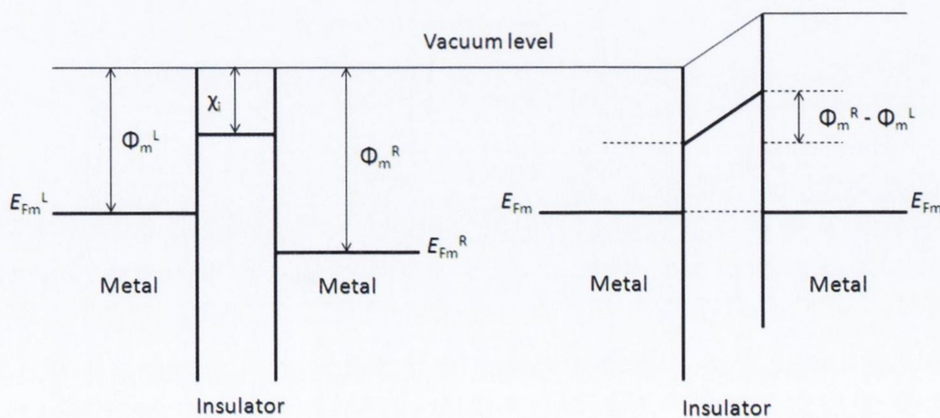

Figure 1.12 *Energy diagrams of two dissimilar metals before (left) and after (right) they have been bought in contact with an insulating layer.*

In truth the situation can be much more complicated, for example the insulating layer may be amorphous or with a low degree of crystallinity and the description of a simple band-picture is limited by the existence of states in the energy gap of the insulator. This influences both the transport characteristics and the barrier formation. However it can be a good approximation for thick barriers, by taking into account the effective density of states into the insulator (Tsymbal, 1998). The tunneling current across the barrier can be evaluated by starting from the Schrodinger equation and a known potential barrier shape (say triangular or rectangular) or from Fermi's golden rule, for which the current is proportional to the occupied density of states on one side, times a matrix element of the transition, times the unoccupied density of states on the other side. The dependence of the transmission coefficient on the barrier height (Rhoderick, 1988) is exponential, of the form $\Theta \propto exp\left(-\frac{q\phi_b}{E_0}\right)$. Such exponential sensitivity of the tunneling current towards changes in the barrier height requires some considerations about the effects that could alter the barrier height. A significant effect is related to the existence of image forces (Simmons, 1963). An electron approaching a metal surface polarizes it; hence there is an additional force and an associated electric potential exists $\phi^i \approx -\frac{q^2}{16\pi\epsilon_i}\frac{0.795x_i}{x(x_i-x)}$ (for rectangular barriers); which affects directly the nominal barrier height and profile (Figure 1.13).

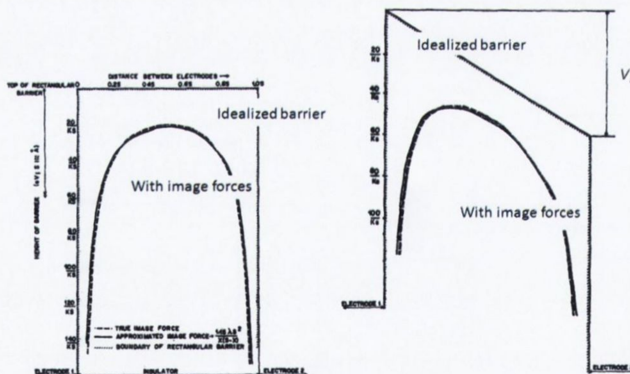

Figure 1.13 *Energy diagram of a rectangular barrier with image force included for the case of zero (left) and a small voltage V_a (right) applied across the junction; from (Simmons, 1963).*

The text book model to treat tunneling from the metal through a (rounded) triangular barrier into a continuum of states is the Fowler-Nordheim model for electron field emission. It predicts:

$$J(F) = bF^2 exp\left[-\frac{4(2m^*)^{1/2}{\Phi_b}^{3/2}}{3\hbar eF}\right]$$

This is independent of temperature. Here F is the electric field; noteworthy the essential assumption is the existence of a continuum of unbound states into which carriers can tunnel. The loosening of this assumption significantly changes the situation. The states in a structure can be represented as the linear combination of Bloch waves

$$\psi_k(x) = u_k(x)exp(ikx)$$

With $u_k(x)$ having the periodicity of the crystal lattice, hence these states may be represented by their associated plane waves. The Bloch states ψ_k must be matched continuously at the boundaries of the system, therefore for the case of elastic tunneling the wave number k should be matched at the interfaces. The direct matching of forward and backward plain waves is required when solving the Schrodinger equation for a system consisting of the three regions, representing the left hand side metal electrode, the insulator and the right hand side electrode (Figure 1.14).

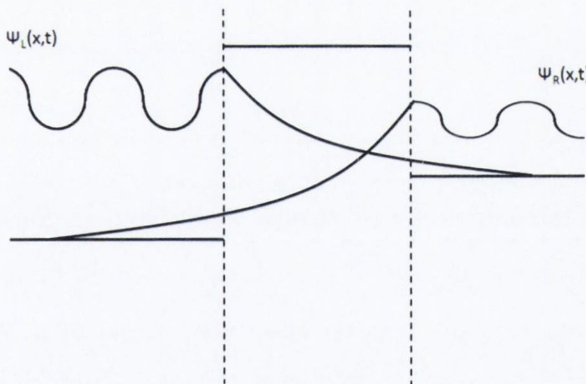

Figure 1.14 *Schematic diagram of the wave function in the three regions, having matching k vectors.*

The solution of the matching procedure leads to a familiar result for the tunneling probability:

$$\Theta \propto \frac{k_L k_R \varkappa_i^2}{(k_L + \varkappa_i^2)(k_R + \varkappa_i^2)}$$

The subscript refers to the left (L) and right (R) hand side of the junction, and x_i includes the barrier parameters. The total tunneling current will not, generally, be directly proportional to the density of states, because of the indirect dependence through the transmission coefficient. A visual description is obtained by projecting the constant energy surface onto the plane of the tunnel interface (a plane parallel to the interface in the *k* space) (Figure 1.15). The tunneling current is proportional to the area of overlap of the projections of the constant energy surfaces (for $E = E_F$) on both side of the junction.

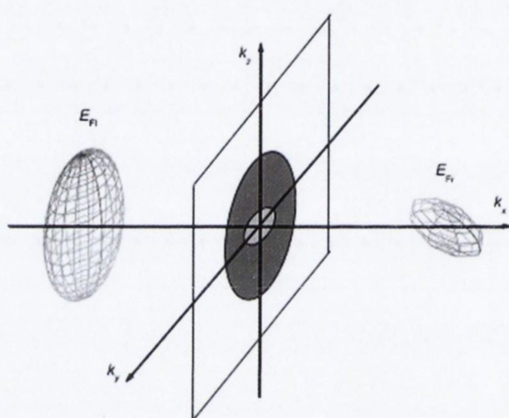

Figure 1.15 *Diagram of two constant energy surfaces of* $E=E_F$ *and their projections on the plane of the tunnel interface. From* (Stamenov, 2007).

When applying these concepts to ferromagnetic junctions, if the spin is conserved upon tunneling, then the conductance of the up and down spin channels would be related to the cross section of the Fermi surfaces for spin-up and spin-down electrons. Whether the magnetization is parallel in the two electrodes, the total conductance equals the sum of the two conductances of the individual channels. For the anti-parallel case, it would be proportional to smallest of the two cross sections (Figure 1.16).

The difference in conductance between the parallel and antiparallel configuration would hence be proportional to the difference of the cross sections of the spin-up and spin-down Fermi surfaces.

A complete treatment of the problem of tunneling of wave functions having a matching *k* vector can be found in (Stamenov, 2007), from whom Figure 1.15 and Figure 1.16 have been taken.

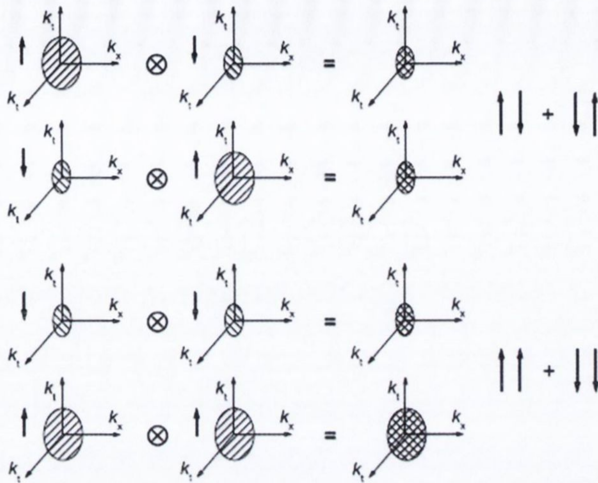

Figure 1.16 *Representation of the two channel model. The differential conductance of the up and down spin channels is related to the transverse Fermi surface cross sections for spin-up and spin-down electrons. When the magnetization of the two electrodes is parallel, the total conductance is equal to the sum of the conductances of the individual channels. For the anti-parallel case, the conductance is smaller, as it is proportional to the sum of the smaller of the two cross sections. From* (Stamenov, 2007).

Organic electronics

Conjugated organic semiconductors as electronic materials have been the subject of intense research because they have processing and performance advantages over conventional semiconductors, for low cost and large area device applications. The two most widely studied types of devices employing organic semiconductors are field effect transistors (OFET) and light emitting diodes (OLED). These devices are currently incorporated into a variety of displays and display drivers and, beyond this, have potentially a wide range of other applications. Because of the intrinsic low mobility of organic compounds, the latter devices cannot rival the performance of those based on crystalline inorganic semiconductors, and are not suitable for use in application requiring high switching speeds. Nevertheless, the processing properties and observed electric characteristics demonstrated that they can be competitive for applications requiring large area covering, structural flexibility, chemical tunability and low-cost processing (Dimitrakopoulos, 2001).

Organic based FET and LED

In the case of OFETs, charge carrier mobility is the primary factor that determines the performance of the devices. Since the first studies on the electrical properties of organic semiconductors (Ebisawa, 1983), the progress in the field-effect mobility value has spanned six orders of magnitude from about 10^{-5} $cm^2V^{-1}s^{-1}$ (Tsumura, 1986) to 16 $cm^2V^{-1}s^{-1}$ (Sokolov, 2011). The improvements are usually obtained by the synthesis or first application of a new organic semiconductor as the active layer in the thin film transistor. The most widely-used organic semiconductors can be broadly classified into two categories: small molecules or oligomers (usually processed in vacuum) and polymers (usually processed by wet chemical techniques). The most representative small molecule compounds employed in this field, having the highest reported mobility, are pentacene and rubrene. Their single crystals displayed mobilities of, respectively, 2.3 $cm^2V^{-1}s^{-1}$ (Lee J. Y., 2006) and 8 $cm^2V^{-1}s^{-1}$ (Podzorov, 2003), and thin film mobilities as high as, respectively, 1.8 $cm^2V^{-1}s^{-1}$ (Masatoshi Kitamura, 2008) and 2.5 $cm^2V^{-1}s^{-1}$ (Hsu, 2007) upon recrystallizing. As deposited amorphous layers, however, do not go beyond 0.01 $cm^2V^{-1}s^{-1}$ (Byoungnam Park, 2008) at the very best, more typically around 10^{-6} $cm^2V^{-1}s^{-1}$ (Seo, 2006). On the other hand, among the most studied polymers, are found the polyphenylene derivatives, of interest mainly for their high luminescence (a feature mainly concerned with light emitting diodes) (Friend, 1999) and the conductive polymers such as polythiophene derivatives. The latter currently display one of the highest hole mobility (around 0.1 $cm^2V^{-1}s^{-1}$) due to their packing in well-organized lamella (Sirringhaus, 1999); slightly higher value of 0.6 $cm^2V^{-1}s^{-1}$ (McCulloch, 2006) and, very recently, 16 $cm^2V^{-1}s^{-1}$ (Sokolov, 2011) have been found in poly-thieno-thiophenes which include fused thiophene rings in their structure.

Pentacene and rubrene devices, both single-crystal and thin-film, have produced some of the highest reported performance transistors, however they require operating voltage around 50 volts in order to display a good current modulation (Butko, 2003), which is too high for applications, while low voltage operating FETs were reported only sporadically (Dimitrakopoulos, 1999). Nonetheless, since they can be grown in the form of large single crystals by vacuum sublimation or physical vapor transport into structures with very limited number of impurities (Jurchescu, 2004), they have provided an ideal platform for fundamental studies on the transport mechanisms (see for example (Endres, 2004) and

references therein), but their slow growth and lack of easy processability further prevent them from being integrated in industrial processes.

The technology that is believed to have the potential to impact the manufacturing cost of transistor devices is the use of a soluble (organic) semiconductor, which could be combined with stamping (printing) techniques, eliminating lithography and, provided that all the steps can be performed by wet techniques, vacuum deposition techniques. As an example of prototypes of all-polymer integrated device for optoelectronics see (Dodabalapur, 1998) (Sirringhaus, 1998), in which polymer based transistors are used to drive organic-LEDs on flexible plastic substrates, or (Sirringhaus, 2000) for printing technique used to fabricated transistor circuits.

Typical solution-processable organic semiconductors are poly-alkythiophene and poly-(3-hexylthiophene) (P3HT). Here a sequence of bonded thiophene rings (polythiophene) is modified by solubilizing long side chains attached to the thiophene rings. Reflecting the properties of the alkyl (or hexyl) side chains, these polymers are soluble in all the common organic solvents. One of the first OFETs obtained via spin-casting a polymer from solution employed P3HT and chloroform onto gold source and drain contacts, led to mobilities around 10^{-5} $cm^2V^{-1}s^{-1}$ (Assadi, 1988). An enormous increase in the mobility was observed when regioregular P3HT was first synthetized (Goedel, 1992) (Chen, 1995). In regioregular polymers there is a symmetric distribution along the molecular chain of the alkyl (hexyl) side chains, which leads to enhanced inter-chain ordering; in contrast with regio-random polymers, which actually are amorphous. When cast from a solution the regioregular P3HT molecules arrange into a structure having some degree of crystallinity, i.e. neighboring chains are aligned, rather than twisted. Their use to fabricate OFET improved the mobility up to 0.045 $cm^2V^{-1}s^{-1}$ (Bao, 1996) and, when spun on chemically modified substrates which favor the molecular alignment, up to 0.1 $cm^2V^{-1}s^{-1}$ (Sirringhaus, 1999) (Mas-Torrent, 2004). Polythiophene incorporating fused thiophene rings (thieno[3,2-b]thiophene) (pbTTT) have been reported having larger crystalline domains than other polymers (around 200 nm) and to exhibit mobilities of 0.6 $cm^2V^{-1}s^{-1}$.

For a more detailed review of the field the reader can refer, among many, to (Roberts, 2009) (Reese, 2007) (Virkar, 2010) (Shuhong Liu, 2010), each of them covers some more specific issues on the subject of OFETs.

It has long been predicted that OLEDs have the potential of capturing a large portion of the display market, principally due to the fact that inorganic LEDs remain fairly expensive to fabricate in comparison. A typical OLED produces photons by recombination of electrons

and holes transporting through the semiconducting organic layer; in 1963 by applying a high voltage to an anthracene crystal a blue light emission was observed, which led to the discovery of the first organic electro-luminescent material (Pope, 1963). Immediately afterwards a LED with balanced electron-hole injection was achieved by selecting appropriate electrolytic contacts (Helfrich, 1965); even though to achieve an observable light emission the LEDs had to be driven with high bias (around 100 volts). The critical breakthrough occurred when a novel structure was employed consisting in a hetero-junction of, respectively, a hole transporting layer and an electron transporting layer (both organic based) sandwiching an emitting spacer. This arrangement could provide a more efficient and balanced carrier injection and recombination (Tang, 1987). The first reported light emission from a conjugated polymer occurred from poly-p-phenylene, while its dielectric properties were being investigated in a sandwich structure among two electrodes (Burroughes, 1990). Intuitively, the color of the emitted light from the OLED can be tuned by modifying the molecular structure of the organic emissive material. This last feature, beside the processability of the emissive polymers, has made this subject a vibrant field of research with many successful proposals of new hetero-structures accompanied by the synthesis of new organic derivatives. Organic LEDs are beyond the interest of this thesis (the main focus of which is the fabrication of field effect transistor with spin-polarized electrodes), therefore here only a very short overview of the field was provided, though more information can be found in (Nuyken, 2006).

Organic spin electronics

In the search for alternative materials with improved properties for coherent spin transport, organic materials have come to the attention of spin electronics, in very recent years. Beside the well-known properties of flexibility, chemical tunability and low production cost, it was the prospect that the spin relaxation times could be much larger than in inorganic materials that first motivated these studies. A significant set of experiments on the spin transfer mechanisms in conductive polymers was originally carried out via electron paramagnetic resonance spectroscopy by (Krinichnyi, 2000), who showed that, depending on the doping level, a spin current could be transported over large time spans. The first successful employment of an organic layer in a spin electronic device was reported in (Dediu, 2002), triggering much research activity in the field. In this work a

lateral device combined two ferromagnetic electrodes of highly-polarized manganite oxide with a conducting nonmagnetic channel of sexithiophene (a pioneer material in OFETs). A large MR signal was found which increased on lowering the temperature, for a channel length of as much as 200 nm. Nonetheless, due to the device geometry having symmetric contacts, the MR could not be directly associated with the magnetization of the electrodes nor their spin polarization, therefore the origin of this effect is not completely clear. A noteworthy step was taken with the fabrication of a vertical spin valve incorporating manganite (LSMO) and cobalt electrodes sandwiching a 130 nm layer of Alq_3 (a widely used luminescent material in OLED applications) (Xiong, 2004). A large MR signal of up to 40% at 11 K was observed. The high observed magneto-resistance represented a huge enhancement in all-electric spin injection and detection via metal electrodes in a semiconductor, in sharp contradiction with what is normally observed in inorganic semiconductors, which typically display very little effect. It was proposed that spin-polarized charge carriers were injected from one ferromagnetic electrode into the organic layer, where they drifted to the collecting electrode, leading to a GMR effect. Further work was carried out on the subject, both experimentally, employing Alq_3 (Wu, 2005) (Wang, 2005) (Pramanik, 2006) (Wang, 2007) (Pramanik, 2007) (Dediu, 2008) (Liu, 2009), pentacene (Shimada, 2008), rubrene (Shim, 2008), and other small organic molecules (Cinchetti, 2009) or polymers (Majumdar, 2006) (Yue Wu, 2007) (Morley, 2008) (Majumdar, 2009), and theoretically (Xie, 2003) (Ruden, 2004) (Ren, 2005).

However, despite the encouraging fact that the reported devices were all showing some sign of magneto-resistance, the widely varying spin diffusion lengths that were extracted pointed out a fundamental lack of reproducibility. At this point, it is curious to note that in all the vertical organic spin valves cited above a significant conduction was achieved at low bias (tens or at most hundreds of mV) while comparable organic light emitting diodes based on Alq_3 require several volts before achieving a reasonable current density flowing through the device (Haichuan Mu, 2008), as charge injection has to overcome the impediment of interfacial contact barriers (Parker, 1994). Device resistance in the order of 25 kΩ and very weak temperature dependence, see for example figures 1.d and 2.a in (Xiong, 2004), are also unexpected results for diffusive transport, as the resistivity ρ of, for example, Alq_3 should be about 10^9 Ω cm (Choudhury, 2005) (Chapter 3, Appendix A).

A key experiment was performed with vertical junctions having a 10-20 nm Alq_3 spacer (Xu, 2007). Here, an MR signal and a junction resistance which increased linearly on decreasing temperature were observed. Due to the non-uniform covering of the surface and

the consequent large effective roughness of their organic film, the authors attributed the effects to the fact that the dominant transport mechanism was tunneling through locally thin regions between the electrodes. The fact that organic molecules can form tunnel barrier that perform as well as most inorganic barrier materials has also been observed, through ultrathin Alq_3 spacer layers, by (Santos T. S., 2007) and (Szulczewski, 2009).

Taking these reports together, it is natural to question whether magneto-resistance in hybrid organic spin valves, such those employing Alq_3, was ever due to spin injection and GMR, as claimed in early works, or just tunneling and TMR. Tunneling may occur through metal inclusions that are formed during the deposition of a metal layer on top of the sensitive organic film, in the widely used vertical device geometry.

Whether or not spin injection has occurred in organic semiconductors is of fundamental interest, because this is the essential requirement for performing spin manipulation within a semiconductor, as is desired for the implementation of triode spin devices.

The mechanism of the spin-dependent transport through an Alq_3 layer has been explained by (Vinzelberg, 2008) in terms of spin dependent tunneling across the barrier between local cobalt chains embedded in the Alq_3 layer and the LSMO electrode. His explanation was supported by the detection of cobalt chains within the organics by transmission electron microscopy and electron energy loss spectroscopy studies. The field and temperature dependencies of the MR, beyond being in agreement with those reported by the works cited above, were shown to resemble typical characteristics of magnetic tunnel junctions with oxide barriers. A similar study on Alq_3-based spin valves with organic layer thickness larger than the tunneling limit has revealed no magneto-resistance (Jang, 2008). Measurements of temperature-dependent I:V curves shown that charge transport was injection-limited, requiring several volts to open up the current across the device. This further supports the tunneling interpretation of the earlier reported MR.

Similar to inorganic semiconductors, the large conductivity mismatch between the metal electrodes and the organic semiconductor seems to prevent spin injection. This difficulty is typically alleviated by introducing an injection barrier (Rashba, 2000) and it was suggested in (Ruden, 2004) that the same approach may apply at the metal-organic interface. The insertion of a tunnel barrier in (Jang, 2008), however, did not improve spin injection in thick Alq_3 junctions, suggesting an intrinsic spin-depolarizing transport within the material. In (Barraud, 2010) a ferromagnetic junction consisting of a sub-nanometer sized tip indented into an Alq_3 layer, deposited on top of magnetic LSMO, has shown TMR values as high as 300 %. This indicates that the ferromagnetic-organic interfaces LSMO/

Alq_3 and Alq_3 /Co can be used for tunneling detection of electrons with defined spin states, respectively. Following this, we infer that the MR signal observed in all the previous works can be explained in the borderline case of only few current paths in the sub-nanometer range, such as pinholes in low quality tunnel junction. Hence the spin injection, transport and relaxation in Alq_3 and other organic semiconductor is yet to be proven.

It is noteworthy that the organic layer immediately below the metal electrode has been reported to have an ill-defined interface containing metal inclusions and pinholes of up to 100 nm thickness, in (Xiong, 2004) (Shimada, 2008) (Jang, 2008) (Vinzelberg, 2008) and to give a non-uniform surface coverage in (Xu, 2007). The introduction of a thin insulating barrier between the soft organic semiconductor and the top metal electrode was claimed to prevent the metal penetration in the organics in (Dediu, 2008), even though no explanation was given on why this should solve the problem. This is a well-known problem in the OFET community; evidences of metal penetration coupled with the formation of clusters following the metal deposition on top of organic layers are well documented and understood for example in (Watkins, 2002). Further, a magnetic dead layer at the Co /Alq_3 interface of thickness several nanometers was observed by (Venkatesan, 2011) and attributed to oxidation of cobalt surface through the organic.

Bottom contact lateral transport structures, using an organic semiconducting layer deposited in a narrow gap between two ferromagnetic electrodes, can avoid the side effect of metal-organic intermixing. In (Burke, 2010) and (Burke, 2011) an attempt was made with single crystals of rubrene and patterned NiFe electrodes, spaced by a gap around 200 nm. A little magneto-resistive effect attributable to weak localization was observed. This suggested that electrons could travel distances in excess of 100 nm inside the crystal without spin flip scattering, as it would destroy the phase memory required for weak localization. The spin information was lost at the ferromagnet-organic interface; however, the introduction of a tunnel barrier did not improve the spin injection. In a recent study (Yuta Kitamura, 2011), the investigation of the electronic structure of the interface between crystalline rubrene and ferromagnetic nickel outlined the presence of a Schottky barrier of height around 0.56 eV; spin injection is thus obstructed by the necessity of carrier thermionic emission over a high barrier, which leads either to injection of hot electrons, requiring thermalisation in the nonmagnetic spacer, or tunneling through a thick barrier (the problem of spin injection through a Schottky and tunnel barrier was discussed in page 11). A similar attempt was made in (Naber, 2010), thanks to the introduction of a common gate an FET behavior was clearly observed; however, possibly due to the

electrode separation in the micrometer range, no spin valve effect was investigated or reported. In (Ozbay, 2009) the conductive polymer P3HT was cast in the gap between two ferromagnetic electrodes of LSMO patterned in a lateral configuration by mean of focused ion beam (FIB) lithography. The gap was about 1 μm and a magneto-resistance up to 20% was observed at low temperature. Though, the detected current flowing through the device was suspiciously high, especially considering the quite long channel (electrode gap), at least three orders of magnitude higher than in comparable devices[2]. Current shortcuts combined with gallium ion doping may be present in the device structure, leading to both the MR and the high current density. In (Schmidt, 2011), a lateral spin valve fabricated by shadow evaporation of the ferromagnetic electrodes and vacuum deposition of small molecule organic semiconductor in the gap between the contacts has been implemented, showing room temperature magneto-resistance. The observed device resistance was in agreement with nano-size tunneling contacts and the observed effect has been entirely attributed by the author to tunneling through lateral pinholes forming at the edges of the electrodes during deposition via a shadow mask.

To the best of our knowledge, no communication exists on the observation of the electrical Hanle effect in vertical spin valves enclosing an organic layer. On the contrary, organic spin valves displaying MR effect have never shown any Hanle effect when tested, strongly suggesting a tunneling nature of the transport[3].

It is our understanding that the dominant interest in the field of organic spin electronics lies with the possibility of having an ohmic contact, at low bias, at the interface between a ferromagnetic metal and a semiconductor such as an organic polymer. When a potential barrier does not build up at the contact area, carrier injection can occur efficiently with, likely, some conservation of spin-polarization. This, combined with the low spin-orbit coupling and the low carrier concentration, could provide the basis for spin transport and manipulation. It has been reported by numerous papers that polymer based OFETs having metal source-drain electrodes and an organic active channel, namely of polythiophene derivatives, can show linear *I:V* characteristics at room temperature (Dodabalapur, 1998) (Brown, 1997). This was understood to occur when the work function of the electrodes matched the ionization potential of the semiconductor, in the simple rigid-band picture typically assumed for undoped conjugated polymers (in the absence of surface states). Due to very low carrier concentration, in intrinsic polymers, the absence of a depletion region

[2] E. Nowak, private communication.
[3] G. Schmidt, private communication.

was argued, and, in the case of level matching, of a Schottky barrier too. Therefore, the contact could in principle be transparent for carrier injection. The vast majority of the experimental studies published on OFETs have extracted the electrical device characteristics under this assumption, of ohmic contact resistance, e.g. (Klauk, 2003) (Salleo, 2004). The pertinence of this assumption largely relies on the device size and it will be discussed later in the chapter, on page 52.

To our knowledge, there are only a few spin transport studies with conductive polymers as spacer material, in hybrid vertical spin valve structures (Kumar, 2006) (Majumdar, 2006) (Dhandapani, 2009), and no reports of substantial MR in vertical devices having polymer spacer thickness significantly larger than 100 nm.

Concluding this literature survey on organic spin electronics, it is worth mentioning the very recent achievements obtained at constructing a fully organic spin electronic device. The only existing organic-based room-temperature ferromagnetic semiconductor, vanadium(tetracyanoethylene), has been employed as spin polarizer in a magnetic tunnel junction incorporating a thin nonmagnetic layer of rubrene acting as tunneling barrier between a ferromagnetic oxide film and the organic magnet (Jung-Woo Yoo, 2010). Therefore, a hybrid magnetic tunnel junction was actually built in which the organic layer does not only act as spacer material, and a small spinvalve effect was successfully found at around 100 K. Vanadium(TCNE) has been recently used also as the electrical spin injector into a GaAs/ AlGaAs light emitting diode (Lei Fang, 2011), further demonstrating the use of organic magnets as spin filters, at least at low temperature.

Materials for organic electronics

A general classification of the organic semiconductors of major interest in electronics can be based upon the molecular weight: small molecule and oligomer, made of a single monomer or few unit repetition, and polymers, built up by the sequential linking of, in principle, an unlimited number of monomer units. Some of the most studied small molecule organic semiconductors are depicted below and in Figure 1.17.

Oligoacenes: a class of aromatic hydrocarbons made up of linearly fused benzene rings. Pentacene ($n = 5$), tetracene ($n = 4$) and their derivatives have received most attention for

electronics, as they form well defined crystal structures. Rubrene (a tetracene molecule substituted with four phenyl rings) has also been the focus of many studies.

Oligothiophenes: a sequence of bonded thiophene rings, for n up to 8 it can be formed a crystalline structure; due to its ease of processing, mechanical flexibility and relatively high field effect mobility, (hexyl)sexithiophene (n=6) was employed for the active channel in the first all-polymer based FET (Garnier, 1994).

Phthalocyanines (abbreviated as H_2Pc) are macrocyclic compounds that have been investigated in solution processed OFETs (Chaidogiannos, 2009). A typical substitute is CuPc.

Tris(8-hydroxyquinolinato)aluminium (Alq_3) consists in a coordination complex wherein aluminium is bonded to three hydroxyquinoline ligands. It has been of vast interest in the OLED community due to its luminescence characteristics (Colle, 2003).

Fullerene: the interest in C_{60} and derivatives mainly comes from their use as electron acceptors in organic blends with polymers for photovoltaic application (Macedo, 2011), and its studies in OFETs (Haddon, 1995).

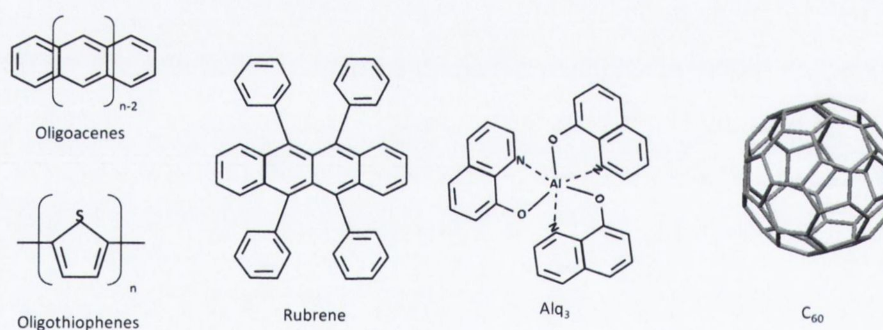

Figure 1.17 *Chemical structures of some of the most studied organic small molecule and oligomers semiconductors.*

On the other hand, among the most investigated polymers what follows can be found (see Figure 1.18).

Poly(p-phenylene vinylene) and *Polyfluorene* (PPV and PF) have been largely investigated in view of their luminescence and stability as light emitting diode polymers (Haiqiao Wang, 2001).

For transistor application, conductive polymers (i.e. intrinsically conducting polymers, among which the above mentioned PPV) are of most interest for the highest mobilities that they display.

Polyacetylene: it consists in the sequential repetition of the unit $(C_2H_2)_n$, the high conductivity found in this material was the actual reason triggering the interest in the use of organics in electronics. Its doped version has conductivity approaching that of silver and led his discoverer to win a Nobel Prize (Chiang, 1978).

Polythiophene (derivatives): they result from the polymerization of thiophene rings. They can become highly conductive when electrons are added or removed from the π-conjugated chain via doping. Their regioregular derivatives, due to the packing in well-organized lamella, display some of the highest intrinsic hole-mobility. As this polymer will be one of the focuses of our research, it will be described in more detail later, in Chapter 4, with particular attention at reviewing the evolution from the amorphous phase to the regio-regular phase, promoted by new synthesis techniques. When sulfur is substituted by the group NH, it is referred as to polypyrrole.

Polyaniline (PANI): it results from the polymerization of aniline units and its interest lies in the fact that it has displayed record conductivity when protonically (acid) doped (Tarver, 2009).

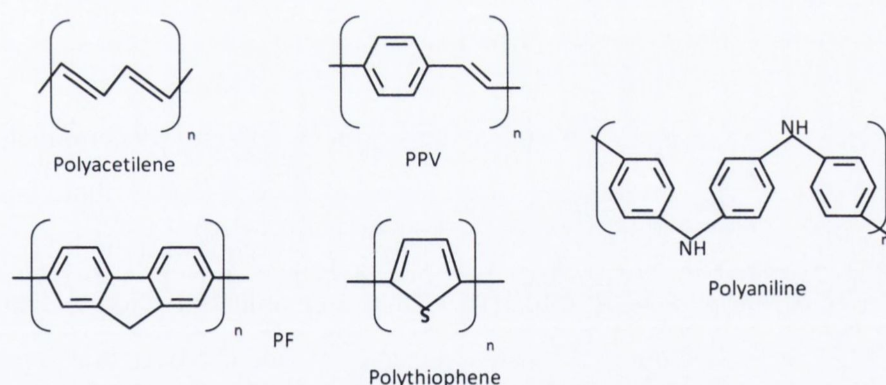

Figure 1.18 *Structure of some polymer semiconductors used in electronics, for LED and FET applications (see text for details).*

The effect of extrinsic doping, in the organic semiconductors summarily described above, does not manifests until reaching quite high doping levels; this is because there is typically a high density of localized states, which are the first to be filled as charge is introduced, pinning the Fermi level deep into the gap.

Organic transistors principally employ the thin film transistor (TFT) geometry rather than MOSFET of crystalline silicon. Here, a conducting channel is capacitively induced at the interface between the dielectric and the organic material. Therefore organic

semiconductors are often used as thin amorphous or polycrystalline films. The big advantage of polymer films, in this case, is that there are easy techniques available to process them, e.g. spin coating. Most of the thin films of small molecules are grown by vapor deposition, even though some techniques exist for processing them from solution (Afzali, 2002). However, they normally require extra care during the lithography, due to their immediate response to the solvents commonly adopted in a patterning process. Nonetheless, they can be grown in the form of large single crystals by vacuum sublimation or physical vapor transport, resulting in structures with a very limited number of impurities (Jurchescu, 2004). As in single crystals the grain boundaries, and the traps contained therein, are eliminated, they are suitable specimens for studying the intrinsic electronic properties of organic material. Single crystals can also be deposited on a substrate from solution (Mas-Torrent, 2004) (Kafer, 2005) (Takeshi Yamao, 2007), but the physical vapor transport method typically provides better results, especially in terms of crystal purity (Laudise, 1998).

Transport mechanisms

The models existing to explain the charge transport in organic semiconductors can be broadly distinguished in two families. One pertains to disordered materials, such as polymers and thin films of small molecules. It is mainly based on hopping transport and combines variable range hopping transport with an exponential energy distribution of traps. The model predicts a thermally activated mobility and a power law dependence on the gate voltage, expectations that have proved very successful in the analysis of OFET characteristics. The second family focuses on highly-ordered molecular crystals. Herein the temptation is to conclude that charge transport occurs via charges in delocalized states as in conventional semiconductors. However, the mobility in molecular crystals is at least moderate; the corresponding mean free path typically does not exceed the intermolecular distance, which is not physically acceptable for diffusion-limited transport. Different mechanisms, able to localize the carriers onto given sites of the organic crystals, have been adopted to explain this contrast (e.g. the self-trapping of polaron states and thermally induced lattice disorder). For understanding the mechanisms relevant to organic

semiconductors, one has to look for "old" books and papers that were written before silicon technology became the dominant paradigm.

Amorphous films

In disordered media, the current is typically the result of charge transport through localized states. The problem can be understood analyzing conduction in glasses containing transition metal ions, as in (Mott, 1968); before extending the treatment to organics. Supposing that in such a system there are N donor levels per unit volume with a mean energy E_d below the conduction band, whereas no acceptors are present, conduction could only occur via thermal excitation of electrons into the conduction band. The energy levels are illustrated in Figure 1.19. An exponential term $\propto exp\left(-\frac{1}{2}E_d/k_BT\right)$ would describe the conductivity (Arrhenius dependence). If cN ($c < 1$) acceptors are also present per unit volume (for example if a glass contains diluted metal ions of two valences), a proportion c of the donors lose their electron to an acceptor, and thus electrons can tunnel from an occupied to an empty donor. At helium temperatures this is the predominant mechanism of conduction. Between occupied and empty donors a potential energy $W_d \sim f(c)\, e^2/\varepsilon R$ builds up. Here R is the distance between donors, ε the dielectric constant and f (c) a number which depends on the proportion of acceptors c in the system. As a consequence, thermal activation is necessary for the conduction, as electron gains or loses the energy W_d from the phonons (Miller, 1960). In Figure 1.19 the spread W_d of energy levels of the donors is shown. The probability of hopping between two states of spatial separation R and energy separation W_d, based on a phonon assisted tunneling, is thus:

$$P = exp(-2\alpha R)exp\left({}^{-W_d}/_{k_BT}\right)$$

Where α is the inverse localization radius (the result of the overlap integral assuming that the wave function of an electron on each centre decays exponentially with distance as $(-\alpha r)$) and hence it refers to tunneling, while $exp(-W_d/k_BT)$ accounts for the thermal activation.

As an effect of the disorder, each hop involves thermal activation (Anderson, 1958) because the states associated with each donor do not form a narrow partially filled band.

This is a critical point, often misunderstood in organic literature, when attempting to describe transport in amorphous organic films in the band-like picture.

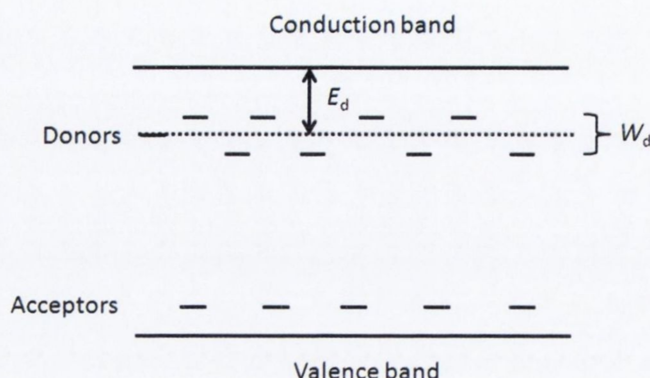

Figure 1.19 *Energy levels in a doped and compensated semiconductor.* E_d *is the ionization energy of a donor,* W_d *the spread of energy levels. From* (Mott, 1968).

This treatment is consistent for a material in which the distortion of the lattice around a charged centre can be neglected, such as the case of germanium, which has been investigated in (Mott, 1961). Instead, in a polar solid or in a medium made of organic molecules, an extra electron distorts the molecule or ring to which it is added. The extra activation energy due to this polarization can become the most important term. The hopping probability is similarly written as $P = exp(-2\alpha R)exp\left({-W}/{k_B T}\right)$ but here

$$W = \frac{1}{2}W_d + W_p$$

showing the contribution of the hopping activation energy W_d due to polarization W_p. A centre charged with an electron produces around it a field in which the potential energy of an electron is $V(r) = e^2/\varepsilon r$. The ions are displaced from their position by this charge, producing a potential well in which the energy of an electron is lowered by $-e^2/\varepsilon_{eff} r_0$, where r_0 is the radius of the cavity in which the ion is located and ε_{eff} an effective dielectric constant. The energy required to polarize the medium is $E_p = e^2/\varepsilon_{eff} r_0$. The energy that results from the polarization of the medium is often referred to as the polaron energy, or polaronic effect (which describes the coupling between the molecular configuration-physical structure, and its electronic energy).

In this case the mechanism by which an electron moves, carrying its polarization cloud, has to account for the configuration of the two molecules involved in the charge transfer. Here the activation energy W_{p} is given by small polaron formula (Holstein, 1959)

$$W_p = \frac{1}{2} E_p$$

The activation energy for hopping is half the polaron energy E_{p}. This can be understood in the picture of a polarization well (Figure 1.20).

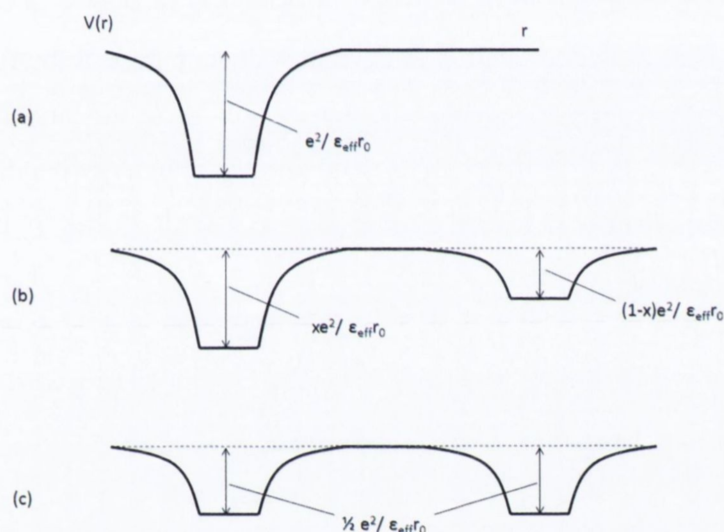

Figure 1.20 *Polarization well for two donor states in a glass, an electron is in the left hand well. a) Unexcited, b) excited, c) fully excited in a way that the electron can hop from one to the other. From* (Mott, 1968).

As a consequence of thermal vibrations, the two wells can be excited in a way that one well is less deep (Figure 1.20 b), for instance

$$V(r) = (1 - x)\, e^2/\varepsilon_{eff} r$$

And

$$V(r) = -x\, e^2/\varepsilon_{eff} r$$

On the two wells the variation in time of x can be considered a simple harmonic oscillator, with x oscillating around an equilibrium point $x = 0$. When $x = 1/2$ (Figure 1.20 c), the electron can tunnel from one well to the next without changing its energy; of course this configuration has the lowest activation energy. In some sense, one can say that the transfer occurs when the molecular states involved are at resonance and the total energy is

indifferent to the charge being on one molecule or the other. Thus the charge hops when this favorable configuration is reached. By adding the energy terms required to make up this configuration (as the energy to raise the level of the electron $\frac{1}{2}x\, e^2/\varepsilon_{eff}r_0$, the polarization energy released and the energy required to form a well on the next site), one can easily find $W_p = \frac{1}{2}E_p$, the Holstein formula.

Following this introduction to the basic concepts of phonon-assisted tunneling, thermal activation and polaron binding energy (or polarization of the medium), we can now turn our attention on analyzing the transport in a disordered system. Here localized carriers may travel through the material from one localized state to the next. Basically, a carrier may hop from one site to the next provided that the initial state is occupied and the final state is empty. Whereas mapping these sites in real space is not trivial, due to the large disorder, in energy space it is easier. It is intuitive that charges would hop in an energy band around the Fermi level, where filled and empty states are closest (Figure 1.21).

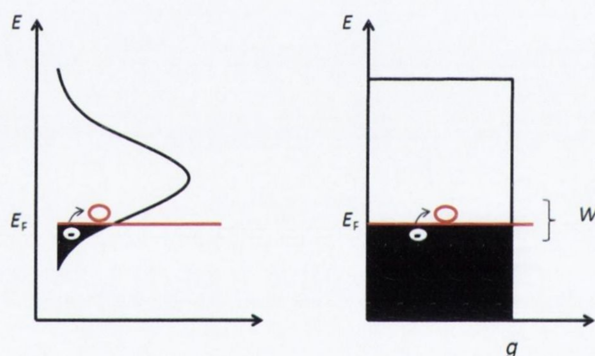

Figure 1.21 *Left: representation of a Gaussian DOS with a charge hopping upwards in an empty state. Right: simplified constant DOS used for the analysis of Mott's variable range hopping.*

A simplified energy distribution of the sites can be assumed, with the density of states g being uniform, $g(E) = g$. The spread of the energy levels W, defined previously, defines both the number of states available for hopping (gW) and the energy to rise for hopping from a well to the next.

When a carrier hops by an energy W and over a distance R, it has $\frac{4}{3}\pi R^3 gW$ sites to choose (g is the density of states per unit energy). At least one site must exist within a range of (R, W) for the hopping to occur, $\frac{4}{3}\pi R^3 gW \cong 1$. The transition probability for moving in space while going up in energy can thus be written as:

$$P = exp(-2\alpha R_{i,j})exp\left(-{}^{W_{i,j}}/_{k_B T}\right) = exp\left(-2\alpha R - \frac{1}{k_B T \frac{4}{3}\pi R^3 g}\right)$$

The most probable hops occur for a distance *R* and energy width *W* that maximize the rate, which can be obtained by setting $\frac{dP(R)}{dR} = 0$; this gives

$$R_{optimum} = \left(\frac{1}{8\alpha k_B \pi g}\frac{1}{T}\right)^{1/4} \quad or \ W_{optimum} = \frac{(8\alpha k_B T)^{3/4}}{\frac{4}{3}(\pi g)^{1/4}}$$

Substituting in P it is found

$$P_{i,j|Max} \propto exp\left[-\left(\frac{T_0}{T}\right)^{1/4}\right]$$

Here T_0 is a constant. This is the Mott's famous variable range hopping equation, which predicts that the conductivity should be proportional to $exp\left[-(T_0/T)^{1/4}\right]$ when the transport mechanism is hopping among localized states at the Fermi level of a semiconductor. A detailed treatment of the problem can be found in (Mott, 1968) or (Tessler, 2009).

The hopping radius *R* is the distance over which the hopping for available energies is possible at a given temperature *T*. It was represented as a sphere around the donor that is effectively conductive. There then exists a critical radius where the spheres just touch each other, thus forming a percolating network of interconnected conductive material spanning the entire sample through which current can pass. This is the idea behind the above calculation. The percolation theory and variable range hopping theory are often fused together. The Mott equation predicts the temperature dependence for hopping in a three dimensional disordered system at the Fermi level. Note that it is analogous to say that the resistivity ρ behaves as $\ln \rho \propto (T_0/T)^{1/4}$, which is very easy to distinguish in a set of experimental data, as plotting the resistance on a log scale versus 1/*T* should give a straight line of slope 1/4 (the proportionality constant is of order unity). So this is a very useful tool to individuate the type of transport mechanism occurring in a system, but to be sure the plot should extend over several orders of magnitude. Later, in (Efros, 1975), the exponent in the Mott equation was changed to $exp\left[-(T_0/T)^{1/2}\right]$ as it was argued that the Coulomb interaction creates a Coulomb gap leading to this dependence at low temperature.

(Aharony, 1992) described the crossover with decreasing temperature from the Mott to the Efros behavior, and the exponent was changed to any value x in between, introducing a function $f : f(x)$. Typically the temperature dependence of processes involving thermally activated transitions (not to just one single level) will in general deviate from simple Arrhenius's behavior. These models have been able to successfully describe the temperature dependence of the resistivity in many amorphous inorganic systems (Gittleman, 1972) (Abeles, 1975) (Entin-Wohlman, 1983) (Zhang, 1990).
In the above derivation, it was first of all assumed that the charges are hopping close to the Fermi level, which is correct when the density of states is changing slowly with energy. When dealing with a non-uniform density of states, transport does not necessarily occur at the Fermi energy. In an exponential DOS, for example, there are many more available states at higher energies and, in fact, it has been shown that hopping under these conditions can be effectively described in terms of activation from the Fermi energy to a specific transport energy, which typically leads to the Arrhenius behavior. Hence it is expected that a derivation similar to the variable range hopping but for a different given distribution, leads to a quite different temperature dependence. Typical distributions adopted are Gaussian or exponential. These concepts are particularly useful for treating amorphous organic structures. Here, organic solids are not composed of donor-acceptor complexes and are characterized by a large band gap (several eV). Conduction takes place through states of the host, not via dilute impurity levels. These states originate from the fact that the conjugated segments are broken into sub-conjugated units by physical defects (which naturally exist due to the non-periodicity of the host), thus the material has unbounded atoms with unpaired electrons. The energetic spread of these states, at least in organic glasses, is due to the weak intermolecular binding: the thermal fluctuation in positions can change the polarization energy on each localized state, hence providing the dominant source of disorder (Bassler, 1981). The fluctuations of the molecular coordinates are reflected in a Gaussian distribution of the energy states. The amount of disorder is measured by the standard deviation (Gaussian width) of the energy distribution of the localized states. These states are accommodated on the molecules, and charged carriers hop between them. The Gaussian width, which is mainly given by the fluctuation in the dipole-dipole and ion-dipole intermolecular potentials, was measured to be around hundred meV from absorption measurement in pioneering work on amorphous organic films (Hesse, 1980). In large band-gap and intrinsic organic material (typically several eV) such a narrow value of structure-induced broadening of the electronic levels prohibits the

formation of a high density of localized states near the middle of the gap, as required for hopping near the Fermi level to become the transport mechanism.

Therefore, the concept of variable range hopping at the Fermi level is not applicable to intrinsic organic solids, in which the density of localized states near the center of the gap is decreasing rapidly (Figure 1.21), and more pronounced temperature dependence of the mobility is expected. Making use of a Monte Carlo simulation, (Bassler, 1982) has shown that the charge transport features in organic glasses can be explained assuming a Gaussian energy distribution of hopping sites in which, being a thermally activated process, the temperature dependence of the mobility follows a non-Arrhenius behavior of the form

$$\mu = \mu_0 exp[-(T_0/T)^2]$$

Even though agreement between simulation and experiments on poly-phenyl derivatives was excellent, when the electron-lattice coupling within the semiconducting molecules of a given material is strong, the resulting localized states (polarons) play a significant role. For instance this was the case in (Waragai, 1995) in his study on oligothiophenes. In this case the hopping motion among the localized polarons within a Gaussian distribution better described the transport mechanism. The polaron theory predicts a simple Arrhenius relationship between the mobility μ and temperature, which was actually observed, and a dependence of *ln* μ on F^2, where F is the electric field. This functional form alone, however, did not reproduce the experiments. It was by taking into account the Gaussian disorder on top of the polaronic effect that (Garstein, 1994) has shown that the polaron model can reproduce the experimentally observed linear dependence of *ln* μ on $F^{1/2}$, at least over a region of data. Hence in oligothiophenes the temperature-dependence of the mobility followed the simple Arrhenius relationship, μ is proportional to $exp(-W/k_B T)$, whereas the activation energy W decreases with increasing electric field as $F^{1/2}$ and, according to their model, is directly related to the polaron binding energy in the material. The charge transport could be interpreted in terms of thermally activated hopping of the polarons between oligothiophene molecules. This temperature and field dependence, of the form

$$\mu \propto exp\left[-\left(E_0 - \beta F^{1/2}\right)\left(T^{-1} - T_0^{-1}\right)\right]$$

is often referred as the phenomenological Gill equation, who first proposed it to empirically describe the relations of the mobility in amorphous films (Gill, 1972). Such an

expression has actually been discussed in the context of the polaron model also by (Bassler, 1993), however the field dependence was again predictable only on a restricted region, whereas the $\propto exp(F^{1/2})$ behavior is observed in a large range of fields, typically starting at about 10^5 Vcm^{-1} (Schein, 1989) (Borsenberg, 1996) (i.e. at 10 V over a gap of 1 μm). It is worth reviewing the dependence of the mobility on F for some of the main existing models, to distinguish the origin of the relation.

It is striking that this dependence closely resembles the Pool-Frenkel (PF) law (Frenkel, 1938)

$$\sigma = \sigma_0 exp[(e^3 F/\varepsilon)^{1/2}/k_B T]$$

where ε is the dielectric constant. The PF behavior is expected to occur as a consequence of the lowering, by the applied electric field F, of the potential barrier a carrier has to overcome, for leaving a charged center (the Coulomb potential is lowered by the field by $\delta V \propto F^{1/2}$). This mechanism, however, is believed not to be in effect in the class of organic polymers, because charged traps are not present in these materials in a sufficient number (Schein, 1989). Therefore the origin of the PF behavior and of the activation energy for the mobility should arise from a different mechanism. The polaron model has been initially employed, as described above. However, as anticipated, the field dependence was predicted only over a restricted region of fields and was not justified in any way, as it was the result of numerical simulations. A different interpretation came from a dipole-trap model (Novikov, 1994). Here the charged centers are dopant molecules in a doped polymer, considered to act as traps having a dipole moment in a matrix in which the charge carrier is motile. The F and T dependence are determined by the escape rate of charges from these traps. For a large enough dipole distribution the site energies are given by the electrostatic energy due to the dipoles, showing the PF behavior. A random distribution of permanent dipoles was also suggested as the origin of the PF field dependence in conjugated polymer OLED (Bozano, 1999) (Malliaras, 1998). However, a dipole concentration unrealistically large (1 every hopping distance) would be required; therefore the model did not fully explain the mechanism. An important step was taken in (Garstein, 1995); with the introduction of some correlation between the energies of neighboring sites, in a Monte Carlo simulation, which actually could reproduce the observed behavior. In this model the energetic disorder is spatially correlated. The spatial correlation is provided by the long range forces, such as charge-permanent dipole interaction with neighbors,

accompanying the fluctuations of the energy site. The spatial correlation has the effect of smoothing the fluctuations of the random potential experienced by a hopping charge and the potential wells from which a carrier has to escape, which has an increased spatial extent, of the scale of the distance between hopping sites, bringing the field dependence to lower fields (sub linear dependence of $ln\ \mu$ on F). Therefore, the PF behavior frequently observed in amorphous polymer could be related to spatial correlation of energetic disorder. This model can actually fit this dependence over the range of field found in experiments. The existence of spatial correlations can be understood as due to the fact that amorphous organic structures are not expected to be completely random systems but to be characterized by some short-range order, which reflects the anisotropy of molecular interactions (Schein, 1992). Indeed, the PF and Gill relation will be treated again later, when dealing with partially ordered films.

As to the amorphous films, however, the scenario is actually wider than described so far. For example, in (Brown, 1997) the temperature dependence of the conductivity of solution processed polyDOT films were well fitted against $T^{-1/4}$, suggesting transport via variable range hopping; whereas in PPV and pentacene processed via soluble precursors it followed an Arrhenius relationship, and the charge transport resembled the characteristics of thermal activation from localized polaronic states. The width of the polaron energy level could be estimated from the activation energy to be of order 0.2 eV. Relevant work was made by (Vissenberg, 1998) to combine a percolation model, of hopping between localized states, and a transistor model, to extract an expression for the field effect mobility in amorphous-material based transistors. Both the gate dependence and temperature dependence of pentacene and PTV, from the data in (Brown, 1997), could be reproduced.

The large variance of behaviors observed (including the frequently appearing PF type) should not surprise us. Depending, for example, on the actual value of electron-lattice coupling, band-gap and degree of disorder (Gaussian width) relevant to a given material, a peculiar behavior can arise among the scenarios illustrated. A single model cannot fully explain the electric field and temperature dependences of the charge-carrier drift mobility in these systems; the reason being that various mechanisms of electronic transport apply in different systems and also in different regimes of temperature and electric field, so no single mechanism can be expected to explain the whole variety of the experimental data. As a matter of fact, a similar comportment is normally observed in inorganic glasses, where the transport mechanisms vary widely depending on the material and, for the same material, on the temperature and field regime. This causes an actual change in the gradient

of the experimental curves, as seen for example in (Le Comber, 1970) and in the illustrative Figure 1.22 which is taken from his work.

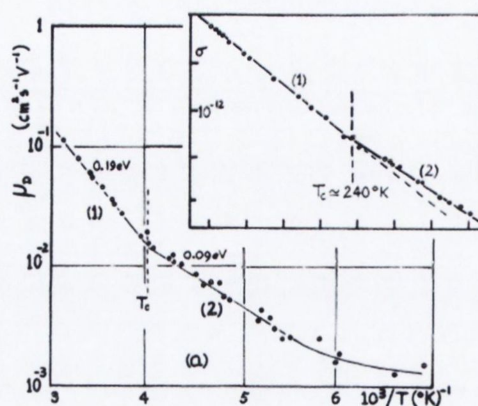

Figure 1.22 *Temperature dependence of the electron drift mobility in amorphous silicon, the inset shows the change in gradient near the temperature T_c, which reflects a change in the transport mechanism. Note the log-linear scale. Taken, as an illustrative example, from (Le Comber, 1970).*

Similarly, one should plot his experimental data on a log-linear scale and identify the transport mechanism there involved, provided that a large enough set of temperatures and fields are spanned.

Partially ordered thin films

Inorganic semiconductors

It was early recognized that the presence of short range order is enough to ensure that the electronic density of states is not significantly different in the amorphous and crystalline phases and that the concept of a forbidden gap corresponding to an energy for breaking valence bonds between the atoms is still adequate (Davis, 1970). Though, the electronic states at the band edges are perturbed in the amorphous phase: the density of states is non-zero in the gap, as foreseen by (Mott, 1967) and documented via optical measurements in (Fagen, 1970). One expects a high density of localized states tailing in from the conduction and valence bands, as shown in Figure 1.23. These states originate from the structural

defects and the variation of density and composition in the material, i.e. the varying valences of the atoms from site to site.

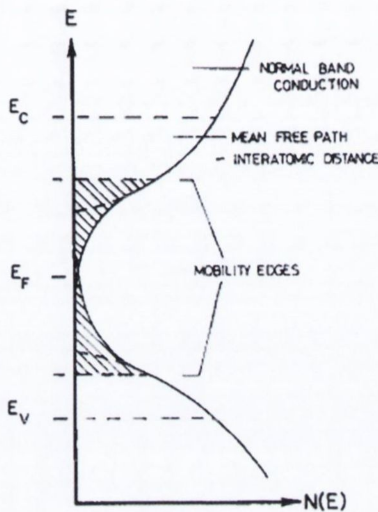

Figure 1.23 *Sketch of density of states of valence and conduction bands, showing the region (shaded) in which the states are localized and the regions in which the carriers move with a short mean free path. From* (Davis, 1970).

The fluctuation in the potential on the atomic scale caused by the disorder, has then the effect of localizing these states (a localized state is defined as one with probability amplitude decreasing exponentially with the distance from the center). These charged states above and below the Fermi level act as trapping centers for electrons and for holes, respectively.

Hence, in a prototypical amorphous material, the lowest states for an extra electron are in the traps, as indeed is often the case in crystalline materials. But there are far more of them (not due to impurities or point defects but to the glassy structure itself). Their number is large enough that an electron can move from one localized state to another by tunneling. This is a thermally activated process, because nearby states do not have the same energy (Figure 1.24). It is called "thermally activated hopping", and it leads to low mobilities (of order 0.1 $cm^2V^{-1}s^{-1}$ in an inorganic semiconductor) (Mott, 1973).

The essential news is that when the traps are sufficient in number (which occurs as the energy is increased to a certain level at the mobility edge), the electron no longer has to have an activation energy to enable it to move, as it can tunnel from one centre to another (referred to as "quantum mechanical hopping"). Here the electron is free from the traps

and has a higher mobility (up to 10 $cm^2V^{-1}s^{-1}$) and his behavior is similar to that of an electron in the conduction band of a crystalline semiconductor, with the exception that the mean free path is very short (distance between atoms). Therefore at these mobility edges the conduction process changes from a low mobility "band transport" with finite value at T = 0, to a thermally activated hopping between localized gap states which disappears at T = 0. Hence the gap in this case represents the gap between mobility edges (rather than between extremities in the density of states, as in crystalline solid) as it was first fully recognized by (Cohen, 1969). Only deep into the bands, band-conduction with long mean free path may occur (Davis, 1970).

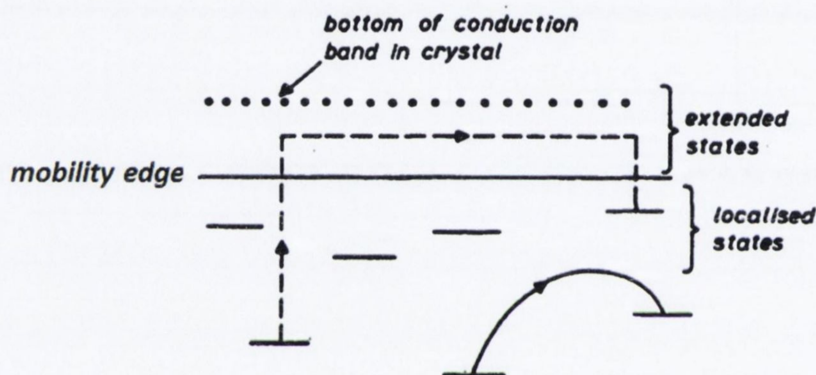

Figure 1.24 *The horizontal lines show the traps in the semiconductor; if the density of trap is high, the bottom of the conduction band is replaced by the mobility edge. Below the mobility edge the electrons move by thermal activated hopping (shown by the arrow) whereas the dotted line show the motion by trap and release, and sequent trapping. From* (Mott, 1973).

The presence of the mobility edges explains why well-defined activation energy is typically observed for the conductivity, regardless of the lack of sharp band edges, and a conduction showing activation energy significantly lower than the energy gap.

A most representative experiment which was carried out to test this model is in (Le Comber, 1970), on electronic transport in high quality amorphous silicon films. Here, measurements of the mobility at low temperatures have shown small activation energy, corresponding to hopping from centre to centre; because at sufficiently low temperatures conduction by carriers in localized states in the gap is expected to predominate. While at high temperatures $T > T_c$ the mobility is trap-limited, the electron being excited to the mobility edge, and the activation energy was about twice as great (Figure 1.22).

From the amount of the low temperature hopping conduction and from the change in conductivity, which results when a thin film of amorphous semiconductor is charged as in a field effect transistor, it is possible to estimate the density of gap states near the Fermi level, provided that one knows the distribution of the localized states, which can be found by transient photoconductivity (Huang, 1983). In (Shur, 1984) it was shown that the transition from below to above threshold operation occurs when the Fermi level, in the accumulation region, moves out from the tail of localized states in the gap. An increase in the electric field generated via the gate causes the accumulated carriers to fill localized levels. As the applied gate continues to increase, the Fermi level positioned in the gap moves towards the band edge. Eventually, the energy gap between the edge and Fermi level will be less than $k_B T$, which causes an increase in the presence of charge carriers above the mobility edge. The mobility varies following the applied gate voltage, whereas in a crystalline semiconductor the mobility is constant, resulting in a linear dependence of the conductivity on the applied gate voltage.

Organic semiconductor

We can now turn our attention to organic materials. By enhancing the control over the structure during the chemical synthesis of conductive polymers it has been possible to produce polymers exhibiting a more ordered arrangement (Chen, 1995), relative to the amorphous structure described in the previous subsection (page 33). The general approach consisted in introducing symmetric units along the polymer chain, as in Figure 1.25, promoting the appearance of a supra-molecular ordering (McCullough, 1992) (McCullough, 1993). Here the polymer chains tend to align one parallel to each other, thanks to the anisotropy of intermolecular interaction introduced by the side elements. Such polymers are normally referred as to regio-regular polymers, and they will be described in details in Chapter 4. The casting of thin films of these polymers typically results in complex microstructures, in which partially ordered "crystalline" domains (of size of tens of nanometers) (Zhao, 2004) are embedded in an amorphous matrix.

Thin films of this type have been often observed to possess a largely enhanced electrical conductivity (Sirringhaus, 1998), relative to predominantly amorphous structures. The effect on the electrical characteristics is that ordered regions favor the formation of band-like states, coexisting with the localized states induced both by the frequent defects and by the disordered region separating the ordered grains. The scenario is very similar to that of

high quality amorphous silicon (or polycrystalline silicon); indeed an equivalent approach can be used to describe the charge-carrier transport mechanisms.

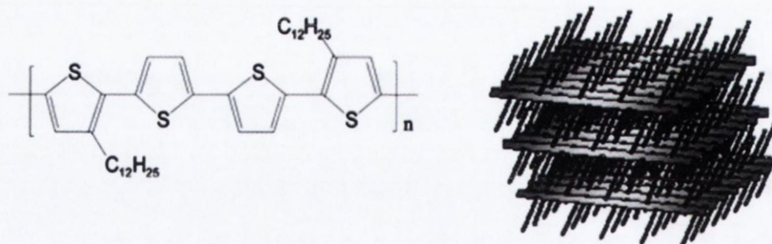

Figure 1.25 *Molecular structure of regio-regular PQT and three dimensional packing of the molecules. Note the symmetric side chain* $C_{12}H_{25}$. *From* (Zhao, 2004).

An important step was taken in (Rakhmanova, 2000), where following the approach of (Garstein, 1995) (previously described) a short-range correlation between energies of the hopping sites was introduced in a Monte Carlo simulation. The correlation arises from the fact that in crystalline regions the sites have a smaller spacing and the energy of spatially close sites is correlated. The scale length of the correlation was obtained by the coherence length measured by x-rays in (Yang C. Y., 1998), in which the polymer MEH-PPV showed crystalline domains of ~5 nm separated by amorphous regions. The spatial correlation between the energies of hopping sites led to prediction of the Poole-Frenkel type behavior, actually observed in the polymer MEH-PPV, as well as in many other having this short range ordering (Horowitz, 1995) (Bao, 1996) (Kapoor, 2002) (Salleo, 2004).

Typically, the transport in these systems is described as a multi-trap-and-release (MTR) process, rather than variable range hopping. Here traps capture a large part of the charge, holding it in place, and conduction occurs by temperature and field assisted excitation from the trap to the bands or, better, to the mobility edge. The temperature dependent mobility is then caused by the thermal equilibrium ratio of trapped and "free" charges. Similarly to the case of polycrystalline silicon, the experimental data on transistors employing regioregular polythiophene are best interpreted by considering the coexistence of a mobility edge and an exponential distribution of traps (Salleo, 2004), from which charges are trapped and released to the mobility edges.

Considering the analogy to the PF type behavior often observed, in terms of the linear dependence of the log of the mobility on the square root of the electric field and on temperature, the MTR model is often mentioned in one breath with the Poole-Frenkel

formalism when dealing with organics, as in (Stallinga, 2011). PF emission was originally proposed to explain the fact that electrons can slowly move through an insulator by means of the fact that, occasionally, thermal fluctuation gives to an electron, trapped on a localized state of an insulator, enough energy to escape its potential well and move to the conduction band. Once there the electron can move in the crystal, for a brief amount of time, before relaxing into another localized state. The Pool-Frenkel emission describes how, in a large electric field, the electron does not need as much thermal energy for being released (as part of this energy comes from the field itself); the potential well is lowered by the field of an amount $\delta V \propto E^{1/2}$. Hence it does not need a large thermal fluctuation and it is able to move more frequently (Figure 1.26).

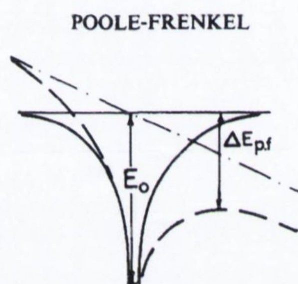

Figure 1.26 *Illustration of the electric field lowering of a Coulomb barrier E_0 by the Pool-Frenkel (ΔE_{pf}) mechanism. From* (Davis, 1970).

The analogy with the MTR mechanism is evident; therefore the use of a mobility edge with the inclusion of traps, in organic polymers, is sometime referred to as the Pool-Frenkel model. In a recent work, on solution processed pentacene FETs (Tomo Sakanoue, 2010), it was shown that at low temperature and small lateral electric field, charges become localized onto individual molecules in shallow trap states, and that a moderate lateral electric field is able to detrap them, resulting in highly non-linear low-temperature transport.

An illustration of the scenarios arising for the conduction mechanism at increasing inter-molecular ordering will be given in Chapter 4, with emphasis on the conductive polymers poly-alkythiophene and poly-hexylthiophene, of particular relevance to this work.

The differences that can be found in the experimental data reported in literature are attributed to the different widths of the shallow localized state distribution at the edge of the bands, due to the structural disorder peculiar of a given material and of a given

deposition technique. As it is known, the use of different solvents for casting a given polymer largely affects the polymer morphology (Nguyen, 2000).

Single crystals

We now focus on crystals of small molecules held together in a solid by Van der Waals forces. Among them, oligoacenes (containing typically two to ten benzene rings) and oligothiophenes (up to eight thiophene rings) (page 29) have been most investigated in literature due to the possibility of making single crystals with only a few defects via repeated sublimation processes. Because of the weak Van der Waals bonding, many electronic properties of these materials are determined by the structure of an isolated molecule. The little intermolecular overlap of the orbitals leads to narrow electronic bandwidth, typically of order 100 meV (at least two order of magnitude smaller than in silicon) and low carrier mobility (at best 1-10 $cm^2V^{-1}s^{-1}$). Time of flight measurements on ultra-purified oligoacene crystals have shown that mobility increases when temperature decreases following an inverse power law (Karl, 1991) (Karl, 1999) (Figure 1.27).

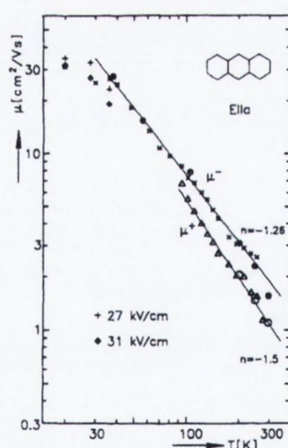

Figure 1.27 *Electron and hole mobilities as a function of temperature for anthracene. From* (Karl, 1991).

In these experiments intrinsic charge transport (not limited by static disorder) was realized in the bulk of the crystal. The temptation was to conclude that charge transport occurred via charges in delocalized states. However, the mobility is quite moderate, and corresponds to an electron mean free path which does not exceed the intermolecular distance. To

account for this inconsistency the description of the transport is typically made based on the polaron models and the small polaron concept (Holstein, 1959) (an electronic state with a correlation among electronic and lattice configuration at the scale of the molecular spacing). Essentially, one should include the possibility of the formation of polarons, which localize the carrier on a given site, or polaron bands, which modify the temperature dependence of the mobility and the effective mass expected for a charge carrier, when dealing with organic solids. Under these circumstances, the effect of the electron-phonon coupling is to make the effective bandwidth (as perceived by the charge carrier) temperature dependent. As the temperature increases, the effective bandwidth decreases as a consequence of stronger vibronic interaction.

The measured intrinsic mobilities of oligoacenes single crystals have in fact shown a band-to-hopping transition occurring at temperature about 100 K (Schein, 1978) (Figure 1.28). This enabled to distinguish two different charge-transport mechanisms in two different regimes, band-like transfer at low temperature, and hopping transfer at high temperature.

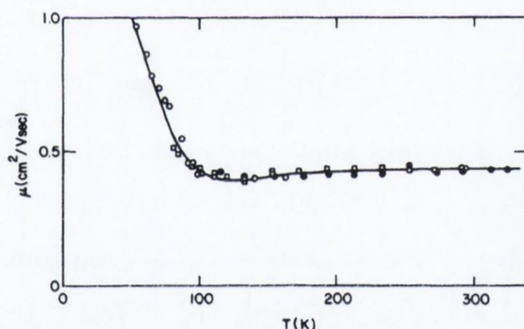

Figure 1.28 *Mobility of naphthalene measured by transient photoconductivity from 54 to 324 K. From* (Schein, 1978).

It is the interaction with the lattice and the consequent localization which is the key element in defining this process. Polaron theory was first introduced to describe conduction in organic crystals by (Silbey, 1980), and further developed by (Munn, 1985) and (Kenkre, 1989). These theories could qualitatively predict the transition between band-like and hopping transport as temperature increases. The quantitative application to data has been recently improved by (Cheng, 2003), who observed that a small polaron band theory is inadequate for describing charge carrier mobilities because the temperature dependence was partially unexplained, and by (Coropceanu, 2009) and (Dongmeng Chen, 2011) who addressed these issue by including the thermal fluctuations of the electronic

coupling. The complexity of developing a model describing the polaronic transport at high temperature is due to the fact that under this circumstance the thermal energy induces lattice vibrations which can be sufficiently strong to destroy the translation symmetry of the crystalline lattice (normally referred to as off-diagonal disorder) (Troisi, 2005). The band description is washed out by the thermal fluctuations, and a disorder induced cross-over between band-like and incoherent hopping is expected to occur.

As established in other works, the electronic wave functions are being localized by the presence of large thermal lattice fluctuations (Troisi, 2006) (Picon, 2007). In the case when the electron-lattice interactions is too weak to induce polaronic self-localization in a potential well, it is only the presence of these kind of fluctuations which can justify the short mean free path (characteristic of incoherent localized states), observed at room temperature in crystals (Fratini, 2009). The latter is an interesting point, as it underlines that when the electronic bandwidth is comparable to the thermal energy, and the bonding between molecule is relatively soft (as in Van der Waals crystals), the disorder on the transfer integral has its origin in the thermal lattice vibrations, and plays the role of localizing the state, as it normally occurs in polaron dominated transport, where charges are typically self-trapped.

This phenomenon is equivalent to having a band tail of localized states extending into the gap between extended band states. An additional transport channel emerges due to the states below the band edge, and both band-like and incoherent states are expected to contribute to the transport. The relative weight will depend on the temperature: the thermal lattice disorder defines how much a tail extends into the gap. This is a very significant difference with the previous models based on a band tail (say MTR model), in which the main role is played by the thermal population of the states. Here, the states their self are created by the thermal excitation; hence, upon increasing the temperature, the band states are progressively ruled out, because the thermal vibration gives rise to incoherent excitations that play the role of confining them, and are responsible for the localized character of the particles.

The polaron model has been applied to early experimental studies on naphthalene (Schein, 1978) (Karl, 1991) with success, by (Kenkre, 1989) (Hannewald, 2004) (Coropceanu, 2009) and others, but there is a significant lack of experimental measurements on bulk conduction for any other crystal, and an abundance of models to predict them. What if the measurements performed by only these two groups (Schein & Karl) were affected by some experimental error, such as current parasitic paths?

The most commonly used tool for studying the electrical properties of organic crystals is the organic FET, probably in view of the possible application of this class of material to electronic circuitry. However, in this device the conduction occurs at the surface, where a conductive channel is induced by a gate. The surface transport may differ from that in the bulk because the density of carriers is orders of magnitude different, and interaction between polaronic carriers may become an important aspect. The recent developments of fabricating highly-pure single crystal organic transistors have enabled the observation of intrinsic transport of field induced surface charges (Schoonveld, 2000) (Butko, 2003) (de Boer, 2003) (Podzorov, 2003) (Takeya, 2003) (Aleshin, 2004) (Lee J. Y., 2006) (Masatoshi Sakai, 2007) (Taishi Takenobu, 2008). In all the cited works the carrier mobility decreases on lowering the temperature, in disaccord with the observations of time of flight measurements in the bulk crystal. Transport is typically, once more, understood in terms of trap and release of charges, but from shallow traps separated by the band edge by only a few k_BT (Gershenson, 2006). Even though the density of structural defects in the channel of a single crystal device is low, these defects are still present, estimated around 10^{10} cm^{-2} on a pristine surface of rubrene (Podzorov, 2004). In (Horowitz, 1995) a multiple trapping and release model was used to model the FET behavior, charge transport was assumed in delocalized bands, with no assumption about whether the process occurred via delocalized charges or polarons, with the only limit of a distribution of traps near the band edge. The result is, of course, very similar to that of the hopping model, with a thermally activated mobility and power law gate dependence.

The difference from the thin film FETs characterized by a disordered organic channel is that the mobility typically decreases monotonically with decreasing temperature within the entire temperature range, whereas in single crystal it is sometime observed a non-monotonic dependence (de Boer, 2003) (Aleshin, 2004), at least nearby room temperature. This was initially understood to occur for high-purity crystals in the presence of shallow traps, following:

$$\mu \propto T^{-n} exp(-E_a/k_BT)$$

For activation energies E_a not much larger than k_BT (shallow traps) this formula accounts for non-monotonic temperature dependence (Karl, 1999). In contrast with the measurements on the transport in the bulk of the crystal, in TOF experiments, in organic field-effect transistors a negative temperature coefficient ($d\mu/dT < 0$) at low temperature, which is often stated to be an indicator of band-like transport in these systems, has not

been observed. The conduction on the surface of a crystal near the dielectric FET surface was revealed to be dominated by the transport of Fröhlich polarons (quasi-particles consisting of a charge carrier surrounded by an ionic polarization cloud) (Hulea, 2006), causing the aforementioned non-monotonic temperature dependence of the mobility, which is not only due, then, to structural disorder and defect states.

A further effort to describe the expected conduction in single organic crystals will be made in Chapter 3, with emphasis on pentacene, of particular interest for this work.

Contacts

The problem of contact resistance in hybrid organic devices has recently been recognized as a major issue. In the earlier stage of research into organic electronics the conductivity of the available media was so low that the current was entirely limited by the organic channel resistance. As new materials with improved mobility have been synthetized, limitations by contact resistance are getting more and more crucial. Reinforcing this concern, modern devices are typically designed with much shorter channel length; e.g. in transistors this is motivated by the need to achieve switching speeds and drive currents that meet the requirements of applications. In these circumstances the contact effects are expected to heavily affect the performance of the devices. Contact resistance at a metal-organic interface is typically detected to fall in the range of 10 kΩ cm – 10 MΩ cm (Zaumseil, 2003) (Necliudov, 2003). In transistors the drain currents scales with the transistor width (the actual contact resistance r_C is inversely proportional to the channel width W, $r_C \propto W^{-1}$). Hence it is convenient to use the product of contact resistance and channel width, $R_C = r_C W$, as a measure of the contact resistance. In inorganic devices, e.g. in FETs, source and drain contacts are typically optimized by selective semiconductor doping, which leads to much lower values, hence it is expected that contact effects will be a dominant effect in short channel hybrid devices.

Although the contact resistance is independent of the channel length L, the actual channel resistance scales with L. Assuming a linear regime, for simplicity, when the channel resistance $R_{Ch} = L/W\mu en$ (where n is the density of charges per unit area and W the channel width) equals the contact resistance R_C, the contacts and the channel equally contribute to the total device resistance. A critical channel length $L_{Cr} = \mu enR_C$ can be

defined for which $WR_{Ch} = R_C$. In an FET, it is only for larger channel devices that genuine field effect behavior can be expected. On the other side, when the channel is shorter than the critical value, the drain bias will mainly drop over the contact regions. Following (Burgi, 2003), for polythiophenes ($\mu \approx 10^{-2}$ $cm^2V^{-1}s^{-1}$, $R_C \approx 50$ kΩ cm, $n \approx 2 \cdot 10^{12}$ cm^{-2}) $L_{Cr} \approx 2$ μm.

The main effect of the contact resistance is a non-linear increase of the output characteristics at low drain voltages. For improving the fit to this kind of experimental data and to simulate the non-linear *I:V* characteristics of pentacene FETs, (Necliudov, 2000) has modeled his devices with a circuit consisting of an FET having a pair of antiparallel Schottky diodes connected to the access resistors, as in Figure 1.29.

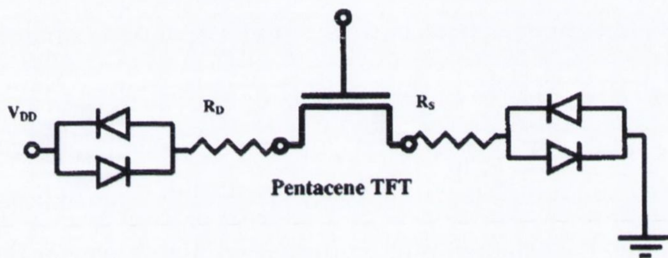

Figure 1.29 *Equivalent circuit of an FET including nonlinear source and drain contact resistances. From* (Necliudov, 2000).

Two diodes in parallel were employed so as to obtain symmetric current-voltage characteristics. The diodes are in series with the contact resistance of source and drain and the intrinsic channel resistance. Whereas the pair of diodes was enough to simulate the non-linearity, an accurate fit to the data over a large range of voltage was achieved by modeling the injection process with a shunt resistor R_L in parallel to the Schottky diodes, in (Necliudov, 2003) and (Gundlach, 2006), again for pentacene FETs (Figure 1.30).

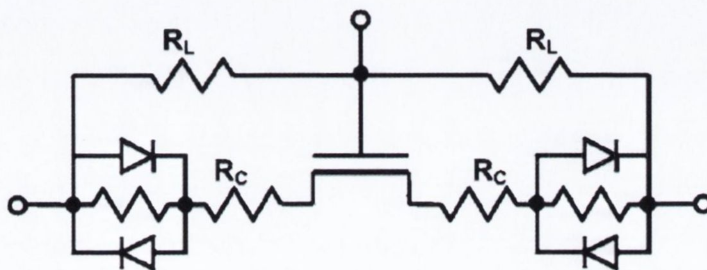

Figure 1.30 *Circuit model from* (Necliudov, 2003). R_L *are resistors responsible for gate leakage currents.*

At low drain biases each Schottky diode contributes to the current conduction only to a very little extent, hence the FET would consists of a pair of shunt resistors in series with the contacts and the channel. In this region of device bias the total device resistance is dominated by the high value shunt resistance and the current-voltage characteristics are linear and the conductance is severely limited. When the drain bias exceeds the diode turn-on voltage, the FET is a combination of the contact resistance and the intrinsic channel resistance.

Such representation is not purely empirical; high contact resistances often originate from the formation of a potential barrier at the organic-metal interface. The common way to describe it is that of a metal /semiconductor contact (as in a previous section, at page 11). In a simple view the barrier height is given by the difference between the metal work function Φ_m and the semiconductor HOMO or LUMO level. Good contacts are expected to occur when Φ_m is close to one of these levels. In the reverse situation, a potential barrier forms at the interface, leading to poor charge injection. Even though this simplification helps to comprehend the origin of the interface barrier, this approximation is often not valid, especially when the interface exhibits an additional dipole barrier that tends to lower the metal work function. As a consequence, even when the bulk levels of the material do match, the interface barrier height remains high, as for example in (Horowitz, 2004), for pentacene and gold. Here a large interface dipole was attributed to the change of the surface dipole of the metal following the adsorption of the organic molecules. As a metal surface is characterized by an electron density tailing from the free surface into vacuum, adsorbed molecules tend to push back these electrons, reducing the surface dipole and decreasing the work function of the metal. The observed characteristic that P3HT films with cupper and chromium electrodes exhibit different contact resistance despite Cu and Cr having analogous work functions was credited to contributions from interfacial dipole layers also in (Burgi, 2003).

As anticipated, the main effect of the contact resistance is the non-linear increase of the output characteristics at low drain voltages (below the diode turn-on voltage), highlighted by an arrow in Figure 1.31, which shows a measured *I:V* curve of a P3HT film on Au electrodes that we have patterned.

The effect of temperature, which is of key importance for charge injection, was studied in (Chwang, 2000), who concluded that diffusion-limited thermionic emission on top of a potential barrier at the semiconductor-metal contact was the dominant process for injection of carriers in organic transistors. Similarly, the contact resistance has been interpreted in

terms of thermionic emission in (Necliudov, 2000) (Street, 2002) (Li T. , 2002) (Necliudov, 2003). The formation of an interface Schottky barrier is indeed well documented by photoemission measurements (Campbell, 1996) (Naoki Nakanishi, 1999). The tuning of the Schottky energy barriers by attaching oriented dipoles layers on top of the metal contacts was also performed in (Campbell, 1996b), which undoubtedly proved the presence of these potential barriers.

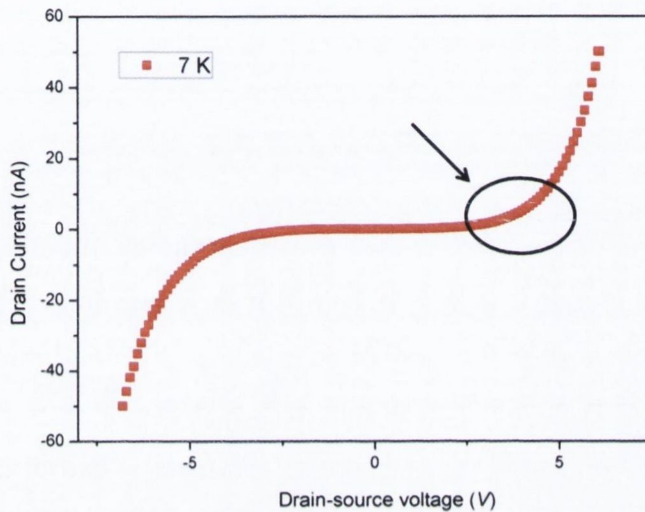

Figure 1.31 *Output characteristics of P3HT thin film transistor with Au electrodes at 7 K. The non-linear increase at low biases is highlighted by an arrow.*

However, the picture will be shown in the following to be more complicated than initially believed. Beyond the non-linearity featuring in the *I:V* curves, the contact resistance manifests itself in abrupt voltage drops in the source and drain contact regions. Taking benefit of this aspect, further analysis was performed by using a technique which give access to the channel and contact resistance separately. The method used an atomic force microscope tip to sense the potential along the channel of a transistor (Seshadri, 2001) (non-contact scanning-probe potentiometry). An analysis of the data on various organic FETs is given in (Burgi, 2003), who revealed the potential profile inside operating devices, with high spatial resolution. In summary, it was found that for electrode-polymer combinations that form bad contacts, with a relatively large Schottky barrier, charge injection across the barrier constitutes the main obstacle leading to high contact resistances and, as expected for Schottky contacts, the voltage drop at the source electrode is much higher than that at the drain (Figure 1.32).

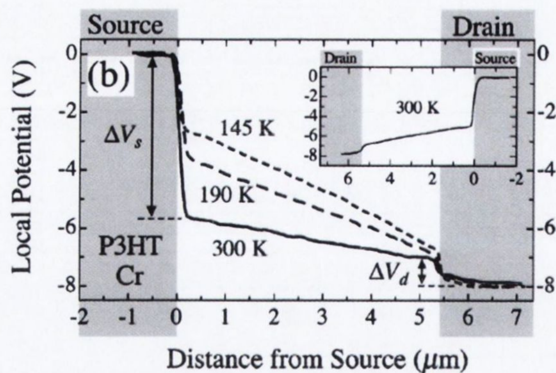

Figure 1.32 *Profiles of the electrostatic potential across the channel of operating transistors with Schottky barrier height > 0.3 eV, from* (Burgi, 2003).

Unexpectedly, from temperature measurements an activation energy of order 100 meV was extracted for the injection process, which is smaller than the activation energy due to the Schottky barrier height. Noteworthy, this feature rules out a diffusion-limited thermionic emission mechanism for describing contact resistances.

In the simple rigid-band picture (assumed for undoped polymers) a barrier is expected for charge injection but not for extraction, and hence no voltage drops at the drain contact area. However, for good contacts combination with a low Schottky barrier (low level mismatch) and small overall contact resistance, the voltage drop were found to be of comparable magnitude at both electrodes (Figure 1.33), showing the same temperature dependence as the mobility of the polymer bulk. Further the contact resistance was directly proportional to the inverse of the mobility of the polymer.

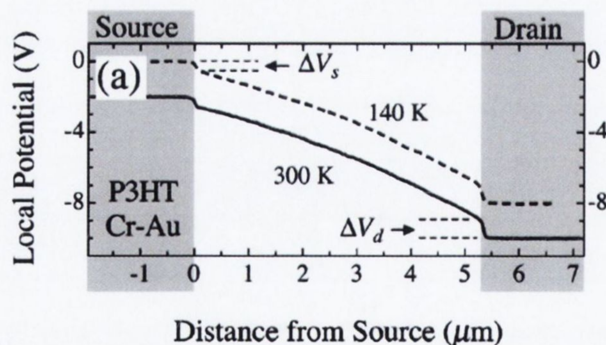

Figure 1.33 *Profiles of the electrostatic potential across the channel of operating transistors with Schottky barrier height < 0.3 eV, from* (Burgi, 2003).

Consequently, bulk transport in the polymer, likely through a narrow depleted region in front of the electrodes, dominates the contact resistance for low Schottky barrier, explaining the symmetry observed between the source and drain, as well as the proportionality of the contact resistance on the inverse mobility.

A possible explanation is that bulk transport occurs through a narrow depleted region in the vicinity of the contacts, where no accumulation layer forms. As the width of the depletion layer depends on the charge carrier density, the contact resistance will depend on the gate voltage in FETs (Figure 1.34).

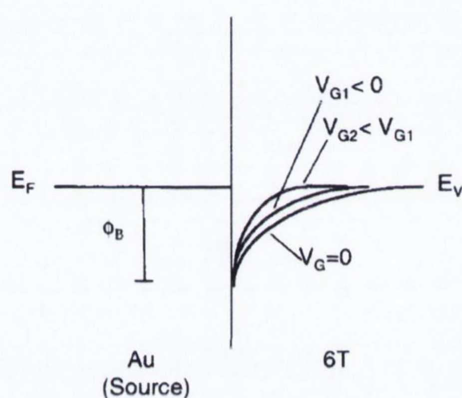

Figure 1.34 *Diagram of the energy levels illustrating the effect of V_G on the hole injecting Au/6T contact. As V_G becomes more negative, the depletion width decreases, due to a higher concentration of induced carriers. From* (Chwang, 2000).

The relatively large drop in the contact area is a consequence of a high density of polymer defects near the contacts. It was suggested by (Li T. , 2003) that the regions immediately adjacent to the contacts are not composed of organic material of the same quality as the rest of the conducting channel and were assumed to display negligible mobility or even contain trapped positive interface charges.

The approach of reducing the contact resistance effects by matching the work function of the electrodes with the ionization potential of the polymer, has to be combined with methods to enhance the bulk mobility in the proximity of the contact areas.

There is some evidence that it is the polymer nano-morphology at the edges of the contacts which greatly affects the charge injection (Singh, 2010). It was observed that the step between the contact and the oxide surface unsettled the self-assembly into semi-crystalline fibrils for polymer thin films transistors and hence affect the charge injection. In this work the effect of the planarization of the device was investigated (i.e. of including the

electrodes within the oxide substrate) on the polymer morphology (Figure 1.35). Accompanying the improvement in the nano-morphology at the edges and over a large area of the polymer thin film, the contact resistance was observed to partially decrease.

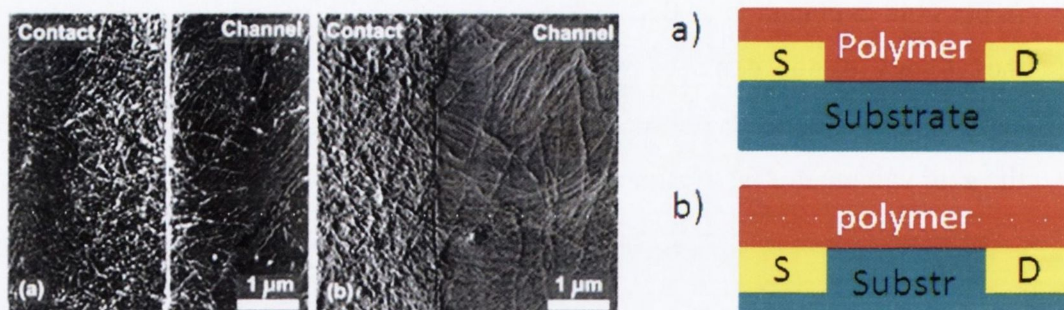

Figure 1.35 *AFM images showing the different nano-morphology of P3HT at the contact edges of a) normal and b) planar FET. The contact edges introduce a visible distortion compared to the continuous semi-crystalline fibrils of the planar FET. From* (Singh, 2010).

Remarkably, the effect of surface native oxides was investigated by (Burgi, 2003) and revealed to play only a minor role as the contact resistance is entirely dominated by the mobility of the polymer before the carriers reach the accumulation layer. Hence it can be neglected.

The first important conclusion is that contact resistance is not fully accounted by diffusion-limited thermionic emission, as was anticipated by considering the small activation energy observed for "bad" contacts. Doubts as to the validity of this model were already posed by (van Woudenbergh, 2001) and (Preezant, 2003), who suggested that alternative injection mechanisms play a dominant role. For instance it has been proposed that thermally assisted tunneling (Abkowitz, 2001) and thermally assisted injection (Arkhipov, 1998) occur from a continuum of states in the metal into localized states of an organic media, whose distribution is smeared at increasing temperature. The energy distribution of populated states in the organic media can be altered as σ^2/k_BT by the temperature (σ is the familiar Gaussian width of the distribution of localized states), and it results in a temperature-dependent activation energy for the potential barrier. Because the depletion layer is actually narrow, of order few nanometers, and the electric fields are quite large in a short channel device, tunneling may well play a dominant role. It is anticipated that in our work the non-linearity of the *I:V* curves is indeed dominantly due to injection by tunneling, with a minor contribution coming from thermoionic emission, which is reflected in the

pronounced temperature-dependence of our contact resistances. The importance of carrier tunneling in defining device characteristics was indeed well recognized also in OLEDs by (Parker, 1994).

All the survey presented so far is on the injection problem occurring at the metal-organic interface, referred to bottom contact geometry, in which the organic material is deposited by some technique on top of pre-patterned electrodes. This ensures having a well-defined interface, with no inter-diffusion. This geometry is actually optimal for studying the properties of the interface and the mechanism of injection. However, a complete different scenario arises when the metal contacts are deposited on top of the fragile organic layer, which is very interesting from the application point of view.

It has been observed, for example in (Necliudov, 2000), that while bottom contact transistors have a highly non-linear output drain current, top contact devices were free from this feature. This is actually a common feature of devices in which the contact is deposited on the organic film, which is manifest in reducing the contact resistance. The difference of bottom and top contacting has been studied by (Tessler, 2001) and, experimentally, by (Watkins, 2002). In the latter work, evidence was found of metal penetration coupled with the formation of clusters and a consequent substantial barrier reduction.

From semiconductor science, it is well known that impurities and defects increase the carrier density inside the surface-depleted region and decrease the barrier width, by increasing the contribution of tunneling to the overall injected current. An increased defect concentration near the semiconductor surface enables charge movement through the semiconductor depletion region (when the defect densities is such that the gap state wave functions begin to overlap); and for high enough defect concentration (e.g. for surface that are mechanically damaged) the otherwise Schottky barriers become ohmic (Brillson, 1983) (Brillson, 2011). Diffusion of metal (or other impurity) into semiconductors is one of the main mechanisms which allows to linearize a contact.

However, it must be noted that for device application the top contact architecture presents a major drawback, when dealing with organics: the patterning of the device through conventional lithography is difficult to achieve. Top contacts are usually deposited through shadow masks, which badly affect the resolution. As to its employment in spin electronic devices, even though a top contact may linearize the *I:V*, as is desirable, the inter-diffused metal clusters might act as scattering sites. In this work we focused on bottom contact

architectures in order to probe the properties of the organic media only in well-defined structures. From our results, further steps may of course be taken.

Attempts in modeling the possibility of having spin injection at an organic interface have been made by (Ruden, 2004) (Ren, 2005) (Ji-yong Fu, 2006) (Atodiresei, 2010). Carriers can be transported by polarons, which carry spin, and spinless bi-polarons (resulting from the coupling of two polaron states). Spin-polarized current results when a significant fraction of all carriers is transported via spin polarons. Analogously to inorganic semiconductor contacts, a spin-selective interfacial resistance (i.e. a tunnel barrier), was suggested to be beneficial for achieving efficient spin polarized current injection. More details will be included later, in Chapter 4.

This Work

In this thesis we are interested in studying the possibility of injecting a spin polarized current from a ferromagnetic metal into an organic semi-conductor. Experiments on spin injection from a ferromagnetic contact are typically performed using a device with simple injector–detector geometry, either in a lateral or a perpendicular configuration, where two ferromagnetic electrodes are separated by a non-ferromagnetic medium. One ferromagnetic metal contact is used to inject spin polarized carriers into the semiconductor material and, if the spacing between both contacts is shorter than the spin flip length, the interface of the second ferromagnet acts as a spin detector, exhibiting either low or high resistance for magnetization parallel or antiparallel to the first magnet. For our study, we opted to employ lateral structures with a layer of conjugated polymer cast in a narrow gap between two ferromagnetic electrodes having different coercive field. Attention has also been devoted at studying thin films of evaporated Alq_3, in view of the open debate about spin injection in vertical spin-valves, outlined in the literature survey at page 24, and on single crystals of pentacene. Lateral transport structures avoid the possible side effect of ill-defined interfaces and provide the ideal platform for studying spin injection in novel materials.

Because we are mainly concerned about testing the transport properties of intrinsic materials; attention was devoted to depositing undoped and ultra-pure organic media. Because the conductivity is low in intrinsic organic semiconductors, we have included in

our devices a gate terminal acting underneath the organic channel, as in field effect transistors. The gate insulator acted as a capacitor when the gate electrode applied an electric field, hence modifying the density of charge carriers at the interface. Besides studies of magnetic and electrical properties, we performed gate dependent measurements. The contact resistance is a dominant limitation in short-channel devices, and it is typically accessed via modeling an equivalent transistor circuit. In Figure 1.36 we show the circuits which best fit our measurements, an example of which is shown in Figure 1.31.

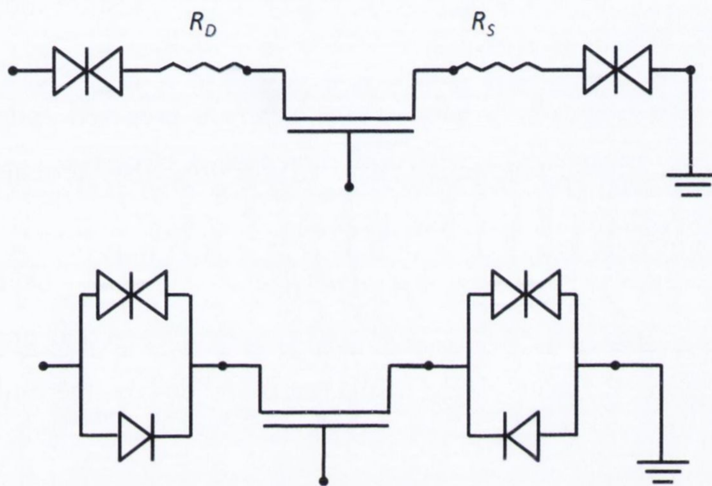

Figure 1.36 *Equivalent circuits of FETs. The top circuit includes a tunnel diode in series with the left and right contact resistances and the channel. To explicitly account for the temperature dependence a diode in parallel with the tunneling contact is added in the bottom circuit.*

The top circuit includes two tunneling contacts in series with the contact and the channel resistances. Considering the weak temperature dependence of the tunneling contacts (page 11) this circuit does not predict any variation of the *I:V* curve with temperature, and the dependence of the channel and contact resistance must be extracted via fitting at various temperature. The elements are expected to be gate dependent, as it will be shown in the fittings. The bottom circuit, which includes two diodes in parallel with the tunneling contacts, provides a better physical description of the injection. In this case, the temperature dependence is explicitly accounted by the exponential dependence of the diodes. As the two elements are in parallel, the current flows through the tunnel contact only above the diodes' turn on voltage. This system greatly complicates the fitting equation (which becomes a system of 6 nonlinear equations with 6 variables), and the extraction of meaningful parameters from our set of *I:V* curves is not possible. Therefore we typically attributed the temperature dependence to the contact resistors. This does not

affect the extraction of the channel resistance, in which we are principally interested for probing the organic contribution, and it leads to the same values which would be given by the bottom circuit.

What follows this introductive chapter is now summarized:

Chapter 2 gives a description of the experimental recipes that we have optimized and adopted during this thesis.

Chapter 3 provides further details about the structure and the transport properties of organic single crystals, together with the characterization we made for pentacene crystals, obtained by physical vapor deposition, and shows the result of the transport measurement herein performed. The data are analyzed based on the contact models mentioned above. Considering the current debate about spin injection in Alq_3, we prepared and measured OFETs with this material too. The techniques that can be adopted to fabricate a single crystal C_{60} hybrid device are shown in the chapter appendix.

Chapter 4 focuses on conductive polymers, and gives details about the chemical and physical structure of polythiophene derivatives, of our measurements and data analysis.

In the conclusion we summarize the main results of the thesis and discuss the future work.

Bibliography

Abeles, B. et al. (1975). *Physical Review Letters, 35*, 247.

Abkowitz, M. A. et al. (2001). *Applied Physics Letters, 66*(10), 1288.

Afzali, A. et al. (2002). *J. Am.Chem. Soc., 124*, 8812.

Aharony, A. et al. (1992). *Physical Review Letters, 68*(26), 3900.

Akerman, J. J. et al. (2002). *Journ. Magn. Magn. Mat., 240*, 86.

Albrecht, J. D. et al. (2003). *arXiv:cond-mat, 1*, 030245.

Aleshin, A. N. et al. (2004). *Applied Physics Letters, 84*(26), 5383.

Anderson, P. W. et al. (1958). *Physical Review, 109*, 1492.

Appelbaum, I. et al. (2007). *Nature, 447*(17), 295.

Arkhipov, V. I. et al. (1998). *Journal of Applied Physics, 82*(2), 848.

Assadi, A. et al. (1988). *Applied Physics Letters, 53*, 195.

Atodiresei, N. et al. (2010). *Physical Review Letters, 105*, 066601.

Baibich, M. N. et al. (1988). *Physics Review Letters, 61*, 2472.

Bao, Z. et al. (1996). *Applied Physics Letters, 69*(26), 4108.

Barraud, C. et al. (2010). *Nature Physics, 6*, 615.

Bassler, H. et al. (1981). *Phys. Status Solidi B, 107*, 9.

Bassler, H. et al. (1982). *Physical Review B, 26*(6), 3105.

Bassler, H. et al. (1993). *Phys. Stat. Solidi B, 175*, 15.

Binash, G. et al. (1989). *Physical Review B, 39*, 4828.

Borsenberg, P. M. et al. (1996). *Jpn. J. Appl. Phys., 35*, 2698.

Bozano, L. et al. (1999). *Applied Physics Letters, 74*(8), 1132.

Bratkovsky, A. M. et al. (2003). *arXiv:cond-mat, 2*, 0307656.

Brillson, L. J. et al. (1983). *Surface Science, 132*(1), 212.

Brillson, L. J. et al. (2011). *Journal of Applied Physics, 109*, 121301.

Brown, A. R. et al. (1997). *Synthetic Metals, 88*, 37.

Burgi, L. et al. (2003). *Journal of Applied Physics, 94*(9), 6129.

Burke, F. et al. (2010). *PhD Thesis Dissertation, Trinity College, Dublin.*

Burke, F. et al. (2011). *Synthetic Metals, 1*, 13332.

Burroughes, J. H. et al. (1990). *Nature, 347*, 539.

Butko, V. et al. (2003). *Applied Physics Letters, 83*, 4773.

Byoungnam Park. et al. (2008). *Applied Physics Letters, 92*(13), 133302.

Campbell, I. H. et al. (1996). *Physical Review Letters, 76*(11), 1900.

Campbell, I. H. et al. (1996b). *Physical Review B, 54*(20), 14321.

Chabinyc, M. L. et al. (2004). *Journal of Applied Physics, 96*(4), 2063.

Chaidogiannos, G. et al. (2009). *Applied Physics A: Materials Science and Processing, 96*, 763.

Chen, T. A. et al. (1995). *J. Amer. Chem. Soc., 117*, 233.

Chen, T. A. et al. (1995). *J. Am. Chem. SOc., 117*, 233.

Cheng, Y. C. et al. (2003). *Journal of Chemical Physics, 118*(8), 3764.

Chiang, C. K. et al. (1978). *Journal of the American Chemical Society, 100*, 1013.

Choudhury, B. et al. (2005). PhD Dissertation. *Iowa State University*, 8.

Chun, S. H. et al. (2002). *Physical Review B, 66*, 100408.

Chwang, A. B. et al. (2000). *J. Phys. Chem. B, 104*, 12202.

Cinchetti, M. et al. (2009). *Nature Materials, 8*, 115.

Cohen, M. H. (1969). *Physical Review Letters, 22*(20), 1065.

Colle, M. et al. (2003). *Advanced Functional Materials, 13*(2), 108.

Coropceanu, V. et al. (2009). *J. Phys. Chem. C, 113*, 4679.

Datta, S. et al. (1990). *Applied Physics Letters, 56*, 665.

Davis, E. A. (1970). *Journal of Non-Crystalline Solids, 2*, 406.

de Boer, R. W. et al. (2003). *Applied Physics Letters, 83*(21), 4345.

Dediu, V. et al. (2002). *Solid State Communications, 122*, 181.

Dediu, V. et al. (2008). *Physical Review B, 78*, 115203.

Delmo, M. P. et al. (2009). *Nature Letters, 457*, 1112.

Dhandapani, D. et al. (2009). *Journal of Applied Physics, 105*, 07C702.

Dimitrakopoulos, C. D. et al. (1999). *Science, 283*(5403), 822.

Dimitrakopoulos, C. D. et al. (2001). *IBM J. Res. Dev., 45*, 11.

Dodabalapur, A. et al. (1998). *Applied Physics Letters, 73*(2), 142.

Dongmeng Chen. et al. (2011). *J. Phys. Chem. B, 115*, 5312.

Ebisawa, F. et al. (1983). *Journal of Applied Physics, 54*, 3255.

Efros, A. L. et al. (1975). *J. Phys. C: Solid State Phys., 8*, L49.

Endres, R. et al. (2004). *Computational Materials Science, 29*, 362.

Entin-Wohlman, O. et al. (1983). *J. Phys. C: Solid State Phys., 16*, 1161.

Esaki, L. P. et al. (1967). *Physical Review Letters, 19*, 852.

Fabian, J. et al. (2004). *Applied Physics Letters, 84*, 85.

Fagen, E. A. et al. (1970). *Journal of Non-Crystalline Solids, 2*, 180.

Fiederling, R. et al. (1999). *Nature, 402*, 787.

Fratini, S. et al. (2009). *Physical Review Letters, 103*, 266601.

Frenkel, J. (1938). *Phys. Rev., 54*, 647.

Friend, R. H. et al. (1999). *Nature, 397*, 121.

Garnier, F. et al. (1994). *Science, 265*, 1684.

Garstein, N. et al. (1994). *Chem. Phys. Lett., 217*, 41.

Garstein, N. et al. (1995). *Chem. Phys. Lett., 245*, 351.

Gershenson, M. E. (2006). *Reviews of Modern Physics, 78*, 973.

Gill, W. D. (1972). *Journal of Applied Physics, 43*, 5033.

Gittleman, J. et al. (1972). *Physical Review B, 5*, 3609.

Goedel, W. A. et al. (1992). *Makromol. Chem., 193*, 1195.

Gregg, J. et al. (1997). *J. Magn. Magn. Mater., 175*, 1.

Gundlach, D. J. et al. (2006). *Journal of Applied Physics, 100*, 024509.

Haddon, R. C. et al. (1995). *Applied Physics Letters, 67*, 121.

Haichuan Mu. et al. (2008). *J. Phys. D: Appl. Phys., 41*, 235109.

Haiqiao Wang. et al. (2001). *Journal of Applied Polymer Science, 83*(10), 2195.

Hammar, P. R. et al. (1999). *Physical Review Letters, 83*(1), 203.

Hanbicki, A. T. et al. (2003). *Applied Physics Letters, 82*(23), 4092.

Hannewald, K. et al. (2004). *Applied Physics Letters, 85*(9), 1535.

Helfrich, W. et al. (1965). *Physical Review Letters, 38*, 229.

Hesse, R. et al. (1980). *Chemical Physics, 49*(2), 201.

Hiro Akinaga et al. (2002). *IEEE Transactions on Nanotechnology, 1*, 19.

Holstein, T. (1959). *Ann. Phys., 8*, 343.

Horowitz, G. et al. (1995). *J. Phys. III France, 5*, 355.

Horowitz, G. et al. (2004). *J. Mater. Res., 19*(7), 1946.

Hsu, C. H. et al. (2007). *Applied Physics Letters, 91*, 193505.

Huang, C. Y. et al. (1983). *Physical Review B, 27*(12), 7460.

Hulea, I. N. et al. (2006). *Nature Materials, 5*, 982.

Hyun Cheol Koo. et al. (2007). *Applied Physics Letters, 90*, 022101.

Hyun Cheol Koo. et al. (2009). *Science, 325*, 1515.

Jang, J. S. et al. (2008). *Physical Review B, 77*, 035303.

Ji-yong Fu. et al. (2006). *Physical Review B, 73*, 195401.

Jonker, B. T. et al. (2007). *Nature Physics, 3*, 542.

Jullière, M. et al. (1975). *Phys. Lett. A, 54*, 225.

Jung-Woo Yoo. et al. (2010). *Nature Materials, 9*, 638.

Jurchescu, O. D. et al. (2004). *Applied Physics Letters, 84*, 3061.

Kafer, D. et al. (2005). *Phys. Chem. Chem. Phys., 7*, 2850.

Kapoor, A. K. et al. (2002). *Journal of Applied Physics, 92*, 3835.

Karl, N. et al. (1991). *Synthetic Metals, 41*, 2473.

Karl, N. et al. (1999). *J. Vac. Sci. Technol. A, 17*, 2318.

Katine, J. A. et al. (2000). *Physical Review Letters, 84*, 3149.

Kenkre, V. M. et al. (1989). *Physical Review Letters, 62*(10), 1165.

Klauk, H. et al. (2003). *Solid-State Electron., 47*, 297.

Krinichnyi, V. I. (2000). *Synthetic Metals, 108*, 173.

Kumar, J. et al. (2006). *Solid State Commun., 138*, 422.

Kyoung-Il Lee. et al. (2009). *Physical Review B, 79*, 195201.

Laudise, R. A. et al. (1998). *Journal of Crystal Growth, 187*, 449.

Le Comber, G. et al. (1970). *Physical Review Letters, 25*, 509.

Lee, J. Y. et al. (2006). *Applied Physics Letters, 88*, 252106.

Lee, W. Y. et al. (1999). *Journal of Apllied Physics, 85*(9), 6682.

Lei Fang. et al. (2011). *Physical Review Letters, 106*, 156602.

Li, C. H. et al. (2011). *Nature Communications, 2*, 245.

Li, T. et al. (2002). *Journal of Applied Physics, 91*(7), 4312.

Li, T. et al. (2003). *Journal of Applied Physics, 93*(7), 4017.

Liu, Y. et al. (2009). *Physical Review B, 79*, 075312.

Lou, X. et al. (2007). *Nature Physics, 3*, 197.

Macedo, A. G. et al. (2011). *Applied Physics Letters, 98*(25), 253501.

Majumdar, S. et al. (2009). *New Journal of Physics, 11*, 013022.

Majumdar, S. et al. (2006). *Applied Plysics Letters, 89*, 122114.

Malliaras, G. G. et al. (1998). *Physical Review B, 58*(20), R13411.

Masatoshi Kitamura et al. (2008). *J. Phys.: Condens. Matter, 20*, 184011.

Masatoshi Sakai et al. (2007). *Physical Review B, 76*, 045111.

Mas-Torrent, M. et al. (2004). *Nanotechnology, 15*, S265.

Mas-Torrent, M. et al. (2004). *Journal of the American Chemical Society, 126*, 984.

Mattana, R. et al. (2003). *Physical Review Letters, 90*, 166601.

McCulloch, I. (2006). *Nature Materials, 5*, 328.

McCullough, R. D. et al. (1992). *J. Chem. Soc., Chem. Commun.*, 70-72.

McCullough, R. D. et al. (1993). *J. Am. Chem. Soc., 115*, 4910.

McGuire, T. R. et al. (1975). *IEEE Transactions on Magnetics, MAG-11*(4), 1018.

Miller, A. et al. (1960). *Physical Review, 120*(3), 745.

Monsma, D. J. et al. (1995). *Physical Review Letters, 74*, 5260.

Moodera, J. S. et al. (1988). *Physical Review B, 42*, 8235.

Moodera, J. S. et al. (1995). *Physical Review Letters, 74*, 3273.

Morley, A. et al. (2008). *Journal of Applied Physics, 103*, 07F306.

Motsnyi, V. F. et al. (2002). *Applied Physics Letters, 81*(2), 265.

Mott, N. F. (1936). *Proc. R. Soc. Lond. A, 153*, 699.

Mott, N. F. (1961). *Advances in Physics, 10*, 107.

Mott, N. F. (1967). *Advances in Physics, 16*, 49.

Mott, N. F. (1968). *Journal of Non-Crystalline Solids, 1*, 1.

Mott, N. F. (1973). *Electronics & Power, 9 August*, 321.

Munn, R. W. et al. (1985). *J. Chem. Phys., 83*(4), 1843.

Naber, W. (2007). *Journal of Physics D: Applied Physics, 40*, R205.

Naber, W. et al. (2010). *Organic Electronics, 11*, 743.

Naoki Nakanishi et al. (1999). *Applied Physics Letters, 75*(2), 226.

Necliudov, P. V. et al. (2000). *Journal of Applied Physics, 88*(11), 6594.

Necliudov, P. V. et al. (2003). *Solid-State Electronics, 47*, 259.

Nguyen, T.-Q. et al. (2000). *J. Phys. Chem., 104*, 237.

Novikov, S. V. et al. (1994). *J. Phys.: Condens. Matter, 6*, 10519.

Nuyken, O. et al. (2006). *Monatshefte für Chemie (Chemical Monthly), 137*, 811.

Oestreich, M. et al. (1999). *Applied Physics Letters, 74*(9), 1251.

Ohno, Y. et al. (1999). *Nature, 402*, 790.

Ozbay, A. et al. (2009). *Applied Physics Letters, 95*, 232507.

Parker, I. D. (1994). *Journal of Applied Physics, 3*, 75.

Parkin, S. et al. (1991). *Applied Physics Letters, 58*, 2710.

Picon, J. D. et al. (2007). *Physical Review B, 75*, 235106.

Podzorov, V. et al. (2003). *Applied Physics Letters, 83*, 3504.

Podzorov, V. et al. (2004). *Physical Review Letters, 93*, 086602.

Pope, M. et al. (1963). *J. Chem. Phys., 38*, 2042.

Pramanik, S. et al. (2006). *Physical Review B, 74*, 235329.

Pramanik, S. et al. (2007). *Nature Nanotechnology, 2*, 216.

Preezant, Y. et al. (2003). *Journal of Applied Physics, 93*(4), 2059.

Rakhmanova, S. V. et al. (2000). *Applied Physics Letters, 76*(25), 3822.

Rashba, E. I. (2000). *Physical Review B, 62*(24), R16267.

Reese, C. et al. (2007). *Mater. Today, 10*, 20.

Ren, J. F. et al. (2005). *Journal of Physics: Condensed Matter, 17*, 2341.

Rhoderick, E. H. et al. (1988). Metal-Semiconductor Contacts. *Oxford: Clarendon.*

Roberts, M. E. et al. (2009). *J. Mater. Chem., 19*, 3351.

Ruden, P. P. et al. (2004). *Journal of Applied Physics, 95*, 4898.

Salleo, A. et al. (2004). *Physical Review B, 70*, 115311.

Santos, T. et al. (2007). *Physical Review Letters, 98*, 16601.

Schein, L. B. et al. (1978). *Physical Review Letters, 40*(3), 197.

Schein, L. B. et al. (1989). *Journal of Applied Physics, 66*(2), 686.

Schein, L. B. et al. (1992). *Phil. Mag. B, 65*, 795.

Schmidt, G. et al. (2000). *Physical Review B, 62*(8), R4790.

Schmidt, G. et al. (2011). *Spinos Abstracts.*

Schoonveld, W. A. et al. (2000). *Nature, 404*(27), 977.

Seo, S. et al. (2006). *Applied Physics Letters, 88*, 232114.

Seshadri, K. et al. (2001). *Applied Physics Letters, 78*, 993.

Shen, M. et al. (2004). *Journal of Applied Physics, 96*, 4319.

Shim, J. H. et al. (2008). *Physical Review Letters, 100*, 226603.

Shimada, T. et al. (2008). *Japanese Journal of Applied Physics, 47*(2), 1184.

Shuhong Liu et al. (2010). *Advanced Materials, 22*, 3857.

Shur, M. (1984). *Journal of Applied Physics, 55*(10), 3831.

Silbey, R. et al. (1980). *J. Chem. Phys., 72*, 2763.

Simmons, J. G. et al. (1963). *Journal of Applied Physics, 34*, 1793.

Singh, K. A. et al. (2010). *Advanced Functional Materials, 20*, 2216.

Sirringhaus, H. et al. (1998). *Science, 280*, 1741.

Sirringhaus, H. et al. (1999). *Nature, 401*, 685.

Sirringhaus, H. et al. (1999). *Adv. Solid State Phys., 39*, 101.

Sirringhaus, H. et al. (2000). *Science, 290*(5499), 2123.

Slonczewski, J. C. (1996). *J. Magn. Magn. Mater., 159*, L1.

Sokolov, A. N. et al. (2011). *Nature Communications, 2*, 437.

Stallinga, P. (2011). *Advanced Materials, 23*, 3356.

Stamenov, P. (2007). *PhD Thesis Dissertation, Trinity College, Dublin.*

Street, R. A. et al. (2002). *Applied Physics Letters, 81*(15), 2887.

Sundar, V. et al. (2004). *Science, 303*, 1644.

Szulczewski, G. et al. (2009). *Applied Physics Letters, 95*(20), 202506.

Taishi Takenobu et al. (2008). *Applied Physics Letters, 93*, 073301.

Takeshi Hirose et al. (2010). *Applied Physics Letters, 97*, 83301.

Takeshi Yamao et al. (2007). *Chem. Mater., 19*, 3748.

Takeya, J. et al. (2003). *Journal of Applied Physics, 94*(9), 5800.

Tang, C. W. et al. (1987). *Applied Physics Letters, 51*, 913.

Tarver, J. et al. (2009). *Chem. Mater., 21*, 280.

Tedrow, P. (1973). *Physical Review B, 7*, 318.

Tessler, N. et al. (2001). *Applied Physics Letters, 79*(18), 2987.

Tessler, N. (2009). *Advanced Materials, 21*, 2741.

Thomson, W. (1856). *Proc. R. Soc. Lond., 8*, 546.

Tombros, N. et al. (2007). *Nature Letters, 448*(2), 571.

Tomo Sakanoue et al. (2010). *Nature Materials Letters, 9*, 736.

Torsi, L. et al. (2005). *Analytical Chemistry*, 381A.

Troisi, A. et al. (2005). *Chem. Mat., 17*, 5024.

Troisi, A. et al. (2006). *Physical Review Letters, 96*, 086601.

Tsumura, A. et al. (1986). *Applied Physics Letters, 49*, 1210.

Tsymbal, E. Y. et al. (1998). *Physical Review B, 58*, 432.

van Woudenbergh, T. et al. (2001). *Applied physics Lettersq, 79*(11), 1697.

Venkatesan, M. et al. (2011). *Journal of Applied Physics, 109*, 07C507.

Vinzelberg, H. et al. (2008). *Journal of Applied Physics, 103*, 93720.

Virkar, A. et al. (2010). *Advanced Materials, 22*, 3857.

Vissenberg, M. et al. (1998). *Physical Review B, 57*(20), 12964.

Wang, F. J. et al. (2005). *Synthetic Metals, 155*, 172.

Wang, F. J. et al. (2007). *Physical Review B, 75*, 245324.

Waragai, K. et al. (1995). *Physical Review B, 52*(3), 1786.

Watkins, N. J. et al. (2002). *Applied Physics Letters, 80*(23), 4384.

Wei, H. et al. (2009). *Applied Physics Letters, 94*, 222109.

Wu, D. et al. (2005). *Physical Review Letters, 95*, 016802.

Wunderlich, J. et al. (2009). *Nature Physics, 5*, 675.

Xie, S. J. et al. (2003). *Physical Review B, 67*, 125202.

Xiong, Z. H. et al. (2004). *Nature, 427*, 821.

Xu, W. et al. (2007). *Applied Physics Letters, 90*, 072506.

Yang, C. Y. et al. (1998). *Polymer, 39*, 2299.

Yang, F. Y. et al. (1999). *Science, 284*(5418), 1335.

Yu, Z. G. et al. (2002a). *Physical Review B, 66*, 201202(R).

Yu, Z. G. et al. (2002b). *Physical Review B, 66*, 235302.

Yue Wu et al. (2007). *Physical Review B, 75*, 075416.

Yuta Kitamura et al. (2011). *Applied Physics Letters, 99*, 043505.

Zaumseil, J. et al. (2003). *Journal of Applied Physics, 93*(10), 6117.

Zhang, Y. et al. (1990). *Physical Review Letters, 64*, 2687.

Zhao, N. et al. (2004). *Macromolecules, 37*, 8307.

Chapter 2

Experimental methods

Overview

In this chapter a description is given of the methods that have been adopted and optimized throughout the work of this thesis, for the nanofabrication, deposition and characterization of hybrid organic devices.

Attention will be devoted to supplying enough information for the reader to be able to reproduce our experiments. The chapter is divided into four sections; at first the process of fabricating electrodes platform in the nanometers range is discussed. In the second section the growth of organic single crystals is described, followed by an overview of the method to place and secure them on pre-patterned substrates and the initial electrical characterization. In section three the procedures to fabricate thin film organic FETs are given, with attention to the wet processing of polythiophene and vacuum sublimation of Alq_3. In the last part, the instrumentation for performing high impedance transport measurements is described.

Nanofabrication

Lithography: elementary concepts

The terms micro and nanolithography typically refers to the patterning methods capable of structuring material on a fine scale. The very basic steps of a usual process are summarized in the following and in Figure 2.1.

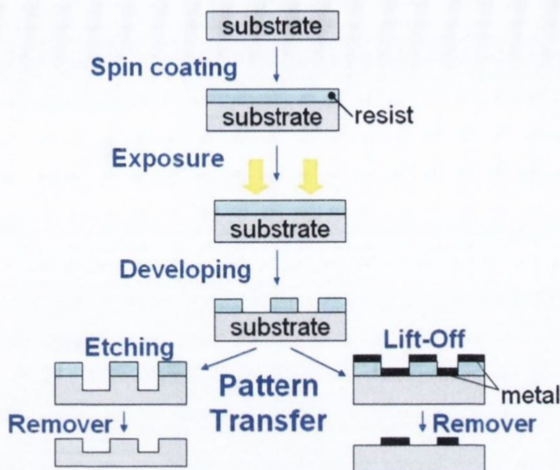

Figure 2.1 *Schematic of the sequential steps included in a typical lithography process. From* (Ramos, 2009).

Sample preparation: the surface of a sample must be clean and free from contamination; typically the specimen is solvent cleaned to remove any organic trace and/or it may be exposed to oxygen plasma.

Spin coating: the substrate is then coated with liquid resist material. Depending on the resist different spin coating conditions may be required, in terms of the initial spin rate and final rotational speed. Important parameters are the achieved resist thickness (dependent on viscosity and spin rate), film uniformity and particulate contamination (hence resist defects). These steps are typically performed in clean room conditions.

Exposure: this part involves the exposure of the resist to either UV radiation or an electron beam, to obtain the desired design. Positive resist, becomes soluble in basic developers when exposed; while negative resist becomes insoluble.

Developing: to create the pattern in the resists over the sample surface the soluble areas of the resist are dissolved by liquid developer, a special chemical solution designed for a specific resist. What is left on the substrate after the development is, effectively, a resist mask adherent to the surface.

Etching: a liquid (wet-) or plasma (dry-) agent removes the upper layer of the substrate in the areas that are not protected by the resist, transferring the exposed pattern into the sample.

Lift-Off: the target material is deposited over the whole area of the wafer, but it reaches the surface of the substrate only in the exposed regions while it stays on the top of the resist in the regions that were not developed. When the resist is washed away, the material on the

top is lifted-off and washed together with it. After the lift-off, the target material remains only in the regions where it had a direct contact with the substrate.

Resist removal: After the etching or lift-off, the residual photoresist can be removed from the substrate, usually using a liquid resist stripper, designed to alter the resist so that it no longer adheres to the substrate.

UV exposure

In order to electrically characterize a device, connections between the smallest features and large area contacts, accessible for wire bonding, must be designed and patterned. The UV lithography technique can be used in order to fabricate the micro-scale platform for contacting the nano-structures. The concept of UV lithography resembles the general process outlined in the previous section; UV light is shone through a mask onto a photoresist covered wafer. The mask stops some of the light from exposing the resist covered surface. A mask aligner is typically used to hold the substrate and the mask in contact (referred to as soft or hard contact depending on whether the wafer is pressed against the mask only by a movable chuck or via vacuum pulling). The light source is usually a multi-wavelength mercury arc lamp, calibrated for the required wavelength (405 nm). This technique has, in our laboratories, a feature limit-size of about 2-3 μm. Normally we used S1813 positive photoresist, which was spun onto the substrate at 3000 rpm, baked at 115° C for 90 seconds and exposed to a 350 Watt lamp for 3.5 seconds. Development in commercial MF319 took about 40 seconds, and was followed by rinsing in de-ionized water.

Electron beam lithography

In electron beam lithography (EBL) a pattern is defined by rastering the beam over the desired areas of a substrate covered by electron sensitive resist. EBL was carried out, in our case, with scanning electron microscopes (Zeiss Supra 40, Zeiss Ultra Plus and Zeiss Auriga) equipped with a Raith50 electron lithography tool (which provides control over the beam blanker and the scan coils, to perform selective exposure-lithography beyond imaging). The beam is generated in a thermal field emission tip, accelerated with a high

voltage (from 0.2 to 30 kV), with a probe current ranging from 4 pA to 10 nA, and collimated by electro-magnetic optics. The beam blanker can turn on and off the beam during the exposure. The apertures are included to set the beam current and to minimize lens aberration. The microscopes have an image resolution of 1.3 nm at 15 kV, via backscattered and secondary electron detectors. Figure 2.2 shows the schematics of the column.

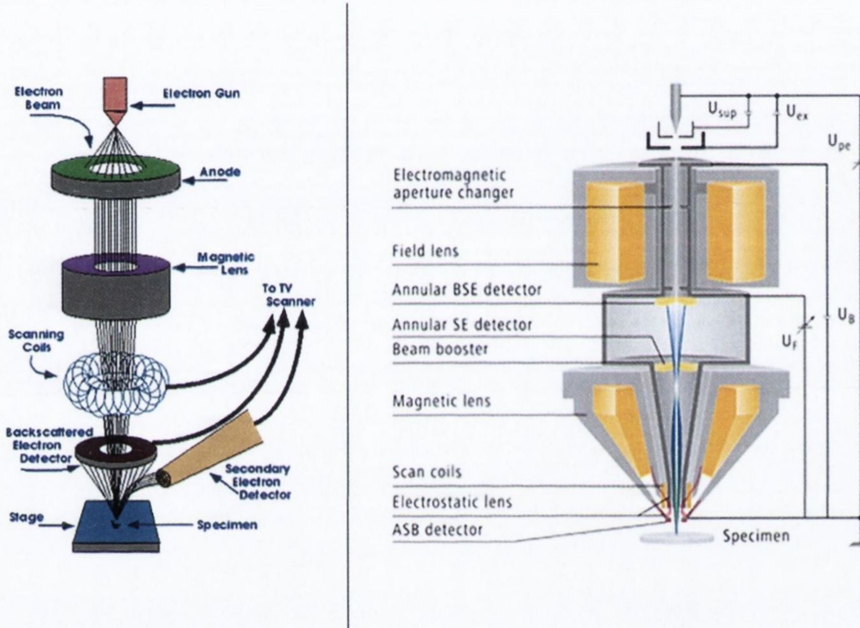

Figure 2.2 *Left: SEM column structure from* pemtron.com. *Right: representation of the various elements in a column of a Zeiss Supra 40; electrons are field-emitted and consequently collimated through electromagnetic lenses, from* Zeiss.com.

Figure 2.3 shows a simulation of the electrons' beam trajectories within the resist and the substrate. While penetrating through the resist, the electrons first experience small scattering events (forward scattering), which broadens the beam diameter. Reaching the underlying substrate, the electrons undergo large angle scattering event (backscattering), which typically gives rise to the proximity effect. This means that the exposure of the resist at some feature of the pattern is dependent on nearby features because backscattered electrons spread to the surrounding areas. The main consequence is that the shape of the final pattern may substantially differ from the shape which is directly scanned by the beam.

Areas are exposed by rastering the beam spot with a certain step size across the designed shape. The energy dose deposited in each point is given by the product of the beam current and the dwell time (time spent exposing each spot), and is usually expressed in $\mu C/cm^2$. To correct for the proximity effect, each feature in the pattern is normally assigned with an independent dose, which takes into account the amount of backscattered electrons received by the surrounding features. For example, small and isolated features need to be exposed with a larger dose than dense features. The appropriate doses to assign to the elements of a design is determined by combining numerical simulation of the electron trajectories in the substrate (we normally used the CASINO software, developed at the university of Sherbrooke, in Québec, Canada, and available as a free download at usherbrooke.ca), and dose tests on matrix copies of the pattern with stepwise increased doses.

The effect of beam broadening due to forward scattering of electrons is usually alleviated by using high accelerating voltage. However, at high voltages the backscattering contribution increases (Figure 2.3), hence an optimal value must exist which gives overall minimum beam size within the resist. In this work we have exposed at relatively low acceleration voltage (details will be given in the next section), because we were mainly concerned of minimizing the proximity effect of dense features.

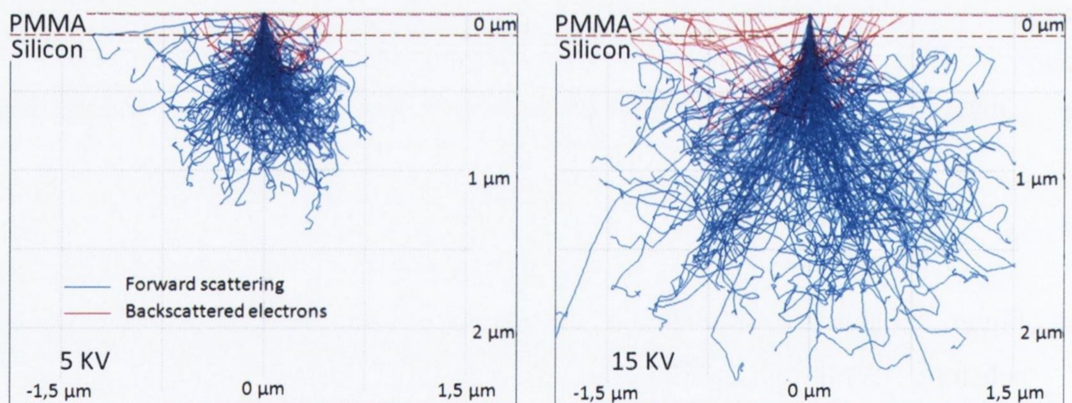

Figure 2.3 *Scattering of electrons in a resist/ siliconn substarte obtained by Monte CArlo SImulatioN of electrOn trajectory in solid (CASINO), at accelaration voltages of 5 KV and 15 KV.*

The write field is the area that can be covered by the electron beam with good precision at a given magnification. It also determines the resolution: each side *W* of the write field is digitalized into 2^{16} points (in a 16 bits analog-to-digital converter), giving a matrix of 2^{16} x 2^{16} points which are sequentially scanned by the beam. The spatial resolution is given by

$W/2^{16}$. For example, in a write field of 100 μm x 100 μm, the spacing between each exposable point is 1.52 nm. It is typically useless to reduce the resolution below half of the effective beam spot size which is achievable on a given sample substrate. The latter depends on the quality of the electron columns, the charging effect of the substrate and the ability of the operator. In modern tools it can be brought down to 5-10 nm. Whereas 2^{16} x 2^{16} points are available, the beam scans only those regions corresponding to a pattern designed on a computer editor. Software such as Raith GDSII Editor converts this design which is then processed by the electron beam controller. A design pattern can consist of several different layers that are exposed independently.

An alignment step is also normally required, so that the nano-size features exposed by the electron beam partially overlap with pre-patterned micro-scale contacts, providing electrical access to the device (say via wire bonding onto the micron size contacts).

Electron sensitive resists

Many different electron sensitive resists are commercially available or can be prepared in a lab, consisting of polymers dissolved in organic solvents, (e.g. polymethyl-methacrylate, PMMA, in anisole or chlorobenzene). The resist is normally spin coated onto the substrate at spin speeds between 1000 and 7000 rpm to form a thin film. The rotation speed and the resist viscosity determine the film thickness. Following the spin coating, substrates are normally annealed to dry out the solvent.

E-beam resists may be positive (e.g. PMMA, ZEP, MMA) or negative (e.g maN, HSQ, TOK). In the first case the polymer chains are broken into fragments by the electron beam, becoming more soluble. In negative resists the polymer chain are cross-linked by beam exposure, hence losing solubility. A negative resist is retained during the development process. Chemically amplified resists (e.g. TOK, HSQ) are those requiring a post exposure annealing following the exposure. This is because the beam exposure activates acidic compounds in the polymer which diffuse upon baking, cross linking the polymer chains.

In the work of this thesis a great deal of attention has been dedicated to optimize the recipes for depositing, exposing and developing the positive resist PMMA 950 and the negative TOK: TGMR-EN103Pe. The optimization was devoted to select the conditions which allow maximizing their resolution. Besides the obvious importance of correcting the design to account for the proximity effect, a certain acceleration voltage must be

determined which minimizes the beam broadening in the resists. Simulations based on the density and the chemical composition of the polymer, together with dose tests, have been carried out for specifying the most appropriate acceleration voltage for these two resists. The resist thickness is, of course, of crucial importance too; a thin resist gives naturally high resolution, as the beam broadening occurs principally in the substrate, but can make the lift-off process very difficult (or impossible) and can also reduce the etching resistance, down to useless time ranges.

In the following are reported the conditions which we advise using for obtaining nano-size features combined with facilitated lift-off or etching (Table 2.1 and Table 2.2). Note that all the parameters have been tested and optimized individually and for our specific use, and often differ from what is normally proposed.

PMMA 950 A3	Positive e-beam Resist
Substrate	Silicon oxide 200nm /silicon
Spin Coating	500 rpm 10 sec – 2000rpm 45 sec
Resist thickness	Approximately 180 nm (at 4000 rpm it becomes 140 nm)
Prebake	180 °C – 120 seconds
Exposure	Beam EHV 15 KV Aperture 10 μm Average current 26 pA Write field 150 x 150 μm Working distance 4 mm Area step size 6 nm Dose ranging from 100 $\mu C/cm^2$, for large features, to 350 $\mu C/cm^2$ for small ones. Writing in *lines mode* – no *meander*
Development	MIBKA: IPA (1: 3) – 70 sec
Wash/Stopper	IPA 30 sec Blow dry gently for about 40 sec

Table 2.1 *Exposure parameters for PMMA 950 A3, optimized for high resolution lithography of dense structures.*

Tok 2.5 cP (TGMR-EN103Pe)	Negative-chemically activated resist
Substrate	Approximately 50 nm of metal (Cu) / Silicon oxide 200nm / Silicon
Primer	HMDS, heat substrates 120 °C (better on vacuum hotplate); spin coat 6000 rpm, baking in vacuum 110 °C for 120 seconds
Spin Coating	500 rpm 10 sec – 4000rpm 10 sec – 6000 rpm 45 sec
Resist thickness	Approximately 150 nm
Prebake	110 °C – 90 sec
Exposure	Beam EHV 18 KV Aperture 7.5 μm Average current around 16 pA Dose x1 around 18 $\mu C/cm^2$ Write field 150 x 150 μm Working distance 4 mm Area step 6 nm Area dwell time 0.0004 ms Writing in *Line* mode – no *meander*
Post exposure bake	110 °C – 100 sec
Development	NMD-3 (2.38% TMAH) 35 sec. Note: more than 40 sec of development (or higher TMAH concentration %) etch the base of the features, which result overturned cones
Rinse	D.I. water at least 60 seconds

Table 2.2 *Exposure parameters for TOK 2.5 cP, optimized for high resolution lithography of dense structures.*

The exposure of single isolated elements, such as square dots of side Y or straight line of width W (tens of μm long), can be made using PMMA 950 A3 or TOK 2.5 cP using the parameters of Table 2.3, in which the required doses to pattern individual features under the aforementioned exposure conditions are given.

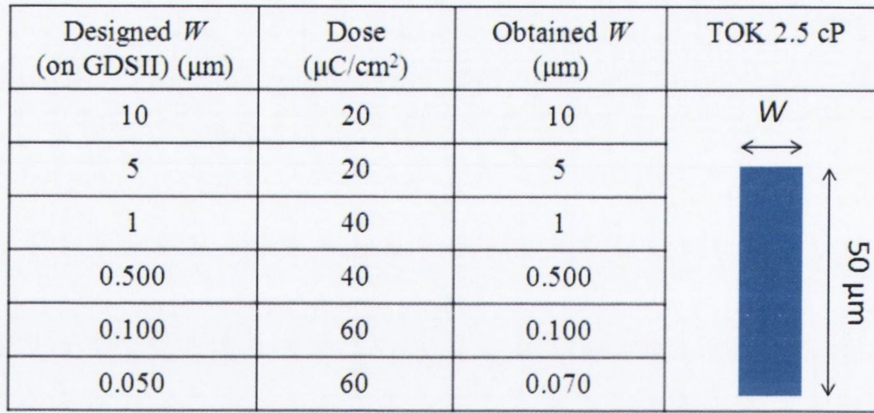

Designed W (on GDSII) (µm)	Dose (µC/cm^2)	Obtained W (µm)	TOK 2.5 cP
10	20	10	
5	20	5	
1	40	1	
0.500	40	0.500	
0.100	60	0.100	
0.050	60	0.070	

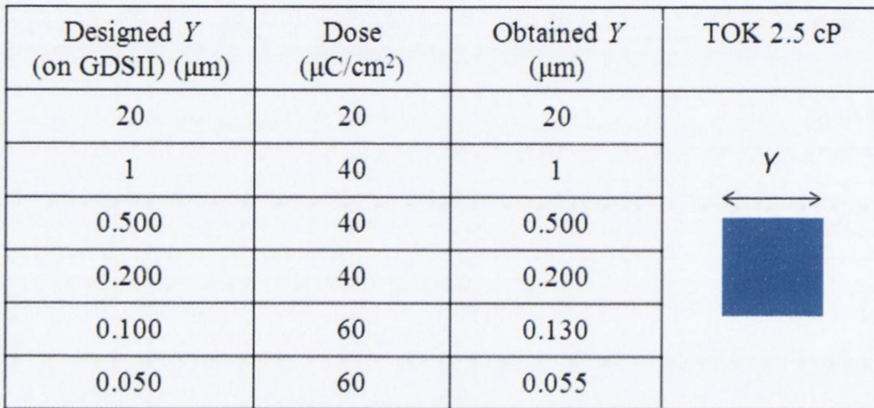

Designed Y (on GDSII) (µm)	Dose (µC/cm^2)	Obtained Y (µm)	TOK 2.5 cP
20	20	20	
1	40	1	
0.500	40	0.500	
0.200	40	0.200	
0.100	60	0.130	
0.050	60	0.055	

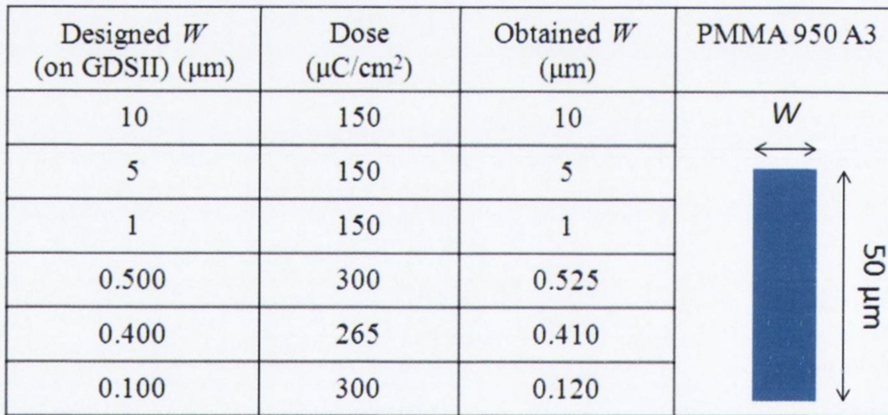

Designed W (on GDSII) (µm)	Dose (µC/cm^2)	Obtained W (µm)	PMMA 950 A3
10	150	10	
5	150	5	
1	150	1	
0.500	300	0.525	
0.400	265	0.410	
0.100	300	0.120	

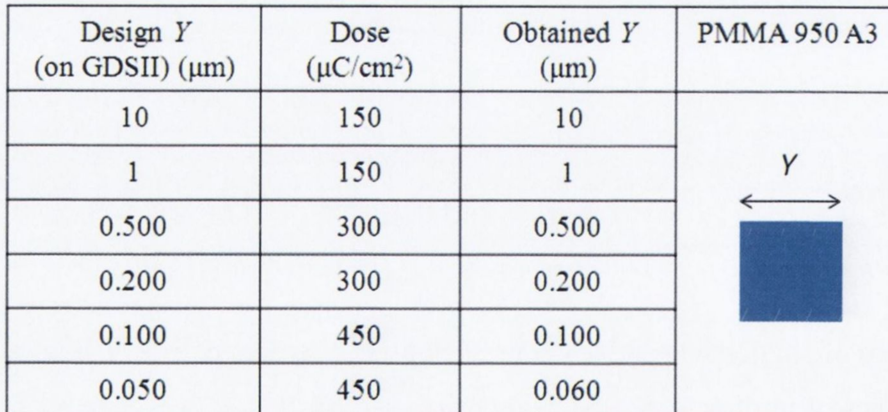

Design Y (on GDSII) (µm)	Dose (µC/cm^2)	Obtained Y (µm)	PMMA 950 A3
10	150	10	
1	150	1	
0.500	300	0.500	
0.200	300	0.200	
0.100	450	0.100	
0.050	450	0.060	

Table 2.3 *Doses to be assigned to the GDSII elements to achieve the feature sizes reported in the third column.*

Sometimes the exposure of large area contacts may be necessary; while this is normally achieved by conventional UV lithography, it may be, in some circumstances, useful carrying it out by EBL. The design is typically larger than the write field size; hence the working area is divided in several write fields, which are exposed one after another with an intermediate translation of the chip, referred to as "stitching". A sufficient overlap of neighboring elements prevents gaps that result from inaccuracies in the chip positioning. When a laser aligned stage is available this is not an issue, otherwise the alignment error can be as large as 50 μm per every mm of stage movement. Following, a recipe to expose large area contacts with negative resist is shown (Table 2.4). The choice of this negative resists relies on the fact that TOK is a so called fast resist, in contrast with most of the positive resists. That is, the dose required to expose the polymer is very low, hence it takes only up to a few minutes the exposure of large area features (hundreds of μm), while it could take hours for PMMA. The same pattern, as with positive resists, can be anyway achieved, simply by changing the lift-off with argon ion milling. Lift-off from an inversed design can also be performed, as the resist layer is quite thick in TOK (around 300 nm).

Tok 2.5 cP (TGMR-EN103Pe)	
Conditions	Exposure of large area features in short time
Spin coating	4000 rpm
Prebake	110 °C – 90sec
Exposure	Beam EHV 10 KV Aperture 30 μm Average current 250 pA Dose x1 around 20 or 25 $\mu C/cm^2$ Dwell time around 1 μsec Write Field 1 x 1 mm Working distance 4.2 mm Area step size 32 nm Using *Meander mode* – not *Line mode*
Post exposure bake	130 °C – 120 seconds
Development	35 sec in NMD-3 Wash in DI water

Table 2.4 *Exposure parameters for TOK 2.5 cP, optimized for fast exposure of large area patterns.*

The acceleration, as it can be noted, has been largely diminished, the reason being that we aim to expose the larger part of the resist in the shortest time. The temperature and the time for the post-exposure bake have been increased to allow diffusion of the acidic activator over larger areas. The resolution achievable in this way will not go beyond a μm, at best.

Proximity effect corrections

A dose test consists of a matrix copy of the pattern with dose increased at steps. The appropriate dose is selected by choosing the most suitable shape obtained after exposure and development of the whole matrix. For design consisting of single elements, such as isolated lines, square or dots, dose optimization alone may give satisfactory results. When considering a design with denser features (i.e. more than one element with spacing from the next of less than 200-300 nm) the proximity effect becomes the most important limitation and correcting the design becomes a fundamental step. At this stage the fact that the backscattered electrons from nearby features contribute to the dose of each element of the pattern must be accounted for. To correct for the proximity effect, each individual element can be assigned manually with a different dose, in a way that small and isolated features receive a larger dose. The effect of proximity normally reveals itself when exposing two electrodes separated by a small gap, say below 100 nm. After developing, some resist is normally remaining in the gap between the two features, impeding a successful lift-off (there will be point contacts between the two elements). The simple approach of increasing the developing time normally does not help. The proximity effect translated into loss of fine details: the edges are no longer sharp but blurred. To reduce this effect one can modify the original design layout to compensate the blur. The design is then deliberately distorted to balance the amount of energy deposited on the image. The overexposure region can be reduced by taking away part of the pattern and the underexposure region can be enhanced by adding some extra features. Eventually the GDSII design can look very different from the patterned structure.

When the pattern geometry becomes very complex, e.g. for a large number of dense features rather than a few pairs of electrodes /lines, the pattern must be divided into smaller areas, and the dose factor assigned to each of them after calculating the energy deposited in each area. This is a model-based method that balances the energy received by the image correcting the dose for each pattern. Since the amount of backscattered electrons strongly

depends on the material of the substrate, the parameters of the model must also be changed for each different sample. It becomes particularly difficult when dealing with multilayers. There exist some software that are built-in the SEM controller, and by specifying a multilayer structure can modify the exposure pattern. Because they typically are very expensive, the above method of manual correction, which relies on a simple set of rules, can be satisfactory; but the accuracy will become poorer at increasing geometry complexity.

Metal and oxide deposition

We have adopted two methods in this work for the deposition of the thin films necessary to define the electrodes in a device. These methods, consisting in sputtering and electron beam evaporation, are not equivalent in terms of the results they can provide when dealing with features with lateral size of order nanometers.

When deposition occurs via sputtering from a target material, atoms or molecules from this target are ejected toward the substrate via momentum transfer. The basic principle is simple: the target is bombarded by accelerated ions resulting in ejection (sputtering) of atoms which deposit onto the substrate, forming a film. The source of the energetic ions is typically a low pressure glow discharge or plasma, which is ignited and sustained between the target and the substrate using a noble gas such as argon at typical pressures of 1-100 mTorr. A high negative potential is maintained at the target, hence positive ions are accelerated from the plasma onto the source material, causing sputtering to occur. The sputtering yield, i.e. the efficiency of momentum transfer, depends on the cross section of the collision, the binding energy of the target atoms, and the kinetic energy of the incoming ions. Placing permanent magnets behind the source allows trapping the charged particles involved in the sputtering in the stray field generated in the vicinity of the target. Hence it is often referred as to magnetron sputtering. By using AC sputtering, in the radio frequency range, it is also possible to sputter purely insulating materials.

The sputtering method offers very good surface topology and it allows easy production of well-controlled alloy, simply via co-sputtering from different source. It must be noted that the distance between the target and the substrate is, in this deposition technique, limited by the fact that ejection can occur in any direction; hence the substrate must be located close to the top of the target.

On the other hand, the deposition techniques employing the evaporation of a source material are typically very simple but, as a drawback, do not offer the same control on topography and alloy preparation as for sputtering. The source material is loaded into a crucible, which is commonly heated by one of three methods: resistive heating, electron beam heating or inductive heating. Upon heating the material, a vapor of atoms is released that, when the shutter is open, travel across the chamber in a straight line and deposit onto the sample substrate. In electron beam evaporation, the material is heated by bombardment of energetic electrons, which are created by thermal emission from a tungsten filament and accelerated to a high voltage on the accelerating electrodes. Electrons are bent toward the source in the crucible by permanent magnets. This method allows evaporating insulating materials by heating them locally, which induces their sublimation. The distance between the source crucible and the sample substrate can be maximized as much as needed, provided that the vacuum level is good enough to offer a long mean free path for the evaporated atoms. For the tool used in this work, a Temescal FC-2000, it is about 75 cm.

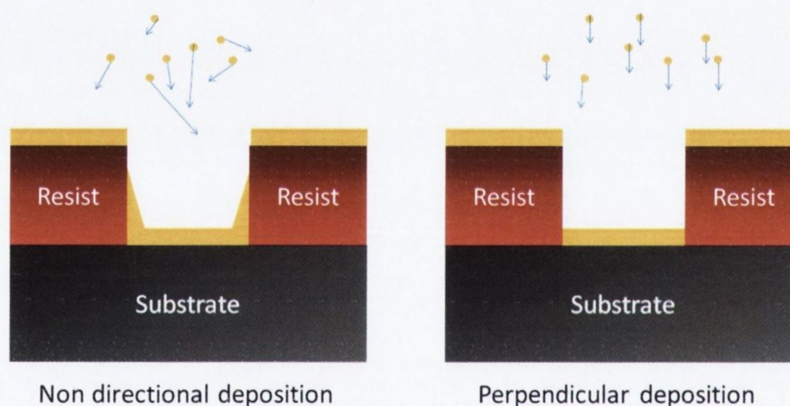

Figure 2.4 *Illustration of the deposition occurring at the edges between the resist and the substrate in the case of directional (right) and non-directional /sputtering deposition (left). This effect becomes more visible when dealing with nanoscale patterns, in which the gap is comparable or smaller than the resist thickness.*

The difference between the two methods is evident: in sputtering the particles hit the substrate at any angle and, unless a pair of shadow masks is placed in series, which select a specific direction, the deposition cannot occur in a directional way. Shadow masks have the inconvenience to reduce the rate and cannot be fitted in any tool. In e-beam evaporation it is relatively easy to obtain a very directional deposition; therefore upon loading the substrate on a stage which faces the source crucible (i.e. a straight line between the crucible and the center of the sample forms a perpendicular angle with the substrate), at

a distance several time larger than the crucible diameter, perpendicular deposition is readily achieved.

The importance of having directional deposition when dealing with nano-structured pattern is readily understood, by considering that non-perpendicular target atoms can deposit on the edge of the resist rather than on the of the substrate (Figure 2.4).

Considering that a typical resist thickness is of order 150 nm, when the gap among the patterned features becomes of comparable size, this issue can cause the loss of fine details and the appearance of the so called "rabbit ears" at the edges of the electrodes (Figure 2.5). For smaller gap, lift-off even becomes impossible.

Combining the techniques described in this section we have fabricated the interdigitated platforms of electrodes used to construct the field effect transistors measured in this thesis. The advantage of this geometry will be described in the next chapter, and it essentially consists in reducing the resistance of the device by increasing the channel section, which is proportional to the channel width (i.e. length of the electrodes).

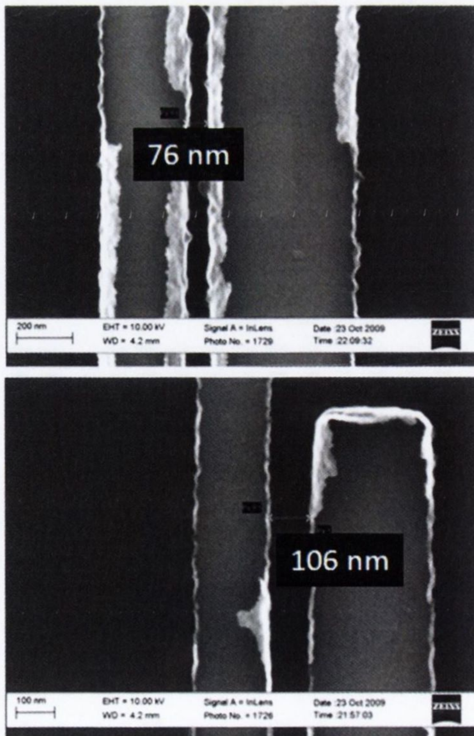

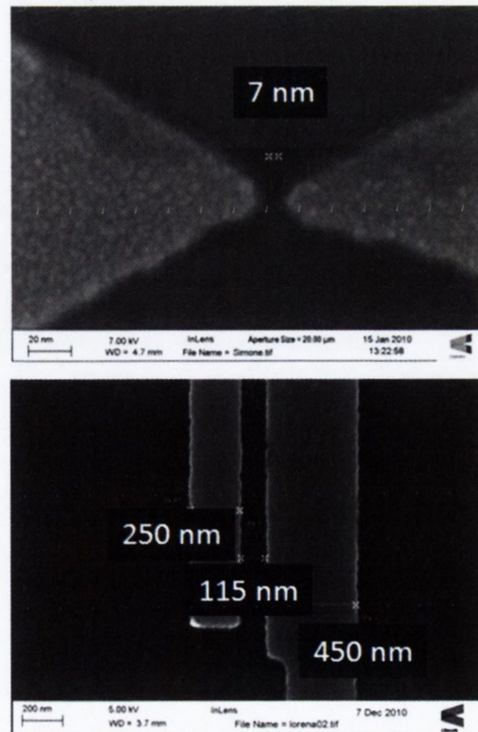

Figure 2.5 *SEM pictures of pair of electrodes resulting by lift-off of structure deposited by sputtering (left) and e-beam evaporation (right). The appearance of "rabbit ears" at the edges of the electrodes is clearly shown.*

Fabrication and initial characterization of single crystal organic FETs

In this section we want to describe the process of fabricating devices for studying lateral spin transport in organic single crystals, in which the carrier mobility is enhanced by a local electric field as in FETs. For magneto-transport measurement, the source and drain electrodes are made of ferromagnetic material and act as injector and detector, separated by a non-ferromagnetic medium (the organic crystal). This geometry resembles that of a spin valve, but having in addition a gate terminal acting underneath the spacer. The main focus of Chapter 3 will be the structural and electrical characterization of these crystals. Figure 2.6 gives an illustration of the device. In the following we will first describe a technique which allows growing highly pure single crystals of pentacene, which will be employed as the non-magnetic semiconductor.

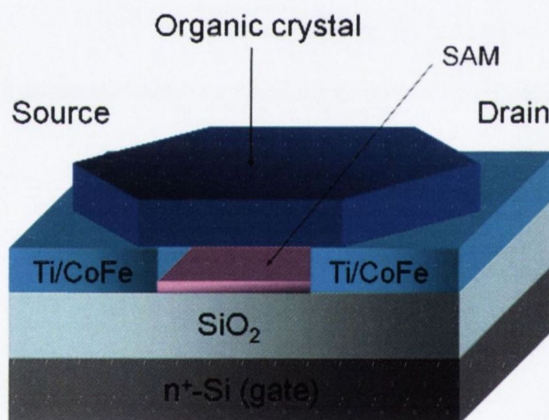

Figure 2.6 *Schematic of a single crystal organic field effect transistor with spin polarized electrodes. The SiO_2 surface is chemically modified with self-assembled monolayer (SAM).*

Vapor processing technique

Physical vapor transport is a deposition technique used to grow vaporized material on a substrate. This physical method relies on the transport in a non-reactive gas of a source material to an area which promotes the growth of the desired thin film or crystal. Typically

it is performed in a furnace in which a quartz tube is inserted; a stable temperature profile is produced over its length by an external heater. The starting material is placed into the area of the tube with the highest temperature, at which sublimation can take place efficiently, and maintained over a specific growth period (Figure 2.7).

The extremities of the tube are sealed, in a way that allows only the injection of pure gas from a pipeline at one end, and the connection of an exhaust into a bubbler at the other end. Typically pure argon is employed as the transport gas.

A crucible which contains the source material is placed within the tube at about the centre of the furnace, surrounded by the heating element. The substrate is also placed inside the tube, but near the end of the furnace, in a colder area. Water cooling of one edge can sometime promote the rapid crystallization of the growth material. The vaporized molecules are transported from the sublimation area toward the lower temperature regions of the tube by the gas, and free-standing crystals grow on the substrate at the appropriate temperature depending on the molecule.

The PVT technique can promote the purification of the starting material, due to the fact that precise temperature control of the furnace can suppress transport of heavy molecular impurities. This is achieved by maintaining the furnace temperature just about the sublimation temperature of the source material: heavier molecular impurities, which require higher temperatures to sublimate, do not vaporize and remain in the starting area. Hence the crystallization region is normally well separated from the impurities.

In this work we grew pentacene single crystals by horizontal physical vapor transport in a flow of argon gas. The source, containing the pentacene powder acquired from Aldrich, was heated to 275 °C (slightly below the sublimation temperature) in the hot zone of the tube furnace, 80 cm long, which showed a temperature gradient of nearly 100°C between the middle and the end. Pentacene single crystals nucleated spontaneously on the wall of glass tube segments designed to fit snugly inside the quartz tube (to allow simplified collection and cleaning) in the colder zone of the furnace. The purest crystals were found where the temperature was 200-220 °C, after about an hour of keeping the temperature of the source zone constant under slow argon flow (about 1scc/sec). They grew as platelets with typical dimensions of several tens of micrometers in width and 2 to 10 μm in thickness, and blue colored. In practice, we first flow argon at room temperature for about 24 hours before starting to heat the tube, then slowly ramp the temperature to 275 °C in 4 hours and keep it constant for an hour. Subsequently, furnace cool down took approximately 2 hours. Some deposit of transparent material was also typically found near

the very end of the tube, in the coldest region adjacent to the bubbler; this likely consisted of lighter impurities.

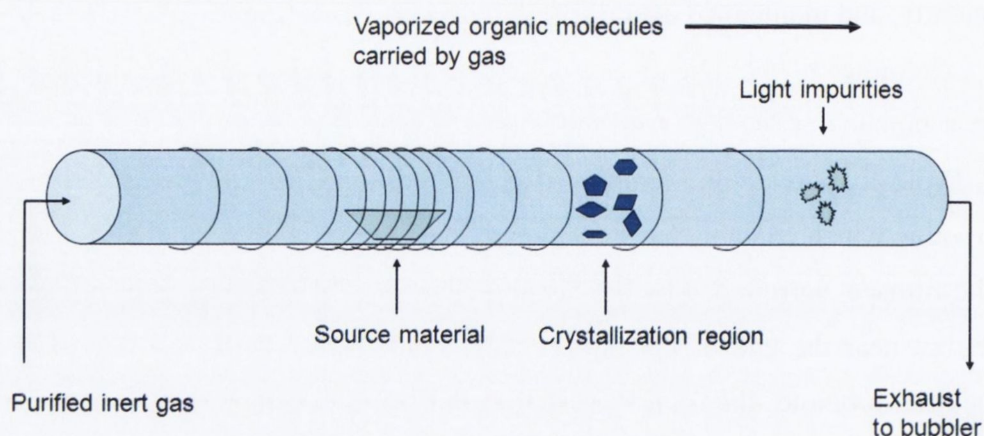

Figure 2.7 *Physical vapor transport method: purified source material is placed in a quartz tube, heated by a resistive heating element to its sublimation temperature, and carried down a temperature gradient by a stream of inert carrier gas. The material resublimes in the coldest zone of the furnace to form crystals.*

Nano-manipulation: dual beam system

The single crystals produced by PVT must now be harvested and placed onto a prefabricated transistor structure.

At first the crystals are "manually" harvested: the glass tubes acting as substrates can be gently shaken to allow their content to fall and deposit onto clean metallized substrates of silicon (Si /SiO_2 /Au). This step is typically made in a glove box, to minimize the exposure to air and humidity. Next, the substrates and the FET platform are loaded, at the same time, into a dual beam electron microscope and suitable sized crystals (about 30 μm wide and a few μm thick) are identified. The assembly of the device consists in placing the crystals onto the existing FET platform. At this purpose, a piezo-manipulator was mounted inside the vacuum chamber and remotely controlled, to allow the precise manipulation of the micron-size objects on the sample surface while viewing via SEM (scanning electron microscopy) and FIB (focused ion beam).

The Zeiss Auriga dual beam system that we have used is equipped with both ion and electron beam columns, placed at 83 degrees to each other, on top of the substrate, which is tilted at about 52 degrees to allow an equivalent exposure to the two beams (Figure 2.8).

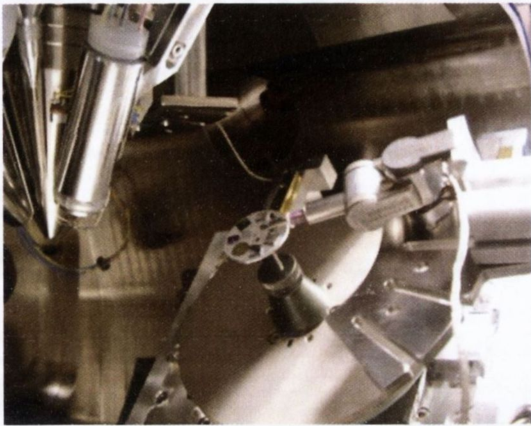

Figure 2.8 *Picture of the internal of the chamber, showing the electron column and the manipulator. The stage is tilted to allow simultaneous exposure to electrons and ions from the SEM and FIB columns.*

The SEM column uses a focused electron beam which scans across the areas of the sample to reveal clear non-destructive images of the sample surface. The FIB works similarly to SEM, except that gallium ions are accelerated to the surface of a sample at energies of 2-50 kV via electrostatic lenses, hence it can be used both for milling and high resolution imaging. Although high quality images can be obtained from this process, it must be kept in mind that a prolonged exposure can be destructive for the sample surface, due to the bombardment of accelerated ions which inherently sputter atoms from the surface. This effect is indeed normally exploited to obtain patterned precision milling of defined structure, simply by scanning the beam over desired regions or lines.

A further option offered by the tool consists in material deposition induced by FIB or SEM assisted chemical vapor deposition, which requires the introduction of precursor gases which are being modified by the interaction of accelerated high energy ions or electrons and deposit onto the sample surface, in the area scanned by the beams.

The possibility of performing dual imaging, of the side and the top of the crystals, largely facilitates the operation of the nanomanipulator, in terms of locating its tungsten tip near the desired objects. In our process, a crystal of suitable size was approached with the tip of the manipulator and, once in gentle contact, SiO_2 straps were deposited by decomposing siloxane gases under the electron beam, to solder the tip to the crystal and being able to precisely move it. The precursor gas was injected close to the sample surface via needle valves remotely positioned near the top of the sample, where the electron beam is focused. The crystal was then moved toward the patterned sample and placed across the nanoscale

gaps to electrically bridge the electrodes. Crystals were normally gently pressed with the tip against the substrate, to enhance electrical contact, and held in position by additional SiO_2 wires, deposited on the edges, to secure them across the gap (Figure 2.9). This was aiming at limiting the movement of the crystal when the device was transported to further vacuum cavity, for the electrical characterization. The tip was finally removed from the crystal simply by pulling it away from the substrate by using the piezo; because the lateral SiO_2 stripes typically provided a much stronger adhesion.

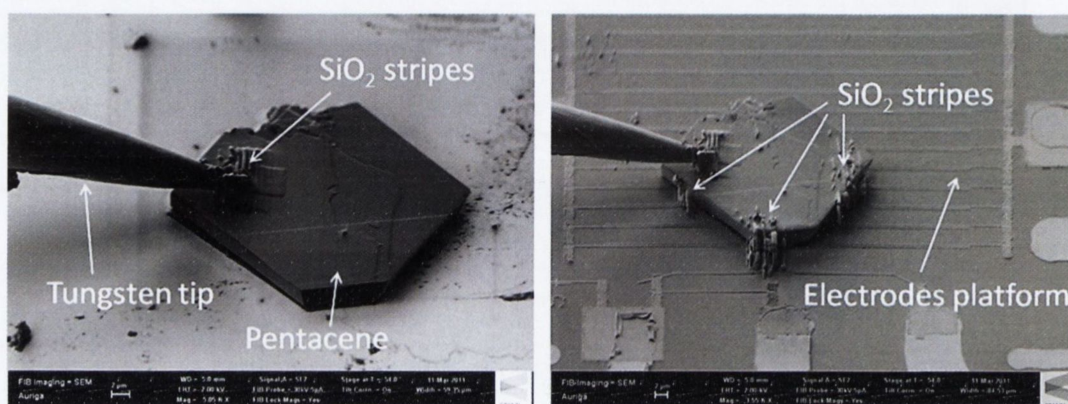

Figure 2.9 *Schematics of fabrication of pentacene single crystal pentacene FET. A crystal is placed on the patterned substrate by mean of a piezo-manipulator mounted inside the FIB vacuum chamber and remotely controlled; in situ chemical vapor deposition (CVD) of SiO_2 allowed securing the micron object.*

Similarly, other kinds of organic crystals could be prepared and placed on top of FET structures. In Chapter 3, Appendix B is provided a description of the process to fabricate a C_{60} micro-rod based device.

High impedance testing station

The atomic flatness of the crystal surface (tested by AFM, see next chapter) ensured reasonable contacts in most cases. However, due to the many steps involved in the fabrication of each sample, the level of reproducibility was quite low, hence an initial electrical characterization was necessary to select those devices displaying reasonably low contact barriers. In some cases, indeed, the crystal could happen to be placed on top of the electrodes in a slightly tilted position. In this situation, intutively, the electrical contact

between the organic media and the electrodes was so poor that even at the highest voltages applied (around 15 V) the overall current was below 10 pA.

While accurate measurements were performed in a Quantum Design Physical Properties Measuring System (PPMS), to initiate the investigation of the quality of the contact between the single crystal and the source-drain electrodes we have installed a high impedance testing station, consisting of tri-axial leads for high impedance measurements, wired by Dr. P. Stamenov, and a Keithly 6430 equipped with a low noise preamplifier. For convenience the sample was hooked up and measured in ambient atmosphere. Preliminary *I:V* curves were scanned and acquired by controlling the multimeter via a simple LabView program.

By using a third connection and a further pair of Keithly /preamplifier, the gate leakage current could also be tested, allowing discriminating whether the gate dielectric successfully survived the fabrication process. Positive devices were then hooked up in the PPMS, for accurate magneto-transport characterization, at temperatures down to 7 K in ultra-high vacuum conditions.

Preparation of organic thin film transistors

We have focused on preparing and testing mainly two kinds of thin films, one consisting of small organic molecules, mainly of Alq_3, deposited via thermal evaporation, and the other of long chain of the conductive polymer poly(3-hexylthiophene), processed by wet techniques. Following are the details of the methods to prepare such thin films.

Thin films of Alq_3

Thin films of Alq_3 have been deposited by thermal evaporation onto patterned substrates in an UHV chamber, with a base pressure in the region of 10^{-10} mBar.

The evaporation cells used for organic materials are similar to standard cells used for inorganic deposition. They consist of a crucible surrounded by tungsten wire for resistive heating. The organic material is in powder form and, once in the crucible, is heated at temperatures below the decomposition temperature, so that sublimation occurs. Crucibles

are made of aluminum oxide, to avoid reactions with the organic material. Only molecules that show crystallization can be evaporated. Polymers with long chains display breakage of the molecular bonds before any evaporation occurs. Here, the Alq_3 source material in the crucible was heated up to 200-220°C, around its sublimation point, and the temperature was monitored via thermocouple adjacent the source and maintained constant throughout deposition via a feedback controller, which allows having very smooth and uniform amorphous films on substrate at room temperature.

This tool was purpose-built as a joint work by Mr. H. Tokuc (in the perspective of investigating small organic spin valves) and myself (for testing lateral transport).

In Figure 2.10 a picture of the chamber is shown: in the part indicated as (1) four ports are recognizable, used for connecting three evaporation cells (two dedicated to organic materials and one to either ferromagnetic or capping metals) and a Knudsen cell, which was committed exclusively to cobalt deposition. The substrate was attached to a manipulator / long arm which provides full control of the sample along x, y and z and rotation around the z axis. This way samples could be easily transferred from a load lock to the main chamber, which avoids the problem of venting it too often. Samples could be resistively heated, and temperature was measured with a thermocouple in contact with the substrate. By using a turbo molecular pump with 400 l/s capacity, backed by a rotary pump, pressures down to low 10^{-8} mbar could be initially achieved. The load lock is also pumped by a turbo and usually stopped in the low 10^{-7} regime. Usually, the base pressure is enhanced by baking the system, to outgas the organic material and dipolar molecules (e.g. water) stuck to the walls of the chamber.

A second version of the tool was, following, designed and assembled by Mr. H. Tokuc, in which a new chamber with similar functionalities was also equipped with an argon ion gun, which allows etching the first few atomic layers of the electrodes prior to deposit the organic film, hence removing the metal native oxide. In this chamber, besides the TMP, an ion pump was working in parallel, allowing the achievement of a vacuum as low as 10^{-10} mBar.

As a remark, the in-situ deposition of an insulating tunnel barrier on top of the metallic contacts may be achieved by natural oxidation of a thin layer of evaporated Al, when pure oxygen is leaked into the chamber via a needle valve.

In these optimal conditions, of low vacuum and ion etching of the native oxide, we have deposited the small-molecule thin films of Alq_3 reported in this thesis; the results are described in Chapter 3, Appendix A.

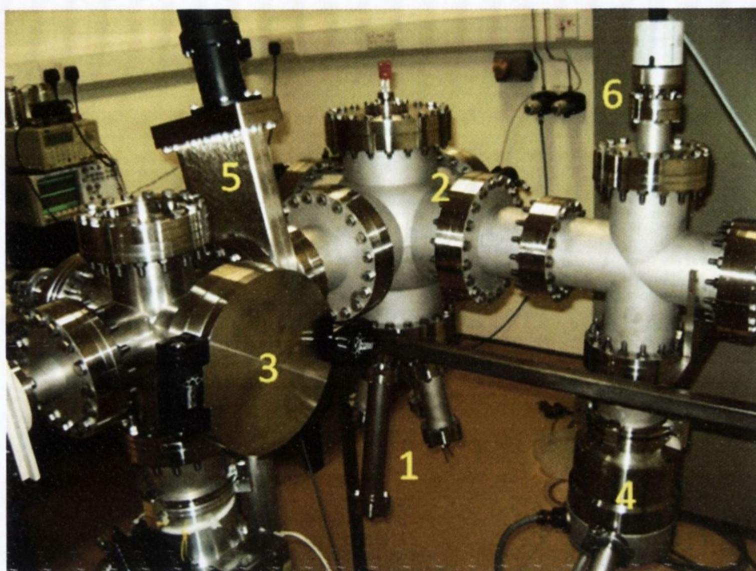

Figure 2.10 *Picture of the first version of the organic vacuum chamber: (1) evaporation sources, (2) main chamber, (3) load lock, (4) turbo molecular pump, (5) gate valve, (6) vacuum gauge.*

Thin films of poly(3-hexylthiophene)

In this subsection some details are provided about the deposition of thin films of conductive polymer via a wet technique.

The films have been deposited on heavily doped n^{++} Si wafer with a thermally grown SiO_2 layer whose thickness was about 200 nm. This way a back contact to the substrate allowed for a gate voltage to control the charge density in the semiconducting film.

The SiO_2 surface was chemically modified with self-assembled monolayer of hexamethyldisilazane (HMDS) in order to obtain an hydrophobic surface, which is reported to promote structural ordering of the cast polymer (Ong, 2004) and enhance its field-effect mobility (Chua, 2005). This chemical agent is reported on literature to be used also to minimize or repair damage to silicon dioxide surfaces, see for example (Suzhu Yu, 2002) (Bo Xie, 2004).

The deposition of a conjugated polymer is known to be achievable by several techniques, such as electrochemical deposition (Koezukaand, 1989), Langmuir-Blodgett (Paloheimo, 1990) contact printing (Seong, 2004) and spin coating (McCullough, 1998); here we have chosen to use the commercially most attractive technique of spin coating.

Spin coating is in fact the primary process for the deposition of uniform thin films of conjugated polymers for device applications. In (Chao-Ching Chang, 2005) is presented an experimental and theoretical analysis of the coating of several representative polymers: dilute solutions show Newtonian rheological properties, the film thickness after spinning is proportional to the initial polymer concentration (weight fraction) and angular velocity. To predict the exact film thickness they accounted for the difference between the polymer solutions density and the solvent density. The method of spin coating a polymer solution onto flat substrates simply consists in first placing an excess amount of solution on the substrate, the substrate is then rotated at high speed in order to spread the fluid by centrifugal force, the rotation is continued for some time, usually of order 1-2 minutes, with fluid being spun off the edges of the substrate, until a final desired film thickness is reached. The physics behind involves a balance between centrifugal forces controlled by spin speed and viscous forces which are determined by the solution viscosity. The solvent is normally volatile giving simultaneous evaporation during spinning, and sequent evaporation during post annealing, which can be carried out onto a vacuum plate in case water and oxygen must critically be removed too. The film-forming process is primarily driven by two independent parameters – viscosity and spin speed.

Here we have spin coated our material from a 0.05 % weight solution of poly(3-hexylthiophene) in de-hydrated toluene. Toluene was preferred to chloroform or chlorobenzene as chlorines were observed to corrupt the source-drain contacts when not made of noble metals. The spin casting was performed using a spinner installed inside a glove box, at a typical spin rate of 1000 rpm, which gave a thick film of about 150 nm (measured in a profilometer). The spin rate was calibrated by measuring the AC voltage induced in a coil by a permanent magnet secured on the rotating stage.

The spin coating was followed by annealing of the substrate to fully remove the solvent, for 30 minutes at 110 °C, in argon atmosphere.

It is important to notice that the polymer was spun on pre-patterned substrates which, following the annealing, were transferred to the PPMS for electrical measurements by using argon jars or sealed sample boxes. If the polymer was coated on the entire substrate, the unpatterned polymer (which has relatively high conductivity) could influence the gate leakage current, because the current would flow through the unpatterned region to the conductive substrate via the edges. Further it could electrically connect among them the large area contacts, while we aim at probing the conduction only through the nano-scale interdigitated electrodes. Therefore, to eliminate the deposition of a conductive layer

around the device a layer of 100 nm of Al_2O_3 was first patterned and deposited covering the whole surface of the substrate but leaving uncovered a window of 100 μm x 100 μm, in which the electrodes were fabricated. This was done immediately after defining a micro-scale contact platform by UV lithography.

To further avoid any possible deposition of the polymer on the edge of the wafer, the sides were normally protected during the spin coating by an adhesive pad, which was removed just before the annealing.

Following these intuitive adjustments, the problem of parasitic current flowing to the gate remained, however, one of the main issues that we have encountered. At this stage, the only possible source of the leakage current consists in physical fractures (of sub-nanometer size) existing on the oxide surface, which are filled by liquid polymer during its spin coating (i.e. we believe that conductive molecules can widen into the fissures when diluted in a solvent). The only possible solution to such an issue is to maintain the silicon oxide surface absolutely pristine throughout the whole sample processing. Adjustments to the surface by HMDS treatment have proven effective only to a small extent.

We presume that these hairline fractures on the surface of the oxide were propagated from the edges of the chopped sample-substrate when dicing the silicon wafer. To avoid their formation several approaches have been tested; the first simply consisted in cutting the whole thickness of the wafer using a dicer saw, therefore not applying any manual stress on it. Ideally the large density of fractures induced by this method should be localized within the first hundreds of μm from the edges, rather than propagated throughout the center of the substrate. Even though this approach slightly improved the situation, the yield was too low to be considered an effective solution.

The best results in terms of working substrates versus chopped samples was given by making a careful alignment of the cutting direction with the cleavage planes of the crystalline silicon substrate. Here a first cut is obtained by drawing a notch at one edge of the wafer and applying (either manually or with a weight) a gentle stress on a bent surface. This way the fracture will propagate from the notch along a certain cleavage plane. From here on, the notches can be drawn perpendicularly to the first cut and propagated in the same way. Even though this process is time consuming and quite laborious, it turned out to be the optimal way to obtain substrates which have pristine dielectric surface, and hence most of the out-coming devices did not display substantial leakage current.

An illustration of the *I:V* curves, which are obtained when the leakage current is high enough to affect them, will be given in Chapter 4.

High impedance transport measurements

The measurements have been performed using a Physical Property Measurement System (PPMS of Quantum Design). The PPMS consists of a helium cooled cryostat which is pumped by a rotary pump in which the sample can be placed and the temperature can be varied between 2 K and 400 K. Although in this study the minimum temperature at which measurements were performed was 7 K. The system is equipped with a 14 T superconductor magnet with a field uniformity of ±0.1 % over 5.5 cm. The resolution of the magnet is 0.03 mT to 1.5 Tesla and 0.3 mT up to 14 T. The sample temperature is controlled with a stability of ± 0.2 % and is monitored by a platinum resistance thermometer with an accuracy of ± 1 % from zero to full range. The DC resistivity of the sample can be normally measured with a HP 34401A multimeter, in the standard four probe configuration; however, to facilitate the measurement of highly resistive organic materials, a probe wired with high impedance tri-axial leads was made by Dr. P. Stamenov, to sense resistance in excess of 100 GΩ at the lowest temperatures. Electrical contacts were made on the sample using quick drying silver paint and 0.075 mm thin gold wire.

A few concluding remarks on the tool: the outer dewar of this cryostat is filled with liquid nitrogen to reduce the temperature gradient between the inner helium dewar and the external atmosphere. This efficient cryogenic design is optimized to only allow approximately 6 liters per day helium boil-off rate. A state of the art electronic feature facilitates sequential operations while maintaining low noise a voltage overload protections. The PPMS setup is also able to be modified to allow for vibrating sample magnetometer measurements, very useful in consideration of the high DC magnetic fields here achievable.

The possibility to apply a gate voltage at the conductive substrate was sustained by the presence of three independent high impedance leads, respectively the high voltage (source), the gate and the ground (drain). This allowed monitoring and recording the amount of gate leakage current during all the measurements. This data is actually important, considering how much it can affect the measurements, but it is very rarely reported on literature, making our measurements particularly reliable for drawing conclusion about the injection and conduction in this family of materials.

Bibliography

Bo Xie, et al. (2004). *Microelectronic Engineering, 76*, 52.

Chao-Ching Chang, et al. (2005). *Thin Solid Films, 479*, 254.

Chua, L. et al. (2005). *Nature, 434*, 194.

Koezukaand, H. et al. (1989). *Synth. Met., 28*, C753.

McCullough, R. D. (1998). *Advanced Materials, 10*(2), 93.

Ong, S. et al. (2004). *J. Am. Chem. Soc., 126*, 3378.

Paloheimo, J. et al. (1990). *Applied Physics Letters, 56*, 1157.

Ramos, R. (2009). *PhD Thesis Dissertation, Trinity College, Dublin.*

Seong, j. Y. et al. (2004). *Journal of the Korean Physical Society, 45*, S914.

Suzhu Yu. et al. (2002). *Journal of Applied Physics, 92*(6), 3338.

Chapter 3

Characterization of crystalline pentacene

Introduction

Traditionally metals and inorganic semiconductors are used as the spacer material in spin-valves. We define a spin-valve as a device with two ferromagnetic electrodes separated by a conductor which allows the transport of spin-polarized electrons between them. It has low or high resistance states depending on the relative orientation of the magnetization of the two electrodes. The possibility of employing organic semiconductors in such devices is attracting rising interest (Naber, 2007); the underlying reason consists in increasing the spin-valve efficiency by reducing the spin scattering due to large atomic weight of the spacer material (Ga, As, In…) by replacing them with organics which mainly consist of light atoms like carbon and hydrogen. The main drawback is the low carrier mobility which is typical of organic conductors.

Charge carrier mobility thus becomes an indicator of the quality of the organic semiconductor and the primary factor that determines the performance of organic devices. The highest mobilities are found in single crystals due to molecular ordering that permits good overlapping among neighboring molecular orbitals. A field effect mobility of 1.5 cm^2/Vs was reported for Pentacene and of 8 cm^2/Vs for Rubrene (Nelson, 1998) (Podzorov, 2003).

Although carrier mobility is low in organic semiconductors, significant improvements can be obtained by applying a voltage at a gate terminal adjacent to the conductive organic channel, as in field effect transistors (FET) (Sundar, 2004) (Torsi, 2005). The gate insulator acts as a capacitor and the gate electrode applies an electric field which modifies the density of charge carriers accumulated at the interface. Thus the current between drain and source can be modulated by the gate voltage.

Here we want to explore the idea of a device for lateral spin transport in which the carrier mobility of an organic single crystal is enhanced by a local electric field induced in a gate terminal. A simple injector-detector geometry with two ferromagnetic electrodes separated by a non-ferromagnetic medium (i.e. the organic crystal), as in spin valves, further having a gate terminal acting underneath the spacer (Figure 3.1).

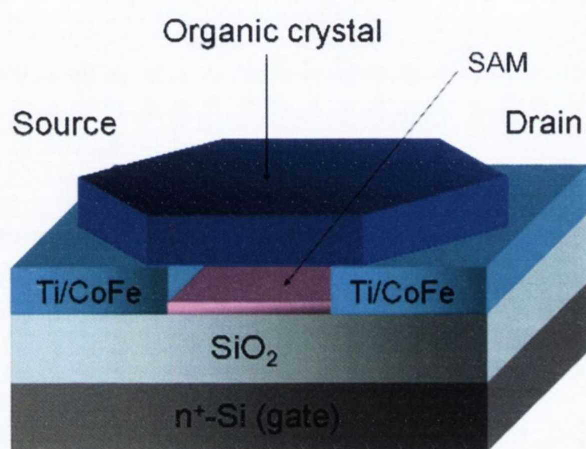

Figure 3.1 *Schematic of a single crystal organic field effect transistor with spin polarized electrodes. The SiO_2 surface is chemically modified with self-assembled monolayer (SAM).*

Fabrication of the crystals

As reported in literature, most of the single crystals used so far for the fabrication of organic FETs have been grown using the physical vapor transport method (PVT) (Roswitha, 2006). In this approach a zone furnace is employed to grow crystals on the wall of a glass tube, subsequently harvested and manually placed onto a prefabricated transistor structure (Lee, 2006).

The high purity organic material used as source is placed in the highest temperature region of a glass or quartz tube; an inert gas (e.g. Ar or N_2) is flowed over the material which is heated near its sublimation temperature. As the material is slowly vaporized, it is carried down the tube by the gas, where it resolidifies in a temperature gradient, as described in Chapter 2. The crystal growth occurs downstream within a relatively narrow range in the temperature gradient furnace. The gradient may be controlled with the use of a second resistive heating element, or by cooling one extremity of the reaction tube near the end of

the furnace. Because organic compounds will sublime at different temperatures based on their composition, this setup also provides further in situ purification.

Here, we grew pentacene single crystals by the horizontal physical vapor deposition method. Pentacene single crystals nucleated spontaneously on the wall of glass tube segments designed to fit snugly inside the quartz tube (to allow simplified collection and cleaning) in the colder zone of the furnace. The purest crystals are found where the temperature is 200-220 °C, after about an hour of keeping the temperature of the source zone constant under slow argon flow (about 1scc/sec). They grew as platelets with typical dimensions of several tens of micrometers in width and 2 to 10 μm in thickness.

Depending on the size and shape desired, the growth process may be extended anywhere from tens of minutes to several hours, and the crystals vary in size from micrometers to centimeters plates (Kloc, 1997) (Laudise, 1998).

Pentacene crystal structure

Pentacene crystallizes in a triclinic unit cell, with two molecules in a unit of dimensions *a* 0.793 nm, *b* 0.614 nm, *c* 1.603 nm and angles among the axis α 101°, β 112°, γ 85° (Campbell, 1961). Molecules are planar, made of five linearly fused benzene rings and crystals are formed by Van der Waals interaction; the properties of the crystals, including the electrical characteristics, are determined by the molecular ordering.

As for many organic crystals, there are two peculiar features in pentacene: the herringbone packing of the planar rod-like molecules in the unit cell, and the formation of layers in the crystalline c direction (Figure 3.2). There are two molecules per unit cell, which are not parallel to each other, but are ordered in a herringbone fashion; the denser packing of the molecules in the *ab* plane leads to a stronger intermolecular interaction, therefore the bandwidths of both the conduction and the valence bands are significantly enhanced in the *a* and *b* directions (Figure 3.7), with an expected large anisotropy within and out of the layers (Nabok, 2007).

Judging from the SEM images (Figure 3.3), the pentacene crystals obtained by PVT appear to have a very smooth surface. AFM investigations on the surface of a single crystal reveal that smooth, flat terraces are separated by monomolecular steps implying that each crystal consists of layers of pentacene sheets stacked on top of each other (Figure 3.4).

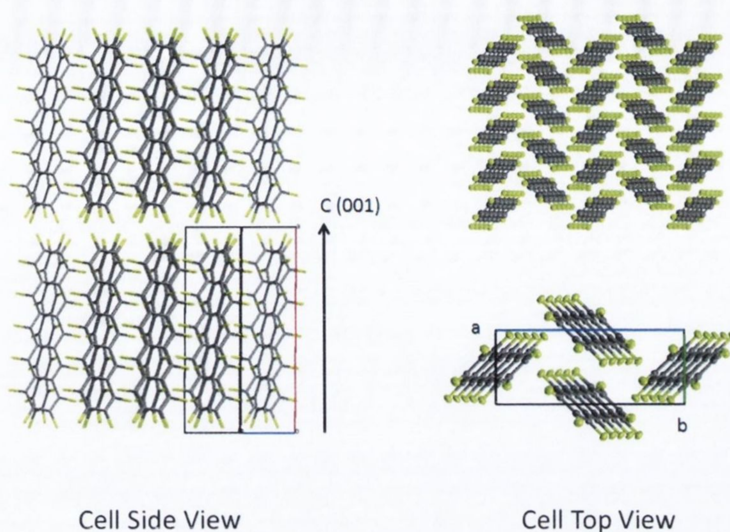

Figure 3.2 *Crystal structure of pentacene. Left: stacked layers of molecules, along the c axis. The unit cell has been simplified by using a simple orthorhombic cell, ignoring α, β and γ to facilitate the view. The side view of the unit cell is also indicated. Right: molecular packing in the a-b layer, it is evident the herringbone arrangement. Developed using Mercury 2.4.5 (developed at Cambridge for crystal structure visualization, free download at www.ccdc.cam.ac.uk).*

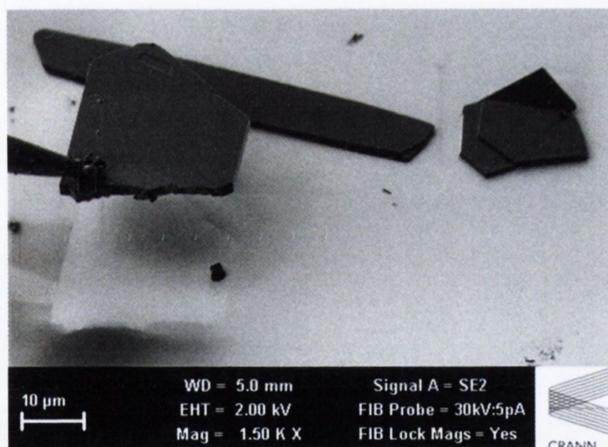

Figure 3.3 *View of independent pentacene crystals on a metallized SiO_2 substrate (SEM). The tungsten tip of a piezo manipulator mounted inside the vacuum chamber is also shown; it allowed precise manipulation of the micron sized objects on the sample substrate while imaging via the SEM.*

The measured rms roughness on the surface of the crystal was determined to be 0.3 nm, while the measured step height of each molecular sheet is approximately 1.4 nm, resembling the length of a pentacene molecule along the main axis, known to be 1.421 nm (Endres, 2004).

Considering the expected molecular structure, pentacene crystals exhibit an anisotropic pattern which forms a flat crystal with a distinctive preferred growth direction. Interestingly, the dimension of the *c* lattice axis resembles the molecular terraces observed by AFM, showing that the sample has single crystal properties. It is evident that the *c*-axis corresponds to the slowest growth direction, normal to the top surface of a flat crystal, and therefore the *ab* plane is parallel the crystal platelet-like surface.

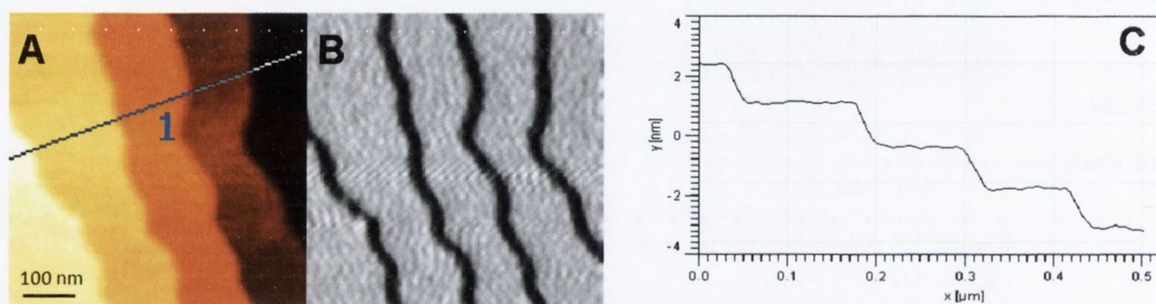

Figure 3.4 *AFM image of the top surface of a pentacene crystal. It is highlighted the amplitude (A), contrast (B), and profile (C) information (C is obtained along line 1) on a 500 x 500 nm scan, molecular steps are separated about 100 nm.*

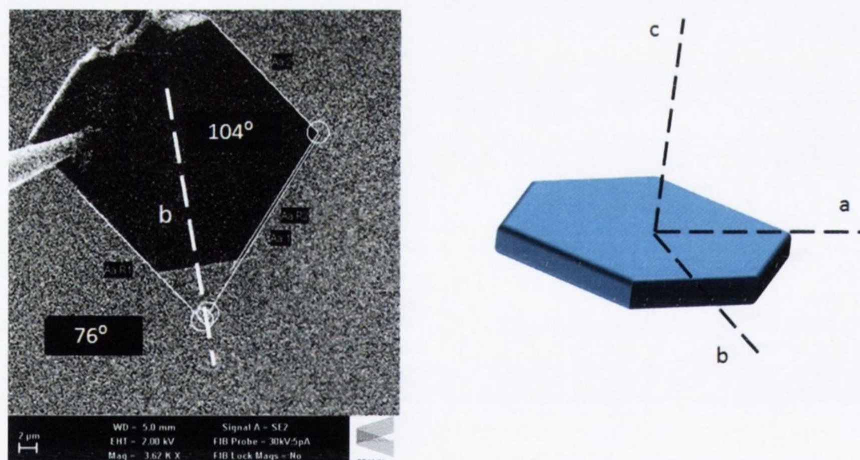

Figure 3.5 *Left: Scanning electron micrograph of a partially broken hexagonal pentacene crystal; the b axis of the unit cell is traced, lying parallel to the top surface. The nano-manipulator tip, used to precisely orientate the crystal during the device preparation, is seen on left side of the SEM image. Right: schematic of a hexagonal crystal and of the three unit cell axes.*

Based on the geometric shape of a single crystal (e.g. a hexagon with precisely defined angles) the *a-b* axis can be precisely traced onto the crystal surface (the preferred cleavage planes can be easily identified) (Figure 3.5).

An EDX elemental analysis on the crystals highlights the fact that the structure, beyond being carbon rich, contains no heavy impurity (Figure 3.6).

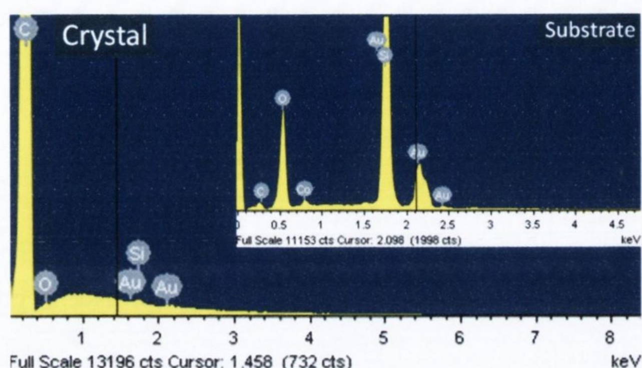

Figure 3.6 *EDX elemental analysis of a pentacene crystal. The structure, very rich in carbon, does not contain any heavy impurity, the Si and Au peaks come from the metallized SiO_2 substrate, as shown in the inset.*

Transport mechanisms in organic crystals

The conventional view is that hole-transport is dominant in organic crystals (Horowitz, 1998) and that the valence band width is of order of 100 meV. The distinction among transporting preferentially holes or electrons does not always rely on the actual values of charge mobilities, but reflects the ease of charge injection from the electrodes. Thus a material is often referred as a hole/electron transporter when its ionization energy/electron affinity matches the Fermi level of the electrode material (Coropceanu, 2007).

In the absence of defects, the charge migration mechanism in an inorganic material is conventionally determined by the band mechanism: the larger the bandwidth the more delocalized the electronic state, with electron-phonon interactions accounting for the scattering of delocalized carriers. We recall that a phonon is a particle-like quantized mode of vibrational energy, coming from the collective oscillations of atoms within the crystal.

As outlined in Chapter1, in the case of organic crystals the nature of charge transport depends strongly on the interplay between electronic and electron-vibration (phonon) interactions. Here the intermolecular forces (Van der Waals) are much weaker than covalent and ionic bonds typical of inorganic materials and the resulting solids are less rigid. In such conditions a propagating charge carrier is able to locally distort its host material; therefore an excess charge combines with the accompanying lattice deformation

induced by its charge, modulating the site energy and providing the possibility for electron trapping. Phonons not only play the role of a perturbation, but the local electron-vibration coupling can be treated as a quasi-particle called a small polaron, which is an electronic charge dressed by a phonon cloud. Therefore a charge carrier localized on a single lattice site has a stabilization energy, which results from the deformations in molecular and lattice geometries, referred to as the polaron binding energy.

The transport mechanism can be understood by comparing the bandwidth of the charge carrier within the crystal with its polaron binding energy. If the electron/hole bandwidth becomes smaller or comparable to the polaron binding energy then excess charges are self-trapped and need thermal activation to migrate from molecule to molecule by a hopping mechanism; the limit size of the trapped small polaron is the lattice constant (Holstein, 1959). The polaron binding energy in pentacene is experimentally estimated to be of order of 200 meV (Brown, 1997).

In band theory the presence of electronic overlap gives rise to transitions in which an electron tunnels to a neighboring site, leading to the formation of Bloch-type bands. In a Wan der Waals crystal the weak coupling results in a narrow width for the valence and conduction band. Endres and coworkers (Endres, 2004) calculated the bandwidths for pentacene from first-principles, the widths were found to depend strongly on the crystallographic direction, along the triclinic reciprocal lattice vectors a*, b* and c* they are all smaller than 75 meV and hence clearly smaller than estimates of polaron binding energy. This is likely to lead to a charge transport based on hopping mechanism of the trapped carriers in these directions. Both the hopping of small polarons and the trap and release models have been suggested (see below). The maximal valence and conduction bandwidths are found along the stacking directions (a* + b*) and (a* - b*), with a maximal for electron transport of about 260 meV and of only 145 meV for hole transport (Figure 3.7). Assuming a cross-over between small polaron and band-like transport at a bandwidth of at least 200 meV, band-like electron transport should be possible in the stacking directions in pentacene (Endres, 2004). Along the c* vector, parallel to the molecular axes, the bandwidth is found to be the smallest, resembling the layered crystal structure, which indicates a highly two-dimensional charge transport (Gilles A. de Wijs, 2003).

The multiple trapping and release model, successfully used to describe the conduction in amorphous silicon by (Le Comber, 1970), was suggested in (Horowitz, 1995) to explain the transport in organic oligomers.

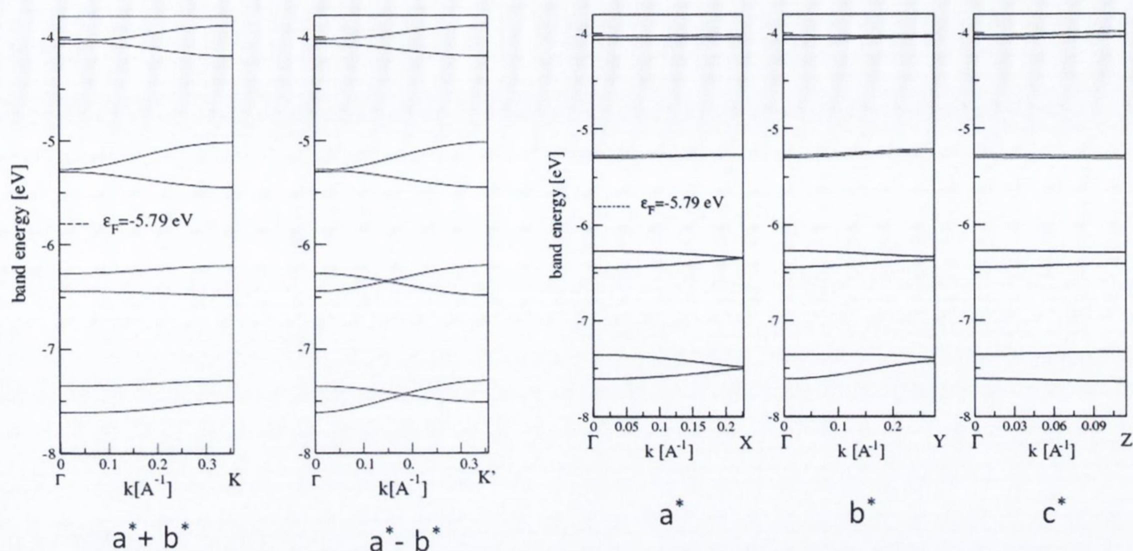

Figure 3.7 *Band structure of pentacene along the stacking directions a^* + b^* and a^* - b^*(from Γ to K and from Γ to K'). In these directions the bandwidths exceed the polaron binding energy and band transport is possible. And along a^*, b^* and c^* (from Γ to X, from Γ to Y and from Γ to Z), here the conduction band shows hardly any dispersion, while a small bandwidth is found for the valence band. From* (Endres, 2004).

In his model a narrow bandwidth is associated with a high concentration of trap levels (lattice defects or impurities) in which the charge carriers are immobilized. This concept was introduced in some more details in Chapter 1. A distribution of localized states is assumed, centered close to the main transport band, extending in the forbidden gap (Figure 3.8) (Lang, 2004). The charges injected, or already present in the organic solid, are trapped into such states with a probability close to one and then released through a thermally activated process.

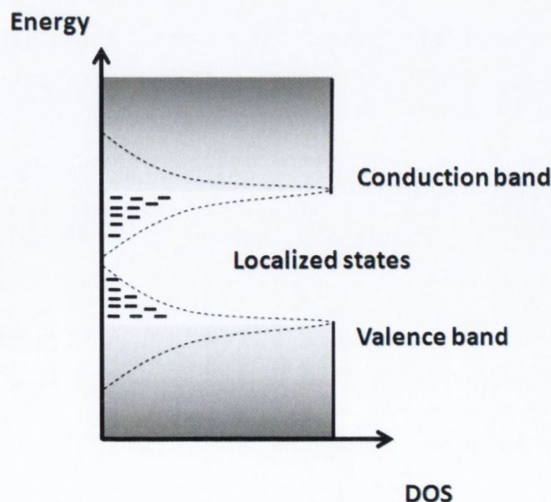

Figure 3.8 *Distribution of localized states centered at the bottom and top of, respectively, the conduction and valence band.*

The drift mobility is trap-controlled via the total time a carrier spends in a localized state; the thermally activated conductivity can be interpreted as a thermal activation of free carrier density (the total density of charges is given by the free plus trapped carriers). With decreasing temperature, the probability of thermal release from a localized state become rapidly smaller, and eventually only hopping near the Fermi level of the trapped electrons to neighboring sites will become the predominant transport mechanism. The transport is then interpreted as phonon assisted hopping between localized states, where the transition rate /activation energy for polarons will depend on the intermolecular reorganization energy.

In conclusion, both charge hopping and temperature "independent" band transport should be obtained depending on the crystal orientation, the latter provided that holes are efficiently injected into the material. Nelson et al. (Nelson, 1998) observed that the variation of the field-effect mobility with temperature can differ from sample to sample, from thermally activated to temperature-independent behavior, for thermal evaporated pentacene films.

We recapitulate that transport is determined by the band mechanism and that the bandwidths reflect the coupling between molecules in neighboring unit cells; the larger the bandwidth the more delocalized the electronic states. If the bandwidth becomes small and comparable to the polaron binding energy characteristic of the material, then excess charges are self-trapped and need thermal activation to migrate by a hopping mechanism (small polaron hopping or trap and release model, at different temperature ranges). Band-like transport should be obtained along the crystal directions in which the bandwidth exceeds the polaron binding energy for a specific carrier (electrons or holes), provided the required carrier can be efficiently injected from the electrodes material into the organic.

Fabrication of short-channel devices

To investigate electrical and magneto-transport in high-quality pentacene crystals we have fabricated short channel OFETs with spin-polarized electrodes. Figure 3.1 showed a schematic diagram of the bottom-contact organic transistor.

The elementary device geometry to detect spin transport is a two terminal spin valve in which a non-magnetic medium is contacted by two ferromagnetic electrodes. The devices

were prepared on a heavily doped Si wafer with a thermally grown SiO_2 layer whose thickness was 200 nm. A contact to the substrate allowed for a gate voltage to control the charge density in the organic crystal. By means of UV lithography we deposited a Ti/Au microscale contact platform, which provided large area contacts to connect the final nanoscale device to the acquisition system. The SiO_2 surface was chemically modified with a self-assembled monolayer of hexamethyldisilazane (HMDS) to prevent water adsorption on the dielectric surface thereby enhancing field-effect mobility (Hamadani, 2007) (Chua, 2005).

Using electron beam lithography and a lift-off technique, Ti/NiFe source-drain electrodes were patterned on the substrate. A bottom Ti layer of 3-5 nm was employed to promote the adhesion of the ferromagnetic layer to the underlying SiO_2 surface. The NiFe alloy was chosen as an adequate contacting material due to the relatively slow oxidation rate of nickel (Salou, 2008); which would increase the probability of having a clean contact interface since the electrodes would be shortly exposed to air during the fabrication process. The electrodes were deposited by e-beam evaporation from a $Ni_{80}Fe_{20}$ source material (permalloy).

The electrode design consisted of a set of interdigitated contacts; 16 pairs of electrodes, with spacing about 90 nm and alternating electrode widths of 200 and 400 nm (Figure 3.9), in order providing magnetic shape anisotropy.

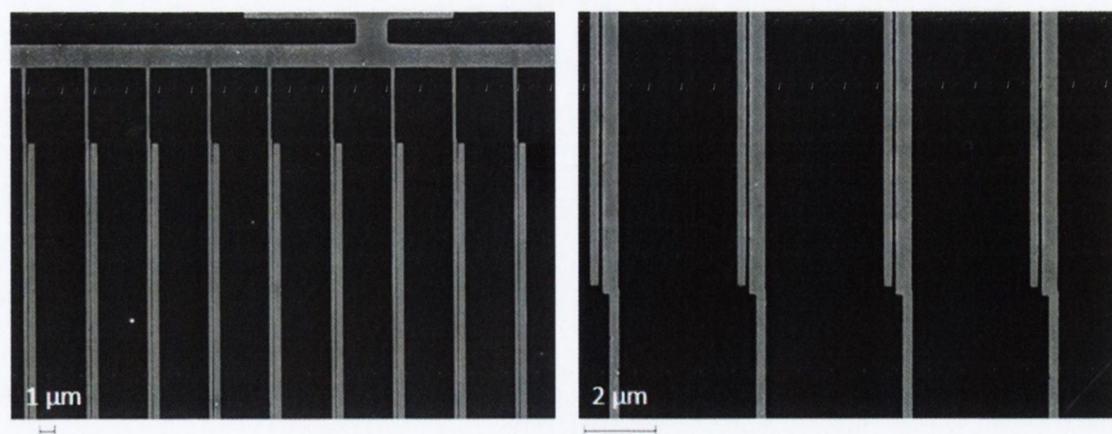

Figure 3.9 *SEM micrographs of a set of interdigitated electrodes. Each pair of electrodes consists of two contacts of different width, as highlighted on the right side of the figure, of 200 and 400 nm, separated by a gap of 90 nm. Each electrode is 60 µm long.*

Each pair is spaced 4 µm apart with respect to the neighboring one. The electric field lines in the interdigitated electrodes run perpendicular to the electrodes axis, and fringing can be neglected (Mas-Torrent, 2004). For this geometry, since the width of the electrodes and the length of the gap are known, it is easy to calculate the mobility and extract useful

parameters. In order to get electrodes with small gaps, we largely optimized the lithographic process modifying the e-beam exposure by means of proximity effect corrections. Conventionally, it is not possible to fabricate interdigitated electrodes with very small spacing and consequently point electrodes are normally preferred. However, the electric field pattern is more complex and the ratio between the channel width and length (W/L) is largely diminished in the point contact configuration. Therefore we opted to design an interdigitated geometry in which W was maximized to maintain W/L >> 10. We emphasize that organic materials are characterized by low mobility, so by maximizing the section of the active channel the resistance of the device can be significantly reduced and the signal-to-noise ratio enhanced, increasing the probability of observing any magneto-resistive effect, even if it is tiny. Using our fabrication adjustments it was possible to regulate the channel length (spacing between the electrodes) down to 90 nm over a channel width exceeding 60 μm (about 1 mm for the whole interdigitated geometry). By using the same optimizing techniques for the e-beam lithography, point electrodes spaced by only 7 nm were also achieved (Figure 3.10). Our devices were made as a part of testing the ultimate limit in size reduction of organic FETs.

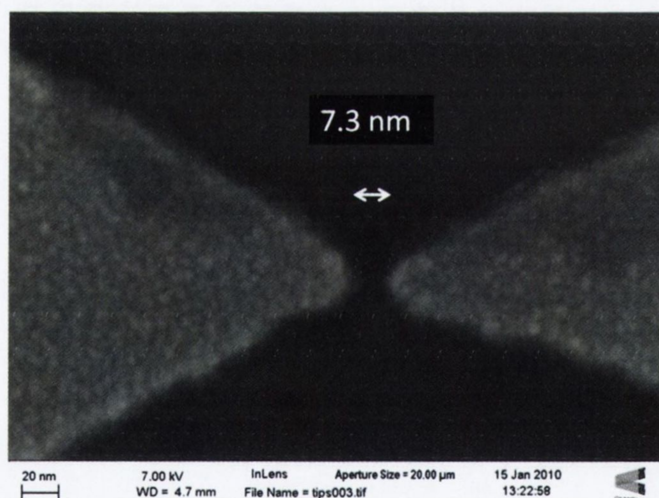

Figure 3.10 *Point electrodes of CoFe separated by about 7.3 nm, prepared by e-beam lithography and lift-off.*

We prepared NiFe electrodes with alternating widths of 200 and 400 nm , their coercive fields depend on their width (due to shape anisotropy, and are expected to be around just a few mT for this alloy), to provide independent switching of the two contacts for spin valve functioning. If the spacing between both contacts is shorter than the spin flip length, then the interface of the second ferromagnet can act as a spin detector, exhibiting either low or high resistance (spinvalve effect) for magnetization parallel or antiparallel to the first

magnet, when spin injection and transport efficiently occur.

Next in the fabrication process, pentacene single crystals were identified by scanning electron microscopy and suitable sized crystals (about 30 μm wide and a few μm thick) could be in situ placed onto the existing FET platform. As anticipated in Chapter 2, a piezo-manipulator was mounted inside the vacuum chamber and remotely controlled, allowing precise manipulation of the micron-sized objects on the sample surface while viewing via the SEM. As shown in Figure 3.11 A, a crystal was first approached with the tungsten tip of the manipulator; once in gentle contact, SiO_2 straps were deposited by decomposing siloxane precursor gases under the electron beam, to solder the tip to the crystal and being able to precisely move it. The precursor gas was injected only close to the sample surface via needle valves remotely positioned near the top of the sample, where the electron beam is focused, for depositing well defined wires by scanning the beam over a desired line (in-situ e-beam assisted chemical vapor deposition). The crystal was moved toward the patterned sample and placed across the nanoscale gap to electrically bridge the electrodes, typically positioned so the current path was along a stacking direction (in between the *a* and *b* axis), where the electronic overlap is stronger (Figure 3.11 B). The pentacene crystal electrostatically binds to the clean metal surface, by Van der Waals forces. The crystal was further pressed with the tip against the substrate to enhance electrical contact and held in position by additional SiO_2 wires deposited on the edges to secure it across the gap (Figure 3.11 C). This ensured that a direct and intimate contact was made between the organic material and the electrodes, besides limiting the movement of the crystal when measured at high voltage or at low temperature in vacuum cavity. The atomic flatness of the crystal surface ensured reasonable contacts in most cases. Figure 3.12 shows an example of final devices with different shaped organic crystals used to bridge the gaps of the interdigitated electrodes; at times more than one crystal was secured onto the platform, to cover most of the contact area (Figure 3.11 D).

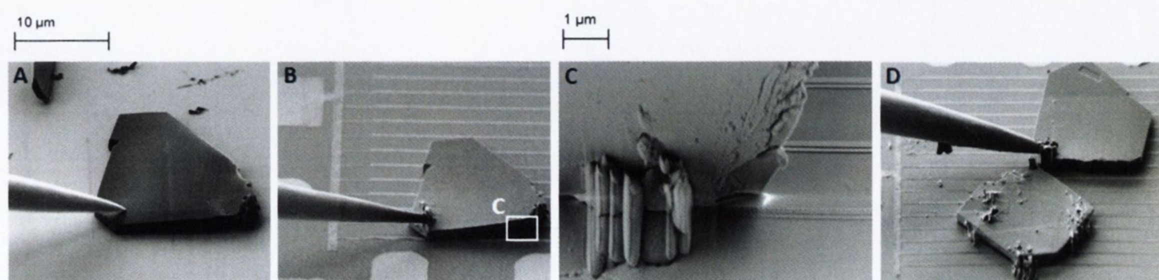

Figure 3.11 *The schematics of the fabrication of single crystal pentacene FET are shown. A crystal is placed on the patterned substrate by mean of a piezo-manipulator mounted inside the FIB vacuum chamber and remotely controlled; in situ chemical vapor deposition (CVD) allowed securing the micron objects.*

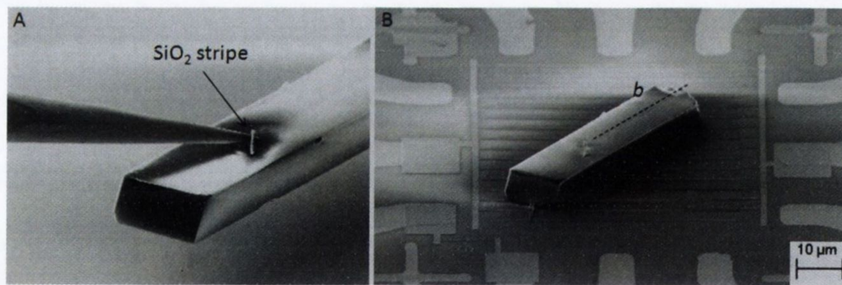

Figure 3.12 *Scanning electron micrographs of organic single crystal FET.*

High-impedance electrical characterization

Electrical characteristics were measured in a Quantum Design Physical Properties Measuring System (PPMS) by making use of tri-axial leads for high impedance measurements, femto-Ampere source-meters (Keithly 6430) and low noise pre-amplifiers. The setup was capable of measuring resistance largely exceeding 100 GΩ. The magnetic field could be applied in plane with respect to the device surface.

To initiate the investigation of electronic transport through single-crystal devices, current vs. voltage curves were acquired with a maximum bias of 15 V. The bias was limited to this upper value due to concerns about overheating the crystal.

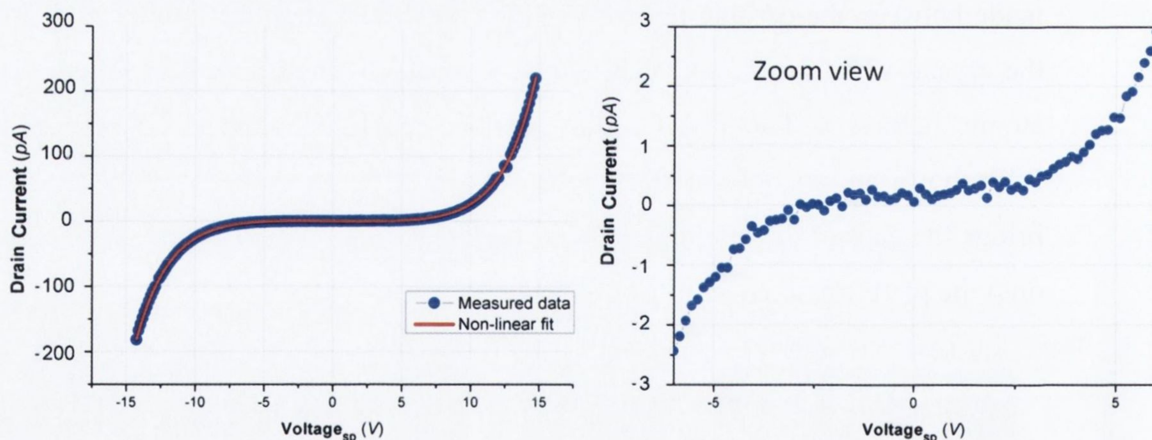

Figure 3.13 *I:V characteristic of the device at room temperature; on the right hand side is shown the zoom view around the origin, to reveal the potential activation barrier.*

The symmetric curve displayed in Figure 3.13 shows a strong non-linear response in the low bias regime, this illustrates the fact that the injection of carriers into the organic

channel is being inhibited by an energy barrier at the interface. At the lowest bias the crystals may appear insulating, but the current rises exponentially at increasing voltages above a threshold. The transport mechanism appears to be tunneling through an interface barrier. As the bias increases the bulk transport properties are reflected in the slower rate of increase of the current, as the curve straightens approaching a more linear curse.

The measured curve resembles the electronic properties of a pair of tunneling diodes connected to the access resistors of an FET, as in Figure 3.14. Given the barrier shape, the expression of the tunneling current is obtained by the product of the carrier charge q, the velocity v_R, density of carriers n and tunneling probability Θ; as $J_n = qnv_r\Theta$. The velocity equals the Richardson velocity, the velocity with which on average the carriers approach the barrier $v_R = \sqrt{\frac{k_B T}{2\pi m_c^*}}$, where m_c^* is the effective mass. For a rectangular or triangular barrier ϕ_b the current was shown in Chapter 1 to be given by:

$$J_n = qv_R N_c exp\left(-\frac{4}{3}\frac{\sqrt{2m_c^*}}{\hbar}\sqrt{q\phi_b x_d}\right)\left[exp\left(\frac{qV_a}{kT}\right)-1\right]$$

The tunneling current shows explicit temperature dependence only in the applied voltage dependent part of its equation; hence for low biases it is often approximated as temperature independent. The term $\propto \sqrt{T}$ from v_R is also typically neglected.

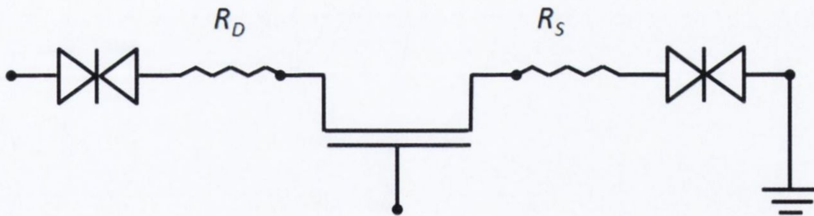

Figure 3.14 *Equivalent circuit of an FET including nonlinear source and drain contact resistances.*

Attempts to fit the curves were successful by using an expression accounting for initial non-linear voltage drops at the tunneling contacts $V_{t|D}$ and $V_{t|S}$, the subscripts D and S stand for drain and source, followed by a constant voltage drop adjacent to the source-drain contacts V_D and V_S, and dissipation across the pentacene channel, which was

assumed to be intrinsically ohmic, with resistance R_{Ch}. A system of equation can be defined to describe the physical picture:

$$\begin{cases} V = V_{t|D} + V_D + V_{Ch} + V_S + V_{t|S} \\ V_{t|D} = \phi_D ln\left(\frac{I - I_{off}}{A_D}\right) - \phi_D ln\left(\frac{I_{off}}{A_D}\right) \\ V_{Ch} = (I - I_{off})R_{Ch} \\ V_{t|S} = \phi_S ln\left(\frac{-I + I_{off}}{A_S}\right) - \phi_S ln\left(\frac{I_{off}}{A_S}\right) \end{cases}$$

Here the first equation includes the fact that the whole voltage drop across the device is given by the aforementioned terms; the second and the fourth express the nonlinear dependence of the current on the applied bias in tunneling contacts, A_D and A_S are the effective contact area, ϕ_D and ϕ_S the barrier activation voltage scale [for reasons of simplicity hereafter just referred to as barrier height, despite the fact that it may and often does depend in magnitude on the barrier width, as well as on the presence of additional transport (current limiting) mechanisms], and I_{off} a current offset. Expressing the equation in the *V:I* form is convenient, as the equations describing the two contact regions are solvable in terms of the individual voltage drops, and the equation for the overall potential drop across the structure is a simple linear summation. The same physical model is equally well describable in terms of current; however, the mathematical formulation is rather heavy and can involve special functions and /or integral forms, that are not readily available in common data processing and fitting packages, such as Origin™. This system can be combined in an equation to be used for the fitting process, as:

$$V = \begin{cases} V_D + IR_{Ch} + \phi_D ln\left[\frac{A_D + I + A_D\left(e^{-\frac{V_D}{\phi_D}} - 1\right)}{A_D}\right] - \phi_D ln\left[\frac{A_D + A_D\left(e^{-\frac{V_D}{\phi_D}} - 1\right)}{A_D}\right] & if\ I > 0 \\ V_S - IR_{Ch} + \phi_S ln\left[\frac{A_S - I + A_S\left(e^{-\frac{V_S}{\phi_S}} - 1\right)}{A_S}\right] - \phi_S ln\left[\frac{A_S + A_S\left(e^{-\frac{V_S}{\phi_S}} - 1\right)}{A_S}\right] & if\ I < 0 \\ 0\ otherwise \end{cases}$$

Each contact was permitted to have a different barrier height $\phi_{D|S}$, active area $A_{D|S}$ and constant voltage drop $V_{D|S}$. The extracted barrier activation voltage, similar on both sides, is about 1.6 V. The resistance of the active channel in pentacene amounts to about 3.5 GΩ,

and about 1.5 volts drop symmetrically at the two contact areas of the device. The voltage drop $V_{D|S}$ at the contacts, in fact, resembles the initial nonlinear contribution of thermoionic emission over the barrier, which adds in parallel to the dominant tunneling contribution. These two terms could be in principle separated, but it would require a greatly complicated system of model equations. Hence, it is convenient simply to add a contact voltage offset; in fact the thermoionic emission shifts toward higher bias the turn on voltage of the tunneling diode, when the two mechanisms occur in parallel. This point will be discussed later, when studying the temperature dependence of the device characteristics.

In this device a thin native oxide layer is present on the surface of the NiFe electrode. The existence of this physical barrier between the crystal and the electrodes can result in weakening the coupling between the two materials, increasing the contact resistance. The oxide layer, along with the mismatch of the work function of metal and pentacene, give rise to the interface barrier which limits the injection of carriers at low biases.

The bottom gate geometry employed in our device enables the investigation of charge transport within an induced electric field. The pentacene FET has been characterized in the literature as p type in nature (Butko, 2003). In Figure 3.15 are shown the transistor characteristics of the device at room temperature. The observed response to a local electric field exhibits the general behavior of a hole transporting system: the drain current is enhanced by negative gate biases.

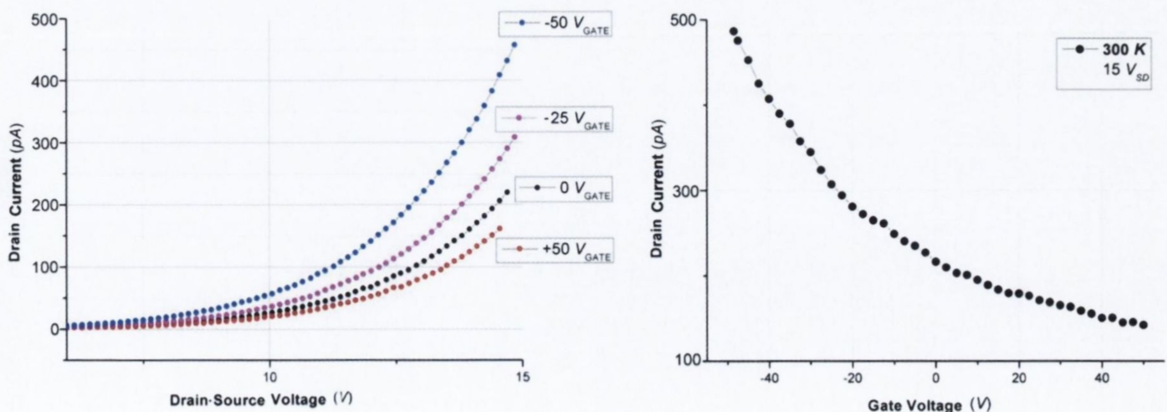

Figure 3.15 *Left: FET characteristics at different gate voltages at 300 K. Right: output characteristic at constant source-drain voltage of V_{SD}= 15 V.*

The application of a gate voltage enhances the conductivity through the device, as it can be clearly seen by scanning the gate voltage at constant source-drain bias (Figure 3.15 right).

The gate leakage current in the fully processed device was lower than 1 pA even at the highest fields, which demonstrated that the dielectric had successfully supported the whole transistor processing.

One can note that the characteristics do not show current saturation. In previous works, short channel organic FETs have been reported to suffer from high space-charge limited current (SCLC) (Collet, 2000), caused by the application of a high source-drain electric field which degraded transistor characteristics, leading to curves without saturation (Takeshi Hirose, 2010). SCLC corresponds to the current obtained when the number of injected charges reaches a maximum because their electrostatic potential prevents the injection of additional charges. In this instance the charge density is not uniform across the material and is largest close to the injecting electrodes. In this work we did not observe clear SCLC behavior ($J \propto V^2$), and we attribute the absence of saturation to the fact that these devices are largely contact dominated, therefore the saturation of the active channel cannot be seen, as it is masked by contacts. One can obtain some information about the direct effect of the gate field on the channel resistance by extrapolating the channel resistance from a family of *I:V* curves recorded at different gate biases, at that point plotting the extracted values versus the applied gate biases, as in Figure 3.16.

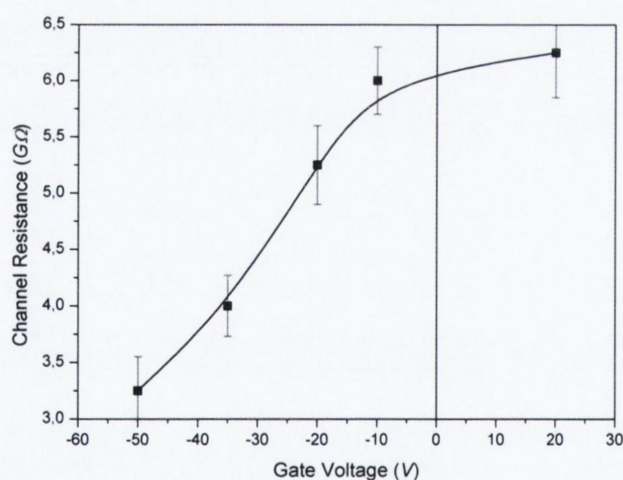

Figure 3.16 *Plot of the channel resistance vs. the applied gate voltage; the values of the resistance are extrapolated from the I:V characteristics recorded at 300 K.*

As it can be noted the effect of the gate voltage on the conductivity of the channel is not very pronounced, hence it does not show clear saturation even at highest gate voltages applied in this work. This is probably due to the fact that the organic crystal is not in direct contact with the dielectric surface, because of the device geometry there is an empty layer

between them corresponding to the electrodes' thickness (about 20 nm), and the threshold was not reached. Even though this geometry is not efficient for gating purposes, it is actually optimal for investigating spin injection; any spurious effect is prevented as the injection truly occurs at a well-defined ferromagnet /organic interface.

It is reasonable to think that the application of the gate voltage reflects on the shape of the injecting barriers; actually reducing their thickness. When applying a large negative gate voltage the alteration of the barrier thickness allows for the injection of more carriers via tunneling. The enhancement of the drain current at increasing gate voltages is then due to the combined effect of enhanced channel conductivity and thinner injecting barriers through which carriers can tunnel more easily.

In Figure 3.17 the results of the low temperature study is shown.

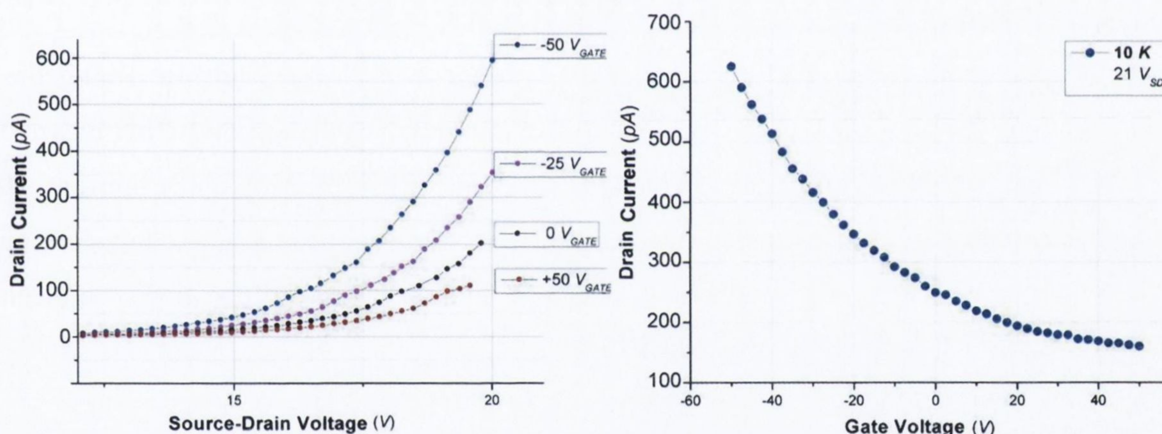

Figure 3.17 *Left: FET characteristics at different gate voltages at 10 K. Right: FET characteristics at constant source-drain voltages,* V_{SD}*= 21 V.*

The gate effect is similar, and it shows comparable quantitative enhancement of the drain current. However at decreasing temperature, the contribution of the contact resistance largely increases and the extraction of meaningful values of channel resistances becomes impractical, because the overall contribution is negligible, at least at the drain voltages examined in this work. Short-channel devices seem not be the best candidate for studying the transport mechanism in pentacene (typically detected by observing the temperature and field dependence), because contacts dominate more and more the overall device resistance at decreasing temperature, masking the channel effects. This is observable in Figure 3.18. Here a family of *I:V* curves measured at the highest negative gate bias voltage are illustrated at temperatures from 10 K to 300 K at 50 K increments.

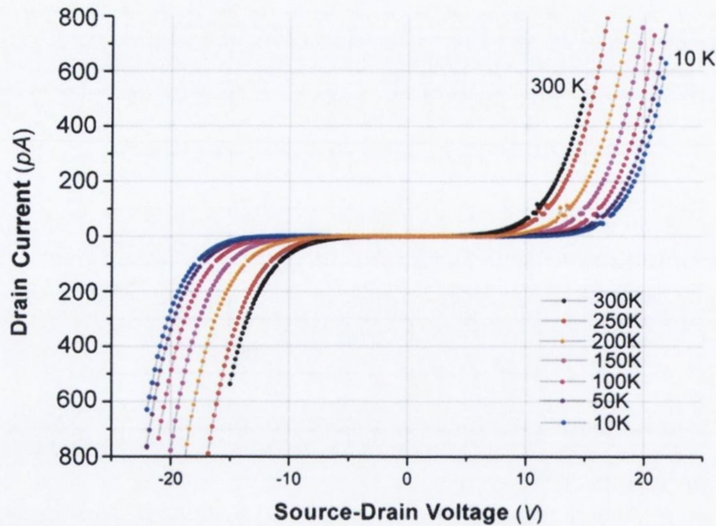

Figure 3.18 *I:V curves at different temperature, from 10 K to 300K, at -50V applied gate. Resistance is plotted as a function of temperature, for different source-drain bias.*

No explicit temperature dependence appears in the expression describing the tunneling current across a barrier. To account for the observed shift toward higher biases of the turn-on voltage of the *I:V* characteristics (the voltage at which the current starts being efficiently injected inside the semiconductor), we propose a new equivalent circuit. This model consists of a tunneling contact in parallel to a Schottky diode, connected to each terminal of the FET (Figure 3.19).

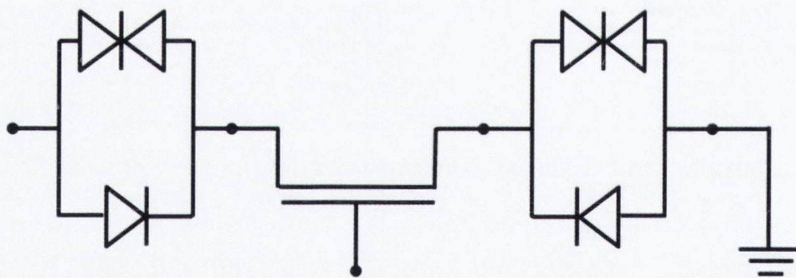

Figure 3.19 *Equivalent circuit consisting of a tunneling contact in parallel to a Schottky diode, at each terminal access of the FET.*

Our device cannot be modeled simply by two back-to-back Schottky diodes because, in that case, one would always be in reverse bias, hence saturating and limiting the current to low values. We, instead, observe an exponential increase, typically attributable to tunneling. The question arising is: where is the temperature dependence of the curves (and

the temperature dependence of the voltage drop at the interface) coming from? To answer this question we need to consider that, in general terms, carriers can be injected both across and above an energy barrier, respectively via tunneling and via thermally activation (excitation); the two mechanisms typically contributing to a different extent. Strong temperature dependence is characteristic of thermoionic emission over the barrier. It is evident that our curves shift toward larger bias at the lowering of temperature: indicating that thermal excitation plays a significant role. The circuit of Figure 3.19 includes the fact that injection can occur in parallel via these two principal mechanisms through the contacts. For each applied voltage, one Schottky diode will be found in reverse bias, hence limiting the overall current flowing in the device. Current can be injected efficiently via the competing mechanism of tunneling only at high enough voltages. Therefore, at low biases, the reverse Schottky diode is shorting the pair of parallel contacts, absorbing all the current, but giving a very weak voltage drop (due to its non-linear characteristic, see Chapter 1). When the Schottky diode reaches saturation, the current can start flowing through the tunneling contact (as per the increased differential resistance of the Schottky component), and an exponential increase of the current is expected. The saturation voltage of the Schottky diodes depends exponentially on the temperature, and it is larger for lower temperature. This explains why the *I:V* curves of Figure 3.18 essentially shift toward higher biases.

The further temperature dependence comes from the change in resistance of the active channel; the term IR_{Ch} in this device is masked, at low temperature, by the contact effects, but will be recollected and extracted in Chapter 4, for conductive polymer devices.

A quantitative treatment of the data with this modeled circuit is, however, not possible with our *I:V* curves. The complexity of the extended model system (6 non-linear equations) would not allow extracting meaningful fitting parameters from just a family of close-to-exponential curves. Hence the simpler circuit of Figure 3.14, consisting of tunneling contacts and access resistors, was used. Here the temperature dependence was attributed to the resistors in the effective circuit, with no concern or discrimination of the physical origin of the mechanisms. This allows the extraction of the activation potential barrier, around 1.7 V for NiFe /pentacene interface, and, in the next Chapter, of the channel resistance over a large temperature range, from the simpler system of 4 equations.

Resistance has been measured as a function of magnetic field up to 100 mT, which ensure the reversal of the magnetization in the NiFe electrodes. Following the information obtained by measuring the electrical characteristics of the device, voltages were applied at

the gate and source-drain contacts that could maximize the current flowing in the device without overheating the crystal. At no temperature, between 10 and 300 K, was any significant magneto-resistance observed (Figure 3.20).

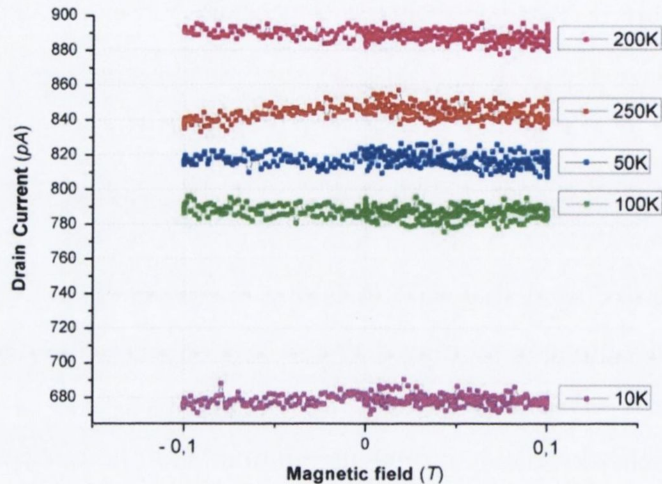

Figure 3.20 *Plot of current vs. magnetic field at temperatures 10-300 K.*

Conclusions

We consider the problem of spin diffusion in small molecules organic semiconductors. We have observed no spin valve effect in our devices, so the question is whether this is due to an intrinsic very short spin diffusion length in the crystal or because spin injection and detection at the metal-organic interface do not occur efficiently. In recent work by a former colleague (Burke, 2010) (Burke, 2011) a magneto-resistive effect observed in hybrid NiFe-rubrene-NiFe devices was fully attributable to weak localization, suggesting that electrons could travel distances in excess of 100 nm inside the crystal without spin flip scattering, as it would destroy the phase memory required for weak localization. It followed that the phonon-assisted transport (band-like or hopping) does not involve spin flip over relatively long distances. Considerations for rubrene should (at least qualitatively) apply to pentacene. It seems that the problem is within the ferromagnet-organic interface, where the spin information is lost. Effective spin injection and detection depend on optimizing this interface. In their work Burke et al. attempted introducing a thin Al_2O_3 barrier between Co

ferromagnetic electrodes and the conduction channel. The presence of a thin oxide layer should create a spin-dependent tunnel barrier through which carriers can pass with conservation of spin direction. Further, it chemically de-couples the organic material from the 3-d metal, preventing formation of interfacial states. However their attempt proved unsuccessful and no spin injection-detection was observed; the introduction of an artificial barrier of Al_2O_3 simply increased the energy barrier for injected carriers. This, on contrary, suggests that there exist other intrinsic mechanisms that might depolarize the spin current during hole transport in oligoacene crystals.

These two opposite deductions do not allow drawing a conclusion, hence further investigation was required. Following their studies, we minimized the channel length as to approach the localization length and employed the same $Ni_{80}Fe_{20}$ as contact material (consisting in the only single crystal-lateral structure reported to show magneto-resistance). By the application of a gate electrode we enhanced the conductivity, therefore raising the signal to noise ratio, but yet no spin valve effect was observed at any temperature.

Spin injection in organics from metals has not been reported in any lateral device, regardless of the kind of barrier observed (transparent contacts leading to linear *I:V* characteristics or Schottky /tunneling type to non-linear curves). Here we confirm the absence of spin signal in NiFe /pentacene samples where the main injection mechanism consisted in tunneling across an interface potential barrier.

Appendix A: Amorphous thin films of Alq_3

We constructed and tested organic FETs with ferromagnetic source and drain in which the semi-conductive channel consisted in a thin film of evaporated organic material. The thin films have been deposited by thermal evaporation onto patterned substrates in a purpose-built UHV chamber described in Chapter 2, with a base pressure in the regime of 10^{-10} Torr. The organic source material was placed in an alumina crucible wrapped by tungsten wire, and heated up to sublimation point. Temperature was monitored and maintained constant throughout deposition via a feedback controller, which gave very smooth and uniform amorphous films. By using an argon ion gun, it was possible to etch the first few atomic layers of the electrodes prior to deposit the organic, hence removing any undesired surface contamination. Here we briefly report the measurements coming from a lateral field effect transistor with cobalt source and drain contacts capped with 2 nm Al_2O_3, acting as a tunnel barrier, and tris(8-hydroxyquinolinato)aluminum (Alq_3) semiconducting material as the conductive channel, with a thickness typically around 100 nm. Figure 3.21 shows an *I:V* characteristic taken at room temperature, with no applied gate bias. The curve is asymmetric and, beyond revealing that the film is highly resistive, it is also quite noisy (especially compared to the single crystal OFET), with a current excursion of about ± 2.5 pA around an average value at given bias. This characteristic is a typical feature of transport through insulators and should not surprise (i.e. it is a property of the channel material rather than of the device geometry), as it actually confirms the occurrence of injection and diffusive transport within the film.

The gate voltage was swept very slowly from -20 V to +20 V at constant a source-drain voltage of -5 V (Figure 3.22); the field effect on the drain current was hysteretic and only slightly reproducible, we believe because of the presence of latent charges being trapped into the naturally occurring morphologic defects of an amorphous film. In this case, the electric field induced by the gate voltage is strongly modified by the presence of extra charges adjacent to the conductive channel. The frequency at which such a device can be measure is related to the releasing time of the trapped charges from the localized states; the latency time necessary for the drain current to stabilize was of order 2.4 seconds per 100 mV change on the gate bias. Magneto-transport measurements were performed, but no spin valve effect was detected, neither at room nor low temperature.

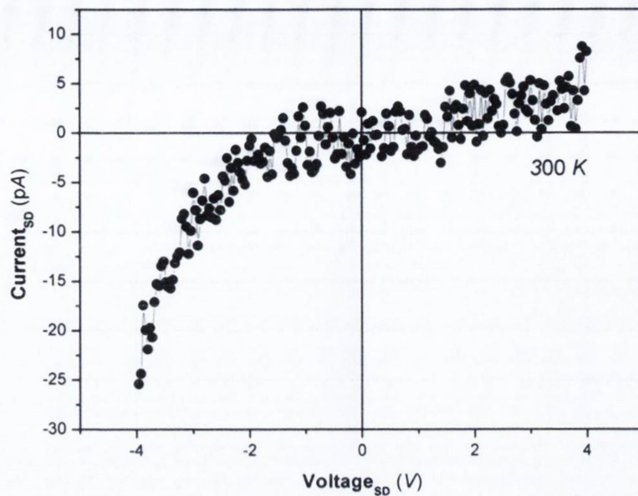

Figure 3.21 *I:V characteristic measured at 300 K, under no gate bias applied.*

Noteworthy, the instability of the transfer characteristics (in which the gate voltage is scanned) cannot be attributed to a voltage fluctuation induced by parasitic gate leakage currents, because such current was constantly monitored and it always displayed values below 1.5 pA (right side of Figure 3.22), even for the highest bias applied, proving a very successful device preparation.

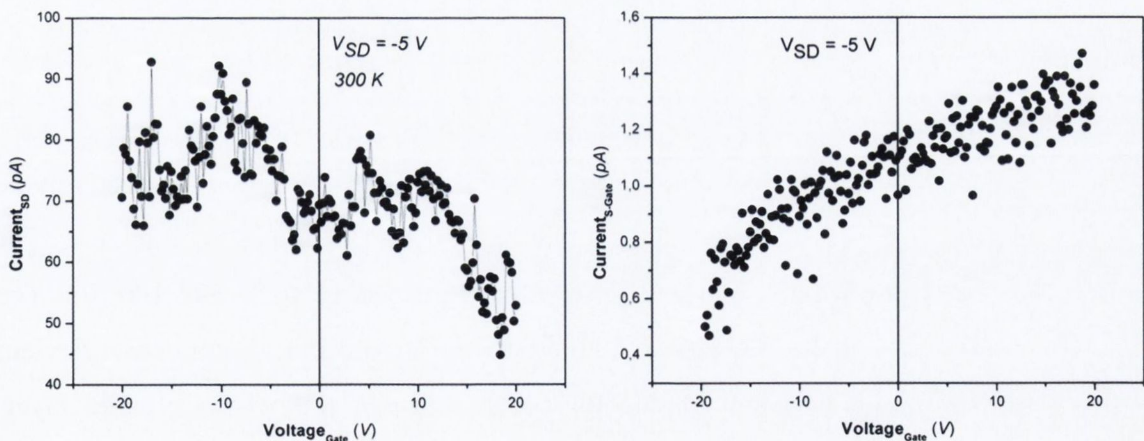

Figure 3.22 *Left: Transfer Characteristic at constant V_{SD}= -5 V, at 300 K; right: leakage current going to gate during the same scan.*

We have fitted the *I:V* curve of Figure 3.21 to an equivalent circuit consisting of a tunneling contact in series to the access resistor of the Alq_3-based FET, at both ends of the device. The junction was permitted to have a different activation voltage, effective area and channel resistance, which was assumed intrinsically ohmic (this allowed deriving an

approximation of the mobility of the film). The fit is shown in Figure 3.23, a *V:I* curve is simpler to fit, because the exponential terms are inversed to logarithmic functions.

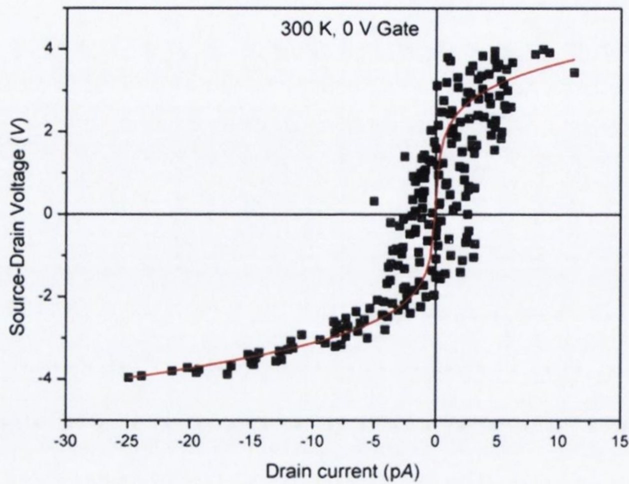

Figure 3.23 *V:I curve at 300 K fitted to two tunneling contacts.*

This analysis allows separating the contribution of the voltage drop due to the contact resistance and to the organic channel. The contribution of the ohmic channel to the whole voltage drop allows estimating the resistivity of the material (Alq_3), separately from the contacts effect

$$\rho = R\frac{S}{L}$$

Where L is the channel length and S the channel cross section, respectively equal to the electrodes gap, ~100 nm, and electrodes width (~1 mm) times the thickness. The thickness of the electrodes and of the organic film is, respectively, 25 and 100 nm. The extracted contribution of the Alq_3 channel amounted to 20 GΩ in our nano-scale device; assuming for simplicity that the conduction occurs through the whole organic layer (different assumptions would not change the estimate significantly), then the resistivity is estimated to be ~$2 \cdot 10^9$ Ω cm. In a typical vertical junction prepared via shadow masking, as often reported in literature, of area 500 μm x 500 μm and thickness 100 nm, we can estimate that the resistance due to the Alq_3 spacer should be around 8 MΩ. The overall resistance of the device should be much higher, as the potential drop at the contacts plays a fundamental role and, typically, several volts are required before observing carrier injection and

revealing the channel transport properties of Alq_3 (Haichuan, 2008). We have observed that the source-drain voltages necessary for beginning to build up a significant current through our device were -2.7 V and +2.0 V, slightly asymmetric for positive and negative biases, due to the asymmetry of the effective contact area, while the contact barrier height was 0.6 eV. We can estimate the mobility, by assuming a carrier concentration of 10^{12} cm^{-2} as in polythiophene, to be around 10^{-5} $cm^2V^{-1}s^{-1}$, which actually agrees with the measurements of (Shun-Wei Liu, 2007).

The investigation performed on Alq_3 based lateral structure triggered the work on single crystal hybrid devices, described in the first part of the chapter, as we wanted to reduce those effects, such as noise and latency, attributable to morphological disorder.

Appendix B: Fabrication of C_{60} single crystal-lateral devices

Carbon nanostructures are known to have unique transport properties (e.g. ballistic transport) (Durkop, 2004); typically they belong to the fullerene structural family, which for example includes carbon nanotubes (Sumio Iijima, 1991) and the C_{60} 'buckyball' molecule (Kroto, 1985). Here we aim at fabricating a two-terminal lateral device consisting in two metal electrodes separated by a nanoscale gap bridged by a single crystal of C_{60} molecules.

A C_{60} fullerene is a molecule composed entirely of carbon, in the form of a sphere. The close packing of C_{60} molecules in a face-centered-cubic crystal fashion results in a relatively high electron mobility (0.1 cm^2 V^{-1} s^{-1}). This made it an attractive material for organic transistors (Dimitrakopoulos, 2002) and over the past several years work has been done mainly with C_{60} thin films that have been incorporated into transistors, diodes and OLEDs (Kobayashi, 2003) (Yohei Ohta, 2008). Most of those films were grown by thermal evaporation. Subsequently nanoscale C_{60} tubes, rods and ribbons have been created using various chemical processes and may be considered for novel applications (Liu, 2002).

We have fabricated high purity single crystals C_{60} rods with uniform sub-micron dimension following the method of (Yizheng Jin, 2006). In detail, a 2 ml solution of 0.3 % wt C_{60} / toluene was slowly dropped with a syringe into 8 ml of IPA at room temperature. The liquid turned immediately brown indicating that the crystals are forming, and a suspension is building up.

The rods are typically 200-800 nm in diameter with a length of 2-10 μm. SEM reveals that each rod has an uniform diameter along the entire length. Small particles of a few tens of nm can sometimes be observed along the rod (Figure 3.24 left); probably being some conglomeration of C_{60} molecules coming from the suspension, but in general the surface is clean (Figure 3.24 right) .

The C_{60} molecules stack in a hexagonal formation along the length of the rod with the tip slightly pointed with a smooth finish. When we crashed a crystallite and observed it via SEM the cross section of the broken crystal showed that the rods are solid, and that the faceted morphology is hexagonal.

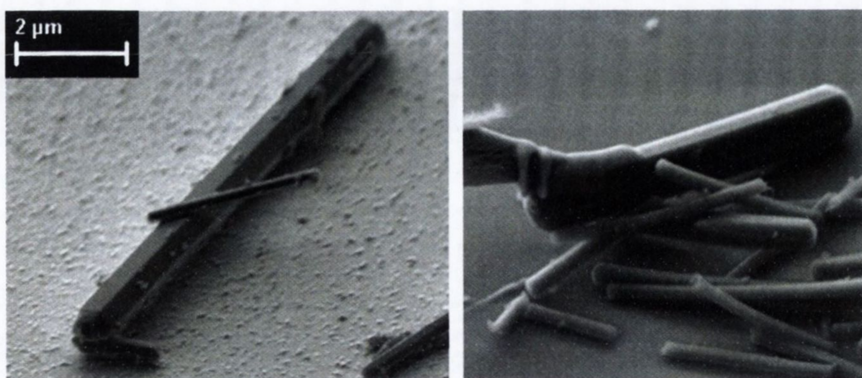

Figure 3.24 *Scanning electron micrograph of sub-micron C_{60} rods.*

The fabrication of lateral C_{60} based structures was achieved by selectively placing the rods on top of a previously patterned pair of electrodes, with a gap around 50 nm. The substrate can in principle be used as a common gate. At first the C_{60} solution was sonicated and a few drops of the suspension that contained the solid product were dropped onto a metallized silicon wafer, and the solvent was allowed to evaporate at room temperature. The bottom metallization facilitates the imaging via the SEM for the next step. The rods were left dispersed all over the chip. SEM was employed to locate rods with a clean surface and the piezo-manipulator was approached and soldered to the crystallite by in situ deposition of SiO_2. Remotely controlling the tungsten tip, the crystallite was located in the desired position, on top of a patterned pair of electrode on a substrate previously loaded inside the SEM chamber, onto the stage. Patterned stripes of SiO_2 secured the micron object across the gap before the tip was removed, either by FIB cutting it or, more advisable to preserve the oxide, by applying a stress to the tiny soldering wires. Figure 3.25 shows the representative steps of device fabrication.

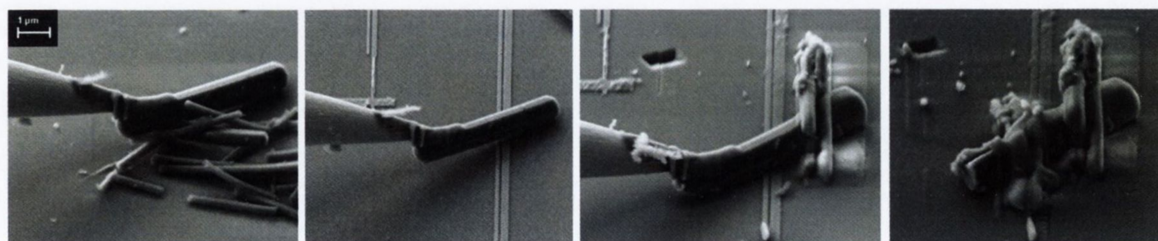

Figure 3.25 *Set of SEM images showing the fabrication steps to place and secure a C_{60} rod on top of pair of electrodes. From the left: the rod is individuated and approached with the tungsten tip of the piezo-manipulator, in situ CVD of a stripe of SiO_2 allows to move the crystallite onto the desired set of electrodes, SiO_2 wires are deposited to hold the rod in position on the substrate, before the tip is FIB cut or, simply, pulled away breaking the tip of the crystallite.*

In the present appendix the method we adopted to prepare a device based on C_{60} sub-micron crystal was illustrated; Figure 3.26 shows a preliminary *I:V* curve obtained at room temperature using a high impedance testing station, with tri-axial leads and a Keithly 6430; for convenience the sample was hooked up and measured in ambient atmosphere. The electrodes consisted in CoFe /Al_2O_3 (2 nm). The bias required to overcome the barrier height and facilitate conduction through this semiconductor is about 2 V. After surpassing the threshold voltage, electronic transport through the crystallite is significantly enhanced.

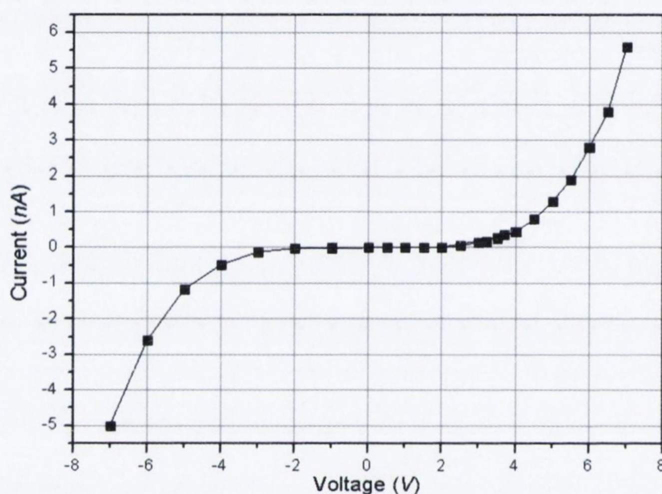

Figure 3.26 *I:V curve of a C_{60} rod between Co/Al_2O_3 electrodes, at room temperature, in air.*

Bibliography

Brown, A. et al. (1997). *Synth. Met., 88*, 37.

Burke, F. (2010). *PhD Thesis Dissertation, Trinity College, Dublin.*

Burke, F. et al. (2011). *Synthetic Metals, 1*, 13332.

Butko, V. et al. (2003). *Applied Physics Letters, 83*, 4773.

Campbell, R. et al. (1961). *Acta Cryst., 14*, 705.

Chua, L. et al. (2005). *Nature, 434*, 194.

Collet, J. et al. (2000). *Applied Physics Letters, 76*, 1941.

Coropceanu, V. et al. (2007). *Chemical Review, 107*, 926.

Dimitrakopoulos, C. et al. (2002). *Adv. Mater., 14*, 99.

Durkop, T. et al. (2004). *J. Phys.: Condens. Matter, 16*, R553.

Endres, R. et al. (2004). *Computational Materials Science, 29*, 362.

Gilles A. de Wijs. et al. (2003). *Synthetic Metals, 139*, 109.

Haichuan, M. et al. (2008). *J. Phys. D: Appl. Phys., 41*, 235109.

Hamadani, B. et al. (2007). *Applied Physics Letters, 91*, 243512.

Holstein, T. (1959). *Ann. Phys., 8*, 343.

Horowitz, G. et al. (1995). *J. Phys. III France, 5*, 355.

Horowitz, G. et al. (1998). *Adv. Mater., 10*, 365.

Jie Qiu, et al. (2007). *Europhysics Letters, 79*, 57004.

Kloc, C. et al. (1997). *Journal of Crystals Growth, 182*, 416.

Kobayashi, S. et al. (2003). *Applied Physics Letters, 82*, 4581.

Kroto, H. W. et al. (1985). *Nature, 318*, 162.

Lang, D. et al. (2004). *Physical Review Letters, 93*, 86802.

Laudise, R. et al. (1998). *Journal of Crystals Growth, 187*, 449.

Le Comber, G. et al. (1970). *Physical Review Letters, 25*, 509.

Lee, J. et al. (2006). *Applied Physics Letters, 88*, 252106.

Liu, H. et al. (2002). *JACS Communications, 124*, 13370.

Mas-Torrent, M. et al. (2004). *Nanotechnology, 15*, S265.

Naber, W. (2007). *Journal of Physics D: Applied Physics, 40*, R205.

Nabok, D. et al. (2007). *Physical Review B, 76*, 235322.

Nelson, S. et al. (1998). *Applied Physics Letters, 72*, 1854.

Parker, I. D. et al. (1994). *Journal of Applied Physics, 3*, 75.

Podzorov, V. et al. (2003). *Applied Physics Letters, 83*, 3504.

Roswitha, Z. et al. (2006). *Chem. Mater., 18*, 244.

Salou, M. et al. (2008). *Surface Science, 602*(17), 2901.

Shun-Wei Liu. et al. (2007). *Applied Physics Letters, 91*, 142106.

Sumio Iijima. et al. (1991). *Nature, 354*, 56.

Sundar, V. et al. (2004). *Science, 303*, 1644.

Takeshi Hirose, et al. (2010). *Applied Physics Letters, 97*, 83301.

Tomohiko Kudo, et al. (1998). *Japanese Journal of Applied Physics, 37*, L999.

Torsi, L. et al. (2005). *Analytical Chemistry*, 381A.

Xiong, Z. H. et al. (2004). *Nature, 427*, 821.

Yizheng Jin. et al. (2006). *J. Mater. Chem., 16*, 3715.

Yohei Ohta. et al. (2008). *Applied Physics Letters, 92*, 173306.

Chapter 4

Short-channel field-effect transistors based on polytiophene with ferromagnetic electrodes

Introduction

Research into solution-processible organic electronics has been a vibrant field of research over the last three decades. Many studies have focused on the realization of devices made with conjugated polymers due to the availability of simple deposition techniques to process these materials. While not destined to replace silicon-based technologies, they promise the advent of fully flexible devices for logic circuits, matrix displays and photovoltaic cells.

A common trait of polymer based-devices is that their performances critically depend on the efficiency with which charge carriers move within the conjugated material. A π-conjugated polymer is a carbon-based macromolecule in the shape of a chain, through which the valence π-electrons are partially delocalized. Due to the geometric structure, polymer chains are quasi-one dimensional systems, characterized by weak inter-molecule electron transfer interaction. Consequently the charge transport between polymer chains is relatively slow.

Research efforts have been devoted to the development of high mobility polymers. Maximum mobilities of order 0.1 $cm^2V^{-1}s^{-1}$ are found in thin films of polythiophene derivatives having enhanced inter-chain ordering (Yong-Young Noh, 2009). This is about 4 orders of magnitude smaller than crystalline silicon, but similar to amorphous silicon. The low mobilities will naturally lead to low frequency electronics.

A focus of recent years has been to incorporate organic semiconductors into spin-based electronics. The weak spin-orbit and hyperfine interactions in these materials leads in principle to the possibility of preserving spin coherence over times and distances much longer than in metals or inorganic semiconductors, which would address one of the major challenges of modern spin-electronics. Numerous studies have been made using small organic molecules, such as Alq_3, in vertical spin valve structures (Xiong, 2004) (Santos, 2007) (Dediu, 2008). The majority of them reports a wide variety of magneto-resistance values and spin coherence lengths, and reaches conflicting conclusions (Jang, 2008). Only a few spin transport studies with high molecular weight polymers are reported (Morley, 2008) (Majumdar, 2009); magneto-resistance was observed at low temperature in thick P3HT based spin valves. In all instances it is still unclear whether the observed effects were based on giant magneto-resistance or tunneling, because intermixing and pinhole formation during metal deposition on top of the delicate organic layer can reduce the effective layer thickness down to a few nm (Vinzelberg, 2008). Studies on lateral structures avoid the possible side effect of pinhole formation and provide the ideal platform for studying spin injection in novel materials. Here we describe the fabrication of lateral spin valve structures with a layer of conjugated polymer cast in the narrow gap between two ferromagnetic electrodes. A gate terminal underneath the semiconductor allowed us to enhance the electrical conductivity of the organic channel (Figure 4.1). The magnetic and electric properties of the device will be described.

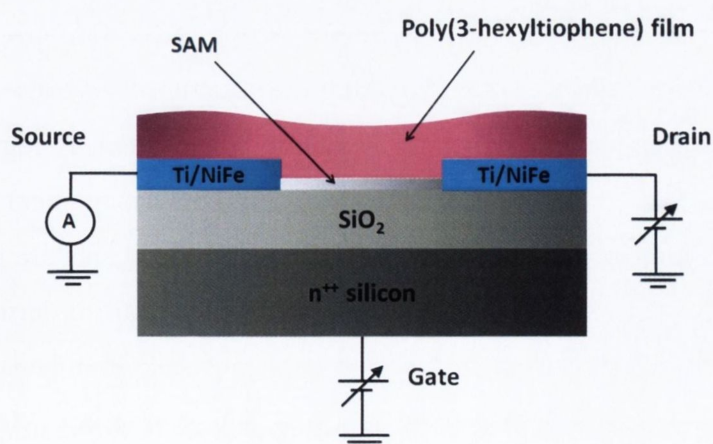

Figure 4.1 *Schematics of a polymer based FET, with NiFe electrodes and a self-assembled monolayer (SAM) between the dielectric and the organic semiconductor.*

Conjugated polythiophene derivatives

In organic chemistry the term "conjugated" refers to an alternation of double and single bonds linking a sequence of atoms. A backbone of sequentially-bonded carbon atoms and conjugated aromatic cycles is referred to as a conjugated-polymer. The peculiarity is given by the π-electrons from the double bonds, which overlap at some extent along the whole chain.

Polythiophene derivatives are an important representative class of conjugated polymers, with non-linear optical response, environment stability and relatively high carrier mobility. The first chemical preparation of polythiophene, consisting of a backbone of bound thiophene rings, was reported in the 1980 (Yamamoto, 1980) (Figure 4.2 A). After that, research has focused on manipulating the configuration of this macromolecule, as to enhance both conduction and mechanical stability (McCullough, 1998).

In the quest for a soluble and processable conjugated polymer, polythiophene was modified by attaching solubilizing long side chains to the skeleton of thiophene rings (Jen, 1985). The resulting molecule, poly-alkythiophene, reflecting the properties of the alkyl side chains, was soluble in all common organic solvents (chloroform, toluene, xylene etc…) (Figure 4.2 B). Casting and spin-coating from any of the aforementioned solvents allowed for the deposition of thin polymer films.

As visible in Figure 4.2 C alkythiophene is not a symmetric molecule. There are two relative orientations when two thiophene rings are coupled to form the polymer. Namely head to head and head to tail, indicating the relative orientation of the side groups. When the two configurations are irregularly distributed along the structure they cause a random twist of the skeleton. Such a disordered pattern is normally indicated as regio-random polythiophene (Figure 4.2 D). On the other hand, when only one arrangement is present along the whole polymer (indicated as regio-regular), the alkyl side chains are symmetric and the molecules have planar conformation with enhanced inter-chain ordering (Figure 4.2 E). The structure controlled synthesis of regio-regular poly-alkythiophene was first reported in 1992 (McCullough, 1992); due to the supra-molecular ordering (McCullough, 1993) thin films of these polymers were observed to possess a greatly enhanced electro-conductivity (Sirringhaus, 1998). The polymer poly-(3-hexylthiophene) (P3HT) has one of the highest regio-regularity (Goedel, 1992), with over 99% head to tail linkages, and will be the focus of this study.

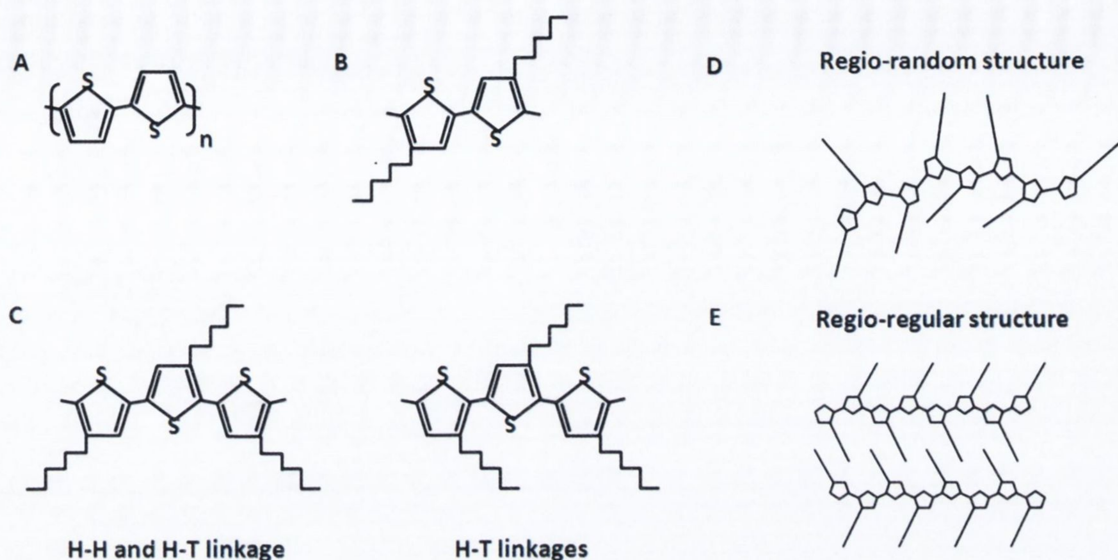

Figure 4.2 *A: Chemical structure of polythiophene; B: Representation of poly-alkythiophene with the solubilizing alkyl side chains; C: Possible regio-chemical couplings of the alkyl-thiophene molecules, the orientation refers to the relative position of the side groups, head to head (H-H) and head to tail (H-T); D: twisted molecule of regio-random polymer; E: Side view of two chains self-assembled in an ordered structure, as confirmed by X-ray studies.*

The casting of regio-regular polymer thin-films normally results in complex microstructures in which ordered "crystalline" domains are embedded in an amorphous matrix. As mentioned, the head to tail linkage favors the planarity of the chains, which look almost like rigid rods (rather than twisted strings). The intermolecular interaction among long linear molecules leads the chains to self-organize them into ordered structures, which constitute the crystalline domains (Figure 4.3 left). X-ray diffraction showed that P3HT has a lamellar structure made up of stacked planar molecules, and that between neighboring lamellas the side chains are arranged in an interdigitated geometry (Northrup, 2007) (Figure 4.3 right, see also Figure 1.25). The size of the ordered region containing the lamellas is of order 10 nm (Sirringhaus, 1999).

Disordered regions between grains are apparent in AFM images (Zhao, 2004), and are made up of amorphous material. About 5-10% of the total material is in the grain boundaries, representing the disordered fraction (Street, 2005). Further, the size of the crystalline lamellas and inter-grain regions was observed to differ from solvent to solvent, with different degrees of film discontinuity, which may occur depending on the solubility of the polymer in the solvent (Bao, 1996) (Mas-Torrent, 2004).

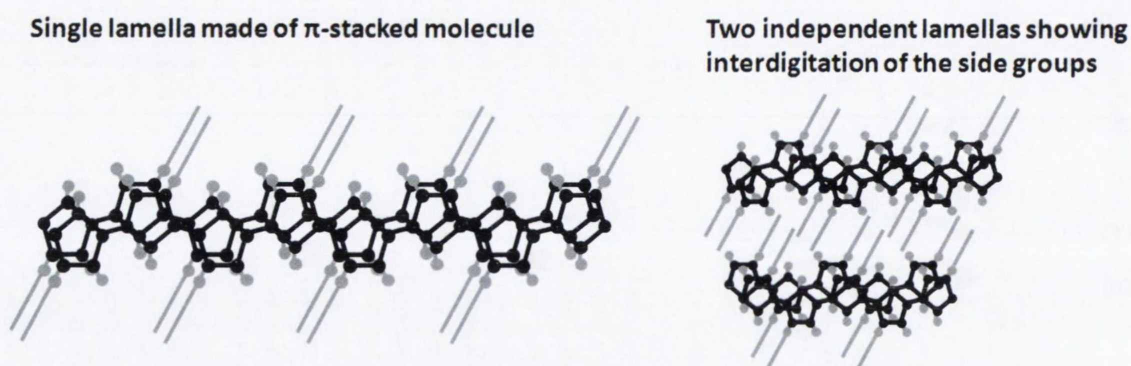

Figure 4.3 *Left: Illustration of the structure of a lamella of regio-regular poly-(3-hexylthiophene). For simplicity it is shown the ordering of only two adjacent chains; it is evident that the thiophene rings face each other, within a single sheet of molecules. Right: Two independent lamellas having interdigitation of the side groups. The delocalization of the carriers occurs within a single lamella, giving a two dimensional character to the transport.*

Because the transport, in regio-random conjugated polymers, is usually limited by the hopping between disordered polymers chains, higher mobilities are found in regio-regular polythiophene thin films, relating to structural ordering induced by the substituted symmetric thiophene rings. Thiophene rings of different molecules are parallel within a lamella, in a π-stacking fashion (DeLongchamp, 2007) (Figure 4.3 left). This allows the delocalization of the carriers between neighboring chains, because the orbitals partially overlap among face to face rings, and gives a two-dimensional character to the charge transport within the polymer.

The mobility in the stacking direction, within a lamella, was calculated to be 31 $cm^2V^{-1}s^{-1}$ in a perfectly organized crystal of P3HT (Northrup, 2007). In polycrystalline thin films, such as those typically employed in field effect transistors, the effective mobility is about 0.1 $cm^2V^{-1}s^{-1}$ for the same material (Sirringhaus, 1998).

Intuitively, the requirement of transport at the edges of the crystalline grain, through disordered regions, reduces the mobility in relation to the value estimated for a perfect crystal.

It is interesting to note that, by using regioregular poly(3-hexylthiophene), about a decade ago the feasibility of prototypes of all-polymer based integrated optoelectronic devices was demonstrated. For instance, a polymer field effect transistor was used to drive a small molecule (Dodabalapur, 1998) and polymer (Sirringhaus, 1998) based organic-light emitting diode.

Transport mechanisms in conjugated polymers

In general terms, the transport characteristics of a semiconductor are strongly dependent on the degree of order of the molecules within the material. In an ideal crystal the peculiar features are the long-range order and the strong coupling among the atoms. These conditions normally result in the formation of energy bands delocalized over the entire structure and separated by a forbidden energy gap. Any extra charge added to the semiconductor moves in these energy bands with a large mean free path, with phonons accounting for the scattering of electrons in delocalized states. Any loss in the periodicity of the lattice can cause a partial localization of the electronic wave functions, and the appearance of tail states extending from the edges of the valence and conduction bands into the forbidden gap. In the limiting case of a totally amorphous structure, due to the disorder of the molecular sites, the concept of band conduction by free charges may not apply. Instead, the formation of localized states is favored and the mean free path is largely reduced, down to about the molecular spacing. In order to participate in the transport, the charge carriers must hop between these localized states, which usually leads to very low carrier mobility.

In the case of a regio-random conjugated polymer, the structure is not completely amorphous. There is a short-range order which reflects the anisotropy of molecular interactions. Molecules tend to pack within a unit cell order but the periodicity is interrupted by the presence of twisted and kinked polymer chains. Due to the variable conjugation length the structure cannot simply have two delocalized energy bands separated by a forbidden gap. And neither can it have an isotropic distribution of localized states. Instead an energetic spread of the transport sites will be present, often approximated by a Gaussian distribution of the HOMO and LUMO levels, due to the random disorder in the material (Bassler, 1982) (Figure 4.4).

The disorder in the material is measured by the standard deviation (Gaussian width) of the energy distribution of the localized states. With increasing disorder the tail of the distribution increasingly extends into the energy gap. The localized states are accommodated along the kinked molecules and charge carriers hop between them (Bassler, 1993).

It is conventionally recognized that charge carriers are stored in localized polaron-like states in conjugated molecules. Spectroscopic studies and molecular-orbital calculations of

the polythiophenes provided detailed information about the change in electronic state and molecular geometry when a positive charge is added to a molecule. The extra charge is confined among adjacent thiophene rings, along the carbon skeleton, and induces a detectable change in the bond length, relative to the neutral form.

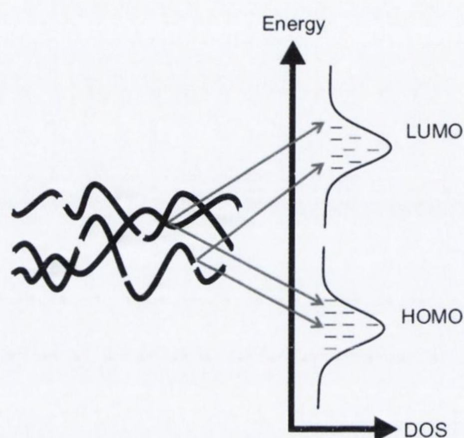

Figure 4.4 *Left: Schematic view of polymer chain segments broken by defects, kinks and twists between which the charge carriers hop. Right: Representation of the energy distribution of the localized states approximated by a Gaussian distribution for the LUMO and HOMO levels.*

Such modification is the result of the migration of the double bond: the single-double bond alternation is re-arranged along a large fraction of the molecule as a response to the presence of an extra charge (Tanaka, 1994) (Hotta, 1991) (Figure 4.5).

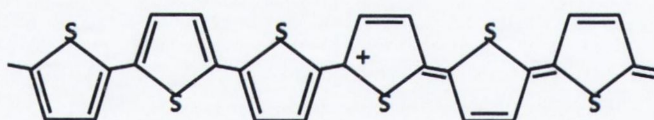

Figure 4.5 *Radical cation (polaron) formed by the removing of 1 electron (a hole is marked with +) on the 4th thiophene ring of a polythiophene chain; the re-arrangement of the bond alternation is shown.*

These structural and electronic characteristics reflect the nature of the polaron, in which the confinement of an extra charge is accompanied by the molecular lattice distortion (the migration of the bond alternation causes a stretch of the structure, as the single and double bond have different lengths). The structure of the charged form of the thiophene molecule may be referred to as molecular polaron (Holstein, 1959). A charge localized on a conjugated molecule has a stabilization energy which results from the deformations in

molecular geometries, referred to as polaron binding energy. In other words, the ground state and the polaron state (in which the bond alternation is mitigated) are non-degenerate. The systematic modulation of the molecular length influences the charge transport. The charge carriers, generated within a polythiophene thin film, are self-trapped as polarons, as a consequence of the induced stabilization energy. The polaron is trapped in an energy well, which separates it from the other sites (as in Figure 1.20). The charge transfer occurs via thermally activated hopping of the polaron, between individual localized states in the Gaussian distribution (Waragai, 1995). A carrier is initially excited at random within the distribution of sites and relaxes energetically in course of its hopping motion. The transport path is determined by a competition between an increasing density of localized states, which favors a high hopping rate, and the decreasing occupancy of the states. In disordered polymers the conduction is dominated by hopping and it exhibits low mobility, about 10^{-5} $cm^2V^{-1}s^{-1}$ (Tsumura, 1986). The temperature dependence of the mobility has been observed to follow a behavior of the form $\propto \exp -(T_0/T)^2$ (Bassler, 1982), or a simpler Arrhenius relation $\propto \exp(-W/KT)$ in systems where the polaron binding energy is the dominant limitation (hence W is an activation energy which reflects the polaron binding energy) (Waragai, 1995).

By enhancing the control over the structure during the chemical synthesis of polythiophene derivatives, it has been possible to produce polymers exhibiting a more ordered arrangement (Chen, 1995). The effect on the electrical characteristics is that ordered regions favor the formation of band-like states beside the disorder induced localized states. Charge transport can be described by a thermal activation process in which charges are trapped and released, from localized states, to a mobility edge at which carriers are no longer localized and significantly more mobile. This view assumes that there is a defined energy (the mobility edge) in the density of states that separates mobile and localized levels (Figure 1.23). Above the mobility edge the current is transported by extended bands, below which there is a tail of sites with much lower mobility. Trapped carriers in the band tail become temporarily mobile by thermal excitation (Figure 1.24). Intuitively, the extended bands are the result of relatively long conjugation length and of the partially ordered stack of adjacent molecules, promoted by symmetric alkyl side chains. This description was originally developed for describing the transport mechanism in high quality amorphous silicon (Shur, 1989), and it is applicable to polarons in partially ordered conjugated polymers (Sirringhaus, 1998) and organic oligomers (Horowitz, 1995).

Here the charge carriers are polarons and the transport occurs via activation from localized polaron states to a certain transport level. The co-existence of localized and extended polaron states is the underlying reason to the enhancement of the room temperature mobility, around 10^{-2} $cm^2V^{-1}s^{-1}$, that was observed in thin films of these polymers (Bao, 1996).

Hopping directly between trapped carriers is a competing transport mechanism, even though transport through thermal excitation to mobile states is the dominating mechanism at room temperature. At sufficiently high temperature, indeed, most of the carriers are by default promoted into the conductive band and the mobility is high as charges drift into the extended states. During the transit they interact with localized states near the band edge, through trapping and thermal release. The conduction, or the drift mobility, typically follows the behavior of a thermal activated process, of the form:

$$\sigma = \sigma_0 \, \alpha \, \exp(-W/KT)$$

Or, similarly:

$$\mu = \mu_0 \, \alpha \, \exp(-W/KT)$$

In which μ_0 is the mobility near the edge of the band and α reflects the distribution of localized states. The activation energy W, typically around 100 meV in P3HT (Sirringhaus, 1999), can tell us that the localized states in P3HT, at thermal equilibrium during transit, extend to about 0.1 eV below the mobility edge. The predominant part of the distribution lies in this range. *W* is expected to be determined by a combination of the polaron binding energy and the degree of disorder of the material (which determines how much the band tails extend into the gap). Many measurements of transport in ordered polymers observed a change in the activation energy in the temperature range below 200 K, with the lower temperature region having smaller activation energy and smaller pre-factor (Kapoor, 2002). This change is believed to occur because with decreasing temperature the probability of thermal release from a localized state becomes rapidly smaller, and eventually hopping of trapped charges between neighboring localized site will become the dominant transport mechanism (carriers can only be promoted in region below the mobility edge). Trapped states lye in the tail of the distribution within the gap, at this stage the hopping activation energy only reflects the polaron binding energy; typically between 50 and 100 meV in polymers (Sirringhaus, 1998). The variation in the dominant exponential dependence at changing temperature reflects the distribution of localized

states. The temperature at which the change of the transport mechanism occurs depends on the energy gap and the band-tail slope. In the prototypical system of amorphous silicon a third region was also observed (Figure 1.22). At very low temperature, the number of carriers thermally excited into the band tail (between the mobility edge and the energy of the lowest lying state) becomes considerably smaller, and the transfer is by hopping near the Fermi energy only (Le Comber, 1970). According to Mott (Mott, 1969) this should lead to variable range hopping with a temperature dependence of the form $\sigma \sim exp(-W/T^{1/4})$.

Over the past decade or so the mobility of polymer thin films has been further increased, to around 1 $cm^2V^{-1}s^{-1}$ by (McCulloch, 2006) (Salleo, 2004) and 10 $cm^2V^{-1}s^{-1}$ by (Sokolov, 2011). The dominant cause of the increase is the improvement in structural order, induced by the high regio-regularity of the synthetized molecules and the preparation of the substrate prior to deposit the film. Here, all the units have on-purpose synthetized symmetric side chains, to promote the self-assembling of the polymer molecules in a crystalline fashion. Intuitively, increased size of the crystalline grain and reduced amount of amorphous material may result in lower density of localized states, which favors band-like transport over hopping, provided that the intrinsic bandwidth is large enough.

Therefore, in these highly ordered polymers, the key aspect of transport is the coexistence of nano-crystalline regions with tiny grain boundaries. Crystallite sizes in P3HT spun on chemically modified substrates are about 20 nm (Grevin, 2003), and for the newly designed polythiophene derivatives can assemble into larger domains. For instance poly-thieno[3,2-*b*]thiophene (PBTTT) is reported to exhibit domain size around 200 nm (McCulloch, 2006) on crystallization from a liquid-crystal phase. In both cases, the width of the disordered regions in the boundary is about 0.5 to 1 nm (the lower limit being the size of a thiophene ring, nearly 0.5 nm).

The π-stacking of the thiophene rings allows hole delocalization within a lamellar sheet (DeLongchamp, 2007). Due to the long alkyl chains, attached to the sides of the molecular backbone, each sheet is widely spaced from the next (1.2 to 3.0 nm) and the electron interaction between neighboring lamellas is almost eliminated. This makes the transport effectively two-dimensional.

To understand more about the hole delocalization, calculations of the atomic and electronic structure for ideal crystalline sheets of polythiophene were performed by (Northrup, 2007). He implemented first-principle density functional calculations, employing the experimentally-determined lattice constant (the stacking distance between chains to as 3.8

Å) and he found that the hole bandwidth in the stacking direction is 0.62 eV, and 1.90 eV along the polymer chain axis. The conduction band, for electron transport, is a factor of three smaller. Experiments of optical absorption on ordered and disorder structure of this polymer showed that the band gap is 0.5 eV smaller in regio-regular material than in the amorphous samples (corresponding to the relative shift of the optical absorption peaks) (Brown P. J., 2003). The origin of this effect is that order-induced delocalization increases the bandwidths and hence reduces the gap. The reduction of the gap comes in larger part from the shift of the valence band edge of 0.3-0.4 eV between ordered and amorphous material, and in minor part from the shift of the conduction band.

The difference in the energy gap among the crystalline regions and the boundaries has important consequences in determining the transport mechanism near the edge of a lamella. Here the band gap increases and the band edge bends across the boundary in a way that confines holes in the lamella (Figure 4.6). Therefore there is an energy barrier to transfer holes into the disordered region because of the different energies of the band edges.

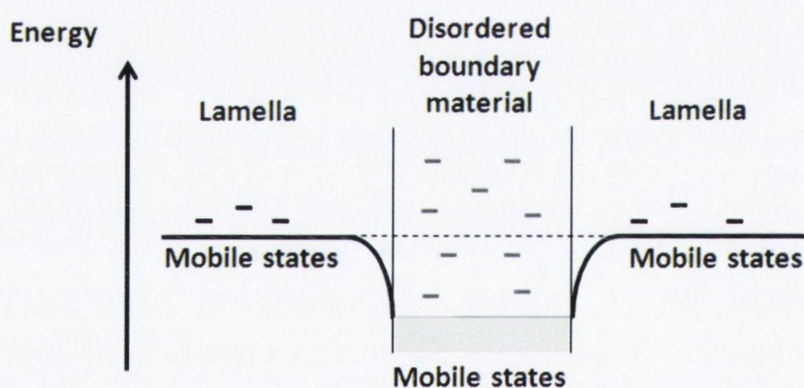

Figure 4.6 *Schematic illustration of how the valence bands of ordered lamellas and disordered grain boundaries line up to give a barrier to holes transfer between lamellas. As in* (Street, 2005).

The crystalline lamellas are randomly oriented, and at the end of each grain some of the chains extend from the ordered region into the boundary. It is expected that the end-to-end structures, those in which the angle between two consecutive lamellas is low with respect to the chain orientation, will exhibit some grain-to-grain interpenetration of the chains, beside the disorder of the boundary (Figure 4.7).

The electronic properties of the borders depend primarily on the relative orientations of the crystallite. Large angle borders have a more disordered structure and a higher density of localized states (naturally associated with bent chains). Where there are polymers chains connecting adjacent lamellas, as it is the case for end-to-end structures with small bond angles, transport across the boundary is relatively easy. Therefore long-range transport is favored across those boundaries where the angle is smallest.

Low angle boundary　　　Large angle boundary

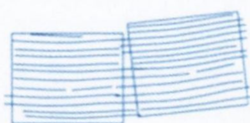

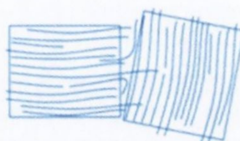

Figure 4.7 *Illustration of possible grain boundary structures for small-angle (left) and large-angle (right) orientations. The large-angle boundary has more disorder. Each line here represents a polymer chain, aligned to the neighboring chain within a lamella, indicated by a square.*

Where there is no low-angle grain boundary connecting the lamellas, transport becomes difficult because holes must tunnel across the barrier and fall into deep trap states coming from the wide band tail of the disordered area. At low temperature tunneling is the only possible mechanism, while at room temperature there can be thermal activation over the barrier into higher energy states of the disordered region. Inter-grains transport is therefore directional, favoring transfer between lamellas at the same orientation, at least at low temperature. In a polycrystalline film, conduction occurs where there is a complete conduction path, through low-angle boundaries, which forms a high-mobility percolation path. Hence carrier transfer is not isotropic, but is dominated by the few paths with higher mobility (Figure 4.8).

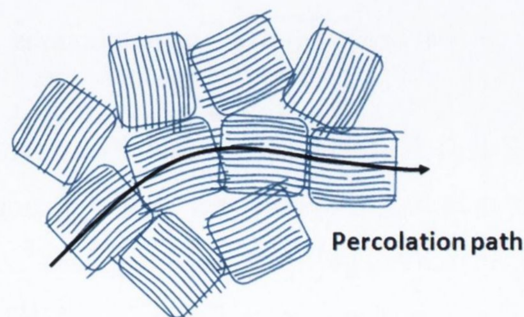

Figure 4.8 *It is shown a transport path along a preferential direction with low-angle grain boundaries, which form a high-mobility percolation path. As in* (Street, 2005).

At low temperature the ordered regions are isolated by the energy barriers at the boundaries and there may be only a few high-mobility percolation paths, through adjacent lamellas having the same orientation.

At sufficiently high temperature, carriers can be promoted by thermal activation over the energy barrier for transport across high-angle boundaries, then the conduction in disordered region is enhanced, and more percolation paths become active. At high temperature the barriers between the lamellas do not considerably limit the transport. Therefore the conductivity can increase with temperature faster than in an isotropic conductive medium.

The percolation mechanism qualitatively explains the enhanced room temperature mobility and the underlying reason for the increase in the mobility when an alignment layer is present underneath the polymer (Sirringhaus, 2000), as more high mobility transport paths are accessible.

Measurements have shown that the polaron energies are substantially different in disordered and ordered poly(3-hexylthiophene) (Brown P. J., 2003). There is a large polaron binding energy in the regio-random polymer, of 0.3 eV, but a tiny energy amounting to only 0.05 eV for the ordered material. The reduction is attributable to hole delocalization, because the polaron energy is sensitive to the localization of the wave function. Therefore polarons play a fundamental role in determining the mobility in amorphous material, by increasing the effective mass, but they are less important in the case of ordered structure.

The transport within an ordered lamella is through extended delocalized states, within bands which are similar from grain to grain. The band edges are well defined, with a narrow distribution of localized states coming from the boundaries, which can in principle trap the carriers.

In a perfect polymer crystal, overlooking the minor contribution coming from the polaron states, the mobility is determined by the scattering from acoustic phonons and it is proportional to the scattering length.

In P3HT an upper limit to the mobility of free carriers in a lamella was estimated by Northrup (Northrup, 2007) employing the acoustic deformation potential model (Karl, 1991). The estimated hole mobility in the π-stacking direction was 31 $cm^2V^{-1}s^{-1}$.

So far, the maximum mobility achieved in thin films of this material (P3HT) did not exceed 0.1 $cm^2V^{-1}s^{-1}$. The conduction in the polycrystalline material is limited by the size of the crystalline region, the transfer across grain boundaries and the long-range

connectivity of the structure. Therefore the mobility achievable in thin film devices is much lower than the estimate for a perfect crystal. Even within a crystalline lamella we can expect the mobility to be smaller than the Northrup estimate, due to possible rotations and distortions of the chains, which reduce the scattering length, and to the presence of polarons. The actual free carrier mobility within the ordered regions of P3HT was estimated by fitting experimental data to be ~ 4 $cm^2V^{-1}s^{-1}$ (Salleo, 2004).

In inorganic covalent semiconductors the mobility is much larger, up to 10^4 $cm^2V^{-1}s^{-1}$. The explanation of this great difference relies on the smaller elastic modulus and the narrow bandwidth due to the weak Van der Waals nature of the inter-chain bonds. The mobility is proportional to the elastic modulus and to the bandwidth and therefore it is unlikely that organic semiconductors can have conductivities comparable to those for the much harder inorganic materials.

Organic FETs operation

Organic field-effect transistors primarily operate in accumulation mode, in contrast to the usual inversion mode of silicon MOSFETs. In the ideal case, the source and drain contacts should behave as ohmic contacts for the majority carrier type of the organic semiconductor. P-type polymer semiconductors (as polyacetylene, polyphenylene and polythiophene) have estimated ionization potentials in the range of 4.4 to 5.4 eV (Bredas, 1983); about 4.7 eV for P3HT (extracted from low-energy photoelectron spectroscopy by (Nakanishi, 1999)). Thus metals such as gold (5.3 eV), cobalt (5 eV), iron (4.8 eV), and nickel (5.0 eV) have been thought to function well as ohmic contacts, due to the similarity of their work function (in brackets) to the aforementioned potentials. In truth, this assumption in unjustified without first examining the output characteristics at low temperature. This is because band offset is hidden by thermal excitation of carriers at high enough temperature and, importantly, it is not the only possible origin of a contact barrier.

As anticipated in Chapter 1, short channel field effect transistors tend to enhance the effects of contact resistances on the output characteristics because the channel resistance is relatively low. Hence, in this work, we will need to extract the conductivity by fitting the *I:V* to a more complete model taking into account the nonlinear contact effect. Nonetheless, in the majority of experimental studies on OFETs the electrical device

characteristics have been estimated using the approximation of ohmic contact resistance, e.g. in (Brown A. , 1997) (Chabinyc, 2004), acceptable for large (microscale) devices at high enough temperature. Here we will briefly review this approach, as it is actually useful to get an insight inside the operation of an OFET. The most widely used model is usually referred to as the gradual channel model, explained in (Shur, 1989). Below we show how the values for the conductivity and mobility are extracted for a p-type semiconductor following this approach.

When a small drain bias is first applied to the transistor, then the source-drain current is small and ohmic, corresponding to the conductivity of the film, σ.

$$\sigma = \left(\frac{L}{Zt}\right)\frac{I_{sd}}{V_d}\bigg|_{V_g=0, V_d\to 0}$$

Where Z is the channel width, L is the channel length and t is the thickness of the semiconductor. As a good experimental approximation for this limit, conductivities can be determined at a drain bias of - 1 V and a gate bias of 0.

If a negative bias is then applied to the gate terminal the voltage is dropped over the insulator and over the semiconductor near the dielectric-organic interface, giving rise to band bending in the semiconductor, the accumulation region. The additional positive charge accumulated in this region is supplied by the ohmic source and drain contacts. If the insulator has a capacitance per unit area C_{ins} then the accumulated charge per unit area is simply $V_g \cdot C_{ins}$, assuming that a negligibly small voltage is dropped across the semiconductor. An equivalent amount of compensating negative charge is stored on the gate at the gate-insulator interface. The semiconductor now contains positive charges both from the 'field effect', which created the accumulation layer, and from doping (given that the samples are handled at some stage in air, at least when hooking them up at the measurements setup, some redox doping with oxygen is to be expected).

If the latter charges are mobile and not trapped, then when a small bias is applied on the drain contact, a current larger than the ohmic current will be measured. Clearly an important material parameter is the ease with which the accumulated charge can move under the influence of an electric field, the mobility, μ.

At a gate bias V_g , when a small increment is applied δV_g it will give rise to an incremental increase in the accumulated charge $C_{ins}\delta V_g$ and a total charge increase over the entire channel of $ZL\ C_{ins}\delta V_g$. If the added charge has a mobility μ, when a small drain bias is applied, an incremental current δI_{sd} will flow:

$$\delta I_{sd} = \frac{Z}{L} \mu C_{ins} V_d \partial V_g$$

If the drain current is measured in function of the gate bias at low voltages, the trans-conductance g will be:

$$g = \left.\frac{\partial I_{sd}}{\partial V_g}\right|_{V_d \to 0} = \frac{Z}{L} \mu C_{ins} V_d$$

And the field effect mobility of the accumulated charge, as a function of the gate bias may be easily extracted:

$$\mu = \frac{L}{Z C_{ins} V_d} \left.\frac{\partial I_{sd}}{\partial V_g}\right|_{V_d \to 0}$$

Practically, this is measured at a drain bias of - 1 V and gives reliable results for negative gate biases of magnitude greater than -2 V. When the transistor is in its on-state (large enough gate biases and I_{sd} depends linearly on V_g) it allows extracting the effective mobility from transfer measurements without having to calculate derivatives of I_{sd} (V_g):

$$\mu = \frac{I_{sd}}{C_{ins}(V_g - V_{on}) V_d} \frac{L}{Z}$$

At low temperature the threshold voltage reflects the trapping of immobile charges in localized states, and there may be alternative transport mechanism; this expression is valid for high enough gate biases, when the device is switched on strongly.

If a positive gate bias is applied, then the opposite band bending arises in the semiconductor at the dielectric interface, leading to depletion of charge (in the case of a doped semiconductor, the positive doping-induced charges within the depletion zone flow out via the ohmic source and drain contacts). With increasing gate voltages, the depletion zone extends into the semiconductor layer until finally the entire thickness is depleted.

Due to the underlying hopping transport, the field-effect mobilities could be increased by doping only at the expense of increased bulk conductivity. This leads to a much smaller on-off ratio; and in transistors constructed from these doped semiconductors the field-effect mobility was found to be largely independent of the gate voltage (Brown A. , 1997). This explains why the focus of research in synthetizing new polythiophene derivatives has

been on finding systems with higher intrinsic mobility, at low doping concentration (McCullough, 1998).

The temperature dependence of the mobilities normally observed in polymer FETS indicates that charge transport is due to a thermal activation process. Generally, due to spatial disorder, there exist polaron states situated deep in the gap, these are the first to be occupied as charge is introduced, locating the Fermi level initially deep in the gap. However, at more negative gate biases the Fermi level will move towards the energy level typical of the polaron levels in the material and become pinned there. The charge transport is thermally activated from the localized polaron states at the Fermi level to a large density of localized states (or extended states, depending on the degree of crystallinity of the polymer) at a certain transport level. Consequently, the mobility is thermally activated and, at high gate biases, the activation energy saturates at a value which reflects the polaron-binding energy (Brown A. , 1997).

Design of the experiment

The primary aim of our study was to evaluate the feasibility of a polymer-based field effect transistor having a built in non-volatile magnetic memory. The possibility of injecting and detecting a spin-polarized current in a semiconductor could combine magnetic storage of information with electronic readout in a single device (Datta, 1990).

The elementary device geometry to detect spin transport is a two terminal spin valve in which a non-magnetic medium is contacted by two ferromagnetic electrodes. A spin polarization of the current is expected from the different conductivities resulting from different densities of states for spin up and spin down electrons in the ferromagnet. For the two terminal spin valve this should result in a conductance which is dependent on the relative magnetization of the two contacts.

The devices were prepared on a heavily doped n^{++} Si wafer with a thermally grown SiO_2 layer whose thickness was 200 nm, bought from Si-Mat. A contact to the substrate allowed for a gate voltage to control the charge density in the semiconducting film. By means of UV lithography we deposited a Ti/Au micro-scale contact platform, which provided large area contacts to connect the final nanoscale device to the acquisition system.

The SiO_2 surface was chemically modified with a self-assembled monolayer of hexamethyldisilazane (HMDS) in order to obtain an hydrophobic surface, which is reported to promote structural ordering of the cast polymer (Ong, 2004) and enhance its field-effect mobility (Chua, 2005). Using electron beam lithography and a lift off technique, source-drain electrodes were patterned on the substrate. A bottom Ti layer of 3-5 nm was employed to promote the adhesion of the ferromagnetic layer forming the source-drain contacts to the underlying SiO_2 surface. An interdigitated geometry for the source-drain contacts was chosen to maximize the width of the active channel (length of the electrodes). The electric field lines in the interdigitated electrodes run perpendicular to the electrode axis, and fringing can be neglected. For this geometry, since the width of the channel and the length of the gap are known, the extraction of transport parameters is facilitated. We adjusted the lithographic process to be able to regulate the channel length (spacing between the electrodes) down to 90 nm over a channel width exceeding 60 μm (about 960 μm for the whole interdigitated geometry). The electrode design consisted in a set of 16 pairs of interdigitated contacts with alternating widths of 200 and 400 nm, their coercive field depends on their size due to shape anisotropy, and provides independent switching of the two contacts. If the spacing between both contacts is shorter than the spin flip length, then the interface of the second ferromagnet can act as a spin detector, exhibiting either low or high resistance for magnetization parallel or antiparallel to the first magnet, when spin injection and transport efficiently occur. A scanning electron micrograph of the patterned interdigitated electrodes was shown in Figure 3.10.

The devices are completed by deposition of an organic semiconductor, the schematic of the cross-section of the device was sketched in Figure 4.1; whilst electrochemical deposition (Koezukaand, 1989), Langmuir-Blodgett (Paloheimo, 1990) and contact printing (Seong, 2004) are available techniques we have chosen to use the commercially most attractive technique of spin coating from a 0.05 % weight solution of poly(3-hexylthiophene) in toluene. Toluene was preferred to chloroform or chlorobenzene as chlorines were observed to corrupt the source-drain contacts when not made of noble metals. The spin casting was followed by annealing to fully remove the solvent. Typical film thicknesses are around 150 nm. Samples are normally handled in argon and electrical measurements are made in high vacuum.

A great deal of attention was devoted to the minimization of parasitic effects, primarily as regard to the leakage current going to the gate. When fractures exist in the dielectric layer, conductive molecules from the polymer can penetrate into the imperfections, especially

during the cast from a liquid phase. This can lead to the formation of leaking channels for the current among the source-drain electrodes and the gate terminal, compromising the functionality of the device. In order to avoid this, the oxide surface must be kept pristine throughout the whole processing of the device. The current can also flow to gate from an unpatterned region of the semiconductor around the device, largely affecting the overall leakage (Steudel, 2006). This requires the patterning of capping layers prior to the deposition of the semiconductor. A description of the techniques adopted for the device fabrication is provided in the section of Chapter 2 dedicated to the preparation of P3HT films. During the measurements the drain current and the gate current were measured simultaneously. A leakage in the fully processed devices of less than about 10 pA was eventually achieved at the highest fields, with 3 to 5 orders of magnitude difference with respect to the drain current, which demonstrated that with a careful device preparation procedure the dielectric supported the whole transistor processing.

High impedance electrical characterization

Electrical characteristics were measured in a Quantum Design Physical Properties Measuring System (PPMS) by making use of tri-axial leads for high impedance measurements, femto-Ampere source-meters (Keithly 6430) and low noise pre-amplifiers. The magnetic field could be applied in plane with respect to the device surface, along the electrodes main axes.

Parasitic effects

Initially a $Ni_{80}Fe_{20}$ alloy was chosen as a suitable material for the source-drain electrodes due to the relatively slow oxidation rate of nickel; which would increase the probability of having a clean contact interface, since the electrodes would be briefly exposed to air during the fabrication process. The electrodes were deposited by e-beam evaporation from $Ni_{80}Fe_{20}$ source material. After mounting the sample onto the head of the cryostat, the cold finger was evacuated with a cryopump to $10^{-7} – 10^{-8}$ mbar. An initial $I{:}V$ characteristic was

measured with no applied gate bias at room temperature so as to test the conductivity of the film, and it is shown on the left side of Figure 4.9.

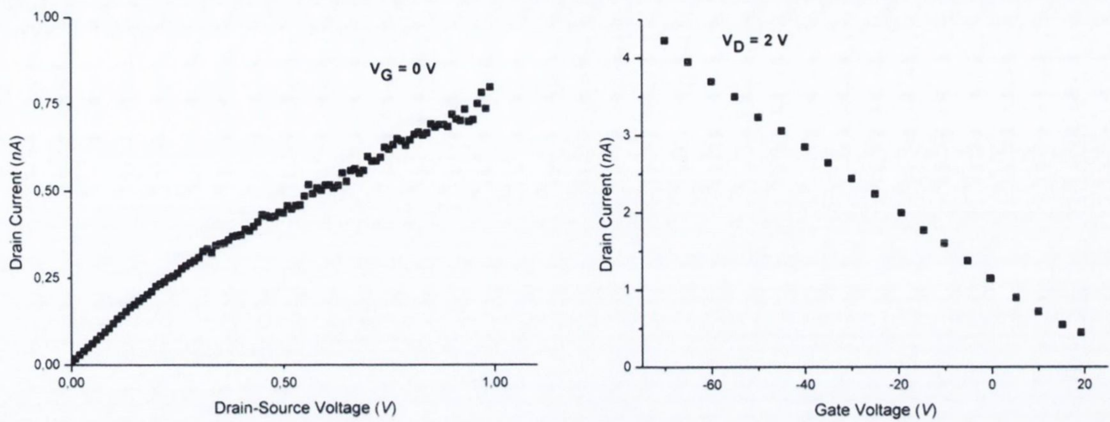

Figure 4.9 *Left: I:V curve with no gate voltage applied, at 300 K. Right: transfer characteristic at 2 V drain-source bias, at 300 K.*

The gate voltage was scanned with constant source-drain bias of 2 V (Figure 4.9 right). The threshold voltage is zero (we recall that OFETs primarily operate in accumulation mode, in contrast to the usual inversion mode of silicon MOSFETs) and no saturation could be observed, up to -70 V (this aspect will be analyzed later). Leakage current to the gate was negligible, around a few pA, and constant over the range of measured voltages. The preliminary device testing was followed by a complete 3D scan of the drain current, gate and drain-source voltages, at room temperature. In Figure 4.10 the anomalous results are summarized, by showing a family of five *I:V* curves at different gate voltages (left) and the transfer characteristic at constant drain-source bias of 2V (right).

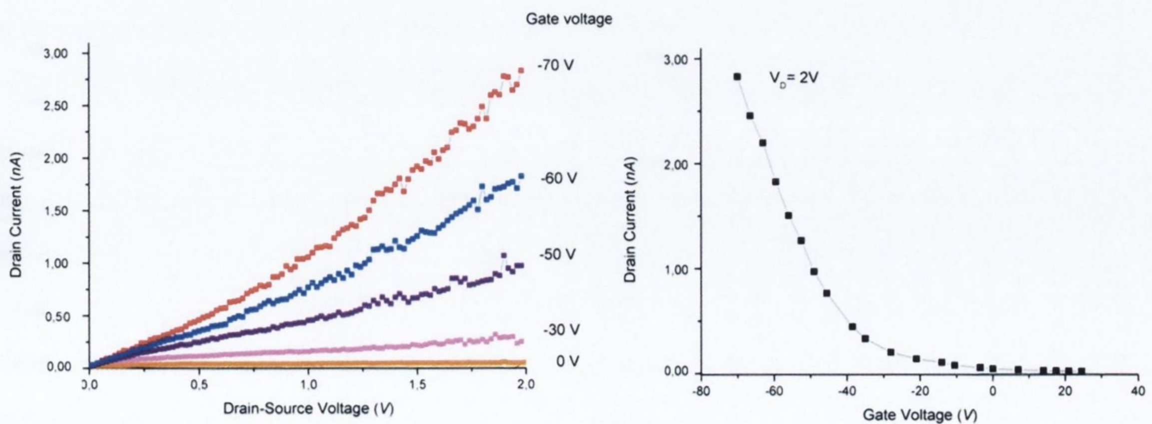

Figure 4.10 *Left: family of I:V curves at different gate voltage, at 300 K. Right: gate scan at drain-source bias of 2 V.*

It is apparent that the threshold voltage has increased to about 30 V, while the conductivity of the films at zero gate has greatly reduced. The features of the electrical characteristics of the device have changed, in a short time. Accompanying this change, an alteration of the parasitical current draining to the gate was contemporarily being detected. For instance, at negative source-drain voltage, the leakage current started to largely increase, non-linearly (Figure 4.11 left). To attempt to understand the nature of this asymmetric leakage the temperature was lowered and stabilized at 150 K.

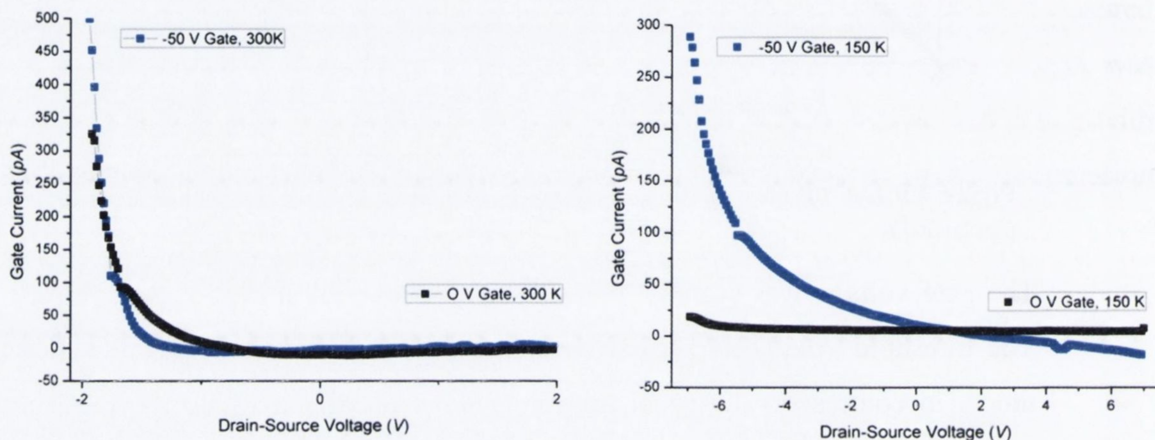

Figure 4.11 *Left: room temperature gate-leakage current with no gate bias applied or at -50 V. Right: gate current at 150K at zero and -50 applied volts on the gate. The leakage at 0 V on gate is largely reduced on lowering the temperature but it persisted for high applied gate.*

On lowering the temperature, the leakage current almost disappeared completely, when no gate bias was applied, and only a little non-linear response was still observable at the most negative source voltages. However the application of a high negative gate (-50 V) could restore the leakage current to its initial character (Figure 4.11 right).

We presume that the origin of the leakage current lies in the presence of tiny fractures on the surface of the silicon oxide, extending within the bulk of the insulating layer. These dislocations were propagated from the edges of the chopped sample substrate when dicing the silicon wafer.

When a film of conductive polymer is deposited onto the substrate, molecules can penetrate into the fissures. Based on how deep a dislocation extends into the insulating layer, there are different mechanisms with which charges can leak from the contacts to the conductive silicon substrate. Below and in Figure 4.12 an overview of these mechanisms is given.

When a fracture extends over the entire oxide thickness, a fraction of the polymer can be in direct contact with silicon (Figure 4.12a). Due to the band offset, a contact barrier arises, as in a diode. Charges are injected /extracted between the two semiconductors by field assisted thermionic emission. We believe this is the origin of the diode-like voltage and temperature dependence of the leakage current. On decreasing temperature, charges do not have enough thermal energy to overcome the contact barrier, hence the leakage current disappears. By applying high gate biases (-50 V, Figure 4.11 right) the Fermi level in the polymer will move towards the valence band, reducing the effective barrier, hence the leakage current is re-established, as observed.

When a dislocation does not extend throughout the entire thickness of the dielectric layer (Figure 4.12b) charges can only tunnel from the pinhole to the substrate. The current will depend exponentially on the distance between the deep end of the fracture and the silicon substrate.

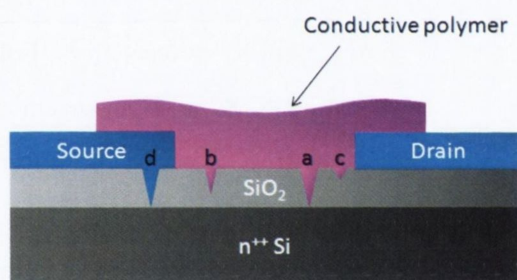

Figure 4.12 *(a) Schematics of a dislocation extending across the whole oxide thickness, which bring the polymer in direct contact with the conductive substrate; (b) a fracture which goes deeply within the dielectric, through which charges can tunnel; (c) superficial defect-fracture and (d) deep dislocation underneath an electrode.*

The overall current draining to gate will depend upon the density of fractures. In a few samples, we observed leakage currents of value about tens pA, only slightly dependent of temperature, revealing this mechanism. Devices with these characteristics were typically discarded, because the gate efficacy was compromised. In fact, these imperfections possess a capacity which is locally higher than that of the rest of the dielectric, due to the reduced thickness of the oxide in between the polymer and silicon. As a consequence, charge can be readily stored in these defects, with a release time that can be much longer than the transit time across the channel. The typical consequence of the presence of latent charges besides the conductive channel is the hysteresis of the transfer characteristic, due to a long discharging time following a change in applied voltage.

When only a number of surface imperfections are present on the substrate (Figure 4.12c), no increase in the leakage current is expected. In the ideal case there should be none or a low density of only these surface defects, next to the channel.

Dielectric fractures can also be located underneath the source-drain electrodes. When such a fracture extends throughout the entire oxide thickness, metal atoms from the contacts can electro-migrate toward the substrate. This mechanism, eventually, creates a direct channel for the leakage current. The contact would be purely Schottky in nature. Under this circumstance, the silicon may shorten the device following the application of a bias. When a device is affected by this kind of leakage channel, at decreasing temperature the drain current reflects the transport properties of silicon. A complete shut-down of the current below 100 K has indeed been observed in a few, discarded, samples.

The nature of the leakage current draining to gate, in the sample under test, has changed in time, at the beginning of the electrical measurement. We attribute this feature to a dynamic evolution of the surface dislocations, which propagated within the insulating layer under the application of high gate voltages. The sample surface is likely characterized by a high concentration of defects, introduced by a spoilt sample processing. Following the application of high gate voltages, a large areal density of channels in direct contact with the underlying silicon must have developed. The electro-migration of the polymer (or, less probable, of silicon) within the fractures occurred immediately following. This explanation justifies the observed time, field and temperature dependence of the leakage current.

In this subsection we wanted to show that distinguishing the presence of parasitic effects in a device is not trivial: leakage currents, for example, become substantially high only at certain applied voltages. However, the leakage affects the overall device characteristics; hence such devices are not reliable for the extraction of any parameter. In the case at hand, the high on-off ratio (around 10^3) shown after the propagation of the defects, reflected the trapping of carriers in localized states at the dielectric interface during their transit, which shut down the drain current at low gate bias, rather than a property of the polymer. The large threshold voltage is associated to trapping of immobile charges in localized states of a damaged surface next to the conductive channel.

At the lowest temperature tested for this sample, 10 K, the leakage was reduced to negligible values ($\sim 10^{-12}$ A) independent of the applied voltages. A high density of immobile charges was "frozen" into the localized states.

Even though the parasitic leakage impairs the modeling of the output characteristics, it is useful to observe the qualitative change of the *I:V* curves on lowering the temperature

(Figure 4.13). Starting from a nearly linear voltage dependence at 300 K, the *I:V* becomes pronouncedly non-linear when cooling the sample. The log-linear plot on the right side of the figure, at 100 K, shows that the relation is a clear exponential.

The tendency toward strongly non-linear voltage dependence at low temperature will be a common trait of our polymer transistors and it will be discussed in the next section.

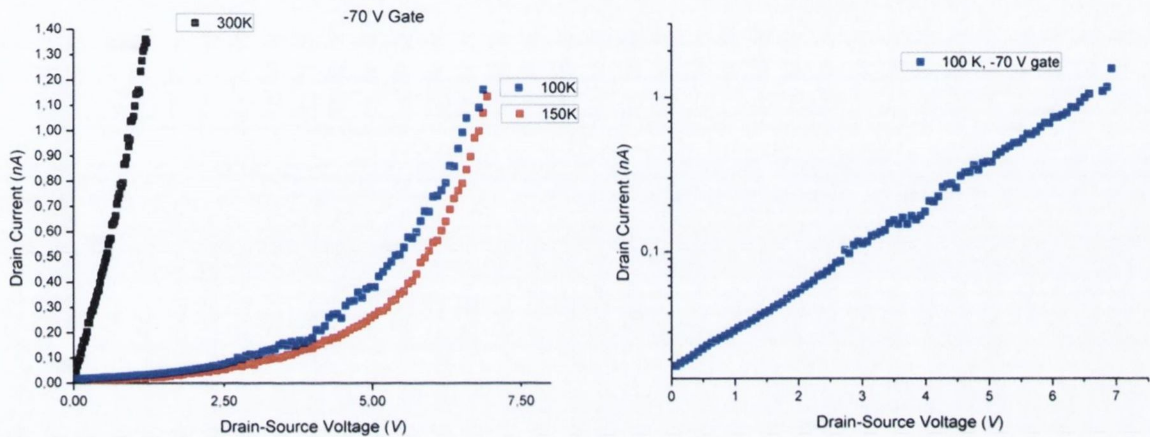

Figure 4.13 *I:V curves at -70 V on the gate at different temperatures from 300 K to 10 K. There is a pronounced non-linearity appearing on the lowering of the temperature. On the right side the log-linear plot of a curve at 100 K is shown.*

Concluding, the fact that polymer based FETs display a large threshold voltage already at room temperature has been often, and wrongly, attributed in literature to intrinsic properties of the polymer. The amplitude of the threshold voltage has also been used to extract the density of gap states in the polymer. Unless the gate leakage current is recorded and proved to be voltage and temperature independent, this feature is likely due to imperfection of the dielectric layer, hence no conclusion about the intrinsic polymer nature can be drawn.

CoFe electrodes

Before describing further devices made with NiFe electrodes, we will illustrate next a temperature study of the electric characteristics obtained with a sample fabricated with $Co_{50}Fe_{50}$ contacts. The results are instructive about the influence of the nonlinear contact resistance. The CoFe alloy has been employed at many stages of our experiments because

of its well established high spin polarization, when compared to other ferromagnetic metals.

The electrodes were evaporated by mean of highly-directional electron beam evaporation, in a tool having a distance of 75 cm between the substrate and the target. As usual, the contacts have been defined by e-beam lithography and lift off.

In Figure 4.14 is shown a family of *I:V* characteristics, taken at decreasing temperatures from 300 to 7 K.

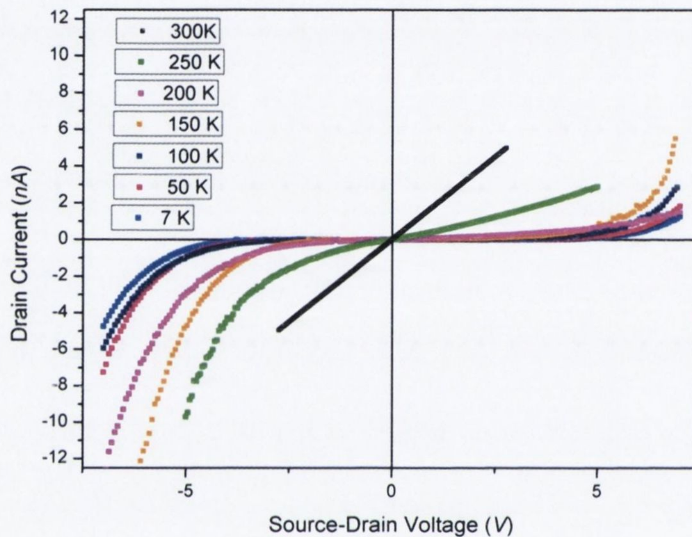

Figure 4.14 *I:V characteristics measured at constant gate bias of – 25 V, at decreasing temperature from 300 to 7 K.*

The *I:V* curve at 300 K is linear over the range of source-drain voltages tested. Upon decreasing the temperature, the characteristics display clear thermally activated temperature dependence, down to about 100 K. Below this point, the thermal activation saturates, and the curves resemble each other. A pronounced voltage asymmetry of the curves is straightforwardly observable; this feature is present at all temperatures below 300 K in this sample.

The bottom gate geometry employed in our device enables the investigation of charge transport with an induced electric field. A constant voltage of -25 V was in fact applied at the gate terminal while recording the *I:V* curves so as to enhance the conductivity. In Figure 4.15 we show the transfer characteristic of the device (obtained scanning the gate voltage at a constant source-drain bias) at different temperatures.

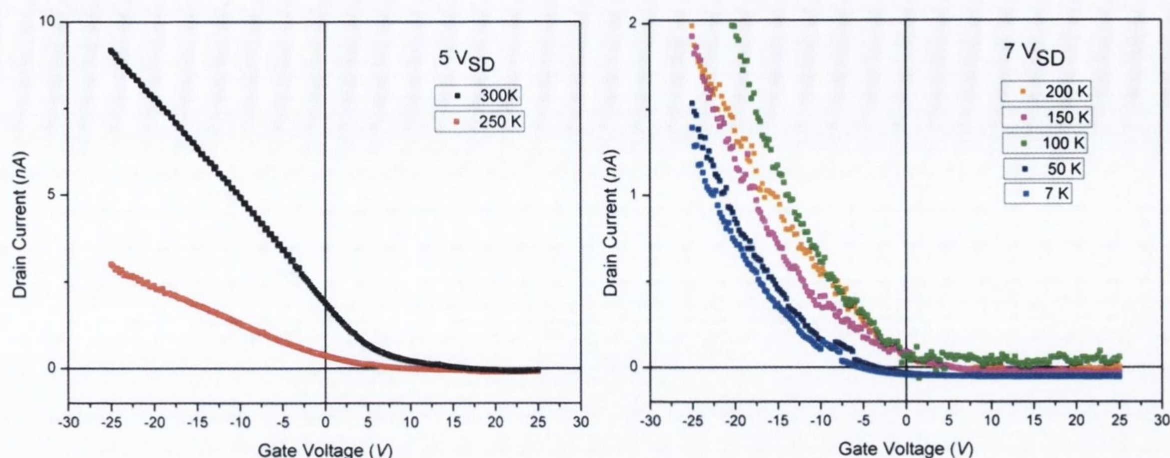

Figure 4.15 *Results of gate scans at different temperatures. The source drain bias was constant at 5 V at high temperatures (left), and 7 V for lower temperatures (right).*

The observed response to a local electric field exhibits the general behavior of a hole transporting system, in which the drain current is enhanced by negative gate biases. The application of positive gate voltages shuts down the conduction in the channel and, further, it leads to a slight n-type conduction (i.e. the sign of the current reverses). The transistor does not show saturation at the gate voltages tested. No major hysteresis in either the output or transfer characteristics was detected.

To understand the thermally-activated temperature dependence of the *I:V* curves, the existence of a potential barrier at the metal /organic interface must be considered. At high enough temperature the energy barrier is hidden by the thermal excitation of carriers, in fact at 300 K we observed a linear *I:V*. At decreasing temperature the nature of the contacts reveals itself, as the injection assumes the feature of a thermal activated process in which the turn-on voltage of the junction (the bias at which a significant current builds up in the channel) shifts toward higher biases for lower temperature.

The temperature dependence is given by the thermionic emission of carriers above the interface barrier (see Chapter 1). Below 100 K, the curves do not show pronounced temperature dependence, hence it is arguable that field emission tunneling becomes the dominating injection mechanism. Both mechanisms typically occur in parallel, but thermo-emission seems to dominate at high temperature and tunneling at low temperature. In both processes the field dependence is exponential (even though one diode is in reverse, hence is a decreasing exponential) and they can hardly be distinguished. However, by using an equivalent circuit model (Figure 4.16) and the system of equations introduced in Chapter

3, it is possible to fit the $I:V$ curves so as to extract both the resistance of the organic channel and the activation voltage of the barriers. It is critical to be able to distinguish the channel and the contact contribution to the overall device resistance, because in short channel devices the contacts typically play a dominant role and tends to mask the more interesting intrinsic organic behavior.

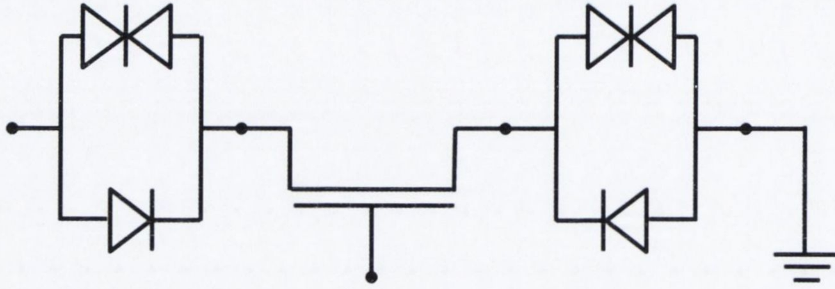

Figure 4.16 *Equivalent circuit consisting of a tunneling contact in parallel to a Schottky diode, at each terminal access of the FET*

The expression adopted to fit the experimental $I:V$ curves derives from the aforementioned system of equations, and was presented in the previous chapter; for appropriately addressing the fitting parameters adopted throughout this section, it is recalled below:

$$V = \begin{cases} V_D + IR_{Ch} + \phi_D ln\left[\dfrac{A_D + I + A_D\left(e^{-\frac{V_D}{\phi_D}} - 1\right)}{A_D}\right] - \phi_D ln\left[\dfrac{A_D + A_D\left(e^{-\frac{V_D}{\phi_D}} - 1\right)}{A_D}\right] & if\, I > 0 \\ V_S - IR_{Ch} + \phi_S ln\left[\dfrac{A_S - I + A_S\left(e^{-\frac{V_S}{\phi_S}} - 1\right)}{A_S}\right] - \phi_S ln\left[\dfrac{A_S + A_S\left(e^{-\frac{V_S}{\phi_S}} - 1\right)}{A_S}\right] & if\, I < 0 \\ 0\ otherwise & \end{cases}$$

The variables have the usual meaning, previously illustrated. Each contact was permitted to have a different barrier height, active contact area $A_{S|D}$ and contact voltage drop. This is the key point to understand the asymmetry observed in the $I:V$ curves. Intuitively, there is no good reason why the contacts should have exactly the same active areas and barrier heights; in fact the fine structure of each electrode can affect the local morphology of the polymer, which in turn affects the injecting barrier and the depleted region (Singh, 2010). The electrodes within a device are nominally the same, but topological differences of the

spin-cast polymer naturally occur. Therefore the voltage asymmetry is an expectable and peculiar feature of OFET *I:V* curves.

As it can be noted by carefully observing Figure 4.14, the temperature dependence of the *I:V*s in the range of temperature between 250 K and 100 K does not follow an obvious course. In fact, the current density at 150 K is higher, at any given bias, than at 200 K, which is quite unexpected. This anomaly can be understood by studying the recorded values of gate leakage current for this measurement, in Figure 4.17.

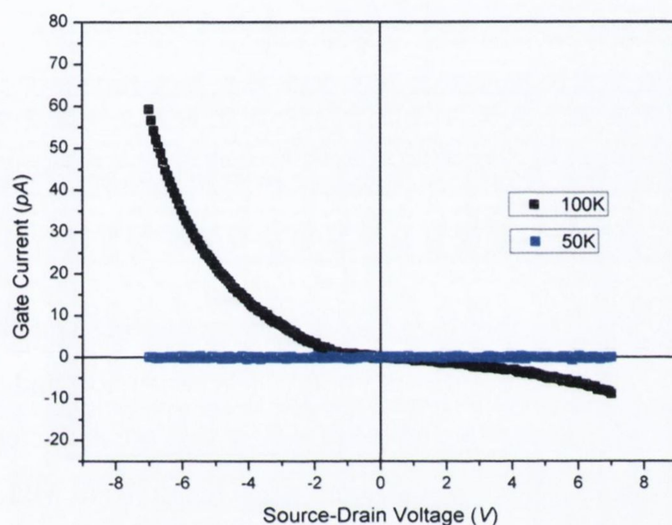

Figure 4.17 *Gate leakage current at 100 and 50 K, with -25 V applied on the gate.*

The leakage characteristics reflect the behavior of back-to-back Schottky contacts at temperature above 100 K. The black curve is plotted as representative of this behavior. The origin of this comportment must be the presence of a direct pinhole contact between the polymer and the doped silicon, as explained in the previous section. The overall current is actually quite small, below 60 pA at its maximum, therefore the density of defects is much lower than in the device previously described.

This tiny leakage can affect the curves in two ways: first by directly subtracting the current which is draining to gate instead than to the drain contact; however this effect is negligible as there are two order of magnitude differences between the two signals in this device; second by altering the efficiency of the gate. This occurs because the nominal gate voltage is locally modified by the leakage current in the channel area. Considering that the ON/OFF ratio in this transistor displays a value which is around 10^2 below 200 K, a variation of the gate bias will greatly modify the drain current. This effect is less

pronounced at high temperature, when the contact junctions are quite transparent and, further, the ON/OFF ratio is only about 10. The leakage channel shuts down completely below 100 K, reflecting the conducting properties of silicon. In Figure 4.17 it is shown in blue the leakage current at 50 K, which appears negligible.

We have extracted the channel resistance by fitting the electrical characteristics at different temperatures; the values are reported in Table 4.1.

Temperature (K)	Resistance (MΩ)
250	10
200	13
150	18
100	140
50	191
7	342

Table 4.1 *Resistance of the organic channel extrapolated from the I:Vs at different temperatures.*

However, we do not dare to infer the transport mechanism by plotting and fitting these values to any model, because the most significant points, in between 250 and 100 K, are impaired by the gate leakage. The aim of this table is to show that the extracted averaged value at high temperature is about 20 MΩ, increasing at a few hundreds of MΩ below 100 K, when a gate voltage of -25 V is applied.

Significantly, the asymmetry of the *I:V* curves is not attributable to the gate leakage, in fact it persists even at the lowest temperatures investigated (when the leakage is negligible) as highlighted in Figure 4.18.

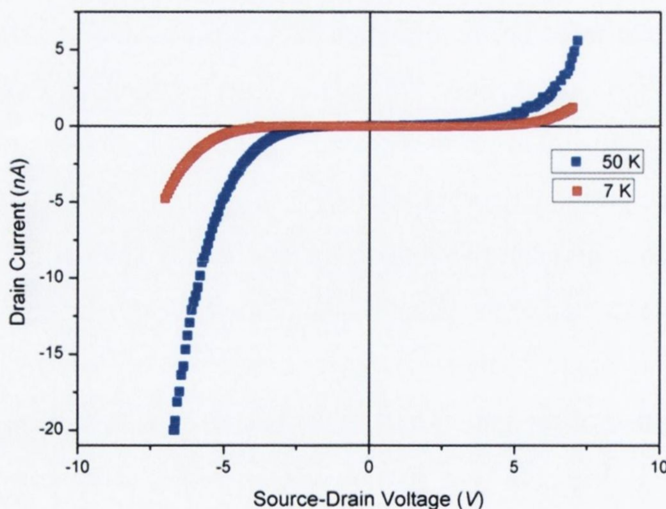

Figure 4.18 *I:V curves clearly showing voltage asymmetry of the drain current, taken at -25 V applied on the gate.*

This fact will be often recalled throughout this thesis, because there are two principal approaches for explaining the non-linear voltage dependence of the drain current. They consist in considering the current in the device as *transport-limited* or *injection-limited*. In the first case, ohmic contact between the polymer and the metal is assumed, and the non-linearity is attributed to the transport mechanism in the organic channel. A familiar approach has been to use a modified Pool-Frenkel model, in which charges in the polymer are detrapped from shallow trap states into mobile states by the application of high enough source-drain electric fields, as qualitatively proposed in (Tomo Sakanoue, 2010). This type of behavior, which resembles the Gill equation introduced in Chapter 1, was however not observed in the characteristics of this device. Instead, the curves are well fitted by exponential plus linear terms corresponding to tunneling contact in series with ohmic channel (Figure 4.19). Here we assume an intrinsic ohmic channel and attribute the nonlinear voltage dependence to the injection mechanism. The assumption of an ohmic organic channel is not a limitation to the study of the conduction mechanism in the organic layer; in fact following this first assumption, the temperature dependence of the resistance can be plotted and fitted to the appropriate conduction model (say variable range hopping or temperature activation to a mobility edge, for example).

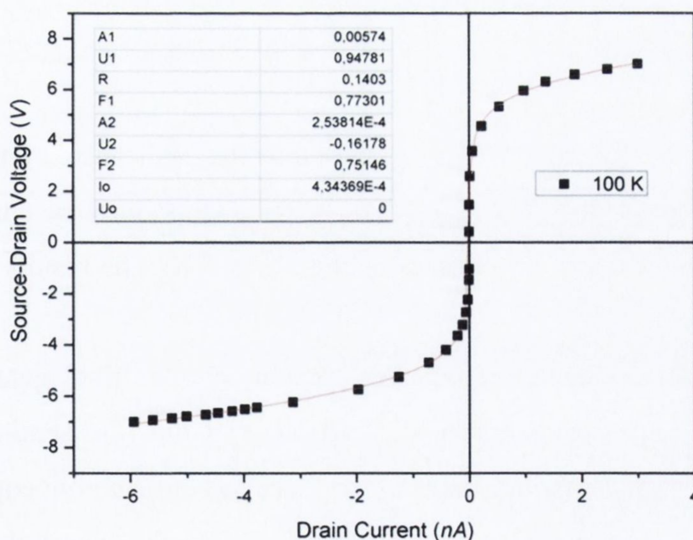

Figure 4.19 *Plot of the V:I characteristic fitted by our circuit model. The fitting parameters are shown in the inset.*

In this particular device, the barrier activation voltage was slightly asymmetric on the two sides of the junction. In the plot of Figure 4.19, a value of 0.77 V and 0.75 V was found at source and drain, respectively.

To study the effect of the gate field on the organic channel we have recorded the electrical characteristics at 7 K as a function of applied gate voltage (Figure 4.20).

The effect of the gate on the drain current is actually quite pronounced, considering that at a source-drain bias of -6 V the ON/OFF ratio is about 10^3 (the drain current is enhanced from -3 pA to -3 nA); this represents a record value for a short channel polymer-FET (Takeshi Hirose, 2010).

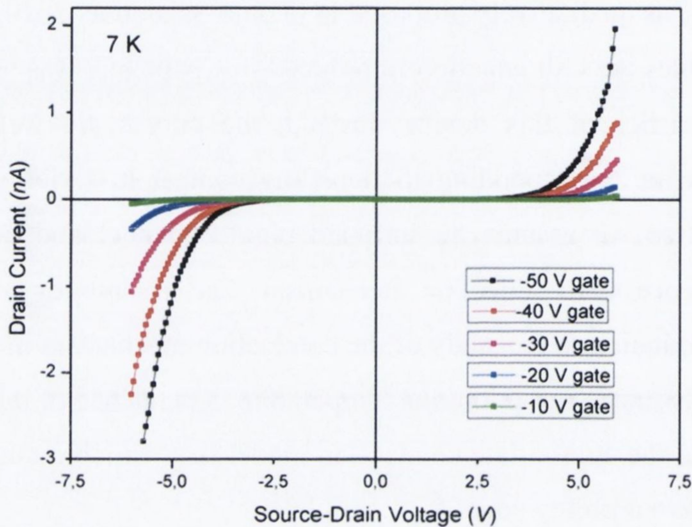

Figure 4.20 *I:V curves at 7 K as a function of the applied gate voltage.*

We have fitted the curves of Figure 4.20 to extrapolate the resistance of the organic channel as a function of gate voltage. We recall that the obtained values are unaffected by parasitic issues, because the leakage current was negligible at 7 K. The results are plotted in Figure 4.21.

Interestingly, the channel resistance approaches saturation for high gate voltages. Saturation is an essential aspect of a transistor, and the fact that the semi-conducting channel displays this characteristic is of primary importance to confirm both correct fitting of the data, and correct device preparation. In short channel FETs the overall drain current often does not displays this feature; this is because the gate can influence the current in two main ways: by accumulating the number of charges n in the active channel, which increases the conductivity $\sigma = n\mu$, and by shifting the Fermi level in the polymer towards higher energy. The latter process occurs because, due to spatial disorder, there exist localized states situated deep in the gap; these are the first to be occupied as charge is

introduced, locating the Fermi level firstly deep in the gap. At more negative gate bias, the Fermi level moves towards the energy level typical of the mobility edges in the material and becomes pinned there. The shift of the Fermi level induces a lowering of the barrier perceived by the carriers, facilitating their injection /extraction. At the same time, it can also reduce the thickness of the depletion region, which becomes more transparent for tunneling. In our short channel devices the current seems to be injection-limited, hence this mechanism is the most relevant, and masks the saturation of the semi-conductive channel. Evidently, we did not apply a high enough gate voltage to saturate the injection, due to concern of blowing the dielectric. Nonetheless, by modeling the device with an equivalent circuit, we could extract the channel resistance and successfully recognize the fingerprint of transistor behavior, i.e. channel saturation.

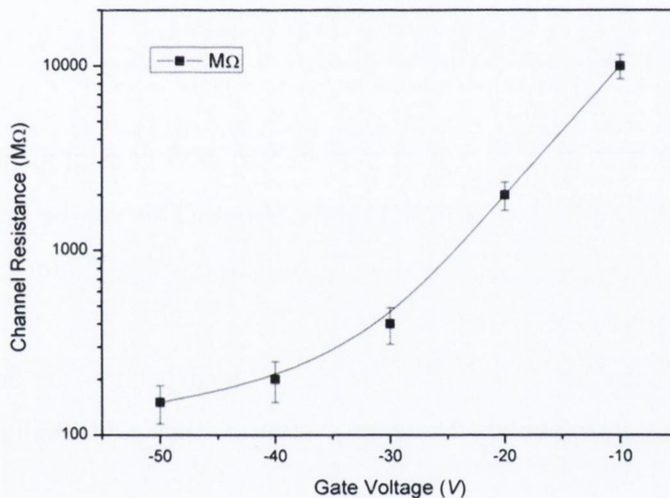

Figure 4.21 *Plot of the organic channel resistance as a function of the applied gate voltage, at 7 K.*

Aiming at testing whether a spin polarized current could be injected and detected into P3HT from CoFe electrodes, the resistance has been measured at 7K as a function of magnetic field up to 1 T. This is a field strength which ensures the reversal of the magnetization in the electrodes. The field was applied along the electrode main axis and scanned from 0 to -1 T, slowly reversed to +1 T along the same direction, and then brought back to zero. On the basis of the electrical characterization performed so far, the gate and source-drain voltages were chosen to be above the respective diode and transistor turn-on voltages. Both negative and positive source-drain bias was tested. A clear spin-valve effect was not observed (Figure 4.22). This result then led us to change the material adopted for the ferromagnetic electrodes.

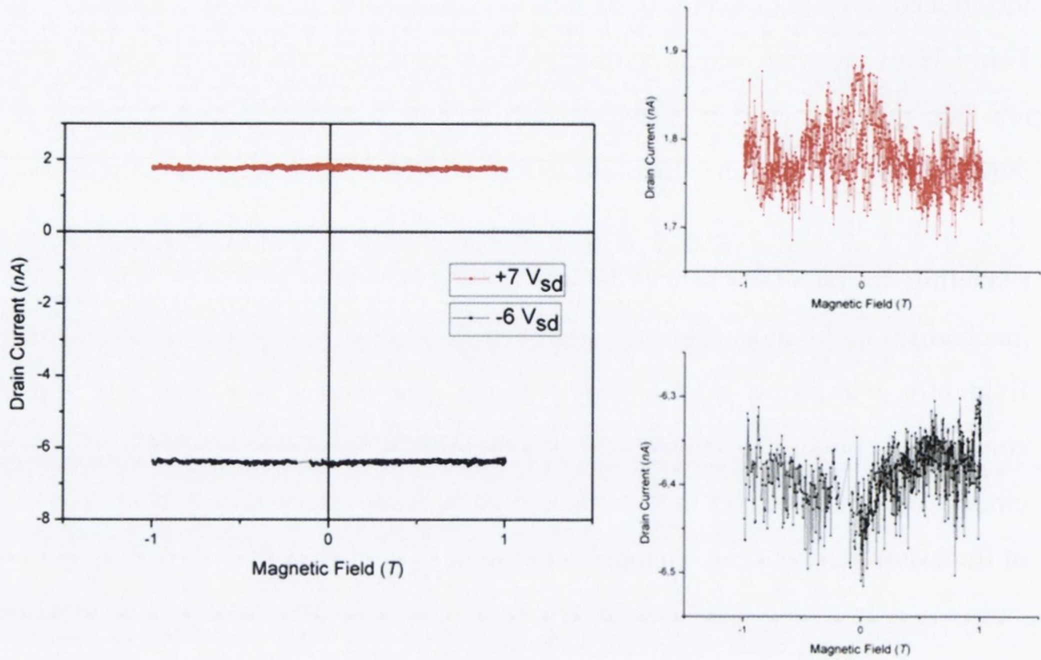

Figure 4.22 *Plot of drain current as a function of applied magnetic field, at 7 K.*

It is interesting to note that following the exposure of the sample in air atmosphere for 14 days, the field effect mobility of the film significantly decreased. This can be inferred from the transfer characteristics of Figure 4.23, and it demonstrates that water and, likely, oxygen induce a deterioration of the film quality.

No further characterization, however, was carried out about this aspect; as the devices have been typically prepared and transported from one site to the next under protected atmosphere.

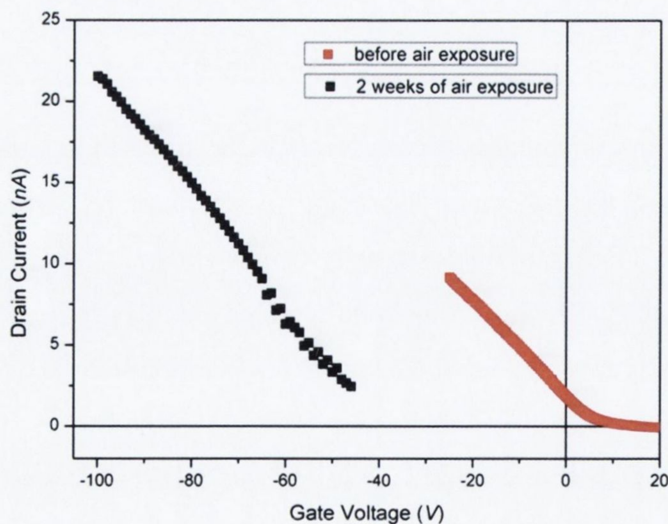

Figure 4.23 *Output characteristics measured before and after exposing the device for 14 days at atmosphere. Constant source-drain bias of 5 V was applied during both scans, at a temperature of 300 K.*

NiFe electrodes

As anticipated, the NiFe alloy is a suitable electrode material thanks to the relatively slow oxidation rate of nickel. Following we report the electrical characterization of a device consisting of $Ni_{80}Fe_{20}$ drain and source contacts and P3HT semiconductor cast in their gap. The main difference from the case of CoFe is that in the latter the contact interface is expected to be significantly altered, due to the rapid oxidation of cobalt when exposed to air. A layer of paramagnetic native oxide could, in principle, destroy the spin polarization of the current from the bulk of the electrode before it even reaches the polymer.

In Figure 4.24 is shown the output characteristic of the NiFe /P3HT transistor after cooling it at 7 K. The *I:V*s were recorded applying constant -50 V and -47 V on the gate.

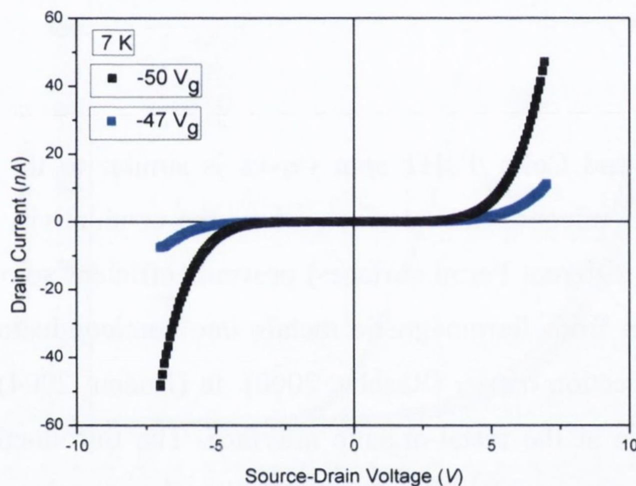

Figure 4.24 *Transfer characteristics of the FET at 7 K and -50 V, -47 V applied on the gate.*

The familiar asymmetry of the current dependence upon the voltage is recognizable, though less pronounced in this sample. The extrapolated channel resistance is 27 MΩ, slightly lower than in the previous sample. The barrier height at the source and drain contact is 0.47 and 0.49 eV. The magnetic field has been scanned in the same way, but no clear difference was detectable compared with the previous device. The drain current displayed some random fluctuations that were not attributable to the magnetization of the electrodes (Figure 4.25). The measurement was repeated several times, here we report two plots for two source-drain voltages, and the outcome ensured that the current variations consisted in random fluctuations.

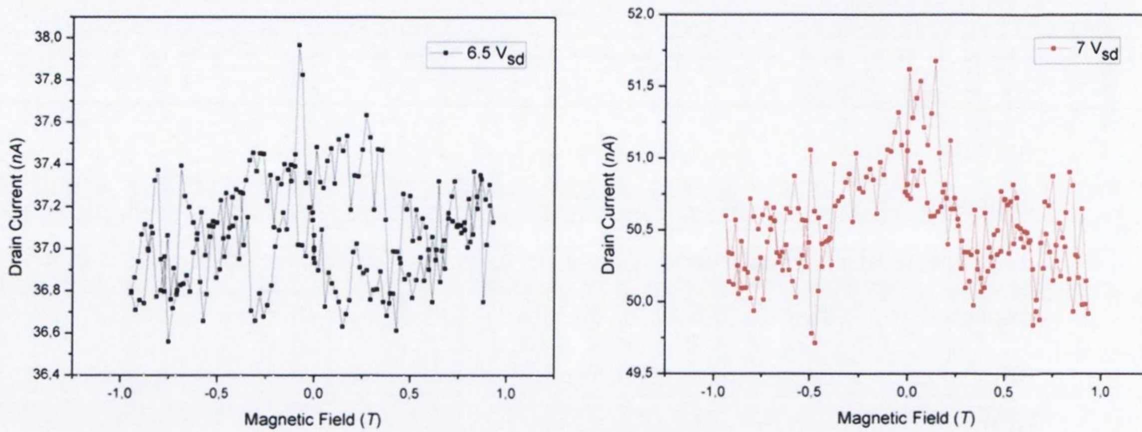

Figure 4.25 *Plot of the drain current vs. the applied magnetic field, at 7 K.*

Insertion of a tunnel barrier

The lack of MR in our NiFe and CoFe /P3HT spin valves is similar to the case of a ferromagnetic metal-inorganic semiconductor interface, where the conductivity mismatch problem (or, better, the vastly different Fermi surfaces) prevents efficient spin injection. The difficulty in spin injection from ferromagnetic metals into semiconductors can be alleviated by introducing an injection barrier (Rashba, 2000). In (Ruden, 2004) the same was proposed for spin injection at the metal-organic interface. The introduction of the barrier could promote spin injection by increasing the probability of connecting states with corresponding wave vectors on both sides of the barrier.

Therefore, here we attempted introducing a thin Al_2O_3 barrier between CoFe ferromagnetic electrodes and the conduction channel. The presence of a thin aluminum oxide layer, beyond creating a spin-dependent tunnel barrier, should prevent the oxidation of the underlying ferromagnetic metal, hence removing the issue related to the scattering occurring in the native oxide layer. Further, this inert layer can de-couple, from the chemical point of view, the organic material from the 3-d metal, preventing formation of interfacial states.

By heating the sample above 100 °C in the glove-box, immediately before casting the polymer, residual water stuck on the surface of the oxide, which was shortly exposed to

air, can be removed. We recall that Al_2O_3, unlike MgO, is hydrophobic, hence the choice to employ it.

The tunnel barrier was initially formed by e-beam evaporation from a source of alumina crystals into a thin film 1.5 nm thick. It is well known that when evaporating an oxide source the stoichiometry between the source material and the deposited film can be significantly different; it is typically displayed an amount of oxygen vacancies due to the partial dissociation of Al_2O_3 molecules during the evaporation. To fight this issue the film was exposed for 60 seconds to an oxygen plasma, following its deposition.

In Figure 4.26 is shown a family of *I:V* curves recorded at temperatures between 200 and 20 K, at constant -50 V on the gate. The familiar temperature activated behavior which saturates below 100 K is reproduced.

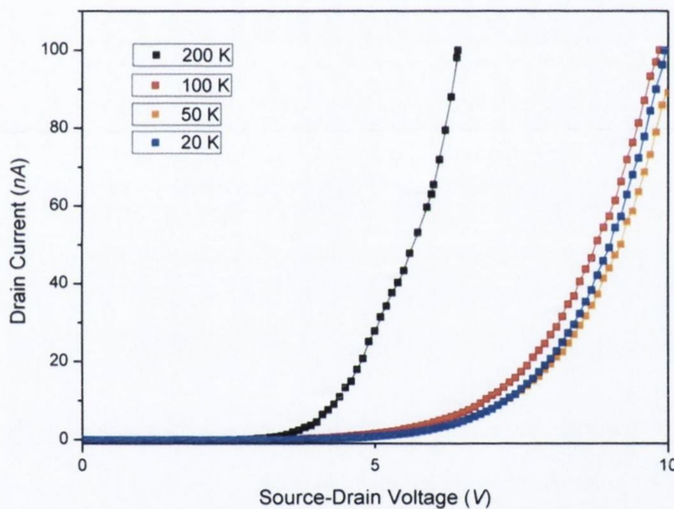

Figure 4.26 *Output characteristics of the Co /Al_2O_3 /P3HT device at decreasing temperature, with -50 V applied on the gate.*

The curves have been fitted to extract the barrier activation voltage of source and drain, respectively of 0.9 V and 0.7 V, and the channel resistance. The values obtained for this parameter are plotted in Figure 4.27 as a function of temperature. It is interesting to note that the channel resistance, at high gate bias, is only slightly dependent on temperature, changing of only a factor of two over 200 K. There are not enough significant points to distinguish a conduction mechanism; however we can infer that the transport at low and high gate bias occurs via different processes. For instance, due to spatial disorder we believe a distribution of states exists situated deep in the gap; these states are the first to be occupied as charge is introduced, locating the Fermi level deep in the gap. This picture

reflects the situation when low gate voltage is applied; here the likely transport mechanism is a thermally activated hopping process. However, at more negative gate biases the Fermi level moves towards the energy level typical of a mobility edge in the material, and become pinned there. The main difference is that the states at this energy are sufficiently high in number that electron no longer has to have an activation energy to enable it to move, as it can tunnel from one centre to another (referred as to "quantum mechanical hopping" in (Mott, 1973)). These mechanisms seem to qualitatively explain the results of our measurements so far.

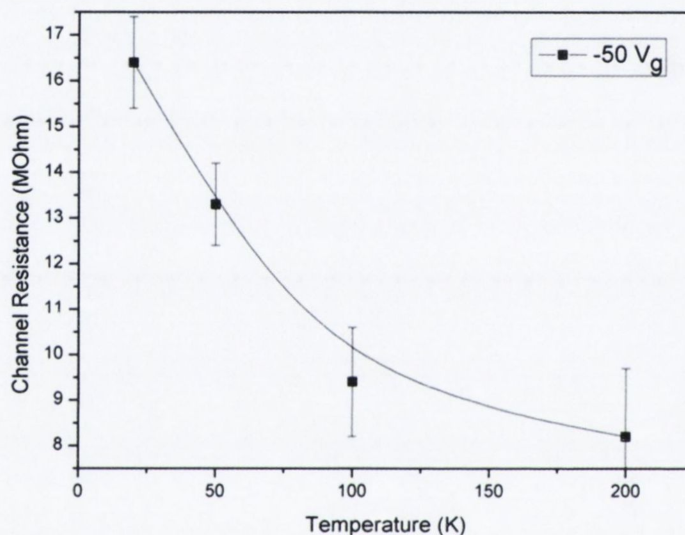

Figure 4.27 *Temperature dependence of the organic channel resistance when -50 V are applied on the gate.*

To verify the effect of the gate a set of *I:V*s was recorded at 7 K (Figure 4.28) at different gate biases. By fitting the curves, a channel resistance is extracted which closely resembles those obtained in the previous sample (Table 4.2). This indicates a good reproducibility of the properties of the spin-coated organic layer.

Gate Voltage (V)	Channel Resistance (MΩ)
-35	51
-40	29
-50	16

Table 4.2 *Values of the extrapolated organic channel resistance at 7 K for different gate voltages.*

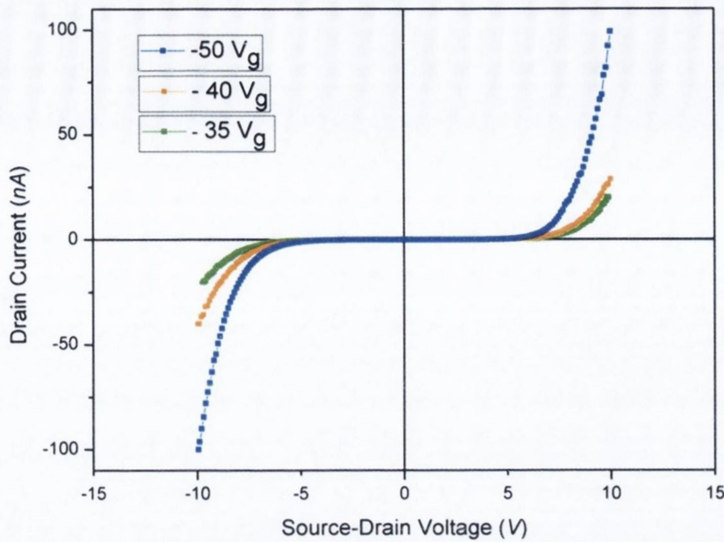

Figure 4.28 *Set of I:V curves at 7 K at different gate voltage.*

The magnetic field was scanned in the usual way, but again no significant spinvalve effect was detected (Figure 4.29).

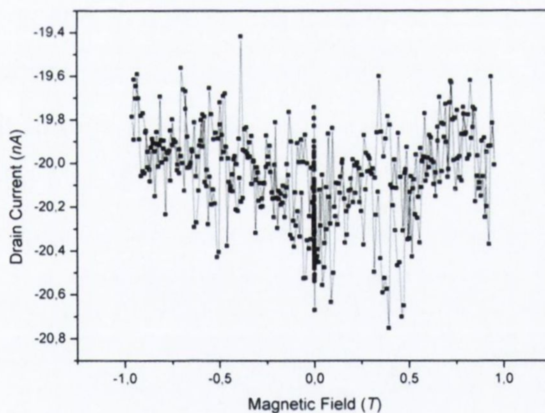

Figure 4.29 *Plot of the drain current vs. the applied magnetic field.*

Due to the different size of the molecule of Al_2O_3 and the atom of the metallic substrate, there is no lattice matching between the substrate and evaporated insulator. As a consequence, the oxide film typically grows by islands. For a thin tunnel barrier, this can be a source of pinholes and other undesired morphological defects. Intuitively, in a lateral junction this issue is less important than in vertical device. Nonetheless, in order to reduce pinhole formation in thin alumina barriers and to improve the as deposited coverage of the

bottom magnetic electrode, we modified our devices forming the Al_2O_3 tunnel barrier by natural oxidation of an ultra-thin Al layer ~ 1 nm, deposited by e-beam evaporation.

The natural oxidation was achieved by a two-step oxidation process, following (Zhang, 2003). The wettability of the substrate by a metal such as Al is largely enhanced; further the two step oxidation is intended to reduce the oxidation of the CoFe bottom magnetic contact. After depositing one layer of Al, 0.6 nm thick, pure oxygen was leaked into the load-lock of the UHV chamber through a needle valve, reaching an oxygen pressure of 50 mTorr within 30 s. The layer was then oxidized for 3 min at this pressure; the second Al layer was deposited onto the previous formed Al_2O_3 layer and oxidized at 100 mTorr for 20 min. The second oxidation can be more robust, since the oxygen atoms /molecules need to cross the Al layer and an already formed Al_2O_3 layer prior to reaching the CoFe layer.

The result of a low temperature study is shown in Figure 4.30. Fitting this *I:V* curve gives a value of the channel resistance at 7 K and -50 V applied on the gate of 15 MΩ, and injecting barrier of 0.6 V and 0.7 V. On the right side of the figure is displayed a magnetic field scan. The fabrication of the barrier by a different means did not modify the previously observed behavior, i.e. the absence of a spinvalve signal.

The concern about the oxidation of the CoFe bottom magnetic contact was however still present in these devices, because of the ultra-thin layer adopted as barriers. If the underlying electrode actually oxidizes, the native oxide can scatter the spin of the carriers before they reach the polymer, and no conclusion could be made about spin injection and transport in P3HT.

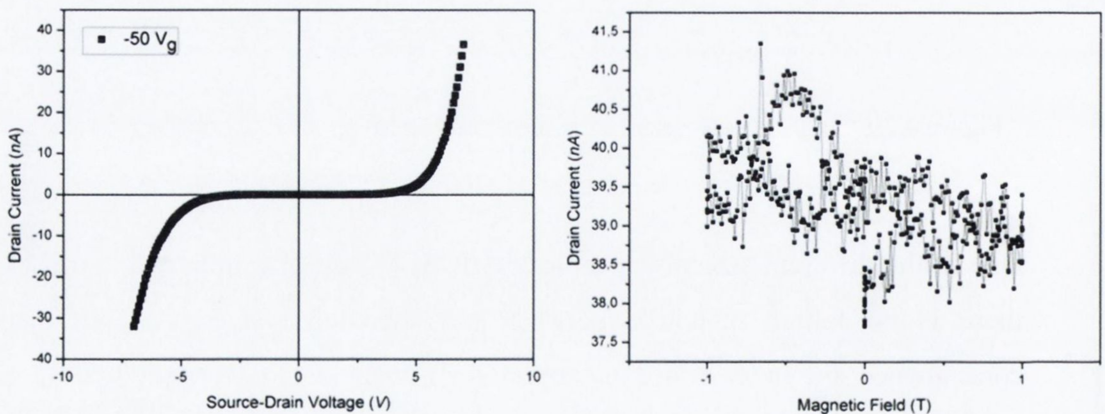

Figure 4.30 *Left: I:V curve at 7 K of CoFe /Al_2O_3 /P3HT; right: magnetic field scan and recorded drain current.*

To fully avoid the oxidation of the CoFe bottom contact, it was thought to evaporate a thick layer of 7 nm of Al directly on top of the ferromagnetic film. The above procedure has been, of course, carried out without breaking vacuum during deposition. Following the deposition, we allowed a short period of natural oxidation at high pressure in ultra-pure oxygen, and immediate lift-off and polymer casting, in argon atmosphere. Aluminum, thanks to the low atomic weight, does not act as a spin scatter over long distances, of order at least hundreds nm. This fabrication technique, which is less than an optimal procedure to fabricate a tunnel barrier, can nonetheless guarantee the protection of the ferromagnetic layer by undesired oxidation. The result of a low temperature study is shown in Figure 4.31, the fitted channel resistance is 20 MΩ at -50 V applied at the gate.

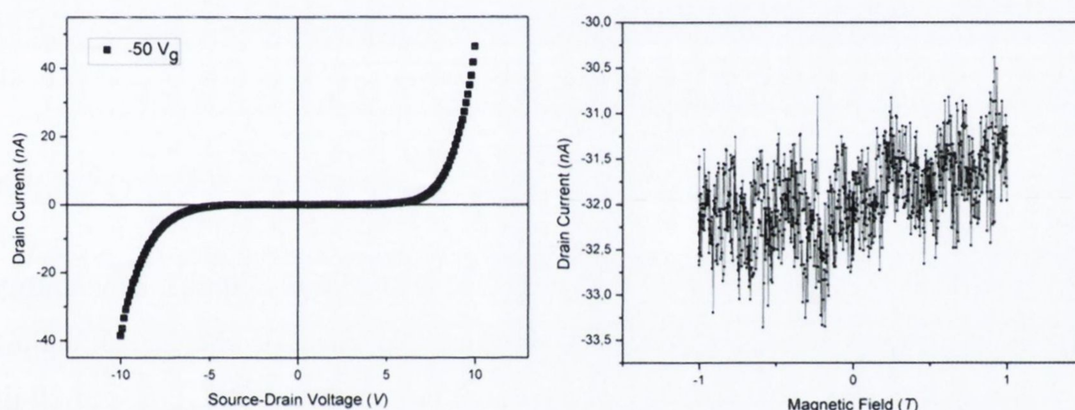

Figure 4.31 *Left: I:V curve at 7 K of CoFe /Al /Al_2O_3 /P3HT; right: magnetic field scan and recorded drain current.*

The scanning of an external magnetic field did not lead to observe any spinvalve effect.

Gold electrodes

Now we would like to investigate the effect of surface oxides on the electrical characteristics of our devices. Most likely a surface oxide is present on all but Au electrodes. Hence we have prepared a sample by e-beam evaporation from a gold source. Before coating the polymer, the metal surface was solvent-cleaned with high grade IPA and heated above 100 °C, in argon atmosphere as usual procedure.

Our aim is detecting whether an interface barrier is still present, or if it was entirely due to contacts oxidation. At room temperature, the familiar thermal excitation of the charges

masks the presence of a barrier; hence performing a low temperature study was needed. Figure 4.32 displays the *I:V* curves at 7 K, as a function of the applied gate voltage.

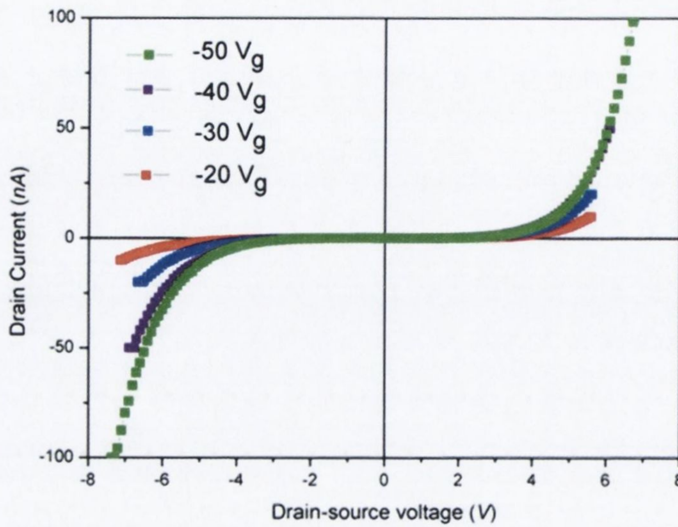

Figure 4.32 *I:V curves of an Au /P3HT device at 7 K at different gate voltages.*

It is clear that the relevant energy barrier is present in this sample, apparently unaffected by the substitution of the contact material. Nonetheless, the actual drain current is significantly enhanced: at any given bias the current in Au /P3HT is 2 to 20 times larger than in previous samples. The extracted activation voltage, which is directly related to the barrier height, does not show a direct relation with the presence /absence of an interface oxide (Table 4.3).

Electrode material	I_d at 7 V_{sd} (nA)	ϕ_s (eV)	ϕ_d (eV)
Au	-80 nA	0.84	0.68
CoFe /Al /Al_2O_3	-4 nA	0.84	0.85
CoFe /Al_2O_3 (as deposited)	-8 nA	0.79	0.66
CoFe / Al_2O_3 (natural oxidation)	-30 nA	0.73	0.58
NiFe	-48 nA	0.47	0.49
CoFe	/	0.70	0.80

Table 4.3 *It listed the value of the drain current at -7 V applied between source and drain, at 7 K and -50 V on the gate. The extracted value of the barrier activation voltage (~barrier height) for the source and drain electrodes is also given, for the set of contact material studied in this work.*

From this observation, step by step, we can understand that the injection process is still occurring via the two parallel mechanisms of tunneling and thermionic emission.
The temperature dependence, given by the thermoionic emission, determines the presence of low-temperature diode turn-on voltage. With respect to the electrode materials previously mentioned, the barrier is quantitatively very similar.
The increase in the drain current must be a consequence of thinner interface barriers, through which carriers can tunnel more easily. At a given source-drain bias, the highest current are obtained for gold electrodes, CoFe /Al_2O_3 defined by two step oxidation, and NiFe, in this order. Lower values are obtained when there is a thick surface oxide. This is in agreement with idea that the current does not flow into the bulk of the oxide, but tunnels across this layer. Due to the exponential dependence of the tunneling probability upon the thickness of the barrier, a higher current density may be expected through gold contacts. The preparation of an Al_2O_3 barrier by two step oxidation proved to give more transparent contacts then as-deposited alumina, likely because it prevents the oxidation of the underlying Co. The surface oxide only contributed at making the barrier thicker, and less transparent for tunneling, but did not affect the barrier height.
Metals such as Au, Co, Fe and Ni have very similar work function; hence it is difficult to distinguish the effect of level matching with P3HT on the formation of the contact barrier. Nevertheless, we recall that a device was prepared with 7 nm top contact of Al. Here the bulk properties of the top material should strongly affect the barrier height, in the rigid band model, because the work function of Al is 1 eV lower than in the other metals used (Table 4.4). This allows discerning the correlation between the work functions of the metals and the injection barrier.

Metal	Work function (eV)
Gold	5.1
Cobalt	5.0
Iron	4.8
Nickel	5.0
Aluminum	4.0

Table 4.4 *Values of the work function of the elemental metal employed in this work. Note that the ionization potential of P3HT is 4.7 eV.*

As visible in Table 4.3 the barrier activation voltage is very similar for gold and aluminum contacts, even though their work functions differ by about 1.1 eV.

This naturally leads to the conclusion that the approximation of a rigid band model is not valid for this case, probably due to polymer nano-morphology at the edges of the contacts the Fermi level is pinned by a large density of surface states and the Schottky barrier height (the barrier at the metal-polymer interface) becomes independent of the work function of the metal used; hence simple modeling is not applicable.

The resistance of the organic channel has been extracted and plotted in Figure 4.33 as a function of the applied gate. Saturation to a value of about 6 MΩ is observed. The lower value, with respect to what measured with oxidized contacts (between 20 and 50 MΩ), seems to reflect the increased number of carriers n injected by tunneling trough the thinner interface barrier, recalling that $\sigma = n\mu$. Since the width of the electrodes and the length of the gap are known, it is easy to extract the resistivity ρ of the film, about 10^4 Ωm. As the mobility μ is defined $\mu = ne\sigma$, by using a density of accumulated charges $n = 2 \cdot 10^{16}$ m^{-2}, as in (Burgi, 2003), a low-temperature field effect mobility $\mu \approx 10^{-2}$ $cm^2V^{-1}s^{-1}$ can be estimated.

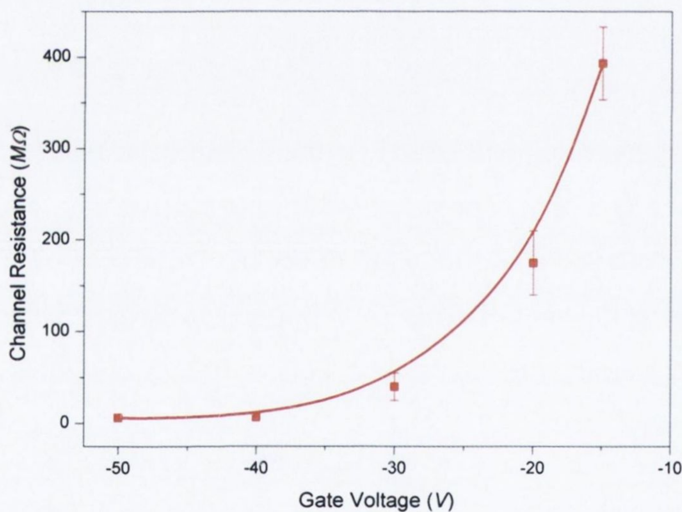

Figure 4.33 *Plot of the extrapolated organic channel resistance as a function of the applied gate bias, at 7 K.*

Conclusions

We consider the problem of spin injection in conjugated conductive polymers. We have observed no spin valve effect in our devices. In the pioneering work of (Krinichnyi V. A., 1996) a spin current in intrinsic polymers was shown to persist over long time periods, via polaronic states: an external magnetic field was applied to split the energy level of the spin

states, and the relative population of the spin currents was dynamically investigated by electron paramagnetic resonance spectroscopy. The question that naturally arises, is why spin injection and detection at the metal-organic interface does not occur efficiently?

By preparing a set of devices based on different contact materials and performing low temperature measurements, we have demonstrated that an energy barrier builds up when a polymer and a metal are brought together. This has fundamental consequences for spin injection: in order to overcome the energy impediment, carriers are typically injected at relatively high bias. Hot carriers thermalize (dissipate energy) by interacting with phonons, typically on a scale of 0.5 eV/ps in non-crystalline semiconductors (Vardeny, 1981). The key point is that electron-spin states depolarize by scattering with such phonons, hence a barrier represents a dominant impediment to the accumulation of spin in the semiconductor.

The origin of the energy barrier arising over the contact area is not simply explained: our measurements have proven that the approximation of a rigid band model is not valid for this interface. Probably due to polymer nano-morphology at the ridges of the contacts, the Fermi level is pinned by a large density of surface states and the Schottky barrier height appeared independent from the work function of the metals we used.

From our observations, we have deduced that the transport of charges at low and high gate voltages occurs via different processes. For instance, due to spatial disorder there exists a distribution of states situated deep in the gap, these states are the first to be occupied as charges are introduced, locating the Fermi level initially deep in the gap. When a low gate voltage is applied, the likely transport mechanism is thermally activated hopping among gap states. At more negative gate biases, the Fermi level moves towards the energy level typical of the mobility edge in the material, and is pinned there. At this energy the number of states is sufficiently high, so that electrons no longer have to be thermally activated in order to move, but they can tunnel from one centre to another by quantum mechanical hopping (Mott, 1973).

The introduction of a thin Al_2O_3 barrier between the ferromagnetic electrode and the semiconductor, could promote spin injection by increasing the probability of connecting states with particular wave vectors on both sides of the barrier. An artificial barrier plays also the important role of chemical de-coupling the organic material from the 3-d metal, preventing hybridization of surface states.

The insertion of a tunnel barrier proved unsuccessful in terms of spin conservation, this supports the idea that the polymer nano-morphology is the origin of the interface states. At

the contact area the self-assembly of polymer into crystalline lamellas is disrupted, resulting in a distorted morphology rich in defects states. Evidences of discontinuity of the polymer morphology in the contact regions were directly observed by (Singh, 2010).

It is well known that the main charge carriers in organic polymers can be spin polarons or spinless bipolarons. The polarons are formed on the chains of the polymer in the initial stage of charge introduction. With increasing carrier concentration, they may recombine into bipolarons. Thus the charge transfer mechanism changes at increasing carrier concentration (Krinichnyi V. A., 1996). Carrier mobility is very low in intrinsic organic semiconductors; in this work it was necessary to apply a gate voltage, in order to induce carrier accumulation and improve the conductivity of the film. Without this, the drain currents, especially at low temperature, would be negligibly small. However, the accumulation of carriers, beyond enhancing the conductivity, might also result in the formation of bipolarons. The existence of spinless bipolarons will affect the magnitude of the current spin polarization, as with increasing concentration of bipolarons the polarization will decay. As a consequence, this suggests that there may exist an intrinsic mechanism that depolarizes the spin current during holes transport in P3HT, beyond the indisputable impediment played by the interface barrier.

Taken together, the low mobility, the energy barrier and the intrinsic depolarization mechanism indicate that a lot of work remains necessary before embracing conductive polymers into spin electronic devices. It naturally raises the question on whether by the time organic channels go into engineering, technologies based on spin in inorganic semiconductor or semimetals would have advanced far more effectively.

Bibliography

Bao, Z. et al. (1996). *Applied Physics Letters, 69*(26), 4108.

Bassler, H. et al. (1982). *Physical Review B, 26*(6), 3105.

Bassler, H. et al. (1993). *Phys. Stat. Sol. B, 175*, 15.

Bredas, J. L. et al. (1983). *J. Am. Chem. Soc., 105*, 6555.

Brown, A. et al. (1997). *Synth. Met., 88*, 37.

Brown, P. J. et al. (2003). *Physical Review B, 67*, 064203.

Burgi, L. et al. (2003). *Journal of Applied Physics, 94*(9), 6129.

Burke, F. (2010). *PhD Thesis Dissertation, Trinity College, Dublin.*

Burke, F. et al. (2011). *Synthetic Metals, 1*, 13332.

Chabinyc, M. L. et al. (2004). *Journal of Applied Physics, 96*(4), 2063.

Chen, T. A. et al. (1995). *J. Am. Chem. SOc., 117*, 233.

Chua, L. et al. (2005). *Nature, 434*, 194.

Datta, S. et al. (1990). *Applied Physics Letters, 56*, 665.

Dediu, V. et al. (2008). *Physical Review B, 78*, 115203.

DeLongchamp, D. M. et al. (2007). *Advanced Materials, 19*, 833.

Dodabalapur, A. et al. (1998). *Applied Physics Letters, 73*(2), 142.

Goedel, W. A. et al. (1992). *Makromol. Chem., 193*, 1195.

Grevin, B. et al. (2003). *Advanced Materials, 15*, 881.

Hamadani, B. et al. (2007). *Applied Physics Letters, 91*, 243512.

Holstein, T. (1959). *Ann. Phys., 8*, 343.

Horowitz, G. et al. (1995). *J. Phys. III France, 5*, 355.

Hotta, S. et al. (1991). *J. Mater. Chem., 1*, 835.

Ikenoue, Y. et al. (1988). *J. Am. Chem. Soc., 110*, 2983.

Jang, J. S. et al. (2008). *Physical Review B, 77*, 035303.

Jen, K. Y. et al. (1985). *Polymer. Mater. Sci., 53*, 79.

Kapoor, A. K. et al. (2002). *Journal of Applied Physics, 92*, 3835.

Karl, N. et al. (1991). *Synthetic Metals, 41-43*, 2473.

Koezukaand, H. et al. (1989). *Synth. Met., 28*, C753.

Krinichnyi, V. A. (1996). *Russian Chemical Reviews, 65*(6), 521.

Le Comber, G. et al. (1970). *Physical Review Letters, 25*, 509.

Majumdar, R. et al. (2009). *New Journal of Physics, 11*, 013022.

Mas-Torrent, M. et al. (2004). *Nanotechnology, 15*, S265.

McCulloch, I. et al. (2006). *Nature Materials, 5*, 328.

McCullough, R. D. (1998). *Advanced Materials, 10*, 93.

McCullough, R. D. et al. (1992). *J. Chem. Soc., Chem. Commun.*, 70-72.

McCullough, R. D. et al. (1993). *J. Am. Chem. Soc., 115*, 4910.

Morley, A. et al. (2008). *Journal of Applied Physics, 103*, 07F306.

Mott, N. F. (1969). *Contemp. Phys., 10*, 125.

Mott, N. F. (1973). *Electronics & Power, 9 August*, 321.

Nakanishi, N. et al. (1999). *Applied Physics Letters, 75*(2), 226.

Northrup, J. E. et al. (2007). *Physical Review B, 76*, 245202.

Ong, S. et al. (2004). *J. Am. Chem. Soc., 126*, 3378.

Paloheimo, J. et al. (1990). *Applied Physics Letters, 56*, 1157.

Patil, A. O. et al. (1987). *J. Am. Chem. Soc., 109*, 1858.

Rashba, E. I. (2000). *Physical Review B, 62*(24), R16267.

Ruden, P. P. et al. (2004). *Journal of Applied Physics, 95*, 4898.

Salleo, A. et al. (2004). *Physical Review B, 70*, 115311.

Santos, T. et al. (2007). *Physical Review Letters, 98*, 16601.

Seong, j. Y. et al. (2004). *Journal of the Korean Physical Society, 45*, S914.

Shur, M. et al. (1989). *Journal of Applied Physics, 66*(7), 3371.

Singh, K. A. et al. (2010). *Advanced Functional Materials, 20*, 2216.

Sirringhaus, H. et al. (1998). *Science, 280*, 1741.

Sirringhaus, H. et al. (1999). *Nature, 401*, 685.

Sirringhaus, H. et al. (1999b). *Adv. Solid State Phys., 39*, 101.

Sirringhaus, H. et al. (2000). *Applied Physics Letters, 77*, 406.

Sokolov, A. N. et al. (2011). *Nature Communications, 2*, 437.

Steudel, S. et al. (2006). *Applied Physics Letters, 89*, 183503.

Street, R. A. (2005). *Physical Review B, 71*, 165202.

Takeshi Hirose, et al. (2010). *Applied Physics Letters, 97*, 83301.

Tanaka, K. et al. (1994). *Synthetic Metals, 66*, 295.

Tomo Sakanoue, et al. (2010). *Nature Materials, 9*, 736.

Tsumura, A. et al. (1986). *Applied Physics Letters, 49*(18), 1210.

Vardeny, Z. et al. (1981). *Physical Review Letters, 46*(18), 1223.

Vinzelberg, H. et al. (2008). *Journal of Applied Physics, 103*, 93720.

Waragai, K. et al. (1995). *Physical Review B, 52*(3), 1786.

Xiong, Z. H. et al. (2004). *Nature, 427*, 821.

Yamamoto, T. et al. (1980). *Journal of Polymer Science, Polym. Lett. Ed., 18*, 9.

Yong-Young Noh. et al. (2009). *Organic Electronics, 10*, 174.

Zhang, Z. G. et al. (2003). *Journal of Applied Physics, 93*(13), 8552.

Zhao, N. (2004). et al. *Macromolecules, 37*, 8307.

Chapter 5

Conclusions

Motivated by the idea of exploring alternative semiconductors with suitable properties for spin electronic devices, we have investigated the class of the organic semiconductors. This family of materials consists in a great variety of compounds, with different morphology and properties. We have optimized the preparation of small-molecule thin films of Alq_3, oligoacene single crystals of pentacene, and conductive-polymer thin films of P3HT. These materials have been included in field effect transistors consisting of ferromagnetic source and drain contacts separated by a tiny gap. The idea was to use the contacts as the injector and detector of a spin polarized current. The device would exhibits low or high resistance for magnetization parallel or antiparallel of the two electrodes, offering a way to electrically verify the occurrence of spin injection and transport inside the organic media.
Lateral structures consisting of Co /Al_2O_3 electrodes with a film of Alq_3 deposited in the gap have been first characterized, in terms of their electric and magnetic transport properties. We have found that amorphous films of Alq_3 are very resistive, about $2 \cdot 10^9$ Ω cm, from which a mobility of, at most, 10^{-5} $cm^2V^{-1}s^{-1}$ can be estimated, characterized by low signal to noise ratio, as expected for conduction in insulators. The effect of a local electric field induced by a gate voltage, in short-channel devices, was almost completely masked by charges temporarily trapped in localized states within the amorphous organic medium. Finally, we did not observe any signature of magneto-resistance, on scanning the magnetic field slowly from 5 to -5 T and back.
These results are actually quite important, in view of the current scientific debate around the occurrence of spin injection and detection in vertical spin valve structures based on Alq_3. In practice, it is unclear whether the reported effects are based on GMR or TMR because pinhole formation during the metal deposition on top of the organic layer can reduce the effective layer thickness to just a few nm. Lateral transport structures avoid this possible side effect, as the organic material is evaporated on top of pre-patterned

electrodes. The fact that no magneto-resistance was detected in our lateral devices suggests that earlier reported MR was probably due to tunneling between pinholes, from the top ferromagnetic contact to the bottom one. This interpretation is reinforced by the fact that the presence of high energy barrier at the contact interface between a metal and Alq_3 is revealed by our measurements. Under these circumstances, the application of several volts between the electrodes is necessary to achieve current injection. This supports the tunneling interpretation of the previous reports, in which significant conduction was achieved at low bias, around tens of mV.

These first results triggered our interest in single crystals of pentacene. Here, reflecting the ordered morphology of the crystal, we have obtained very stable drain currents. In a previous work a magneto-resistive effect was observed in hybrid NiFe /rubrene devices, attributable to weak localization (Burke, 2011). This suggested that electrons could travel distances in excess of 100 nm inside the crystal without spin flip scattering, because it would destroy the phase memory required for weak localization. The contacts were revealed to be Schottky barrier limited. The introduction of a thin Al_2O_3 barrier between the ferromagnetic electrodes and the conduction channel should promote spin accumulation in the non-magnetic material; however, in the case of rubrene, the attempt of Burke and coworkers proved unsuccessful, suggesting, that there may exist an intrinsic mechanism that depolarizes the spin current during hole transport in oligoacene crystals. In our NiFe /pentacene structures we approached the problem by minimizing the channel length to less than the reported localization length. The application of a gate electrode enhanced the conductivity, raising the signal to noise ratio; the effect was actually not very pronounced, with on /off ratio of about 5, presumably due to the geometry of the device in which the crystal is not in direct contact with the dielectric surface. Nevertheless, the response to a local electric field clearly exhibited the general behavior of a hole transporting system, in which the drain current is enhanced by negative gate bias. The non-linear electrical characteristics indicate that injection is via thermionic emission and tunneling across an interface barrier of extracted activation voltage around 1.6 V. The barrier at the organic-metal interface, and associated high contact resistance, originate in this device from a combination of mismatch of the work function of metal and pentacene along with the metal native oxide and the likely presence of a vacuum-gap at the contact area (due to the terraced morphology of the crystal surface).

We have observed no magneto-resistance at temperatures ranging from 10 to 300 K. Interestingly, spin injection-detection in oligoacene crystals via ferromagnetic metal

electrodes has not been measured for either contact nature (tunneling, in our device, or Schottky, in (Burke, 2011)).

Several mechanisms were shown, in Chapter 1, to contribute to localize charge carriers in pure organic crystals: the polaronic effect, the thermally induced disorder and the narrow bandwidth intrinsic of this class of materials. As a consequence, charge transfer occurs preferentially via the mechanisms of multi trap and release or hopping. Both processes are, typically, phonon assisted, hence it may be expected that spin-states are depolarized by phonon scattering, in our crystals.

Then, we have considered the problem of spin injection in conjugated conductive polymers. The use of soluble organic semiconductors has long been envisaged to have the potential to impact the manufacturing cost of electronic devices. In the pioneering work of (Krinichnyi V. A., 1996) a spin current in intrinsic polymers, investigated by electron paramagnetic resonance spectroscopy, was shown to persist over long time periods, via polaronic states. Here we have observed no spin valve effect in hybrid ferromagnetic metal /P3HT devices, which naturally raises the question on why spin injection /detection at a metal-polymer interface does not occur efficiently.

As illustrated in chapter 4, by preparing a set of devices based on different contact materials and performing low temperature measurements, we have revealed that an energy barrier builds up when a polymer and a metal are brought together. This has fundamental consequences for spin injection: in order to overcome the energy impediment, carriers are typically injected at relatively high bias. Hot carriers thermalize (dissipate energy) by interacting with phonons, typically on a scale of 0.5 eV/ps in non-crystalline semiconductors (Vardeny, 1981). The key point is that electron-spin states depolarize by scattering with such phonons, hence a barrier at the contact represents a dominant impediment to the accumulation of spin in the semiconductor.

The origin of the barrier at the contact area is not easy to discern: our measurements have proven that the approximation of a rigid band model is not valid for this interface. Presumably, the polymer nano-morphology at the ridges of the contacts creates a large density of surface states, which pin the Fermi level; therefore the Schottky barrier height becomes independent of the work function of the metals used.

We have prepared field effect transistors with ferromagnetic electrodes and P3HT, and observed a pronounced effect of a gate voltage on the drain currents, with on /off ratio among 10^2 and 10^3. These actually represent record values for short channel polymer-FET (Takeshi Hirose, 2010). For the first time, the low-temperature (7 K) field effect mobility

of P3HT was estimated, around 10^{-2} $cm^2V^{-1}s^{-1}$. Our observations suggest that charge transport at low and high gate voltages occurs via different mechanisms. Due to the spatial disorder, a distribution of states extending in the energy gap of the polymer exists; these states are the first to be occupied as charges are introduced, locating the Fermi level initially deep in the gap. At low gate voltage, the likely transport mechanism is thermally activated hopping among these gap states. At more negative gate biases, the Fermi level moves towards the energy level typical of the mobility edge in the material, and becomes pinned there. At this energy the number of states is sufficiently high so that electrons no longer have to be thermally activated in order to move, but they can tunnel from one centre to another by quantum mechanical hopping (Mott, 1973).

As previously described, the introduction of a thin Al_2O_3 barrier between a ferromagnetic electrode and a semiconductor typically promotes spin accumulation in the non-magnetic material. Here, an artificial barrier also plays the important role of chemical de-coupling the organic material from the 3-d metal, preventing hybridization of surface states. The insertion of a tunnel barrier proved unsuccessful in terms of spin conservation in our devices, this supports the idea that the polymer nano-morphology is the origin of the interface states. At the contact area, the self-assembly of polymer into crystalline lamellas is disrupted, resulting in a distorted morphology rich in defects states. Evidence of discontinuity of the polymer morphology in the contact regions was in fact directly observed by (Singh, 2010).

In Chapter 4 we anticipated that the main charge carriers in organic polymers can be either spin polarons or spinless bipolarons. Polarons are formed on the chains of the polymer when charge is first added, but at increasing carrier concentration they may recombine into bipolarons. Thus the type of charge carriers changes at increasing carrier concentration, from a polaron which has spin ½ to a bipolaron which has no spin. It is interesting to note, at this point, that in this work the application of a gate voltage was adopted to induce carrier accumulation in the organic channel. The underlying reason is that carrier mobility is very low, and without enhancing the conductivity the drain current would be negligibly small (i.e. there would be no signal to measure). However, the accumulation of carriers has the counter effect of creating bipolarons. At increasing concentration of spinless bipolarons the spin polarization of the current will decay. In other words, to have a reasonably high signal to noise ratio, a mechanism which depolarizes the spin current is automatically invoked. This acts in addition to the impediment provided by the interface barrier.

It was foreseen in Chapter 1 that in order to realize three-terminal devices utilizing spin polarized electronic currents, materials and structures have to be found to act as spin-polarized current injector, transmitters, manipulators and detectors. The metal /organic interface did not prove to be an efficient injection structure for this purpose.

The transmission and manipulation of spins pose the requirement of materials with large spin diffusion length, small effective masses and high mobility, in order to have spin-ballistic transmission. The organic semiconductors tested in this work, have displayed fairly low field effect mobility. The presence of intrinsic depolarizing mechanisms, associated with high carrier concentrations, limits the possibility of increasing the conductivity via gating or doping the channel; hence materials with intrinsically higher mobility are necessary.

The work of this thesis has revealed the presence of various obstacles to the employment of spin polarized electrical current in organic based electronic devices. The search of suitable materials for the realization of a spin field-effect transistor is far from a conclusion. Our experience suggests that organic semiconductors are not of immediate consideration for this purpose; the synthesis of new, more conductive, compounds could promote their use in electronic devices, while technologies based on spin would also require new methods to engineer the contact area.

Bibliography

Burke, F. (2011). *Synthetic Metals, 1*, 13332.

Krinichnyi, V. A. (1996). *Russian Chemical Reviews, 65*(6), 521.

Mott, N. F. (1973). *Electronics & Power, 9 August*, 321.

Singh, K. A. et al. (2010). *Advanced Functional Materials, 20*, 2216.

Takeshi Hirose, et al. (2010). *Applied Physics Letters, 97*, 83301.

Vardeny, Z. et al. (1981). *Physical Review Letters, 46*(18), 1223.

Electron and Spin Injection in Short-Channel Organic Semiconducting Devices

Simone Alborghetti

School of Physics, Department of Science

Trinity College Dublin

A thesis submitted to the University of Dublin in partial fulfillment of the requirements for the degree of

Doctor of Philosophy

October 2011